The
Stability and Characteristics
of the
Flow past Rings

by

Gregory John Sheard

A Thesis submitted to Monash University

for the degree of

Doctor of Philosophy

February 2004

Department of Mechanical Engineering

Monash Universty

For Irene.

Statement of Originality

This thesis contains no material that has been accepted for the award of a degree or diploma in this or any other university. To the best of the candidate's knowledge and belief, this thesis contains no material previously published or written by another person except where due reference is made in the text of this thesis.

Candidate: Gregory J. Sheard

February 2004

Big whorls have little whorls

That feed on their velocity,

And little whorls have lesser whorls,

And so on to viscosity.

Lewis F. Richardson, 1920.

In fluid dynamics, you have to smooth whatever you can, whenever you can, as much as you can.

A. Jameson, 1994.

Abstract

A numerical study of the flow past rings is presented. The study is limited in scope to the low-Reynolds-number range $Re \lesssim 350$ which is sufficient to include the important two- and three-dimensional wake transitions. Flow transitions that are investigated include the transition from attached to separated flow, and the transitions to both unsteady flow, and non-axisymmetric flow.

The ring geometry is described by a single geometric parameter, the aspect ratio, Ar, which is the ratio of the mean ring diameter to the ring cross-section diameter. By varying the aspect ratio from zero to infinity, a continuous geometric variation from a sphere to a straight circular cylinder is described. The ring therefore provides a useful geometry for a study of the flow past bluff bodies, as probably the two most widely studied and well-understood bluff bodies are represented by the rings corresponding to the minimum and maximum limiting aspect ratios.

A spectral-element method is applied to compute the flow past rings. Meshes have been constructed to model a significant number of aspect ratios over the range $0 \leq Ar \leq 40$. Thorough spatial resolution studies verify that the meshes maintain a spatial accuracy in the order of 0.1%, while a domain study reveals that an accuracy in the order of 1% is expected, when compared to the idealised case of flow in an infinite domain.

For different aspect ratios, the axisymmetric flows past rings are computed, and a combination of flow visualisation, wake recirculation bubble measurements and velocity transient measurements have enabled the identification of three aspect ratio ranges which exhibit unique flows. Wakes comprising a steady attached recirculation bubble, a detached recirculation bubble, and an attached annular recirculation ring were observed. In addition, drag coefficient and Strouhal number measurements were also made for these axisymmetric flows.

The stability of the axisymmetric wakes to non-axisymmetric perturbations was studied by employing a linear stability analysis technique. This technique enabled three flow regimes to be identified for $0 \leq Ar \lesssim 3.9$, where the non-axisymmetric transition preceded the transition to an axisymmetric vortex street. Three vortex street instability modes were predicted for the wakes behind rings with $Ar \gtrsim 3.9$. These included analogues of the Mode A and B instabilities familiar from studies pertaining to the wake of a circular cylinder, and an additional instability, Mode C, which was

subharmonic.

Non-axisymmetric computations are employed to study the wake structure and non-linear transition behaviour of the modes. The Landau model is applied to determine which of the transitions are subcritical and which of the transitions are supercritical. Non-axisymmetric amplitude measurements in the vicinity of the transitions are used to verify the predicted hysteretic properties of the bifurcations.

Following the presentation of drag force and velocity spectra, as well as discrete azimuthal mode energy evolution, an analysis of the vortex streets in the wakes behind rings is performed. Both the azimuthal domain and the Reynolds number are varied, and it is shown that regardless of the presence of a period-doubling mode in the wake for some aspect ratios, the transition to turbulence occurs as irregularities emerge in the vortex streets through the development of spatio-temporal chaos.

A coupled dynamical model is developed which describes the three-dimensional flow regime for the flow past a circular cylinder. The model accurately predicts the Strouhal–Reynolds number profile throughout the flow regime. In addition, a linear stability analysis is performed on spanwise-averaged base flows constructed from the three-dimensional wakes corresponding to Mode A and B in the wake of a circular cylinder. The analysis assists in describing the discrepancy between the predicted and measured onset of Mode B in the wake. A theory is developed which explains the Reynolds number ranges for the Mode A regime, the mixed Mode A/B regime, and the Mode B regime in the vortex street behind a circular cylinder.

Acknowledgements

For their assistance over the duration of my candidature, I would like to thank my supervisors, A/Prof. Mark C. Thompson and Kerry Hourigan, whose enthusiasm for the subject of fluid mechanics has been infectious.

I am grateful to the Department of Mechanical Engineering, Monash University, for providing the office space and resources necessary for the completion of this study. Furthermore, I wish to acknowledge the Victorian Partnership for Advanced Computing (VPAC), for granting access to their high performance computing facility. Thank you also to Jane Moodie for suggesting structural improvements to the thesis in the final stages of its preparation.

I wish to express my gratitude for the financial backing provided through an Australian Postgraduate Award (APA) scholarship, and briefly, a Monash Departmental Scholarship (MDS).

My thanks also extends to Thomas Leweke, whose enthusiasm and expertise motivated the experimental flow visualisation work performed for this study. Without his assistance and advice during his stay at Monash University over the summer of 2002/2003, the experimental phase of this project may not have come to fruition.

To Kris and Craig, my fellow postgraduate students and office-dwellers: Thankyou for providing good company and a stimulating environment for research (and sometimes for procrastination!) over the course of our degrees.

I would like to thank my family (in order of increasing age/wisdom), Emma, Nick, Mum, Dad and Nana, for their ongoing love and support. Now there is just one more thesis in the immediate family to be submitted. . .

Finally, thankyou also to the Tan family; Mr. and Mrs. Tan, Lilian, and (most importantly!) Irene, for the enjoyable times we have had over the last four years, including the many feasts (all those poor lobsters!) and some delicious curry recipes.

Publications Relating to Thesis

Sheard, G., Thompson, M.C. & Hourigan, K. 2001 A 2D numerical study of the flow around bluff rings. *In proceedings of the 1st Melbourne Graduate Fluids Conference*, Monash University, Victoria, Australia, July 2001.

Sheard, G., Thompson, M.C. & Hourigan, K. 2001 A numerical study of bluff ring wake stability. *In proceedings of the 14th Australasian Fluid Mechanics Conference*, University of Adelaide, Adelaide, South Australia, Australia, December 2001.

Sheard, G., Thompson, M.C. & Hourigan, K. 2002 On Axisymmetric Bluff Body Wakes: Three-Dimensional Wake Structures and Transition Criticality of the Torus. *In proceedings of the 3rd Conference on Bluff Body and Vortex Induced Vibrations*, Rydges Reef Resort, Port Douglas, Queensland, Australia, December 2002.

Sheard, G., Thompson, M.C. & Hourigan, K. 2003 Criticality and structure of the asymmetric vortex shedding modes of bluff ring wakes. *In proceedings of the 5th Euromech Fluid Mechanics Conference*, Centre de Congrès Pierre Baudis, Toulouse, France, August 2003.

Sheard, G., Thompson, M.C. & Hourigan, K. 2003 A Coupled Landau Model Describing the Strouhal–Reynolds Number Profile of a Three-Dimensional Circular Cylinder Wake. *Phys. Fluids* **15**(9), L68–L71.

Sheard, G., Thompson, M.C. & Hourigan, K. 2003 From Spheres to Circular Cylinders: The Stability and Flow Structures of Bluff Ring Wakes. *J. Fluid Mech.* **492**, 147–180.

Sheard, G., Thompson, M.C. & Hourigan, K. 2004 Asymmetric Structure and Non-Linear Transition Behaviour of the Wakes of Toroidal Bodies. *Euro. J. Mech. B (Fluids)* **23**(1), 167–179.

Sheard, G., Thompson, M.C. & Hourigan, K. 2004 From Spheres to Circular Cylinders: Non-Axisymmetric Transitions in the Flow past Rings. *J. Fluid Mech. (In Press).*

Nomenclature

A list of nomenclature used throughout the thesis is included here. Mathematical symbols are presented, followed by Greek alphabet nomenclature and English alphabet nomenclature.

Symbol	Description
$\S$	Thesis section
$\int$	Integration
∇	Vector gradient operator (grad)
∇^2	Del squared (or div grad) operator
$\sum_{i=a}^{b}$	Sum of arguments with j incrementing from a to b
α_1^A	Cubic saturation coefficient for Mode A amplitude in coupled Landau model
α_1^B	Cubic saturation coefficient for Mode B amplitude in coupled Landau model
α_2^A	Quintic saturation coefficient for Mode A amplitude in coupled Landau model
Γ_i	Inlet wall boundary of computational domain
Γ_o	Outlet boundary of computational domain
Γ_t	Outer transverse wall boundary of computational domain
Γ_{axis}	Wall boundary of axis of symmetry in computational domain
Γ_{ring}	Wall boundary of ring cross-section in computational domain
γ_1^A	Cubic coupling coefficient for Mode A amplitude in coupled Landau model
γ_1^B	Cubic coupling coefficient for Mode B amplitude in coupled Landau model
ΔE_i	i^{th} uncertainty in computations
ΔE_{tot}	Overall error in computations
Δx	Change in a given variable x
δ	Boundary layer thickness

Continued on the next page.

Continued from previous page.

Symbol	Description
η_{diff}	Landau diffusivity constant
θ	Azimuthal cylindrical polar coordinate
λ	Wavelength
λ_i	Wavelength based on i–scale
$\lambda_{i_{max}}$	Maximum wavelength based on i–scale
μ	Fluid viscosity, Floquet multiplier
μ^A	Linear evolution equation multiplier for Mode A
μ^B	Linear evolution equation multiplier for Mode B
ν	Kinematic viscosity
ξ	Real variable in equation solved to find Gauss-Legendre-Lobatto quadrature points
ρ	Density, magnitude of the amplitude A in the Landau equation
ρ_{sat}	Amplitude of A at saturation (Landau model)
ρ_{sat}^A	Magnitude of amplitude of Mode A at saturation for coupled Landau model
ρ_{sat}^B	Magnitude of amplitude of Mode B at saturation for coupled Landau model
σ	Linear growth rate in the Landau equation and linear stability analysis
σ_n	Growth rate of a linear instability mode over the n^{th} period in linear stability analysis
τ	Shear strain rate
Φ	Phase angle of the amplitude A in the Landau equation
Φ^A	Phase angle of the amplitude of Mode A in the coupled Landau model
Φ^B	Phase angle of the amplitude of Mode B in the coupled Landau model
ϕ	Deformation angle of a fluid element under continuous shear
$\Psi_{cylinder}$	Normalising coefficient in the L_2 norm integral
Ω	Computational domain of the ring model
$\boldsymbol{\omega}$	Vorticity field
ω	Angular frequency

Continued on the next page.

Continued from previous page.

Symbol	Description
ω^A	Angular frequency in linear term of the coupled Landau model amplitude equation for Mode A
ω^B	Angular frequency in linear term of the coupled Landau model amplitude equation for Mode B
ω_i	i–direction vorticity component
ω_{sat}	Angular frequency of A at saturation (Landau modelling
ω^B_{sat}	Angular frequency of amplitude of Mode B in the coupled Landau model
A	First real coefficient of Strouhal–Reynolds relationship for laminar vortex shedding, Complex amplitude in Landau equation, Mode A amplitude in coupled Landau model
a	Frequency shift factor in the Strouhal–Reynolds number relationship for rings proposed by Leweke & Provansal (1995)
$A_{frontal}$	Projected frontal area of ring
A_i	Amplitude of Mode A evaluated at i^{th} time step in coupled Landau model
A_n	n^{th} period of the coupled evolution equation for Mode A proposed by Barkley *et al.* (2000)
Ar	Ring aspect ratio
B	Second real coefficient of Strouhal–Reynolds relationship for laminar vortex shedding, Mode B amplitude in coupled Landau model
B_i	Amplitude of Mode B evaluated at i^{th} time step in coupled Landau model
B_n	n^{th} period of the coupled evolution equation for Mode B proposed by Barkley *et al.* (2000)
C	Third real coefficient of Strouhal–Reynolds relationship for laminar vortex shedding
c	Landau constant
c_1^A	Complex coefficient of cubic term for Mode A amplitude equation in the coupled Landau model
c_1^B	Complex coefficient of cubic term for Mode B amplitude equation in the coupled Landau model

Continued on the next page.

Continued from previous page.

Symbol	Description
c_2^A	Complex coefficient of quintic term for Mode A amplitude equation in the coupled Landau model
C_d	Drag coefficient
C_{d_ν}	Viscous component of drag coefficient
C_{d_p}	Pressure component of drag coefficient
D	Mean diameter of ring
d	Diameter of ring cross-section, Reynolds number length scale
d_1^A	Complex cubic coupling coefficient for Mode A amplitude in coupled Landau model
d_1^B	Complex cubic coupling coefficient for Mode A amplitude in coupled Landau model
$\mathbf{DN}(\mathbf{u})$	Linearised advection term operator in the Navier–Stokes equations for linear stability analysis
DS_i	i^{th} mesh employed in domain study
E_q	Kinetic energy of the q^{th} azimuthal mode of velocity at a point in the wake
$\mathcal{F}$	Fourier transform
f_0	Dominant frequency of oscillation
f_i^A	Right hand side of Mode A coupled Landau model equation evaluated at i^{th} time step
f_i^B	Right hand side of Mode B coupled Landau model equation evaluated at i^{th} time step
F_d	Total drag force
F_{l_ν}	Viscous component of lift force
F_{l_p}	Pressure component of lift force
Fr	Froude number
$f(x)$	Function of x (employed in Gauss-Legendre-Lobatto quadrature)
$g(Re)$	Strouhal frequency shift function of Re from the Strouhal–Reynolds number relationship for rings proposed by Leweke & Provansal (1995)
i	Imaginary number ($\mathrm{i} = \sqrt{-1}$)
J	Number of azimuthal Fourier planes in non-axisymmetric numerical formulation

Continued on the next page.

Continued from previous page.

Symbol	Description
j	Counter for number of planes in non-axisymmetric numerical formulation
K	Ring curvature
l	Cubic saturation term in Landau equation
L_0	Azimuthal span corresponding to the Mode A instability
L_2	A norm of the azimuthal or spanwise velocity field
l_i	Inlet domain length of computational mesh of the ring model
l_o	Outlet domain length of computational mesh of the ring model
l_t	Outer transverse domain length of computational mesh of the ring model
L_{teth}	Tether length in tethered-body computations
l_{axis}	Inner transverse domain length of computational mesh of the ring model
m	Azimuthal or spanwise mode number of an instability
$m^\star$	Mass ratio for tethered-body computations
m^A	The gradient of the growth rate, $\sigma^A(Re)$, from the coupled Landau model
Ma	Mach number
M_d	Critical azimuthal mode number beyond which viscous dissipation dominates
$N_{\Delta E}$	Number of uncertainties in computations
$\mathbf{N}(\mathbf{u})$	Non-linear advection term operator in the Navier–Stokes equations for liner stability analysis
$N[\mathbf{u}'(t)]$	Norm of perturbation field at time t
N^2	Number of nodes per element employed in computations
N_t	Number of spanwise-averaged velocity field snapshots included for spanwise-averaged linear stability analysis
P	Scalar pressure
p	Kinematic pressure
$\hat{p}$	Complex perturbation pressure field amplitude for linear stability analysis

Continued on the next page.

Continued from previous page.

Symbol	Description
$\hat{p}_m$	Azimuthal Fourier component of decoupled perturbation kinematic pressure field
p'	Perturbation field kinematic pressure for linear stability analysis
p'_m	Fourier component of the perturbation pressure field for linear stability analysis, with azimuthal mode number m
P_m	Legendre Polynomial of order m
r	Radial cylindrical polar coordinate
$R_{blockage}$	Blockage (area) ratio of frontal projected areas of body to computational domain
Re	Reynolds number
Re^A_{last}	Highest Reynolds number at which evidence of Mode A is observed in the wake of a circular cylinder
Re^B_{first}	Lowest Reynolds number at which evidence of Mode B is observed in the wake of a circular cylinder
Re_c	A critical or transition Reynolds number
Re_{C1}	Flow separation transition Reynolds number for the wake of a circular cylinder
Re_{C2}	Hopf transition Reynolds number for the wake of a circular cylinder
Re_{C3}	Three-dimensional transition Reynolds number for the wake of a circular cylinder
Re_{S1}	Flow separation transition Reynolds number for the wake of a sphere
Re_{S2}	Regular non-axisymmetric transition Reynolds number for the wake of a sphere
Re_{S3}	Hopf transition Reynolds number for the wake of a sphere
Re_{T1}	Ring flow separation transition Reynolds number
Re_{T2}	Ring unsteady flow transition Reynolds number
S	Ring solidity parameter
St	Strouhal number
St_0	Strouhal frequency for parallel shedding in the wake of a circular cylinder
St_{3D}	Strouhal frequency for a three-dimensional or a non-axisymmetric flow
St_c	The Strouhal number at Re_{T2} for a given Ar

Continued on the next page.

Continued from previous page.

Symbol	Description
St_{C2}	The Strouhal number of parallel shedding at Re_{C2} for the circular cylinder
T	Period of an oscillating flow
t	Time (non-dimensionalised)
$\hat{t}$	Time (dimensional)
t_0	Initial time
T_{2D}	Period of a two-dimensional or axisymmetric flow
T_{3D}	Period of a three-dimensional or non-axisymmetric flow
U	Fluid velocity magnitude scalar for parameter relationships
U_∞	Mean free-stream velocity
u	Axial cylindrical polar velocity component, Cartesian x–direction velocity component
$\mathbf{u}$	Velocity vector
$\hat{\mathbf{u}}$	Complex perturbation velocity field amplitude for linear stability analysis
$\hat{u}_m$	Amplitude of the m^{th} azimuthal Fourier mode of the axial velocity component of the perturbation field
$\mathbf{u}'$	Perturbation field velocity vector for linear stability analysis
$\mathbf{u}'_m$	Fourier component of the perturbation velocity field for linear stability analysis, with azimuthal mode number m
$\mathbf{u}^*$	Velocity field at first substep
$\mathbf{u}^{**}$	Velocity field at second substep
$\mathbf{u}_{2D}$	Two-dimensional base flow field for linear stability analysis
$\bar{\mathbf{u}}_{3D}$	Spanwise-averaged base flow field for linear stability analysis
$\mathbf{u}^n$	$\mathbf{u}$ at the n^{th} timestep
$\mathbf{u}^{n+1}$	$\mathbf{u}$ at the $(n+1)^{\text{th}}$ timestep
u_j	u–velocity component of the j^{th} azimuthal expansion in the non-axisymmetric numerical formulation
$\tilde{u}_1$	Complex variable for velocity in the axisymmetric coordinate system
$\tilde{u}_2$	Complex variable for velocity in the axisymmetric coordinate system
V	Volume of the computational domain

Continued on the next page.

Continued from previous page.

Symbol	Description
v	Radial cylindrical polar velocity component, Cartesian y–direction velocity component
$\hat{v}_m$	Amplitude of the m^{th} azimuthal Fourier mode of the radial velocity component of the perturbation field
v_j	v–velocity component of the j^{th} azimuthal expansion in the non-axisymmetric numerical formulation
w	Azimuthal cylindrical polar velocity component, Cartesian z–direction velocity component
$\hat{w}_m$	Amplitude of the m^{th} azimuthal Fourier mode of the azimuthal velocity component of the perturbation field
w_j	j^{th} Gauss-Legendre-Lobatto weighting coefficient, w–velocity component of the j^{th} azimuthal expansion in the non-axisymmetric numerical formulation
x	Cartesian streamwise coordinate
x_j	j^{th} Gauss-Legendre-Lobatto quadrature point
y	Cartesian transverse coordinate
z	Axial cylindrical polar coordinate, Cartesian spanwise coordinate

Contents

Introduction

A numerical study of the flow past rings is presented in this thesis. Over the following sections of this introduction, an overview of the problem is provided, the aims of the investigation are stated, and some basic concepts and parameters fundamental to fluid mechanics are introduced. Following this, a description of the problem is provided, assumptions of the study are explained, and finally, the structure of the thesis is outlined.

Overview of the Problem

The study of the flow past a submerged body, and the wake and vortex structures which result, is an ongoing area of research in the field of fluid dynamics. This research is of practical importance, as an understanding of the two- or three-dimensional structure of steady and unsteady wakes is paramount when considering practical engineering problems such as vibration, fatigue, acoustic noise and turbulent flow.

Studies continue into the dynamics of various bodies in open flows (e.g. Roshko 1955; Balachandar *et al.* 1997), including bluff bodies such as spheres (Johnson & Patel 1999; Tomboulides & Orszag 2000; Ormières & Provansal 1999; Thompson *et al.* 2001a), discs (Roos & Willmarth 1971; Natarajan & Acrivos 1993), circular cylinders (Williamson 1996b; Thompson *et al.* 2001b), normal plates (Taneda 1956b), and elongated bodies such as flat plates (Hourigan *et al.* 2001; Mills *et al.* 2002, 2003) and aerofoils. The significant role that the geometry of a body plays to determine the flow characteristics is apparent from the variety of flows observed in these studies. It is imperative to gain a solid understanding of the dependence of the characteristics of the flow field on the body geometry, as well as the parameters describing the fluid flow.

From a geometric perspective, a ring provides an excellent model to study the effect that altering a geometry has on the downstream flow. Despite the simplicity of the ring geometry being considered in this study, it has been afforded little attention

in the research field. In this study, the rings are aligned normal to the direction of flow. A pleasing feature of the ring geometry is that it may be described by a single geometric parameter, known as the aspect ratio Ar. The aspect ratio will be defined shortly, however, it may be noted that a diverse set of geometries are described by this single parameter. At the small-aspect-ratio limit, a sphere is described, and with an increase in aspect ratio, firstly closed rings are described, which resemble blood platelets, and secondly, open rings are described, which increase in slenderness. Local to the ring cross-section, the geometry approaches a straight circular cylinder at the large-aspect-ratio limit (see Monson 1983; Leweke & Provansal 1995). Therefore, two of the simplest and most well-understood bluff bodies provide reference points for the present investigation into the unknown wake dynamics and transitions of the flow past rings.

Aims of the Study

This study aims broadly to compute the flows around rings over a wide range of aspect ratios with a view to understanding the different flow structures as a single geometric parameter is altered. By employing a combination of numerical schemes, both axisymmetric and non-axisymmetric flows are to be computed. A linear stability analysis is to be applied, which will provide predictions as to the spatio-temporal symmetries of the non-axisymmetric instabilities in the wakes. Furthermore, the study aims to ascertain the values of the Reynolds number parameter at which the instabilities occur in the flow.

The study aims to assess the suitability of the Landau model to describe the non-axisymmetric transitions in the wakes behind rings. Verification of this suitability is to be performed by comparing Landau model predictions pertaining to the non-linear transition behaviour at the onset of the instability, with corresponding non-axisymmetric computations of the wakes.

It is intended that a comprehensive mapping of the drag coefficient variation with Reynolds number and aspect ratio be completed, through which an understanding of the effects of variation in a geometry on measurable physical parameters of a bluff-body flow may be ascertained.

The study aims to validate the results the numerical studies by comparing flow visualisation from simulated-particle computations with experimental dye visualisations.

The vortex streets in the wakes behind rings with large aspect ratios will be investigated in the context of the development of chaotic and turbulent flows, and these studies will be compared with the flow past a straight circular cylinder.

Finally, the study aims to shed new light on the three-dimensional transition scenario in the wake of a circular cylinder, through application of both a coupled oscillator model and a modified stability analysis technique.

Fundamental Fluid Dynamics Concepts

Before discussing the problem addressed in this work, it is helpful to review some of the relevant fundamental concepts of fluid dynamics. More detail may be found in texts such as White (1999).

A fluid may be defined as a medium that deforms continuously when subjected to any finite strain. The two most common examples of fluids in nature that are recognisable to the lay-person are air and water. In fact, all matter in a liquid or gaseous phase satisfies this definition of a fluid.

This investigation is concerned with an idealised class of fluids known as Newtonian fluids. For a Newtonian fluid element with dimensions δy high and δx wide, a shear stress τ causes a continuous shear deformation at a rate $\delta\phi/\delta t$. Following White (1999, pp. 22–23), a relationship for the shear stress as a function of the velocity gradient may be written

$$\tau = \mu \frac{\mathrm{d}u}{\mathrm{d}y},$$

where the viscosity, μ, is the constant of proportionality.

The Reynolds Number and the Strouhal Number

Throughout this work the fluid density ρ is assumed to be almost constant, and is combined with the viscosity μ to form the kinematic viscosity

$$\nu = \frac{\mu}{\rho}.$$

The importance of the relationship between the kinematic viscosity, a representative velocity of a fluid (e.g. U) and a suitable length scale (e.g. d), was first discovered by Reynolds (1883) (reprinted in Reynolds 1901), from a series of experiments investigating the development of unsteady and turbulent flow in pipes. The non-dimensional group, Ud/ν, is known as the Reynolds number (Re) and is the most important dimensionless

parameter in fluid mechanics as it determines the nature of a flow. Steady laminar flows are observed at low Reynolds numbers, while unsteady and turbulent flows are observed at high Reynolds numbers.

When considering unsteady flows, it is convenient to non-dimensionalise the frequency, f, of the flow. The classic "Aeolean harp" experiments performed by Strouhal (1878) concerned the flow of air normal to cylindrical wires, and through that work the importance of the dimensionless group fd/U was established for unsteady flows. The dimensionless group has since come to be known as the Strouhal number (St).

Vorticity

Vorticity ($\boldsymbol{\omega}$) is a fundamental concept relating to the structural and dynamic properties of a flow field and is employed to characterise and understand various features of the computed flows. It is written

$$\boldsymbol{\omega} \equiv \text{curl } \mathbf{u} \equiv \nabla \times \mathbf{u}, \tag{i}$$

and is equal to twice the local angular velocity. In nature regions of high vorticity may be observed in swirling river flows and in atmospheric events such tornadoes.

Components of the vorticity field have the useful property of being independent of the reference frame of the observer. This is referred to as Galilean invariance. Expanding equation i into its components in Cartesian coordinates gives

$$\omega_x = \frac{\partial w}{\partial y} - \frac{\partial v}{\partial z}, \tag{ii}$$

$$\omega_y = \frac{\partial u}{\partial z} - \frac{\partial w}{\partial x}, \tag{iii}$$

$$\omega_z = \frac{\partial v}{\partial x} - \frac{\partial u}{\partial y}. \tag{iv}$$

In the case where the flow field is two-dimensional, only ω_z is non-zero, and hence the rotational state of the flow is described by the z–vorticity component.

The Ring Flow System

The system investigated in the present study consists of a ring of circular cross-section, submerged in a fluid, and orientated normal to the direction of flow (i.e. the axis of symmetry of the ring is aligned with the flow). The geometry is axisymmetric, in that it does not vary in the azimuthal direction. This symmetry leads to a reduction in dimensionality, which simplifies the numerical formulation of the model.

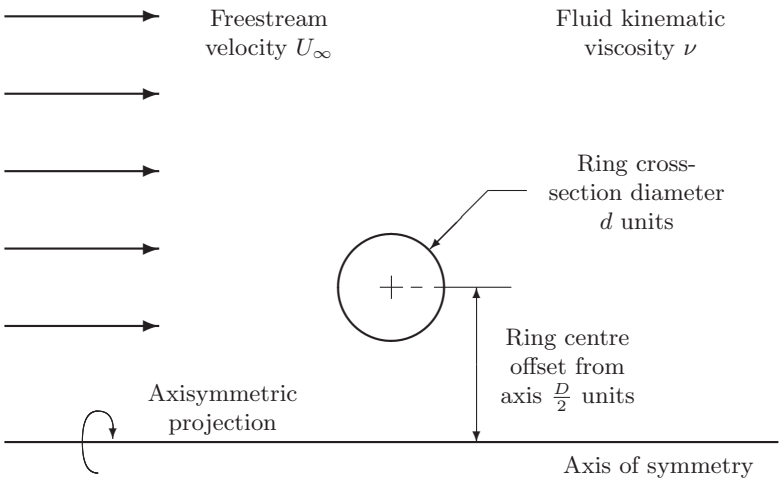

FIGURE I: Schematic representation of the ring model.

Numerically, the flow past a ring is modelled on a rectangular mesh, which is appropriate for the uniform stream condition in the far flow field. The density of macro-elements is increased both downstream of, and around, a circular wall-boundary in the mesh, which models the cross-section of the ring. An axisymmetric projection of the mesh about the axis provides the desired ring geometry by *wrapping* the circular cross-section around the axis to form a ring. Figure I illustrates the concept behind the development of the ring model from the axisymmetric plane.

The diagram in figure I shows that the ring with cross-section d is subject to a uniform free stream velocity U_∞. Defining the kinematic viscosity of the fluid as ν, and the length scale of the ring as the cross-section diameter (d), the Reynolds number for the ring system is defined as

$$Re = \frac{U_\infty d}{\nu}. \tag{v}$$

For computational convenience, the length and velocity scales are non-dimensionalised with d and U_∞.

The choice of the cross-section diameter as the most important length scale of the system is consistent with both previous studies of the flows past rings (Monson 1983; Leweke & Provansal 1995), a sphere (Tomboulides & Orszag 2000) and a circular cylinder (Bloor 1964; Barkley & Henderson 1996).

The Aspect Ratio Parameter

An aspect ratio parameter (Ar) defines the geometry, and is written

$$Ar = \frac{D}{d}. \tag{vi}$$

The aspect ratio is defined as a ratio of the diameter through the centreline of the ring cross-section, to the diameter of the ring cross-section itself.

The present aspect ratio definition differs from the study of Leweke & Provansal (1995), who defined their aspect ratio as the mean circumference of the ring to the cross-section diameter ($\pi D/d$). The alternative aspect ratio definition employed in the present work is used for two reasons. Firstly, the present definition is more intuitive with respect to the numerical formulation, as the computational length d is taken as unity, thus equating Ar with D. Secondly, no long-standing parameter definition exists in the literature for describing the ring geometry. An earlier study (Monson 1983) employed a solidity parameter, S, loosely related to the reciprocal of the aspect ratio defined in the present study, whereas Bearman & Takamoto (1988) and Miau *et al.* (1992) employ a ratio (similar to the present study) of the mean ring diameter to the projected frontal ring width, in studies of the flow past rings of non-circular cross-section.

The aspect ratio parameter may vary between zero and infinity ($0 \leq Ar < \infty$). From figure I it is clear that for aspect ratios $Ar \leq 1$ ($D/2 \leq d/2$), there is no space between the inner surface of the ring cross-section and the axis of symmetry. Over this aspect ratio range closed rings are defined, which approach a sphere as $Ar \to 0$.

Visualisation of Rings with Different Aspect Ratios

In figure II, orthogonal and isometric views of several rings with small aspect ratios are presented for visualisation.

As the aspect ratio increases, the local geometry with respect to the ring cross-section approaches a straight circular cylinder with diameter d. An azimuthal curvature, K, about the ring is defined by the relationship

$$K = \frac{2}{D}, \tag{vii}$$

and decreases as the aspect ratio increases. As $Ar \to \infty$, $K \to 0$, and locally, the cross-section of the ring approaches a straight circular cylinder. This trend is illustrated in figure III.

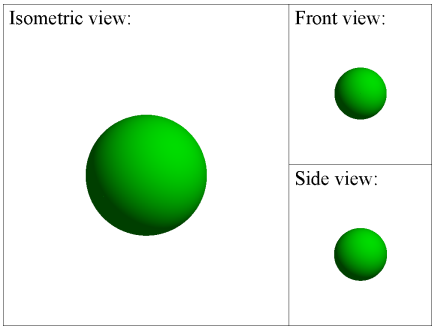

(a) $Ar = 0$ (sphere).

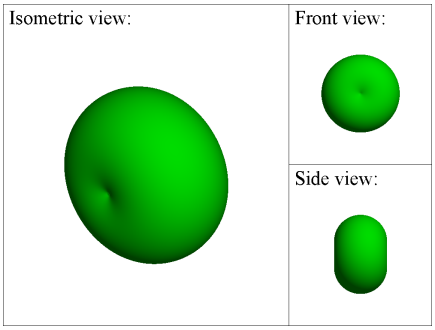

(b) $Ar = 0.5$ (closed ring).

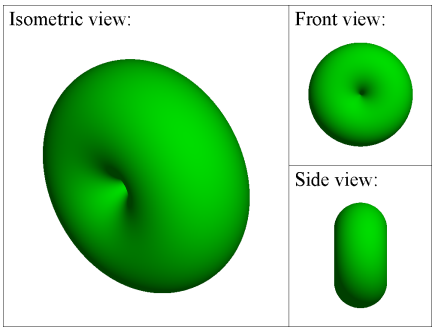

(c) $Ar = 1$ (closed-open transition).

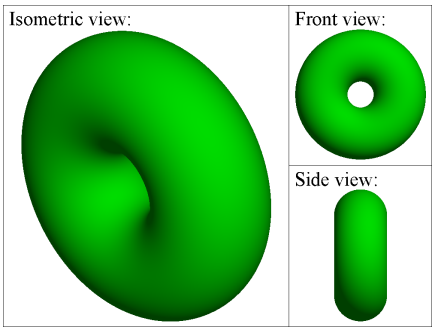

(d) $Ar = 1.5$ (open ring).

FIGURE II: Orthogonal and isometric views of a sphere, and closed and open rings with $0 \leq Ar \leq 1.5$.

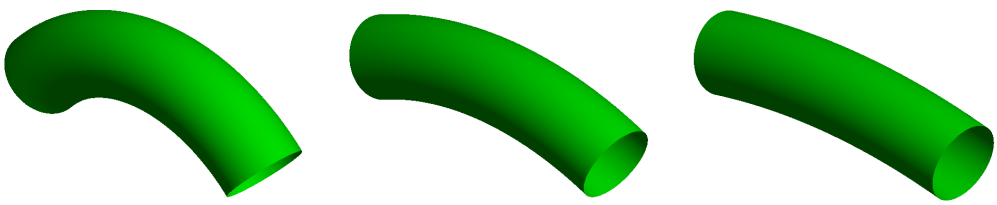

(a) $Ar = 5$, $K = 0.4$.

(b) $Ar = 10$, $K = 0.2$.

(c) $Ar = 20$, $K = 0.1$.

FIGURE III: Ring sections of various aspect ratio, elucidating the increased local similarity to a circular cylinder as the aspect ratio is increased.

It is apparent that a wide range of geometries can be studied with variation in the aspect ratio The ring flow system presents a unique opportunity to examine the effect of geometric variation on the wake dynamics and transition behaviour in the Reynolds number range prior to the development of wake turbulence.

Constraints Imposed in this Study

For the purposes of the present study of the flow past rings, the fluid is assumed to be Newtonian, incompressible and isothermal. Far from the body, the fluid stream is assumed to be laminar, uniform and continuous, with a constant velocity.

The Newtonian fluid assumption specifies that the fluid has a linear relationship between shear stress and shear strain. This assumption is valid for a large range of liquid and gaseous fluids, including air and water, but it does not hold for many fluids such as solutions of polymeric molecules.

The incompressibility constraint specifies that the fluid density remains approximately constant for all time, everywhere in the flow. While this condition is never completely satisfied in practice, its effects have been shown to be negligible for flow speeds less than approximately 30% of the speed of sound in a fluid. For example, as the speed of sound is approximately 340m/s in air, the incompressibility condition applies for speeds of less than approximately 100m/s in air.

The isothermal fluid constraint specifies that the temperature remains constant throughout the fluid. This constraint is appropriate as heat-transfer and thermal convection are not considered in the present study.

The laminar flow constraint in the far wake implies that there is a zero turbulence intensity in the flow. This constraint ensures that the low-Reynolds-number flow transitions being investigated can be modelled in the absence of external disturbances. Furthermore, the body of the ring is taken to be perfectly smooth. This is appropriate for the Reynolds number range of the present study. Surface roughness effects become important at significantly higher Reynolds numbers, and influence the turbulent transition of the boundary layer around the body.

Structure of the Thesis

The preface of the thesis, which comprises the preceding pages, includes a dedication, title page, statement of originality, abstract, acknowledgments, a list of the publications

by the author pertaining to the thesis, nomenclature, the table of contents, and finally, this introduction.

The body of the thesis consists of a literature review in chapter 1, a numerical methods chapter (chapter 2), results chapters (chapters 3–7), and conclusions (chapter 8). Chapters 3–7 contain results from axisymmetric, linear stability analysis, and non-axisymmetric computational studies, as well as a study of the transitions which lead to turbulence in the vortex streets behind rings, and a study which revisits the three-dimensional transitions in the wake of a circular cylinder.

Chapter 1

A Review of the Literature

From the formulation of the ring flow system described previously, it is clear that a review of studies of the flow past a ring would be incomplete without consideration of the flow past a sphere and a circular cylinder. Over the sections to follow, previous studies of the flow past a sphere, a circular cylinder and a ring are reviewed in turn. Despite the limitation of the scope of the present study to a Reynolds number range $Re \lesssim 400$, a more complete overview of the wake dynamics for these geometries is considered for completeness.

1.1 The Flow past a Sphere

The flow past a sphere has been of significant practical importance for centuries. Applications in military fields include ballistics and projectile dynamics, and applications in civil fields range from ball sports to atmospheric particle dynamics.

1.1.1 Attached Flow

One of the earliest analytical studies of the flow past a sphere was performed by Stokes (1851) as part of a study into the resistance on the motion of a pendulum. Stokes solved equations of motion which excluded advection, but included viscous diffusion, and assumed a no-slip condition at the sphere surface. The solution of this problem has become known as Stokes flow, and represents the low velocity limit of the flow of a viscous incompressible fluid past a sphere as $Re \to 0$. Flows at low Reynolds numbers that approximate Stokes flow (generally considered to be flows with $Re < 1$) are known as creeping flows. Creeping flows exhibit a remarkable property known as reversibility. For reversible flow past a symmetrical body such as a sphere, the flow streamlines are symmetrical both upstream and downstream of the body, as shown in figure 1.1(a).

Another feature of reversibility is that if a motion through a fluid is reversed exactly, the fluid particles return to their original positions.

Despite efforts to gain a better analytical description of the far wake of the flow past a sphere over the century following the work of Stokes, it has only been since the middle of the twentieth century that many advancements have been made in the study of the flow past a sphere.

Proudman & Pearson (1957) sought to extended the solution of Stokes (1851) to higher Reynolds numbers. They developed separate locally valid stream function equations for the flow fields near to and far from the body. This formulation reduced the problem to a single set of boundary conditions for each expansion; a no-slip boundary at the sphere surface for Stokes flow, and a uniform stream condition in the far flow field for Oseen flow.

Further efforts were made to extend this analytical description of the flow past a sphere by Chester & Breach (1969). They extended the analysis of Proudman & Pearson (1957) from an expansion of order $Re^2 \log Re$, to an order $Re^3 \log Re$. Consistent with the previous study, they employed expansions for the inner flow which satisfied the no-slip condition of Stokes flow, and expansions for the outer flow field which satisfied the uniform stream condition of Oseen flow.

Chester & Breach (1969) reported that their solution only agrees with experimental measurements over a Reynolds number range $0 < Re \lesssim 0.5$. The limited range over which their solution was accurate suggested that an inappropriate form of the expansions was used, however a more fundamental problem existed: the governing Navier–Stokes equations provide an often insurmountable obstacle when an analytical solution to a fluid flow problem is sought. Their method, which divided the flow field into a near field dominated by viscous diffusion, and a far field dominated by advection, provided an inadequate description of the flow, as flow features such as separation, non-axisymmetry, and unsteady flow were suppressed.

The technological revolution of the latter half of the twentieth century brought about a revolutionary analysis technique known as computational fluid dynamics. Instead of deriving solutions to the Navier–Stokes equations with analytical methods, approximate solutions are obtained with computational numerical methods.

An early computational study of the flow past a sphere was performed by Rimon & Cheng (1969). Their study employed a time-dependent axisymmetric stream-

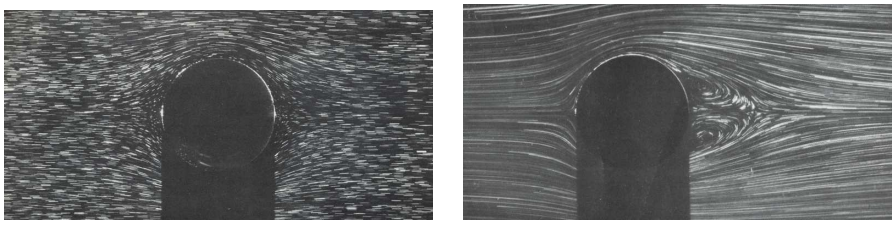

(a) Attached creeping flow at $Re = 0.1$ (photographed by M. Coutanceau).

(b) Separated flow at $Re = 56.5$ (photographed by M. Payard and M. Coutanceau).

FIGURE 1.1: Images of the steady flow past spheres at low Reynolds number (Van Dyke 1982).

function/vorticity formulation, with a finite-difference method used for the spatial discretisation of the vorticity transport equation, and a second-order central-difference scheme used for space and time integration. Their work provides early treatment of the difficulties in constructing a pressure field from vorticity when the velocity field is unknown. Considering the age of the computations, a relatively small sphere to domain diameter ratio of approximately 1 : 8.2 (blockage percentage approximately 1.49%) was employed.

1.1.2 The Transition to Separated Flow

The computations of Rimon & Cheng (1969) predicted that the flow past the sphere remained steady and attached for $Re \lesssim 25$, and for $Re \gtrsim 25$, the flow separated from the rear of the sphere, forming a recirculation bubble. They computed a linear relationship between the bubble length and $\log Re$ for $Re \lesssim 150$. They reported a secondary separation of flow for $Re \approx 1000$, but earlier experimental flow visualisations of the flow past a sphere (Magarvey & Bishop 1961b,a; Magarvey & MacLatchy 1965) suggested that the computational assumption of axisymmetric flow was nonphysical at these higher Reynolds numbers. Despite this, a good correlation between the computed drag coefficient C_d, and experimentally measured values of C_d was found for $0 \lesssim Re \lesssim 1000$.

A semi-analytical numerical study was conducted by Dennis & Walker (1971), for the wake around a sphere. They employed Legendre functions to reduce the governing equations to a series of ordinary differential equations, which were then solved numer-

ically. Only a steady axisymmetric flow was considered, with solutions being sought for the vorticity and stream-function equations. By assuming that at separation, the change in vorticity in the tangential direction at the rear of the sphere would be zero, they interpolated a value for the separation transition Reynolds number of approximately $Re_{S1} \approx 20.5$, between flows computed at $Re = 20$ and $Re = 40$.

Taneda (1956a) performed an experimental study of the flow past a sphere being towed through a tank, for Reynolds numbers $5 \leq Re \leq 300$. By extrapolating the linear relationship between the measured recirculation bubble length and $\log Re$ to zero, he obtained a transition Reynolds number for flow separation from the sphere of approximately $Re_{S1} = 24$. Taneda commented on the potential for discrepancies when measuring the transition Reynolds number for flow separation in the wake. He noted that attempts to identify the initial formation of the recirculation bubble visually was difficult, as the bubble was initially very small and formed near to a stagnation in the flow where the velocities were very small. Extrapolation of the recirculation bubble length against Reynolds number was the preferred method for calculating the separation transition Reynolds number, as the length of the bubble could be measured easily at higher Reynolds numbers.

Recent numerical computations have allowed the separation transition Reynolds number to be accurately determined. By extrapolating the variation in length of the recircualtion bubble with Reynolds number to zero from direct numerical computations, a value of $Re_{S1} = 20$ was determined from several studies (Tomboulides *et al.* 1993; Johnson & Patel 1999; Tomboulides & Orszag 2000). This value is remarkably consistent with the value obtained from the early study by Dennis & Walker (1971).

It has been widely reported that the length of the recirculation bubble increases proportional to $\log Re$ (Taneda 1956a; Tomboulides *et al.* 1993; Johnson & Patel 1999; Tomboulides & Orszag 2000). Studies have also observed that at a critical Reynolds number Re_{S2}, the recirculation bubble becomes unstable to non-axisymmetric flow.

1.1.3 The Transition to Non-Axisymmetric Flow

In the experimental study by Taneda (1956a), it was observed that the axisymmetric recirculation bubble became unstable with an increase in Reynolds number. The stability of the axisymmetric wake of a sphere to axisymmetric and non-axisymmetric disturbances has been studied numerically with varied success by Kim & Pearlstein

(1990) and Natarajan & Acrivos (1993).

The numerical stability analysis of Kim & Pearlstein (1990) employed a spectral method to solve the axisymmetric stream function form of the governing equations for the base flow. An axisymmetric stability analysis was performed, which employed the same method, and a non-axisymmetric stability analysis was performed, which employed a modified primitive variables form. Their computations predicted that the axisymmetric wake undergoes a non-axisymmetric Hopf bifurcation at $Re = 175.1$, with an azimuthal mode number $m = 1$. The instability that they predicted had an imaginary component giving a predicted linear oscillation frequency of $St = 0.0955$ at the onset of the instability. These predictions were at odds with the observations from experimental studies, as unsteady flow was generally only observed for $Re \gtrsim 300$ (Taneda 1956a; Magarvey & Bishop 1961b,a; Magarvey & MacLatchy 1965).

The more recent numerical study performed by Natarajan & Acrivos (1993) proved to be more successful. They employed a robust finite-element method for spatial discretisation of the flow past a sphere and the flow past a disc. They verified that a high grid convergence was obtained in their computations by monitoring various wake parameters, and an excellent agreement was obtained between the computed drag coefficients of spheres and discs, and the previous experiments of Roos & Willmarth (1971), up to $Re = 200$. Natarajan & Acrivos (1993) based their Reynolds number length scale on the radius of the sphere and disc, whereas here they are converted to Reynolds numbers based on the diameter for consistency with other reported results. They predicted that the first bifurcation of the steady axisymmetric wake of a sphere occurred at $Re = 210$, with an azimuthal mode number $m = 1$. This instability was predicted to occur through a regular (steady to steady flow) transition. They predicted that a secondary mode occurs at $Re \approx 277.5$. This secondary instability was predicted to occur through a Hopf bifurcation to unsteady flow, with an azimuthal symmetry of $m = 1$. Despite the axisymmetric base flow not providing a physical representation of the wake beyond the primary non-axisymmetric instability, the predicted Hopf mode was still qualitatively consistent with the experimental observations of the onset of unsteady flow in the wake ($270 < Re_{S3} < 300$). The predicted azimuthal symmetries of the primary and secondary non-axisymmetric instabilities were in excellent agreement with experimental observations of the non-axisymmetric wakes over similar Reynolds numbers (Magarvey & Bishop 1961a,b).

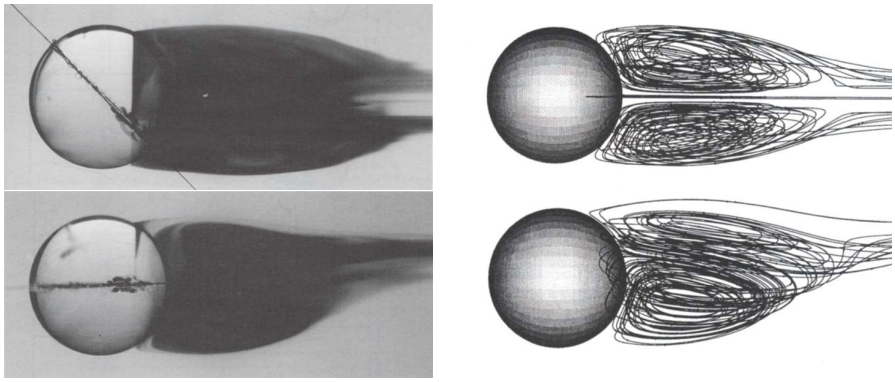

(a) Experimental dye-visualisation.

(b) Computed non-axisymmetric particle traces.

FIGURE 1.2: Comparison between experimental and computational flow visualisation of the steady non-axisymmetric wake of a sphere at $Re = 250$ (from Johnson & Patel 1999). Plan and elevation views at the same time are presented.

Stability of the sphere wake was studied using the complex wave amplitude Landau equation (Ghidersa & Dušek 2000; Thompson *et al.* 2001a). The coefficients of the linear and cubic terms of the Landau model were estimated from non-axisymmetric numerical computations close to the transition Reynolds numbers. The initial asymmetric transition was found to be a regular type transition, occurring at $Re_{S2} = 212$, and the subsequent transition was identified as being a Hopf transition at $Re_{S3} = 272$. The critical Reynolds numbers of the transitions are in excellent agreement with previous studies. The analysis demonstrates that both transitions are predicted to occur through continuous supercritical bifurcations, and hence no hysteresis is expected in the vicinity of either transition. The Hopf transition in the wake of a sphere was the subject of a recent study by Schouveiler & Provansal (2002). They verified the supercritical nature of the transition, and through experimental measurements of the wake of a sphere, they determined coefficients of the Landau model to test the suitability of the model in describing the wake dynamics.

1.1.4 Steady Non-Axisymmetric Flow

Experiments and numerical computations performed by Johnson & Patel (1999) found the axisymmetric wake to undergo a regular bifurcation through a shift of the steady recirculating bubble behind the sphere from the axis at approximately $Re_{S2} = 211$. They

observed the double-threaded wake consistent with previous experimental observations (Magarvey & Bishop 1961a,b). The numerical studies of Tomboulides *et al.* (1993) and Tomboulides & Orszag (2000) find a similar value, $Re_{S2} = 212$. The flow visualisations in figure 1.2 provide a detailed representation of the non-axisymmetric wake beyond the transition. The shift of the recirculation bubble from the axis is evident, and to the far right of the images, the pair of streamwise vortices which form the double-threaded wake may be observed.

1.1.5 The Transition to Unsteady Flow

Taneda (1956a) perceived a small periodic "pulsing" with a long period at the rear of the recirculation bubble for $Re \gtrsim 130$. However, the far wake was observed to be completely laminar up to $Re \approx 200$, and the vortex ring was attached to the sphere up to $Re \approx 300$. In light of the more recent results reported here, it is reasonable to assume that the observed pulsing was the result of an extrinsic instability associated with the towing apparatus, as it was localised to the tail of the recirculation bubble. This observed pulsing does suggest, however, that the recirculation bubble is sensitive to perturbations in the vicinity of the transition.

Striking flow visualisations of the wakes behind spherical liquid droplets descending through a tank were presented by Magarvey & Bishop (1961a). The liquid droplets remained relatively uniform in size and shape, and provided a useful approximation to the flow past a fixed solid sphere. They controlled the Reynolds number by judicious selection of appropriate droplet size and liquid phases, as the Reynolds number depended on the terminal velocity of a given droplet. They presented visualisations of various wake states, including a steady, axisymmetric wake at $Re = 200$, and several images of unsteady wakes at Reynolds numbers $350 \leq Re \leq 500$. Some examples of the dye-visualisation images that they obtained are reproduced here in figure 1.3. In all cases, the unsteady wakes that they observed consisted of vortex loops being shed into the wake from the alternate sides of the sphere. A plane of reflective symmetry was observed in the wake up to approximately $Re \approx 500$, and they observed that the wake at $Re \approx 600$ no longer exhibited periodic shedding, and had lost its planar symmetry.

In Magarvey & Bishop (1961a), an approximately linear Strouhal–Reynolds number trend was estimated to a qualitative accuracy of approximately 10%, ranging from

(a) Axisymmetric wake at $Re = 200$.

(b) Vortex-loop wake at $Re = 380$.

FIGURE 1.3: Reproductions of dye visualisation photographs from Magarvey & Bishop (1961b), which show spherical droplets falling through a liquid. For illustrative purposes, the flow is presented here from left to right.

$St = 0.11$ to 0.125 for $Re = 350$ to 500.

Their followup paper (Magarvey & Bishop 1961b) reports similar experiments over a wider Reynolds number range $0 < Re < 2500$. Their experimental rig enabled detailed images of the trailing wakes to be obtained, as the droplets were motionless in the reference frame of the camera. Attention was paid to classifying the observed wakes, which were summarised as follows: "Class I" ($0 < Re < 210$) exhibit a single thread wake, "Class II" ($210 < Re < 270$) exhibit a double thread wake, "Class III–V" ($270 < Re < 700$) exhibit planar-symmetric unsteady wakes, and "Class VI" ($Re > 700$) exhibit asymmetrical aperiodic wakes.

Detailed photographs presented in Magarvey & Bishop (1961b) illustrate examples of an axisymmetric "Class I" wake observed at $Re = 170$. Images of the "Class II" double-threaded wake show a steady non-axisymmetric wake caused by a loss of axisymmetry of the recirculation bubble. A distinction is drawn between the "Class III" wakes ($270 < Re < 290$), in which a waviness evolves downstream of the double-threaded wake, and the "Class IV–V" wakes, which display a well-defined shedding of vortex loops. The effect of having no transverse restraint on the free-falling droplets on the observed wakes remained an open question from their work. They estimated a linear Strouhal–Reynolds number relationship for the single-loop shedding observed for $290 < Re < 410$, which varyied between $0.05 < St < 0.065$ (for reference, in Magarvey & Bishop 1961a, the Strouhal–Reynolds number profile represents data obtained from the double-loop shedding observed for "Class V" wakes).

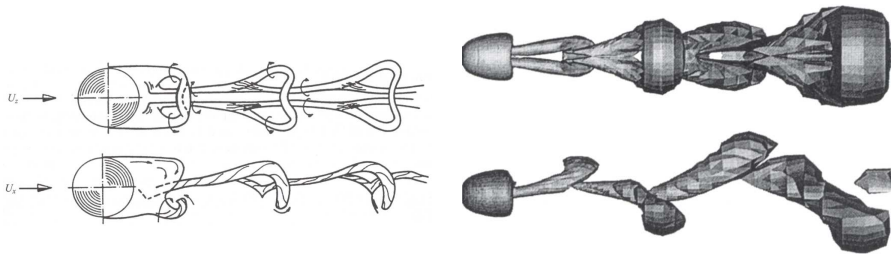

(a) Sketch of the wake vortex configuration from Achenbach (1974).

(b) Plan and elevation views of the vortical structure at $Re = 300$ from Johnson & Patel (1999).

FIGURE 1.4: Comparison between a sketch of the vortex loop shedding pattern in the wake of a sphere, and flow visualisation from recent numerical computations.

A later work by Magarvey & MacLatchy (1965) analysed the formation and evolution of the unsteady wake of a sphere with a careful image-acquisition technique. They proposed a "sheet involution" mechanism for the shedding process, whereby instead of vorticity convecting directly into the axisymmetric wake for $Re \lesssim 200$, vorticity is first transferred to the region behind the sphere, where a loop is formed. They described that below the critical Reynolds number for unsteady flow ($Re_{S3} \approx 300$), sufficient vorticity was transported into the wake via the double-threaded tails to maintain a steady wake, and beyond the critical Reynolds number the wake becomes unstable, and a periodic shedding of vortex loops ensues. A series of photographs capturing the evolution of the initial vortex loop following the destruction of symmetry in the wake was presented, representing a "Class III" wake at $Re = 340$. A sketch of the vortex configuration for the vortex-loop wake behind a sphere was included in the study of Achenbach (1974), and is reproduced here in figure 1.4(a).

The flow visualisations from various numerical computations (Tomboulides *et al.* 1993; Johnson & Patel 1999; Tomboulides & Orszag 2000) support the bifurcation scenario predicted by Natarajan & Acrivos (1993), with unsteady wakes being observed for $Re \gtrsim 280$. Each of these studies found that the unsteady wake consisted of vortex loops or hairpins that shed downstream from the sphere, in the same plane as that of the steady double-threaded wake. The observed wake structures are in good agreement with the experimental observations of Magarvey & Bishop (1961a,b) and Magarvey & MacLatchy (1965), pertaining to the shedding of vortex-loops into the wake, and as

an example, figure 1.4(b) is included, reproducing the isosurface plots of the computed vortex-loop wake structure from Johnson & Patel (1999).

1.1.6 The Flow at Higher Reynolds Numbers

Computations by Mittal (1999a,b) verified both the earlier computations (Tomboulides *et al.* 1993; Johnson & Patel 1999) and experimental observations (Magarvey & Bishop 1961b; Magarvey & MacLatchy 1965) of the periodic wake of a sphere. They showed that the wake remained planar-symmetric up to a Reynolds number of $Re \approx 375$, beyond which the symmetry was lost. Combining a Digital-Particle-Image Velocimetry technique with a spatio-temporal reconstruction technique, the non-axisymmetric structure of the wake of a sphere was analysed by Brücker (2001), who observed a similar loss of symmetry occurring within the Reynolds number range $400 < Re < 500$.

Tomboulides *et al.* (1993) observed fine scale flow structures in the wake of a sphere computed with a large-eddy simulation method, for a Reynolds number range of $500 < Re < 1000$. Magarvey & Bishop (1961b) observed a breakdown in periodicity of the hairpin shedding for $Re > 600$ also. These results are considered to mark the onset of turbulence. Measurements indicating the development of similar fine-scale structures are reported by Chomaz *et al.* (1993) and Tomboulides & Orszag (2000), who speculated that these structures developed from a Kelvin-Helmholtz instability of the shear layer separating from the sphere. The smoke-wire visualisations presented by Kim & Durbin (1988) show fine-scale wake structures behind a sphere for $Re = 32000$, consistent with a Kelvin-Helmholtz instability of the separating shear layer.

Achenbach (1972) performed wind-tunnel experiments over a range of Reynolds numbers $5 \times 10^4 < Re < 6 \times 10^6$. At these Reynolds numbers, the wake was observed to be highly turbulent. However, the flow could be considered incompressible, as the Mach number (fluid flow speed/speed of sound) of $Ma \approx 0.1$ was far lower than the critical Mach number requiring consideration of compressible flow ($Ma \approx 0.3$). To overcome skin friction effects, the sphere was highly polished, and measurements of both pressure drag and skin friction were made.

At a critical Reynolds number, Achenbach reported a massive reduction in drag from $C_d \approx 0.5$ at $Re = 3 \times 10^5$, to $C_d \approx 0.06$ at $Re \approx 3.7 \times 10^5$. He identified four flow regimes over the Reynolds number range he investigated. These flow regimes included a subcritical regime for $4 \times 10^4 < Re \lesssim 3 \times 10^5$, a critical regime for $3 \times 10^5 \lesssim Re \lesssim$

3.7×10^5, a supercritical regime for $3.7 \times 10^5 \lesssim Re \lesssim 1.5 \times 10^6$, and a transcritical regime for $1.5 \times 10^6 \lesssim Re < 6 \times 10^6$.

Achenbach measured a relatively constant drag of $C_d \approx 0.5$ throughout the subcritical regime. Through the supercritical and transcritical regimes, the drag increased with Reynolds number from a minimum at $Re \approx 3.7 \times 10^5$, to $C_d \approx 0.2$ at $Re \approx 6 \times 10^6$. He concluded that the critical regime marked the development of turbulence in the boundary layer around the sphere.

In the subcritical regime, the viscous (or friction) component of the drag force was found to vary with approximately $Re^{0.5}$. A laminar boundary-layer separation was measured to occur at $Re = 1.62 \times 10^5$, at an angle of 82° with respect to the front of the sphere, and flow recirculation was measured beyond this angle. Achenbach observed the point of laminar boundary-layer separation to move downstream, to 95° at $Re = 2.8 \times 10^5$. He hypothesised that further increases in Reynolds number through the critical regime cause a laminar separation and turbulent reattachment of the flow past a sphere. It was determined from skin friction and pressure measurements that the supercritical regime was characterised by a laminar-turbulent boundary layer transition prior to separation, and the transcritical regime was characterised by a fully turbulent boundary layer.

The wake dynamics over this high-Reynolds-number range was investigated by Taneda (1978), employing surface oil-flow visualisation and smoke visualisation to gain an understanding of the wake dynamics and structure. The experimental setup enabled Reynolds numbers to be studied over the range $10^4 < Re < 10^6$. He observed evidence of a progressive wave motion in the wake for $10^4 < Re < 3 \times 10^5$, and a streamwise pair of vortices for $3.8 \times 10^5 < Re < 10^6$. Consistent with Achenbach (1972), a sharp drag decrease was found over the critical Reynolds number regime to $Re \approx 3.8 \times 10^5$. From oil patterns, he observed boundary layer separation in the subcritical regime to occur at an angle of 80° at $Re = 2.3 \times 10^5$, in good agreement with the 82° measured by Achenbach (1972). Further observations confirmed that the critical regime comprised a laminar separation at 100°, and a turbulent reattachment at 117°, followed by a turbulent separation at 135°. In addition, he observed a slow irregular rotation of both the subcritical wavy planar wake, and the supercritical turbulent double-threaded wake.

In a subsequent work, Achenbach (1974) studied the vortex shedding in the wake of a sphere for Reynolds numbers $400 < Re < 5 \times 10^6$. Water channel measurements were

taken for $Re < 3\times10^3$, and from flow visualisation, his famous schematic representation of the vortex-loop configuration of the unsteady wake of a sphere at $Re = 1000$ was sketched. Visualisations of the wake for $Re \lesssim 400$ showed a steady, non-axisymmetric wake. Useful Strouhal–Reynolds number measurements were made, illustrating, among other points, the large discrepancy between the measured shedding frequency of the wake of a fixed sphere, and the liquid droplets from Magarvey & Bishop (1961a,b).

At higher Reynolds numbers, wind tunnel measurements of the Strouhal–Reynolds number profile presented by Achenbach (1974) showed an increase in Reynolds number from $St \approx 0.125$ at $Re \approx 6\times10^3$ to $St \approx 0.2$ at $Re \approx 3\times10^5$. An attempt was made to predict the stability of the spiral shedding wake observed over this Reynolds number regime by Monkewitz (1988b). In that study, the spiral mode was predicted to be absolutely unstable for Reynolds numbers $Re \gtrsim 3.3\times10^3$, which implied that the spiral mode developed from a local oscillation in the near wake. Beyond the critical regime, no dominant frequency was observed, which was consistent with earlier flow visualisations that identified a turbulent double-threaded wake in this regime (Achenbach 1972). Achenbach hypothesised that some critical Reynolds number existed in the range $3\times10^3 < Re < 6\times10^3$, where a sharp drop in Strouhal number would occur. The wind tunnel measurements were made from temporal fluctuations in the local skin friction immediately upstream of the separation point of the sphere, whereas the water channel measurements were estimated from the time taken for 50 shedding cycles to be observed.

An experimental study by Taylor & Whitelaw (1984) determined that for the flow past a sphere, the transition Reynolds numbers and size of the near-wake region was highly dependent on blockage in confined flows. Blockage ratios of approximately 25% to 50% were considered.

As part of an experimental study investigating the acoustic excitation of the wake of a sphere for Reynolds numbers $500 < Re < 6\times10^4$ by Kim & Durbin (1988), hot-wire probe measurements suggested that the wake of a sphere in the subcritical regime was characterised by two incommensurate frequencies. A low frequency oscillation ($0.1 < St < 0.2$) was measured in a large number of positions throughout the wake for all Reynolds numbers in the range $500 < Re < 1\times10^5$. Despite a decrease from $St \approx 0.2$ to 0.1 over the Reynolds number range $6\times10^3 < Re < 9\times10^3$, the Strouhal number for the low-frequency mode remained otherwise constant. The values agree well with those obtained by the wind tunnel work of Achenbach (1974). In addition, a high Strouhal

Sphere wake transition	Experimental Re_c	Computational Re_c
Boundary layer separation	24–25	20–21
Regular non-axisymmetric transition	200–210	210–211
Unsteady Hopf transition	270–280	277.5

TABLE 1.1: Transition Reynolds numbers from experimental and computational studies of the flow past a sphere (Taneda 1956a; Natarajan & Acrivos 1993; Johnson & Patel 1999; Tomboulides & Orszag 2000).

frequency was observed, varying approximately with $Re^{0.75}$, for $Re \gtrsim 800$. The high-frequency mode was only detected in the wake immediately behind the sphere, and interestingly, the Reynolds number in which it first occurred was consistent with the Reynolds number at which a loss of planar symmetry was observed by Magarvey & Bishop (1961b).

The observation of two frequencies in the wake was verified by Chomaz *et al.* (1993). The Strouhal frequencies that they measured for the high-frequency mode correllated well with the Strouhal frequencies measured for the vortex-loop shedding mode by Achenbach (1974). The observations of Chomaz *et al.* (1993) support the speculation that the high-frequency mode is due to a Kelvin-Helmholtz instability of the separating shear layer, and the low-frequency mode is associated with some longer-timescale instability, such as the slow wake rotation observed by Taneda (1978).

A summary of the transitions in the flow past a sphere at low Reynolds number is presented in table 1.1.

1.2 The Flow past a Circular Cylinder

A review of previous work pertaining to the flow past a circular cylinder is now presented.

1.2.1 Attached Flow

Experimental observations of the flow past a circular cylinder at very low Reynolds numbers show that the flow is steady and attached (Taneda 1956b). In figure 1.5(a), the creeping flow past a circular cylinder is shown. The reversibility associated with creeping flow can be observed in the figure.

1.2.2 The Transition to Separated Flow

The initial transition in the flow past a circular cylinder occurs with the separation of flow at the rear of the cylinder, which results in the formation of a steady recirculation bubble. This transition was predicted to occur at $Re_{C1} = 5$ from low-dimensional numerical computations performed by Noack & Eckelmann (1994b). In the experimental study by Taneda (1956b), the low-Reynolds-number flow past a circular cylinder was investigated. Taneda observed from flow visualisation and extrapolation of the wake length to zero that the separation transition occurred in the vicinity of $Re_{C1} \approx 6$. With further increases in Reynolds number, a steady symmetrical recirculation bubble was observed to grow in the wake. The wake length was found to be proportional to $\log Re$, which is consistent with the corresponding recirculation bubble in the wake of a sphere (Taneda 1956a). The recirculation bubble remained steady, two-dimensional and symmetrical about the centreline of the flow until a subsequent transition to asymmetric flow was observed for Reynolds numbers $Re \gtrsim 40$.

One of the pioneering computational studies of fluid mechanics was performed by Payne (1958), who numerically modelled the wake of a circular cylinder. The Helmholtz vorticity equation was employed, incorporating viscosity, and a finite-difference scheme was employed for spatial discretisation. For temporal integration a forward-difference technique was employed. Although an unsteady solver was employed, the computations were only evolved for sufficient time for the flow to evolve from the inviscid startup condition to the viscous steady-state solution. In the study, a variation in the computed drag coefficient was reported. At $Re = 40$, the drag coefficient varied over $3 < C_d < 1.8$ between $t = 0$ and $t = 6$. At $Re = 100$, the drag coefficient varied over $1.2 < C_d < 1$ between $t = 0$ and $t = 6$. A later study by Ingham (1968) extended the computations of Payne (1958) to $t = 24$. Ingham reported a concern with the resolution of the computations at $Re = 100$. At $Re = 40$, an asymptotic drag coefficient of $C_d = 1.5$ is achieved.

An attempt to model the unsteady viscous flow past a circular cylinder was performed by Ta Phuoc Loc & Bouard (1985), who employed a numerical method comprising finite-difference discretisations of fourth-order for the stream-function equation, and second-order for the vorticity transport equation. The computations modelled only one half of the wake, therefore suppressing the natural development of a vortex street. The Reynolds numbers of the computations were $Re = 3 \times 10^3$ and $Re = 9.5 \times 10^3$, and

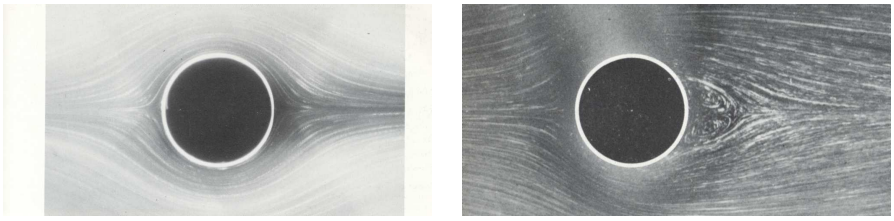

(a) Attached flow at $Re = 0.16$. (b) Separated flow at $Re = 13.1$.

FIGURE 1.5: The steady flow past a circular cylinder at low Reynolds numbers (from Van Dyke 1982, photographs by S. Taneda).

the computations were evolved for $0 \leq t \leq 5$. Solutions were computed with transverse domains of $9.2d$ and $5d$, with little variation being observed between the computed wakes.

In Coutanceau & Bouard (1977a), experiments were conducted in which a cylinder was raised through a tank, with images of the wake being captured at the tank midpoint, minimising wall, surface and startup effects. The study concerned the steady wake behind a circular cylinder, and visualisations were obtained by illuminating magnesium particles with a 1mm thick laser sheet. A steady recirculation bubble was observed in the wake for $5 < Re < 40$, which consisted of a counter-rotating vortex pair. The visualisations compare favourably with the early experiments of Taneda (1956b), who observed a steady recirculation bubble in the wake for $Re > 6$. Images of both the attached and separated flow past a circular cylinder are provided in figure 1.5. An experimental study by Nishioka & Sato (1974) provided velocity measurements in the wake behind a circular cylinder for Reynolds numbers $10 < Re < 80$. Included was a detailed analysis of the velocity profiles in the recirculating eddies in the wake, and it was shown that a similarity existed in the returning stagnation streamline for Reynolds numbers $10 < Re < 40$, which corresponded to observed steady flow.

1.2.3 The Transition to Unsteady Flow

As a followup to their earlier work, Coutanceau & Bouard (1977b) studied the decay of unsteady transients in the wake of a circular cylinder, subsequent to an impulsive initiation of motion. They observed a more rapid decay of transients at smaller Reynolds numbers. At $Re = 20.2$ unsteady transients decayed within $t \approx 7$ time units (where $t = U_\infty \hat{t}/d$, and $\hat{t}$ is the measured time), and at $Re = 40$ the transients decayed

within $t \approx 12$. Flow parameters such as the vortex position and separation angle were monitored, and it was observed that transverse flow features evolved more rapidly than longitudinal flow features. The parameters associated with the recirculation bubble evolved more rapidly than the surrounding flow field.

Pertaining to the development of unsteady flow, the study by Coutanceau & Bouard (1977a) reported that a steady asymmetry was observed in the recirculation bubble behind a circular cylinder for $Re > 40.3$. This asymmetry marked the onset of the transition to unsteady flow in the wake.

The stability of the steady flow past bluff bodies was considered by Taneda (1963). In that study, the flow past both a plate and a circular cylinder in a water channel was investigated. A Reynolds number range of $0.8 < Re < 60$ was considered for the circular cylinder, and from measurements of wake oscillations Taneda proposed that the critical Reynolds number below which all disturbances were damped was $Re \approx 1.0$ for the flow past a circular cylinder. An analysis was performed assuming parallel flow, and a general critical value of $Re \approx 3.2$ was proposed for the flow past bluff bodies of any shape. In earlier experiments, Taneda (1956b) reported an oscillation in the far wake, despite a steady recirculation bubble being observed in the near wake at $Re \approx 30$.

An explanation for the detection of oscillations below the critical transition Reynolds number for unsteady flow can be made by considering the nature of the instability responsible for the development of unsteady flow past a circular cylinder (e.g. see Provansal *et al.* 1987; Monkewitz 1988a). In these studies, absolute and convective instabilities are defined, with absolute instabilities displaying exponential growth at the location of their generation, whereas convective instabilities are transported away from the source, leaving the flow ultimately undisturbed. The terms *local* and *global* are also applied, where local instabilities are confined to a small region of the flow, and global instabilities evolve everywhere in a flow, with a linear growth rate that is independent of position.

In Monkewitz (1988a), the stability of transverse profiles of the wake of a circular cylinder was investigated at low Reynolds numbers. A critical Reynolds number $Re \approx 2$ was predicted for the transition between stability and convective instability. This prediction corresponds with the observed measurement of unsteady transients downstream of the cylinder by Taneda (1963), at Reynolds numbers $Re \approx O(1)$. A second critical Reynolds number $Re \approx 25$ was predicted for the transition between convective and

absolute local instability in the wake. This prediction corresponds with the measurement of oscillations in the near wake behind a circular cylinder at $Re \approx 30$ by Taneda (1956b).

The critical Reynolds number for the transition to unsteady flow was predicted to be $Re_{C2} = 54$ from a numerical study by Noack & Eckelmann (1994a), however, the Galerkin method they used appeared to have too few modes to accurately capture the instability. The experimentally derived results of Williamson (1988a, 1989), which observe a critical Reynolds number of $Re_{C2} \approx 49$ are widely regarded as more accurate. In Nishioka & Sato (1974), an extrapolation of experimental data for finite-length cylinders to an infinite length ratio achieved a value of $Re_{C2} \approx 48$. Jackson (1987) calculated a value of $Re_{C2} \approx 46.2$ from *Richardson extrapolation* of finite-element computations, and more recently, further computational refinement of the critical Reynolds number has been made. Dušek *et al.* (1994) obtained a value of $Re_{C2} = 47.1$ through numerical computation and the application of the theoretical Landau model. They also verified the prediction of Provansal *et al.* (1987), who identified the transition to occur through a continuous supercritical Hopf bifurcation. A recent and highly accurate stability analysis of the steady flow past a circular cylinder was recently performed by Motallebi & Norbury (1999). They predicted a critical Reynolds number of $Re_{C2} = 47.0$ from linear stability analysis computations which employed an eigensolution method for global stability analysis.

1.2.4 The Kármán Vortex Street

At Reynolds numbers beyond the Hopf transition Reynolds number Re_{C2} for the flow past a cylinder cylinder, the wake shear layer rolls up and vortices are shed downstream from the rear of the cylinder, forming the classic Kármán vortex street. Beautiful images of the Kármán vortex street in the wake of a circular cylinder were captured with a smoke visualisation method by Zdravkovich (1969). Photographs of both a laminar and turbulent Kármán vortex street are provided in figure 1.6.

A numerical study performed by Fromm & Harlow (1963) included a detailed description of the evolution of the Benard–von Kármán instability responsible for the formation of the vortex street in the flow past a bluff plate. They observed that the instability manifests itself through a development of asymmetry between the counter-rotating vortices in the recirculation bubble. This in turn initiates a transverse shift in

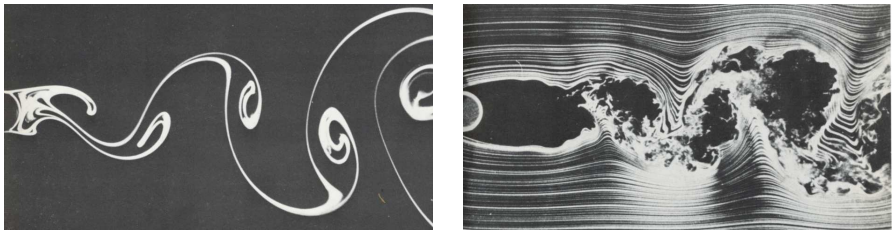

(a) Laminar two-dimensional wake at $Re = 140$ (photographed by S. Taneda).

(b) Turbulent wake at $Re = 1 \times 10^4$ (photographed by T. Corke and H. Nagib).

FIGURE 1.6: The laminar and turbulent Kármán vortex streets in the wake of a circular cylinder (from Van Dyke 1982).

the position of the vortices, to the point where a detachment occurs, and an oscillatory shedding of vortices from alternating sides of the body into the wake every half-period is initiated.

The experimental study of Gerrard (1966) reported on experiments conducted on the flow past a circular cylinder at $Re = 85$, 235 and 2×10^4. The study observed flapping in the wake analogous to a flag. Although Gerrard provided no flow visualisation, it is probable that this flapping was due to the convection of the visualisation matter downstream in the vortex street. As well as parallel modes of shedding, Gerrard was able to distinguish both oblique shedding modes and vortex street dislocations in the wake.

An experimental study was performed by Wen & Lin (2001), employing a soap-film visualisation method to model the two-dimensional Kármán vortex street in the wake of a circular cylinder. The technique achieved a two-dimensional flow, which was confirmed by the measurement of a continuous Strouhal–Reynolds number profile which was in close agreement with values computed numerically for two-dimensional flows up to $Re = 560$.

1.2.4.1 Extrinsic Instabilities of the Vortex Street

The wake of a circular cylinder is fundamentally different to the wake of a sphere, in that the maximum spanwise length of the wake is not limited by the symmetry of the body (e.g. a maximum azimuthal span of 2π radians is permitted for the flow past a sphere). The wake of a circular cylinder is susceptible to extrinsic instabilities that

propagate from the cylinder ends.

In an experimental study by Tritton (1959), drag force measurements were made for the flow past a circular cylinder by measuring the deflection of quartz fibres in a stream over a Reynolds number range $0.5 < Re < 100$. A discontinuity was measured in the Strouhal–Reynolds number profile, suggesting that a transition in the vortex street occurred at $Re \approx 90$, from parallel to non-parallel shedding. Tritton proposed that this transition was due to a shift in the origin of the vortex street from the wake to the cylinder. From the flow visualisation images provided in the study, it is observed that the vortex rollers rapidly become non-parallel as they convect downstream, at Reynolds numbears $Re = 78$, and at $Re = 88$, the rollers are shed from the cylinder in a non-parallel fashion. In a later study, Tritton (1971) performed experiments in a wind-tunnel to verify the existence of the transition at $Re \approx 90$. A transition in the variation of a parameter $ReSt$ was measured at $Re = 110$, and it was proposed that this shift in the transition Reynolds number was influenced by experimental conditions including background turbulence intensity.

Gaster (1971) reports on experiments performed on the flow past a tapered cylinder. Such a geometry imposes a local variation in Reynolds number along the span of the cylinder, and also in the Strouhal frequency associated with a particular measured frequency. Gaster observed a significant discontinuity in the measured Strouhal–Reynolds number profile for the geometry at $Re \approx 100$, with a second less-pronounced discontinuity at $Re \approx 115$. The vortex street was observed to be composed of cells, with different shedding frequencies in each cell. The cell positions shifted along the span with velocity, and therefore correspond to localised regions of flow where the vortex shedding frequency was roughly aligned with the local length scales of the model. Gaster proposed that the Strouhal–Reynolds number discontinuities that had been reported by Tritton were likely due to the formation and movement of vortex street cells in a slightly non-uniform flow, which supports the observation by Tritton (1971) that background turbulence strongly influenced the transition Reynolds number.

More recent experimental studies have reported a similar discontinuity in the Strouhal–Reynolds number profile for the laminar shedding in the wake of a circular cylinder in a water channel, which occurred at $Re \approx 60$. Flow visualisations confirmed that this discontinuity was consistent with the development of oblique shedding in the wake (Williamson 1989; Hammache & Gharib 1991). At Reynolds numbers $Re \gtrsim 64$ oblique

shedding was reported in the wake of a circular cylinder (Williamson 1988a, 1996b), where the inclination of the vortex rollers to the cylinder caused a reduction in the Strouhal frequency of shedding. A mathematical relationship was developed which described the Strouhal frequency of shedding as functions of both the Reynolds number, and the angle of oblique shedding.

These studies verify that the transition from parallel to oblique vortex streets in the wake of a circular cylinder is sensitive to the end-conditions of the cylinder and the experimental apparatus. The influence of side-wall blockage on the wake of a circular cylinder was studied experimentally by Shair *et al.* (1963). A change in drag coefficient of approximately 18% was measured when the blockage ratio was increased from 5% to 20%. A staggering change in the critical Reynolds number for the onset of unsteady flow in the order of 300% was recorded by varying the blockage ratio. They determined that $Re_{C2} \approx 40$ for a blockage ratio approaching zero, and $Re_{C2} \approx 135$ for a blockage ratio of 20%.

In an experimental study by Gerich & Eckelmann (1982), the effect of placing plates at the ends of a circular cylinder on the wake was considered, with one and two plates being added, and Strouhal frequency measurements being made both near to the plates and in the unaffected region. Importantly, they found that frequencies 10–15% less than the regular shedding frequency were measured at distances between $6d$ and $15d$ from the end of the cylinder. Norberg (1994) considered the effect of varying the cylinder aspect ratio (length/diameter) on the measured wake parameters including base pressure coefficient. It was found that aspect ratio variation had an increased effect at lower Reynolds numbers, presumably due to the sensitivity of the laminar vortex street to end effects.

1.2.4.2 The Stability of a Vortex

The stability of an array of vortices was studied by Robinson & Saffman (1982). They predicted that a single row of vortices was unstable to two-dimensional perturbations, whereas a Kármán street was predicted to be unstable to three-dimensional perturbations for a range of vortex roller spacings. In addition, a symmetric vortex street was found to be unstable to either two- or three-dimensional disturbances, depending on the spacing ratio.

The stability of a rectilinear vortex with an elliptical cross-section was studied

numerically by Robinson & Saffman (1984). The flow field was assumed to be steady, and the vortex was subject to an irrotational strain field. They determined that the analytical weak-strain instability was applicable to finite-strain flows. Importantly, they predicted that such a flow is more unstable to a three-dimensional perturbation than a two-dimensional perturbation in the regions of the parameter space relevant for practical applications. More recently, the stability of two-dimensional visco-elastic elliptic flows was investigated by Haj-Hariri & Homsy (1997), who identified additional instability modes to the inertial modes predicted from previous studies.

Marshall (1992) studied the stability of an axially stretched pair of counter-rotating vortices to three-dimensional perturbations. In that study, it was found that when the stretching rate is greater than zero, the perturbation amplitude initially grows, however it always decayed to zero over large times. The predictions of the analysis were compared with observations of hairpin vortices in turbulent flows, which in the absence of any stretching were observed to become unstable and quickly dissipate.

1.2.4.3 Linear Instabilities of the Vortex Street

Experiments have observed the parallel periodic vortex street in the wake of a circular cylinder to become unstable to a three-dimensional instability at $Re \approx 178$ (Williamson 1988a, 1996b, see figure 1.7(a)). This transition was studied using a linear Floquet stability analysis (Barkley & Henderson 1996). They found that at $Re = 188.5$ the cylinder wake becomes unstable to three-dimensional perturbations with a spanwise wavelength of 3.96 diameters. A second instability of the two-dimensional base flow was predicted to occur at $Re \approx 259$, with a spanwise wavelength of $0.822d$. These instability modes are referred to as Modes A and B, respectively.

The numerical predictions of Barkley & Henderson (1996) pertaining to the spanwise wavelength of the vortex street instabilities were in good agreement with both experimental flow visualisation, and experimental measurements. In a study by Mansy *et al.* (1994), the spanwise wavelength of the three-dimensional component of the vortex street was calculated for Reynolds nubmers in the range $170 < Re < 2200$. They measured a spanwise wavelength of $\lambda_d \approx 3.5d$ at a Reynolds number of $Re \approx 200$, and a spanwise wavelength which decreased from $1d$ to $0.6d$ for Reynolds numbers which increased from $Re \approx 260$ to 2000. By employing a Particle Image Velocimetry technique in a plane normal to the wake, Brede *et al.* (1996) computed spatio-temporal

reconstructions of the three-dimensional wakes corresponding to the Mode A and B instabilities. Interestingly, they calculated a reduction of circulation in the streamwise vortices in the wake by a factor of two from Mode A with $160 \lesssim Re \lesssim 240$ to Mode B with $Re \gtrsim 240$. The estimated spanwise wavelengths they reported were approximately $4.5d$ and $1.0d$ for Modes A and B, respectively. Ma & Karniadakis (2002) modelled the three-dimensional transitions in the wake of a circular cylinder using a low-dimensional model. Snapshots of the most energetic modes from high-resolution direct numerical simulations were obtained, and predictions of the Strouhal discontinuity at the onset of Mode A were made. A Strouhal number of $St_{2D} \approx 0.194$ was predicted at $Re \approx 183$, and a Strouhal number of $St_{3D} \approx 0.183$ was predicted at $Re \approx 185$. Their model could not predict the hysteresis (or bi-stability) that was both calculated and measured at the onset of Mode A (Williamson 1996b,a; Henderson 1997).

Photographs of the Mode A and B instabilities in the vortex street behind a circular cylinder are reproduced in figure 1.7. The first numerical computations that captured both the Mode A and B instabilities in the three-dimensional wake of a circular cylinder were performed by Thompson *et al.* (1994, 1996). These studies provided isosurface plots of the streamwise vorticity in the Mode A and B wakes, which correspond to the spatio-temporal mode symmetry predicted by Barkley & Henderson (1996). The results of simulated-particle computations were also presented, which were almost indistinguishable from the experimental dye visualisation of the modes from Williamson (1988b, 1996b).

A detailed Floquet analysis was performed by Thompson *et al.* (2001b), to attempt to identify the physical mechanism of the Mode A transition. They showed that although the instability was complex, the mechanism was consistent with an elliptic instability of the vortex cores. Evidence suggests that the transition is in fact a co-operative elliptic instability (Leweke & Williamson 1998), with the elliptic instability dominant in initiating the growth of the three-dimensional flow structures in the near wake. Advection then transports some perturbation into the braid regions where it is amplified as the vortex rollers convect downstream.

The wake behind a square-section cylinder provides an interesting complement to studies of the wake behind a circular cylinder. The flow past a square cylinder has fixed separation points imposed by the corners of the body. No such restrictions are imposed on the flow past a circular cylinder. An early experimental study by Vickery (1966)

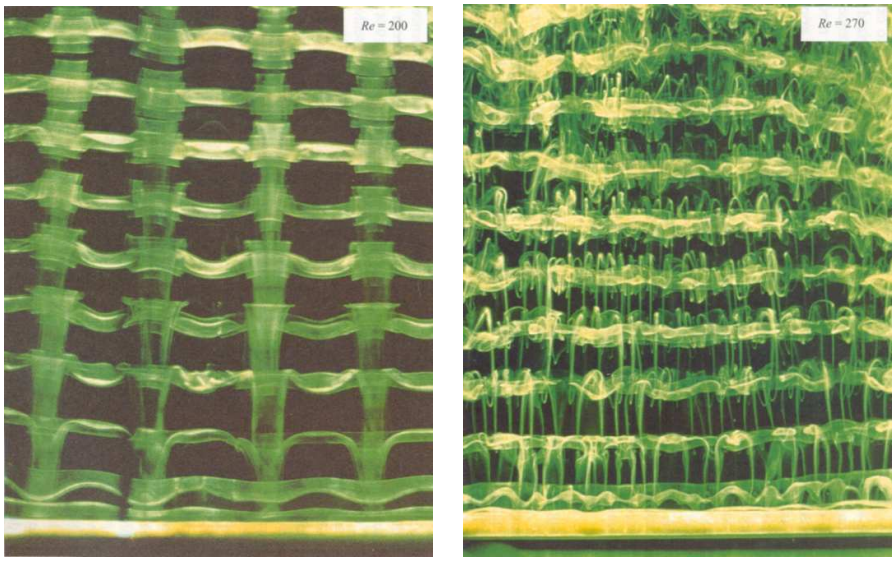

(a) Mode A at $Re = 200$.

(b) Mode B at $Re = 270$.

FIGURE 1.7: Three-dimensional instabilities of the vortex street behind a circular cylinder (from Williamson 1996b). Flow is upwards, and the wake is viewed from above.

measured lift and drag coefficients from square cylinders for various angles of attack. That study explored a Reynolds number range $4 \times 10^4 < Re < 1.6 \times 10^5$. A peak in the root-mean-square of the lift coefficient was recorded for an angle of attack of 0°, and a minimum root-mean-square of the lift coefficient was recorded for an angle of attack of 45°. Vickery also reported that a higher variation in fluctuating lift coefficient was measured in a turbulent stream than in a smooth stream.

Computations of the flow past a square cylinder with an angle of attack of 0° have been reported in numerical studies (Robichaux *et al.* 1999; Blackburn & Lopez 2003). In a numerical stability analysis of the wake of a square cylinder, Robichaux *et al.* (1999) predicted that the two-dimensional vortex street was unstable to the Mode A and B instabilities reported previously for the wake of a circular cylinder, as well as an instability mode with $\lambda_d \approx 2.8d$. They named this new instability Mode S, and predicted that it was subharmonic with a 2T symmetry, meaning that the instability was periodic over two shedding cycles of the base flow. This predicted symmetry for Mode S contrasted the 1T symmetries of Modes A and B, which were periodic over a single period of the base flow. The spanwise wavelengths that they predicted for Modes A and B were approximately 40% larger than the predicted wavelengths for the

corresponding modes in the wake of a circular cylinder, which indicated that the vortex street and the instability modes scaled on the diagonal length of the square cross-section. In experimental and numerical studies of the flow past a circular cylinder perturbed by a trip-wire, Zhang *et al.* (1995) had earlier observed a similar intermediate-wavelength instability in the wake. They referred to this observed mode as Mode C, and measured a spanwise wavelength of $\lambda_d \approx 2d$ for the mode. The spatio-temporal reconstructions of the mode which were provided in their study indicated that the instability had properties consistent with a subharmonic mode.

The stability analysis technique employed by Robichaux *et al.* (1999) is known as the power method, which is described in chapter 2. A recent study by Blackburn & Lopez (2003) employed a Krylov method to solve the stability of the flow past a square cylinder, and showed that Robichaux *et al.* had incorrectly classified Mode S as a real subharmonic mode. The application of the Krylov method reavealed that the dominant Floquet mode of the Mode S instability bifurcated as a complex-conjugate pair. The imaginary component of the mode was small compared with the negative real component, which explained the incorrect identification by Robichaux *et al.*, as the perturbation field would have alternated in sign from one period to the next, however a perfect 2T symmetry would not have been maintained. Based on their findings, Blackburn & Lopez (2003) proposed that for all bodies that preserved a reflective symmetry about the wake centreline (this includes both circular and square cylinders), a generic bifurcation scenario exists, consisting of real Modes A and B, and an additional complex-conjugate mode. This proposed scenario is supported by the stability analysis of Ryan *et al.* (2001) for the wake of elliptical leading-edge plates. The wakes behind these plates preserved the reflective symmetry of the vortex street, and their study predicted that instabilities which corresponded to Mode A, Mode B, and a complex-conjugate mode occur at various plate lengths.

Henderson (1997) computed the three-dimensional wake of a circular cylinder through the Mode A and B transitions. The span of the computations was varied by up to 4 times the spanwise wavelength of the Mode A instability. The interaction between the Mode A and Mode B instabilities was studied by monitoring the proportion of energy present in each of the spanwise Fourier modes in the computations. Isosurface plots were presented which showed the three-dimensional wake structures at $Re = 265$. These showed an instantaneous coexistence of both Mode A and Mode

B wake structures in the wake. In the study a spontaneous switching between Mode A and B was observed, which explains the presence of two distinct Strouhal frequencies in the wake over the Reynolds number range $230 \lesssim Re \lesssim 260$, as measured by Williamson (1988b). An attempt was made to study the physical mechanism which leads to the formation of streamwise vortical wake structures (Mittal & Balachandar 1995b); however, the computational domain they employed spanned only a single cylinder diameter, which resulted in the artificial suppression of Mode A structures. They did, however, observe the formation of well-defined vortical structures in the braid region of the vortex street, associated with Mode B shedding. Beyond the onset of these three-dimensional transition modes in the vortex street, the remnants of these instabilities persist even in turbulent flows. For example, the Particle Image Velocimetry measurements of Wu *et al.* (1996) in a plane aligned with the wake flow record evidence of a spanwise wavelength of approximately $0.7d$ in the wake at $Re \approx 500$.

1.2.5 Pattern Breakdown and the Route to Chaos

The route to turbulence associated with an increase in Reynolds number for the flow past bluff bodies has been the subject of a significant body of research over many years. Simple geometries such as the sphere (Taneda 1956a; Magarvey & Bishop 1961b; Tomboulides & Orszag 2000), the circular cylinder (Williamson 1988a, 1996b), and flat plates (Sato & Kuriki 1961; Hourigan *et al.* 2001) have all been studied to gain an understanding of the intermediate flow states and the transitions that can occur between the steady attached laminar wakes of low-Reynolds-number flows (typically $Re < 5$ for the flow past of a circular cylinder), to the chaotic and turbulent wakes of high-Reynolds-number flows (typically $Re > 400$ for the flow past a circular cylinder).

Despite a surge in activity over recent years, with research into the transitions and mechanisms associated with the development of turbulence in the wakes behind bluff bodies (Henderson 1997; Prasad & Williamson 1997a,b), the nature of the mechanism describing the route to chaos in a vortex street behind non-cylindrical geometries is still poorly understood.

1.2.5.1 Turbulent Flow and Chaos

Turbulent flow is characterised by a continuous spectrum of frequencies, due to the development of fine scale vortical structures. A uniform flow at low Reynolds number will contain few, if any, frequencies. A natural tool for modelling the development of

these additional frequencies in the wake is chaos theory.

Chaos theory is concerned with the development of apparently random behaviour from simple systems. Some excellent introductory reading on the subject may be found in Gleick (1993), and for more technical reading, Otto (1993) is useful. A feature of chaotic systems that is analogous to turbulent flows is self-similarity. Self-similarity determines that the distribution of scales within a system remains consistent for all scales. For turbulent flows, self-similarity is observed in homogeneous regions of the flow, however, the series of smaller and smaller vortical scales is eventually truncated at a finite scale by viscous diffusion (Henderson 1997).

1.2.5.2 The Period-Doubling Cascade: Excitement Through a Subharmonic Instability

Different routes to turbulence have been suggested for open flows in fluid mechanics. These include the aforementioned spatio-temporal chaos, itermittency, bursting chaos and a period-doubling cascade (Karniadakis & Triantafyllou 1989; Rockwell *et al.* 1991; Tomboulides *et al.* 1992; Karniadakis & Triantafyllou 1992; Mittal & Balachandar 1995b). The period doubling cascade is of particular interest to this study, as it was shown to occur in fluid flows similar to the von Kármán wake of the cylinder, such as a row of vortices (Braun *et al.* 1998). A period-doubling cascade causes the response of a periodic system (i.e. a three-dimensional vortex street) to undergo a succession of period-doubling bifurcations with the increase of a given parameter (in this case the Reynolds number Re). This cascade renders the response chaotic, with an effectively infinite period. It was proposed that a period-doubling cascade arises in vortex streets through the evolution of a subharmonic instability (Tomboulides *et al.* 1992). Computational studies of the flow past a circular cylinder (Karniadakis & Triantafyllou 1992; Tomboulides *et al.* 1992; Mittal & Balachandar 1995a) showed that the transition to a three-dimensional vortex street caused a period-doubling bifurcation of the wake. These studies employed compuational domains with a spanwise length insufficient to capture the Mode A instability. The predicted route to chaos from these studies is therefore questionable, as the three-dimensional bifurcation scenario of the vortex street was incorrectly computed. Computations which include a Mode A instability have shown that a period-doubling bifurcation is not observed in the wake (Thompson *et al.* 1994, 1996; Henderson 1997).

1.2.5.3 Chaos in Spatially Extended Systems

Spatially extended systems include at least one spatial dimension. These systems may be either constant (i.e. steady flow) or uniformly varying in time (i.e. two-dimensional periodic flow) when at equilibrium. An increase in the control parameter (for the fluid flows considered here, the Reynolds number is the control parameter) beyond the equilibrium point causes patterns to develop. Efforts to model a vortex street as a spatially extended dynamical system have been performed by Leweke & Provansal (1994, 1995). In an experimental study of the flow past a circular cylinder, Roshko (1967) determined that the critical Reynolds number for the transition to turbulent flow in the near-wake region was proportional to a ratio of the cylinder length to the cylinder diameter.

Henderson (1997) performed an extensive numerical study of pattern development in the vortex street in the wake of a circular cylinder. He identified the mechanism through which turbulence appears in the wake of a circular cylinder with a large span. It was observed that a breakdown of the regular saturated Mode B wake occurred through a development of spatio-temporal chaos in the wake, whereby local disturbances destroyed the global pattern of the wake, forming a wake consisting of random fluctuations in both space and time, and no discernable overall pattern. These computational measurements are consistent with earlier experimental observations by Gerrard (1977), which show the breakdown of the vortex street in the wake of a circular cylinder at $Re = 344$. A significant conclusion from the study by Henderson is that with an increase in the span, the vortex street becomes unstable to instabilities such as vortex dislocations and spatio-temporal chaos, whereas with an increase in Reynolds number, turbulence appears in the wake through the development of small-scale vortical structures.

1.2.6 The Flow at Higher Reynolds Numbers

The flow past a circular cylinder comprises three distinct shear flows (Williamson 1996b). These include the wake (located downstream of the cylinder), the mixing layer (located in the near-wake region), and the boundary layer (located around the cylinder). It was shown that turbulent flow emerges progressively in the wake in the form of small-scale vortical structures for Reynolds numbers $Re \gtrsim 300$ (Roshko 1954; Bloor 1964; Gerrard 1977; Unal & Rockwell 1988; Williamson 1996b; Henderson 1997; Prasad & Williamson 1997a,b).

Roshko (1953, 1954) describes three distinct regimes of flow past a circular cylinder. These were a "stable range" ($40 \lesssim Re \lesssim 150$) over which regular vortex shedding was observed, a "transition regime" ($150 \lesssim Re \lesssim 300$), and an "irregular regime" ($Re \gtrsim 300$) over which turbulent velocity fluctuations were measured in addition to the periodic vortex street. Respectively, the stable range and the transition regime describe the two- and three-dimensional flow regimes discussed previously. Roshko proposed that turbulence entered the flow through a laminar-turbulent transition of the free shear layers propagating from the separation points from the cylinder. Roshko measured the decay of discrete energy in the wake as turbulent flow dissipated the vortex rollers in the wakes in the irregular regime. He observed that within 50 diameters, the vortex street was completely obliterated, and the decay was consistent throughout a Reynolds number range $300 \lesssim Re \lesssim 10,000$.

A significant contribution to the understanding of the development of turbulence in the wake of a circular cylinder was made by Bloor (1964). In that study, it was observed that the location of the transition to turbulence in the wake moved towards the cylinder with an increase in Reynolds number. A shift in wake dynamics was observed when the turbulent transition in the wake entered the near wake formation region, which corresponded to a shift from the transition regime identified by Roshko to the irregular regime, at Reynolds numbers of $Re \gtrsim 400$ in the Bloor study. Over the irregular regime a decrease in the base pressure coefficient (Roshko 1993) and the fluctuating lift coefficient (Norberg 2001) have been measured. Bloor (1964) observed that in the irregular regime, the development of wake turbulence occurred through distortion of the vortex street due to large-scale three-dimensional effects. This is essentially a description of spatio-temporal chaos, which Henderson proposed as a mechanism through which turbulence developed in vortex streets.

A markedly different mechanism for the development of turbulence in the irregular regime ($1.3 \times 10^3 < Re < 8 \times 10^3$) was proposed by Bloor. In that case, turbulence was observed to occur following the breakdown of Tollmien–Schlichting waves in the separated shear layers. Over the irregular regime, laminar flow was still detected within the formation region, exhibiting a dominant fundamental frequency. Moving downstream in the formation region, Bloor measured turbulent bursts which imposed higher-frequency components on the fundamental shedding frequency. The study by Unal & Rockwell (1988) provides base pressure coefficient and velocity fluctuation measurements which

confirm the transition to turbulence within the formation region, however a higher Reynolds number of $Re \approx 1.9 \times 10^3$ is proposed for the onset of the irregular regime. A local minimum in both the base pressure coefficient and the velocity fluctuation at the transverse edge of the formation region was also measured at the beginning of this irregular regime. Norberg (2001) also reported a local minimum in the fluctuating lift coefficient variation with Reynolds number at the beginning of the irregular regime.

Above the intermediate range, the study by Bloor (1964) provided measurements at $Re = 1.95 \times 10^4$, 2.95×10^4 and 4.5×10^4. For each of these Reynolds numbers, the laminar–turbulent transition occurred in the formation region, approximately $0.2d$–$0.25d$ from the rear of the circular cylinder.

A review of base pressure coefficient measurements of the wake of a circular cylinder was conducted by Roshko (1993), up to $Re \approx 10^7$. The intermediate range proposed by Bloor (1964) is shown to coincide with an increase in base pressure coefficient, corresponding to the development of a Kelvin–Helmholtz instability in the separating shear layers. The observed increase in base pressure coefficient continued up to $Re \approx 1.2 \times 10^5$. Beyond this Reynolds number, a dramatic decrease in both the drag and base pressure coefficients are observed, as the "critical transition" in the wake occurs. Roshko described that the flow past a cylinder at the critical transition experienced a separation followed by a reattachment, which allowed a later separation at approximately 140° from the front of the cylinder. This reduced the width of the wake, which in turn reduced the drag coefficient.

At still higher Reynolds numbers, the "supercritical regime" and the "post critical regime" are found. In the supercritical regime low drag coefficients are measured, as the boundary layer separates, becomes turbulent and reattaches to the cylinder, before again separating. In the post critical regime, the boundary layer is fully turbulent, and separation occurs at approximately 100°, giving rise to an increase in base pressure coefficient measurements.

This completes the review of the flow past a circular cylinder. A summary of the transitions in the flow past a circular cylinder at low Reynolds number is presented in table 1.2.

Circular cylinder wake transition	Experimental Re_c	Computational Re_c
Boundary layer separation	6	5
Hopf transition to unsteady flow	48	47
Three-dimensional transition – Mode A	180	188.5
Three-dimensional transition – Mode B	230–260	259

TABLE 1.2: Transition Reynolds numbers from experimental and computational studies of the flow past a circular cylinder (Taneda 1956b; Noack & Eckelmann 1994b; Nishioka & Sato 1978; Williamson 1988a; Dušek *et al.* 1994; Barkley & Henderson 1996; Henderson 1997).

1.3 The Flow past Rings

Having reviewed significant findings in the literature pertaining to the flow past a sphere and a circular cylinder, the relatively small body of work dedicated to the flow past rings is now explored.

1.3.1 Rings with Circular Cross-Section

As part of a detailed experimental study of the development of turbulence in vortex streets behind circular cylinders (Roshko 1953, 1954), the flow behind rings was studied for comparison purposes. In Roshko (1954), rings were constructed by bending wire into circles ranging from 4mm to 1.6cm in diameter. These were supported by three fine wires in the order of 0.1mm in thickness, equi-spaced around the ring. This enabled aspect ratios of $Ar = 5.1$, 9.5 and 10.0 to be modelled, with experiments varying in Reynolds number over $70 < Re < 500$. It was noted that for a ring with $Ar = 10.0$, the wake consisted of annular vortex rings, which appeared similar in structure to the vortex shedding street observed behind a circular cylinder. Quantitatively, a reduction in Strouhal frequency of vortex shedding was observed when compared with the wake of a circular cylinder. At $Re = 100$, the Strouhal frequency of shedding was approximately 6% lower for the wake of a ring with $Ar = 10.0$, and at $Re = 500$, the Strouhal frequency was approximately 3% lower. Evidence of an asymmetry between the shed inner and outer vortices comprising the annular vortex wake was measured with a hot-wire probe. A less-pronounced discrepancy was also observed for circular cylinders, so it remained an open question as to whether this asymmetry was due to the axisymmetric geometry, or interference of the probe.

The experiments of Roshko (1954) involving a ring with $Ar = 5.1$ showed that the wake exhibited remarkably different properties. Between Reynolds numbers $89 \leq$

$Re \leq 153$, the wake consisted of vortex-loop shedding consistent with observations of the wake behind a sphere (Magarvey & Bishop 1961b; Mittal 1999a), with Strouhal frequencies being measured in the range $0.051 < St < 0.060$. An increase in Reynolds number caused a rapid jump in Strouhal number, to between $St = 0.147$ and 0.212 up to $Re = 455$. This increase corresponded to a switch in wake dynamics from the vortex-loop type shedding, to the shedding of annular vortex rings consistent with the wake behind larger rings, and analogous to the vortex street in the wake of a circular cylinder.

The culmination of several years of work was presented in a landmark publication by Monson (1983). He provided for the first time a systematic study of the wakes of a wide range of aspect ratios, at various Reynolds numbers over the range $Re < 1000$, which included the viscous regime relevant to the present study. Flow visualisation was performed by coating rings in dye, and allowing them to fall freely through a tank. As with the sphere studies of Magarvey & Bishop (1961a), the vertical descent of the rings was influenced by hydrodynamic forces acting on the rings, which in some cases induced transverse motions, no doubt influencing the characteristics of the observed shedding modes in the wake.

Monson used a parameter based on the projected frontal solidity, S, to describe the rings. The solidity relates to the aspect ratio parameter employed in the present work by

$$Ar = \frac{2}{S} - 1 + 2\sqrt{\frac{1}{S^2} - \frac{1}{S}}. \tag{1.1}$$

Based on observations of the types of wakes observed, Monson categorised the rings into three groups. Small aspect ratios in the range $1 \leq Ar \lesssim 7$ exhibited wakes similar to solid bodies, with rows of oblique vortex loops being shed into the wake. He reports that at higher Reynolds numbers, these wakes experienced a change, shedding counterrotating vortex rings, and experiencing a sharp rise in Strouhal frequency, similar to that measured by Roshko (1954). Such a transition can only be observed from the wake visualisations presented by Monson for aspect ratios $Ar \gtrsim 4.42$. At $Ar = 4.42$, this transition occurrs between $94 < Re < 97$. Visualisations of smaller aspect ratios show solid-body type shedding to high Reynolds numbers (i.e. $Re = 2940$ at $Ar = 1$, and $Re = 347$ at $Ar = 2.60$).

An intermediate aspect ratio range is proposed for $7 \lesssim Ar \lesssim 25$, where either a wake consisting of parallel or oblique shedding was observed, with counterrotating

vortex rings, or helical counterrotating vortex spirals being observed, respectively. With an increase in Reynolds number, the uniform vortex rings became irregular, forming "turbulent annular puffs".

Finally, for aspect ratios $Ar \gtrsim 25$, the wakes behind the rings were observed to consist of only parallel counterrotating vortex rings, and with an increase in aspect ratio, the wake characteristics approached those observed behind a circular cylinder.

1.3.1.1 Rings Approximating a Circular Cylinder

These earlier studies provided the inspiration for a comprehensive study by Leweke & Provansal (1995) of rings with large aspect ratios ($Ar \gtrsim 10$), to study the wake behind a circular cylinder without the end-effects usually associated with experimental studies. Some of the findings in that study were also reported in Leweke & Provansal (1994).

Roshko (1953) showed experimentally that laminar vortex shedding from rings occurred at frequencies lower than for the circular cylinder by up to a few percent. This behaviour was quantified experimentally by Leweke & Provansal (1995). They defined a Strouhal–Reynolds-curvature relationship for laminar shedding for a ring diameter at least 10 times greater than its cross-sectional diameter. Their study also investigated the flow regimes for $Re < 400$, and employed slender rings to model a straight circular cylinder without end-effects. Roshko (1953) noted that at smaller aspect ratios, the wakes of the rings exhibited a vastly different Strouhal–Reynolds number variation.

Asymmetric wakes were observed by both Monson (1983) and Leweke & Provansal (1995), in the form of helical vortex rings analogous to the oblique shedding observed by Williamson (1989) for circular cylinders. Whereas the oblique wake of a circular cylinder can be observed at arbitrary angles to the cylinder axis depending on the experimental end conditions and cylinder length, the helical vortex rings were observed to shed as discrete modes consisting of single, double or triple helices, due to the imposed periodicity of the ring geometry. Smoke-wire flow visualisation of the vortex shedding modes in the wake behind a ring are provided in figure 1.8.

The experiments of Monson (1983) involved observing a ring falling through a liquid, rendering Strouhal number measurements difficult. However, the study by Leweke & Provansal (1995) employed a fixed ring mounted in a wind tunnel. This permitted accurate measurement of the Strouhal number by a hot-wire probe. The appearance of the three helical modes was studied for different aspect ratios, and it was found that

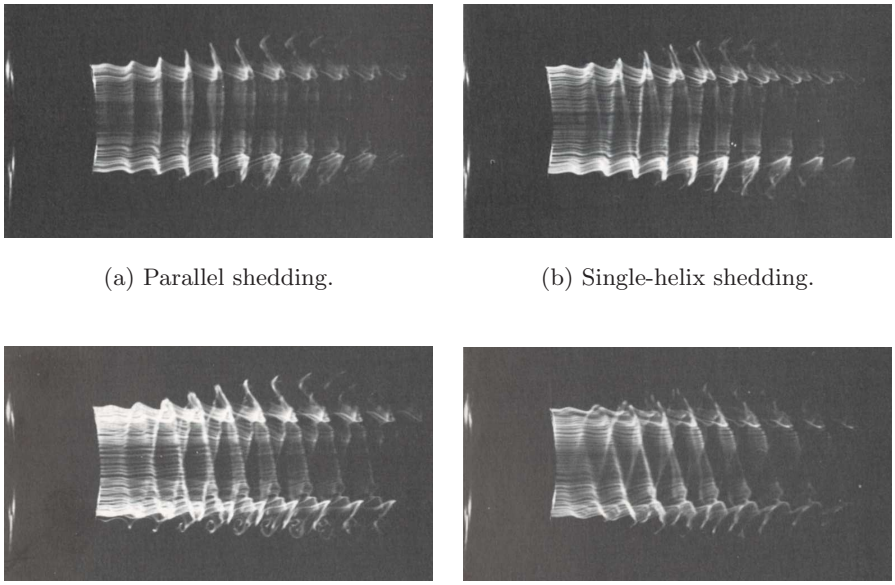

(a) Parallel shedding. (b) Single-helix shedding.

(c) Double-helix shedding. (d) Triple-helix shedding.

FIGURE 1.8: Vortex-shedding modes in the wake behind a ring with $Ar = 24.3$ at $Re = 105$ (from Leweke & Provansal 1995). The modes were identified by observing the deformation of a cylindrical smoke sheet.

the double and triple helices could only be observed for larger rings of aspect ratio approximately $Ar > 18$. The stability of the helical modes was also studied. Higher-order helical modes were less stable, being observed only at higher Reynolds numbers than for parallel shedding. Furthermore, it was observed that a decrease in aspect ratio led to a corresponding increase in the relative critical Reynolds numbers for the respective helical modes.

The Strouhal–Reynolds number profiles of Leweke & Provansal (1995) over the asymmetric transition range for the rings compare in an interesting way to the corresponding profiles reported by Williamson (1988a, 1996b) for the circular cylinder. The former observed a discontinuity, marked by a drop in Strouhal frequency of about 5%, in the vicinity of the Mode A transition for the cylinder, consistent with the corresponding drop in the cylinder profile. At the Mode B transition, however, Strouhal number profiles for the ring exhibit a difference in the behaviour. For the circular cylinder, there is evidence of two distinct frequencies in an overlap region before the wake becomes dominated by the Mode B instability at $Re \cong 260$. In contrast, the wake of the ring appears to undergo a continuous transition as the Reynolds number increases.

At higher Reynolds numbers ($Re > 300$) there is a return to consistency between the cylinder and ring profiles for the range of aspect ratios studied.

1.3.1.2 Oblique Shedding Modes

The phenomenon of oblique shedding in the wakes behind rings was observed by Monson (1983) and Leweke & Provansal (1995). It is analogous to the oblique shedding in the wake of a circular cylinder (Williamson 1989; Hammache & Gharib 1991). Williamson (1989) showed that the Strouhal frequency of the oblique vortex streets adheres to a cosine function of the parallel Strouhal frequency, and the oblique shedding angle. Leweke & Provansal (1995) verified that the same law holds for the oblique shedding from rings. The azimuthal periodicity of the ring geometry locks the oblique shedding modes to helical spirals. Oblique shedding modes including up to three spirals have been observed (Leweke & Provansal 1995).

1.3.2 Rings with Non-Circular Cross-Section

The study of rings of various cross-section has been fuelled by the myriad practical applications of these geometries to internal flows. Examples of these flows include propulsion systems, carbuerettor jets, combustion chambers, and flame stabilisers.

A short work by Takamoto & Izumi (1981) included interesting dye visualisation images of both the annular vortex rings shed from a ring comprising a circular disc with a large hole at the centre, giving a diameter ratio of approximately $D/d = 5$. They observed a predominantly axisymmetric wake, which in cross-section appeared similar to the vortex street in the wake of a circular cylinder, however a pairing of the inner to the outer shed vortices was observed. Evidence of weak streamwise structures can be observed in their photographs, especially at early times in the run. The ring was started impulsively, so it is likely that these non-axisymmetric irregularities of the annular vortex rings was a by-product of their startup conditions. The evolution of intrinsic non-axisymmetric instabilities of the wake analogous to the three-dimensional instabilities in the wake of a circular cylinder would be surprising for the Reynolds number range of their experiments ($51 < Re < 68$).

Experiments on a ring with a trapeziodal cross-section were performed to assess the characteristics of such a geometry in open flow (Bearman & Takamoto 1988), and a confined flow (Miau *et al.* 1992), which introduces an additional parameter pertaining to the pipe diameter in which the ring was enclosed.

1.3.3 Analogous Flows to the Flow past Rings

The vortex streets observed in the wakes behind rings bear some similarities to the wakes observed in the flow past pairs of bluff bodies. A similarity is also observed between the flow past a circular cylinder in the vicinity of a boundary, and the flow past a ring.

1.3.3.1 The Flow past A Cylinder Near to a Boundary

A geometric analogy exists between the two-dimensional circular cylinder placed close to a wall, and the circular cross-section ring at small aspect ratios, where the ring cross-section lies in the vicinity of the axis. Essentially both the axis of the ring and the boundary near the cylinder constrain and deform the wake. A free surface with a Froude number dominated by gravity ($Fr = 0$) is essentially a boundary with zero tangential stresses. Hourigan *et al.* (2002) modelled such a case with numerical computations at a Reynolds number $Re = 180$. They showed that as the cylinder approached the free surface, the Strouhal number for the vortex shedding street increased by 10% from the reference cylinder with no boundaries in its vicinity. This maximum shedding frequency occurred where the gap between the cylinder and the wall was 0.7 times the diameter of the cylinder ($0.7d$). A further reduction in this gap saw a rapid drop in frequency, until for gap ratios less than $0.1d$ no vortex shedding was observed.

1.3.3.2 The Flow past a Pair of Cylinders

In considering the diverse wake structures observed to shed from rings, Roshko (1954) drew analogies with studies of a pair of circular cylinders aligned normal to the flow, and the coalescence of the vortex streets as the gap between the cylinders is reduced (e.g. also refer to the more recent study by Bearman & Wadcock 1973). In Williamson (1985b) the oscillating flow past a circular cylinder and a pair of circular cylinders was investigated experimentally. The study of flows around oscillating bodies is not relevant to the present work. However, in a subsequent work, Williamson (1985a) considered the case of fixed circular cylinders, side by side in a flow. By varying the gap ratio between the cylinders, several flow regimes were identified.

Williamson provided striking experimental dye visualisations of both antiphase vortex shedding modes (the vortex shedding behind one cylinder is a reflection of the other), and in-phase modes (one wake appears as a topological copy of the other).

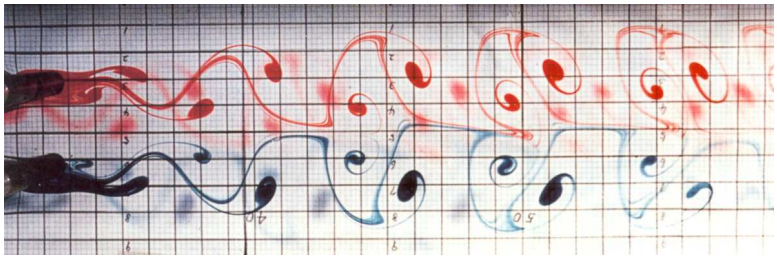

(a) Antiphase shedding.

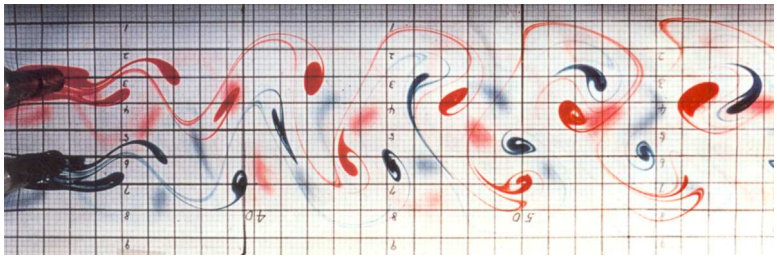

(b) In-phase shedding.

FIGURE 1.9: Dye visualisation images of the wakes behind a pair of circular cylinders at $Re = 200$ (from Williamson 1985a). Flow is from left to right, and the cylinders are separated by 2.4 cylinder diameters.

These flow visualisations are reproduced here in figure 1.9. Williamson found that the antiphase configuration to be stable even for gap ratios in the order of three cylinder diameters ($3d$). The in-phase vortex street tended to break down for small gap ratios ($2d$–$4d$), as like-signed vortices from each cylinder coalesced, forming a large diffused vortex street far downstream. Wind tunnel smoke visualisations confirmed that fluid was indeed passing from one side of the wake to the other. Observations were made of an asymmetry in strength which occurred between steady wakes behind the two cylinders for lower Reynolds numbers ($Re \approx 55$) and small gap ratios (approximately $1d$). This asymmetry induced a large-scale waviness in the far wake, as the shear layer developed an instability.

The study of the interferences of the wakes behind closely aligned bluff bodies is not limited to circular cylinders. Indeed, in Hayashi *et al.* (1986), the flow behind two, three, and four normal flat plates was studied experimentally.

1.3.3.3 The Flow past a Pair of Spheres

A number of recent experimental and numerical studies treat the wake interference between two spheres in proximity. The experimental study by Leweke *et al.* (1999), provided both striking and detailed flow visualisations of the non-axisymmetric and unsteady wakes behind a sphere at $Re = 270$ and 300, respectively, and also presented images that showed the wakes behind spheres for which the distance between the centres varied from $1.0d$ (i.e. surfaces touching) to $2.8d$. They observed coupling of the unsteady wakes at $Re = 360$ for separation distances less than $2.2d$. For larger separations ($2.5d$–$5.0d$), no coupling was observed, with an independent phase of shedding measured from each sphere. Separations between $1.9d$ and $2.2d$ showed predominantly in-phase shedding. A reduction in the separation to between $1.3d$ and $1.6d$ caused antiphase shedding. Finally, for very small separations ($1.0d$–$1.1d$), the spheres were observed to behave as a single body, generating an unsteady wake with a similar vortex-loop structure to that observed behind a single sphere.

The three-dimenional numerical computations of Brydon & Thompson (2001) support the experimental observations of Leweke *et al.* (1999), with no coupling observed for a separation of $3.5d$, coupled in-phase shedding observed for a separation of $2.5d$, and a strongly interacting antiphase wake observed for a separation of $1.5d$. Leweke *et al.* (1999) and Brydon & Thompson (2001) provide experimental dye visualisation images which verify the existence of the flow regimes they identified. These images are reproduced in figure 1.10. In recent publications (Schouveiler *et al.* 2002, 2004), the numerical and experimental results are compared, and the coupling scenario for varied sphere separations is verified.

In summary, the coupling scenario for spheres with an increase in gap ratio includes initially a single-body wake, followed by coupled antiphase shedding, in-phase shedding, and for sufficiently large gap ratios, coupling is no longer observed. For wakes of pairs of cylindrical geometries the scenario is somewhat different. Small gap ratios can induce single-body behaviour, and antiphase shedding is stable for a range of gap ratios, which maintains the reflective wake symmetry. In-phase shedding is unstable for intermediate gap ratios, and an antisymmetrical large-scale wake is observed. For the wake behind a ring, an added complexity is introduced, as the vortex rollers observed on opposite sides of the ring are in fact sections of the one annular vortex street.

(a) Separation of $3d$.

(b) Separation of $2d$.

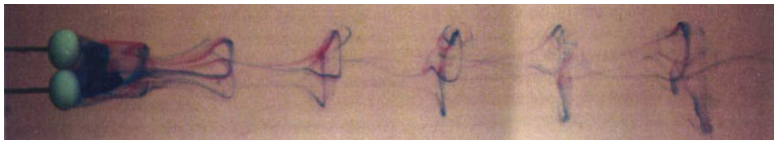

(c) Separation of $1d$.

FIGURE 1.10: Dye visualisation images of the wakes behind a pair of spheres at $Re = 350$ (from Leweke *et al.* 1999; Brydon & Thompson 2001). Flow is from left to right, and sphere separation is measured from the centre of the spheres.

1.4 Review Summary

This review of the literature has revealed that further studies are required to better understand the low-Reynolds-number flow past rings. Broadly speaking, rings with small aspect ratios exhibit wake dynamics similar to solid axisymmetry bodies such as a sphere or a disc, and rings with large aspect ratios exhibit wakes similar to the circular cylinder. Presently there is only limited knowledge and understanding of the precise flow regimes that exist over the aspect ratio/Reynolds number parameter space.

In the next chapter, methodologies for the numerical, analytical, and experimental aspects of the study are discussed. Following this, chapters present the results of studies pertaining to the axisymmetric flow past rings, the stability of the axisymmetric flow past rings, the non-axisymmetric transition modes in the flow past rings, the transitions which lead to turbulence in the vortex streets behind rings, and finally, analysis of the

three-dimensional transitions in the vortex street behind a circular cylinder is presented.

Chapter 2

Numerical Methods and Experimental Techniques

This chapter introduces numerical techniques employed throughout the research programme. A computational technique known as the *spectral-element method* is employed to compute the flow fields being investigated. A linear stability analysis technique is also employed, as is a non-axisymmetric formulation of the numerical code. The numerical formulation of these techniques will be expanded upon in § 2.1.3 and § 2.1.4, respectively.

The numerical formulation of the spectral-element method is described in § 2.1. In § 2.2, the method by which the numerical scheme is applied to the flow past a ring is elucidated. Results of a grid-resolution study from which the computational domain size and spatial resolution for the axisymmetric computations was determined is presented in § 2.2.1. A discussion regarding the accuracy of the computations and application of the results is included in § 2.2.3.

2.1 Computation of the Flow past Rings

The previous studies that have investigated the flow past a ring have all been experimental in nature (e.g. Monson 1983; Bearman & Takamoto 1988; Leweke & Provansal 1994, 1995). No attempt has been made to investigate the low-Reynolds-number flow past rings numerically. A motivation for the present computational study is the lack of understanding of the low-Reynolds-number flow transitions which occur in the flow past rings. The scope of the present work includes the stability and structure of the wakes behind rings at low Reynolds numbers, and hence computational methods are an ideal tool to investigate the current problem.

As previously stated, the spectral-element method was chosen as the preferred method of computational simulation. Despite the existence of some "meshless" methods for fluid flow computation, most methods acquire their solutions by approximation of the governing equations for fluid motion over a grid of discrete points, where the flow field is approximated by simple shape functions (often linear or quadratic polynomials) between these points. The spectral-element method is an efficient and accurate method, as it combines the exponential convergence rate of the less adaptable global spectral methods, with the adaptability of finite-element methods.

2.1.1 The Governing Flow Equations

The above computational methods all obtain their solutions by approximating the governing equations of motion for a fluid, subject to the various boundary and initial conditions imposed by the system geometry and starting state. Named after the nineteenth-century scientists credited with their derivation, the governing equations are known as the Navier–Stokes equations. In their most general form the equations are highly complicated, and analytical solutions have only been obtained for very limited and specific cases. The Navier–Stokes equations apply to Newtonian fluids (i.e. fluids which exhibit a linear relationship between shear stress and shear strain). For the present study, only Newtonian fluids are considered, and the flow is assumed to be incompressible. The incompressibility constraint implies that the fluid has a constant density in both space and time. It is generally considered appropriate to assume incompressibility for flows at Mach numbers $Ma \lesssim 0.3$. As was discussed earlier, these assumptions are valid for the flow systems considered in the present work.

In vector form, the incompressible Navier–Stokes equations are written

$$\frac{\partial \mathbf{u}}{\partial t} = -(\mathbf{u} \cdot \nabla)\mathbf{u} - \frac{1}{\rho}\nabla P + \frac{1}{Re}\nabla^2 \mathbf{u}, \tag{2.1}$$

$$\nabla \cdot \mathbf{u} = 0, \tag{2.2}$$

where equation 2.2 is the continuity relationship, derived from the principle of conservation of mass, and equation 2.1 describes the momentum relationship, and contains from left to right a non-linear advection term, a pressure term, and a diffusion term. To maintain dimensional consistency, the velocity ($\mathbf{u}$) and time (t) are considered in non-dimensionalised form. It is convenient in the computational formulation to combine the (constant) density and pressure to form the kinematic pressure $p = P/\rho$. The Reynolds number is given by Re.

2.1.2 The Spectral-Element Method

The spectral-element method is used to discretise the incompressible Navier–Stokes equations to solve the flow past rings. The chosen scheme employs a Galerkin finite-element method in two dimensions, with high-order Lagrangian interpolants used within each element. Some inherent efficiencies common to the spectral method are also achieved with the spectral-element method. The node points within each element correspond to the Gauss-Legendre-Lobatto quadrature integration points, producing diagonal matrices. As the functions at internal nodes only depend on the boundary nodes, matrix manipulation allows the internal nodes to be eliminated from the matrix subproblems of the pressure and diffusion substeps through static condensation.

2.1.2.1 Spatial Discretisation

The treatment of spatial discretisation for the spectral-element method has been well-documented (e.g. see Patera 1984; Tomboulides *et al.* 1993; Tomboulides & Orszag 2000; Blackburn & Lopez 2002; Pregnalato 2003). A description of some important aspects of the spatial discretisation are provided here.

The computational domain in the r–z plane is broken up into quadrilateral elements. Within each element, Gauss–Lobatto–Legendre quadrature is employed for integration, which provides exponential convergence. Karniadakis & Sherwin (1999) describe that the Gauss-Lobatto-Legendere quadrature points are the roots of the equation

$$(1-\xi^2)P'_m(\xi) = 0 \quad \text{with} \quad -1 \leq \xi \leq 1. \tag{2.3}$$

Kreyszig (1993) provides an expression for the Legendre polynomial (P_m) using *Rodriguez's formula*, which is written

$$P_m = \frac{1}{2^m m!}\frac{\mathrm{d}^m}{\mathrm{d}\xi^m}(\xi^2-1)^m \quad \text{where} \quad m = 0, 1, 2, \ldots. \tag{2.4}$$

The weighting coefficients of Gauss-Legendre-Lobatto quadrature are given by

$$w_j = \frac{2}{m(m+1)}\frac{1}{[P_m(x_j)]^2} \quad \text{with} \quad j = 0, 1, \ldots, m. \tag{2.5}$$

These weighting coefficients and quadrature points permit the integrals resulting from the application of the weighted residual method to be determined using Gauss-Legendre-Lobatto quadrature in two dimensions.

It should be noted that Tomboulides *et al.* (1993) employed Lagrangian interpolants based on zeroes of Jacobi polynomials in the elements along the axis of symmetry, whereas in the present formulation, Gauss-Legendre-Lobatto interpolants are used throughout the domain. To avoid the singularities associated with $r \to 0$ at the axis, the singular terms in the fluid equations are set to zero. This follows the study by Blackburn & Lopez (2002), which showed that such a formulation is equivalent to the assumption that variables approach zero as $r \to 0$ faster than r^2. The efficiency of the spectral-element method is therefore retained, and spectral convergence is preserved for flows in an axisymmetric coordinate system.

2.1.2.2 Temporal Discretisation

A three-step splitting scheme is used for the temporal discretisation, as described in Karniadakis *et al.* (1991). The substeps of this process treat the advection, mass conservation/pressure, and diffusion terms of the Navier–Stokes equations. For use with this method the Navier–Stokes equations are considered in conservative form, which provides discrete energy conservation.

In the first substep, an intermediate velocity field $\mathbf{u}^*$ is computed from the non-linear convection term by the equation

$$\frac{\mathbf{u}^* - \mathbf{u}^n}{\Delta t} = -\mathbf{u} \cdot \nabla \mathbf{u}, \tag{2.6}$$

which is solved by a third-order Adams-Bashforth scheme.

In the second substep, a second intermediate velocity field $\mathbf{u}^{**}$ is computed from the pressure term by the equation

$$\frac{\mathbf{u}^{**} - \mathbf{u}^*}{\Delta t} = -\nabla p^{n+1}. \tag{2.7}$$

The divergence of equation 2.7 reduces to *Poisson's equation* for the pressure,

$$\nabla^2 p^{n+1} - \frac{1}{\Delta t} \nabla \cdot \mathbf{u}^* = 0, \tag{2.8}$$

where the divergence-free condition (equation 2.2) has been applied to the intermediate velocity field $\mathbf{u}^*$. Equation 2.8 is then solved directly.

In the third substep, the velocity field $\mathbf{u}^{n+1}$ is computed from

$$\frac{\mathbf{u}^{n+1} - \mathbf{u}^{**}}{\Delta t} = \frac{1}{Re} \nabla^2 \mathbf{u} \tag{2.9}$$

using an implicit Crank–Nicholson scheme with a theta modification (see Canuto *et al.* 1988). The Crank–Nicholson method maintains second-order accuracy in both space and time, and overall, the splitting scheme achieves a second-order time-accuracy when first-order pressure boundary conditions are imposed, as described in Karniadakis *et al.* (1991).

In the axisymmetric computations, the velocity and pressure fields vary with the spatial coordinates z and r, and time t, and are independent of θ. In the non-axisymmetric computations, the velocity and pressure fields vary also with θ, and a description of the non-axisymmetric formulation of the method is provided in § 2.1.4.

The following section provides a description of the stability analysis technique that is employed in chapter 4 to determine the stability of the axisymmetric wakes behind rings to non-axisymmetric transitions.

2.1.3 Floquet Linear Stability Analysis

Conceptually, Floquet analysis takes a two-dimensional periodic base flow, and computes the growth rate of a three-dimensional perturbation of a chosen spanwise wavelength using the linearised three-dimensional Navier–Stokes equations. The magnitude of the perturbation field is monitored from period to period. The stability of the base flow to the particular spanwise perturbation is described by the Floquet multiplier μ. The flow is unstable for $|\mu > 1|$, and stable for $|\mu| < 1$. Neutral stability occurs when $|\mu| = 1$, which represents a system in which the perturbation will neither grow nor decay. The Reynolds number for a flow giving $|\mu| = 1$ is the critical Reynolds number for the onset of the instability of the chosen azimuthal wavelength.

2.1.3.1 Formulation of the Linear Stability Analysis Technique

The formulation of the Floquet linear stability analysis technique begins from the non-dimensionalised incompressible Navier–Stokes equations

$$\begin{aligned} \frac{\partial \mathbf{u}}{\partial t} &= -\mathbf{N}(\mathbf{u}) - \nabla p + \frac{1}{Re}\nabla^2 \mathbf{u}, \\ \nabla \cdot \mathbf{u} &= 0, \end{aligned} \tag{2.10}$$

where the non-linear advection term $\mathbf{N}(\mathbf{u}) \equiv (\mathbf{u}\cdot\nabla)\mathbf{u}$. Expanding about the axisymmetric base flow, a non-axisymmetric perturbation $\mathbf{u}'$ is added to the system such that the velocity field is written as $\mathbf{u}(z, r, t) + \mathbf{u}'(z, r, \theta, t)$. The perturbation field is subtracted

from the base flow equation, which yields the linearised Navier–Stokes equations

$$\begin{aligned} \frac{\partial \mathbf{u}'}{\partial t} &= -\mathbf{DN}(\mathbf{u}') - \nabla p' + \frac{1}{Re}\nabla^2 \mathbf{u}', \\ \nabla \cdot \mathbf{u}' &= 0, \end{aligned} \tag{2.11}$$

with the linearised advection term $\mathbf{DN}(\mathbf{u}') \equiv (\mathbf{u}' \cdot \nabla)\mathbf{u} + (\mathbf{u} \cdot \nabla)\mathbf{u}'$. The perturbation field is assumed to be periodic with the base flow, and from period to period, a norm of the perturbation field, $N(\mathbf{u}')$, is evaluated.

The perturbation fields are written as a Fourier expansion

$$\begin{aligned} \mathbf{u}'(z, r, \theta, t) &= \sum_m \hat{\mathbf{u}}(z, r, m, t) \mathrm{e}^{\mathrm{i}m\theta}, \\ p'(z, r, \theta, t) &= \sum_m \hat{p}(z, r, m, t) \mathrm{e}^{\mathrm{i}m\theta}, \end{aligned} \tag{2.12}$$

and the linearity of the system permits the azimuthal Fourier modes which comprise the perturbation field to be decoupled. The Floquet modes are assumed to be real, and from the analysis of Barkley & Henderson (1996), a typical term in the expansion takes the form

$$\begin{aligned} \mathbf{u}'_m(z, r, \theta, t) &= \langle \hat{u}_m \cos(m\theta), \hat{v}_m \cos(m\theta), \hat{w}_m \sin(m\theta) \rangle, \\ p'_m(z, r, \theta, t) &= \hat{p}_m \cos(m\theta). \end{aligned} \tag{2.13}$$

The perturbation remains in the same form under equation 2.11, and provides Floquet modes of the same form. Therefore, the stability of a perturbation field $\mathbf{u}'$ to an axisymmetric base flow $\mathbf{u}$, is a function of Reynolds number Re, and the Floquet mode number m, of a discrete Fourier mode. The aims of the analysis are to determine the dominant Floquet multiplier μ for each mode number, and to determine the critical Reynolds number at which the mode is neutrally stable ($|\mu| = 1$).

For analysis, the dominant Floquet multiplier is defined as

$$\mu \equiv \mathrm{e}^{\sigma T}, \tag{2.14}$$

and the magnitude of the dominant Floquet multiplier is obtained from

$$|\mu| = \frac{N[\mathbf{u}'(z, r, \theta, t + T)]}{N[\mathbf{u}'(z, r, \theta, t)]}. \tag{2.15}$$

In fact, the perturbation field is not necessarily periodic with the base flow. Subharmonic modes, where the mode occurs with a Floquet multiplier $\mu = -1$, have a period twice that of the base flow (2T symmetry). In addition, the instability can occur through a complex-conjugate pair Floquet mode, in which case an additional

frequency is introduced, which renders the mode aperiodic. It is therefore necessary to monitor the perturbation field periodicity and sign when the instabilities are classified. With the present linear stability analysis technique, a subharmonic mode will exhibit a converged Floquet multiplier, with a perturbation field that alternates in sign from period to period. Likewise, a complex-conjugate pair mode will produce an aperiodic perturbation field, with Floquet multipliers that oscillate about a mean value.

2.1.3.2 Treatment of Periodic and Steady Base Flows

It was mentioned earlier that the linear stability analysis technique applies to time-periodic flows. In the present work, base flows that are steady in time are also analysed. The present linear stability analysis technique may be applied to steady base flows, as shown here. Time-periodic flows satisfy the definition

$$\begin{aligned} \mathbf{u}(t) &= \mathbf{u}(t-T), \\ p(t) &= p(t-T), \end{aligned} \tag{2.16}$$

which states that for any time t, the flow field is identical to the flow field from the preceding period $t-T$, where T is the period of the flow. Clearly, a flow that is steady in time satisfies this definition for any arbitrary value of T, as it is identical for all t.

If the value of T is kept constant in the analysis of a steady flow, a similar consistency between measured values of $|\mu|$ is achieved, which from equation 2.14 then varies only as a function of the growth rate of the instability (σ). It is through this approach that the present analysis is to be applied to the steady flow past rings in chapter 4.

2.1.3.3 The Power Method Versus the Krylov Method

The present formulation of the stability analysis technique adopts the *power method* described by Blackburn & Lopez (2003). In this method, the perturbation field is temporally evolved with the base flow field, and the magnitude of the dominant Floquet multiplier $|\mu|$ is determined by monitoring the change in magnitude of a norm of the perturbation field ($N[\mathbf{u}'(t)]$) over a period of the base flow (T), so that

$$\mathrm{e}^{\sigma_n T} = N[\mathbf{u}'(t+T)]/N[\mathbf{u}'(t)], \tag{2.17}$$

where σ_n is the growth rate of the mode over the n^{th} period. The perturbation field is renormalised to unity after every period, and after a sufficient number of periods, the magnitude of the Floquet multiplier may then be determined from the norm of the

perturbation field at the end of the period,

$$|\mu| = N[\mathbf{u}'(t+T)]. \tag{2.18}$$

This method carries the advantage of lending itself to simple extension to parallel computing, with the base flow being computed on one processor, and any number of perturbation fields of different spanwise wavelength being computed on additional parallel processors. Obviously, it is necessary to send the base flow velocity and pressure fields to the perturbation field processors at each time step.

Two significant drawbacks of the present formulation when compared to the *Krylov method* described by Blackburn & Lopez (2003), and the methods of Natarajan & Acrivos (1993) and Barkley & Henderson (1996), are the assumption of real eigenmodes, and the inability to isolate multiple dominant eigenmodes. Blackburn & Lopez (2003) employed a method that included complex eigenmodes, which permitted standing-wave and modulated travelling-wave modes to be distinguished for complex-conjugate Floquet modes. These alternative methods simultaneously evolved fields of less dominant multipliers, whereas the present formulation provides only a linear combination of any dominant modes. This presents a difficulty when secondary modes occur at a given wavelength.

2.1.3.4 Classification of Instability Modes

The exclusion of phase information from the Floquet multipliers means that care must be taken when classifying instability modes. Several recent works treat this subject (Blackburn & Lopez 2003, 2004; Blackburn *et al.* 2004), which is briefly summarised here. The Floquet mode may adopt any one of three forms: A real bifurcation ($\mu = 1$), a subharmonic bifurcation ($\mu = -1$) and a complex-conjugate bifurcation ($\mu = a \pm \mathrm{i}b$).

Real bifurcations maintain the periodicity of the instability mode with the base flow (although non-linear evolution usually results in a frequency shift). Examples of real bifurcations are Mode A and Mode B in the wake of a circular cylinder (Barkley & Henderson 1996), and the primary non-axisymmetric instability in the wake of a sphere (Natarajan & Acrivos 1993; Tomboulides & Orszag 2000).

Subharmonic bifurcations result in a doubling of the period of the mode, as the mode alternates in sign each base flow period. Thus, the mode will give converged Floquet multipliers with application of the power method, and the perturbation field must be studied to determine if the mode bifurcates through $\mu = -1$ or $\mu = 1$.

Complex-conjugate bifurcations may introduce an incommensurate frequency to the mode, which causes the Floquet multipliers obtained using the power method to oscillate around some mean value, rather than converge to a particular value. Hence complex-conjugate modes are easy to identify, however there is an additional complication. Complex-conjugate modes can adopt either a modulated standing-wave solution, with the evolving mode fixed in the spanwise direction, or a travelling-wave solution, where the mode shifts along the span. The decomposition of the spanwise modes in the linear stability analysis technique employed in the present study (see equation 2.13) excludes spanwise phase information. Therefore, the present analysis technique provides no distinction between standing-wave and travelling-wave complex-conjugate modes. To model travelling-wave modes, a complex spanwise expansion of the Floquet modes must be employed.

2.1.4 Non-Axisymmetric Flow Computations

The computation of non-axisymmetric flow past rings employs a Fourier expansion in the azimuthal direction (θ) of the flow field in the r–z plane. The present formulation of the method was successfully applied to the wake of a sphere (Thompson *et al.* 2001a). It is based on the method described in Tomboulides *et al.* (1993).

The azimuthal periodicity of the ring geometry makes it an ideal geometry for application of a Fourier expansion to model non-axisymmetric flow structures in the wake. At each point on the mesh, the velocity and pressure variables that comprise the axisymmetric formulation of the numerical scheme are replaced by a Fourier series expansion of wavelength $\lambda_\theta = 2\pi/m$ in the azimuthal direction, where J r–z planes are included. The azimuthal mode number m is included, to permit the scheme to model spanwise-periodic flows with an azimuthal wavelength less than 2π, such as the non-axisymmetric modes in the vortex street behind open rings. For further details on the techniques applied here, see Canuto *et al.* (1988), Tomboulides *et al.* (1993) and Pregnalato (2003).

The velocity and pressure fields are decomposed with a Fourier expansion in θ, which gives

$$\left\{ \begin{array}{c} u(z,r,\theta,t) \\ v(z,r,\theta,t) \\ w(z,r,\theta,t) \\ p(z,r,\theta,t) \end{array} \right\} = \sum_{j=-J/2}^{J/2-1} \left\{ \begin{array}{c} u_j(z,r,t) \\ v_j(z,r,t) \\ w_j(z,r,t) \\ p_j(z,r,t) \end{array} \right\} \mathrm{e}^{\mathrm{i}mj\theta} \tag{2.19}$$

For an axisymmetric geometry, the largest possible azimuthal wavelength ($\lambda_{\theta_{max}}$) is

limited by the azimuthal symmetry of the geometry such that $\lambda_{\theta_{max}} = 2\pi$.

For an axisymmetric coordinate system, the operators ∇_{mj} and ∇^2_{mj} are defined as

$$\nabla_{mj} = \left\langle \frac{\partial}{\partial z}, \frac{\partial}{\partial r}, \frac{\mathrm{i}mj}{r} \right\rangle, \tag{2.20}$$

$$\nabla^2_{mj} = \frac{\partial^2}{\partial z^2} + \frac{1}{r}\frac{\partial}{\partial r}\left(r\frac{\partial}{\partial r}\right) - \frac{m^2 j^2}{r^2} = \nabla^2_{rz} - \frac{m^2 j^2}{r^2}. \tag{2.21}$$

These expressions, and equation 2.19, are substituted into equation 2.1 of the governing equations to form

$$\frac{\partial u_j}{\partial t} = \mathcal{F}_j\left[-(\mathbf{u}\cdot\nabla)\mathbf{u}\right]_z - \frac{\partial p_j}{\partial z} + \frac{1}{Re}\left(\nabla^2_{rz} - \frac{m^2 j^2}{r^2}\right)u_j, \tag{2.22}$$

$$\frac{\partial v_j}{\partial t} = \mathcal{F}_j\left[-(\mathbf{u}\cdot\nabla)\mathbf{u}\right]_r - \frac{\partial p_j}{\partial r} + \frac{1}{Re}\left[\left(\nabla^2_{rz} - \frac{m^2 j^2 + 1}{r^2}\right)v_j - \frac{2\mathrm{i}mj}{r^2}w_j\right], \tag{2.23}$$

$$\frac{\partial w_j}{\partial t} = \mathcal{F}_j\left[-(\mathbf{u}\cdot\nabla)\mathbf{u}\right]_\theta - \frac{\mathrm{i}mj}{r}p_j + \frac{1}{Re}\left[\left(\nabla^2_{rz} - \frac{m^2 j^2 + 1}{r^2}\right)w_j - \frac{2\mathrm{i}mj}{r^2}v_j\right], \tag{2.24}$$

where $\mathcal{F}_j$ is a Fourier transform in the azimuthal direction. The non-linear terms are given by

$$\mathcal{F}_j\left[-(\mathbf{u}\cdot\nabla)\mathbf{u}\right]_z = -u_j\left(\frac{\partial u_j}{\partial z} + \frac{\partial v_j}{\partial r} + \frac{\mathrm{i}mjw_j}{r}\right), \tag{2.25}$$

$$\mathcal{F}_j\left[-(\mathbf{u}\cdot\nabla)\mathbf{u}\right]_r = -v_j\left(\frac{\partial u_j}{\partial z} + \frac{\partial v_j}{\partial r} + \frac{\mathrm{i}mjw_j}{r}\right), \tag{2.26}$$

$$\mathcal{F}_j\left[-(\mathbf{u}\cdot\nabla)\mathbf{u}\right]_\theta = -w_j\left(\frac{\partial u_j}{\partial z} + \frac{\partial v_j}{\partial r} + \frac{\mathrm{i}mjw_j}{r}\right). \tag{2.27}$$

It can be seen that equations 2.23 and 2.24 are strongly coupled. It is convenient to introduce complex variables which decouple the equations, as described in Tomboulides & Orszag (2000). The complex variables are defined as

$$\tilde{u}_1 \equiv v_j + \mathrm{i}w_j, \tag{2.28}$$

$$\tilde{u}_2 \equiv v_j - \mathrm{i}w_j, \tag{2.29}$$

and reduce equations 2.22–2.24 to a set of equations for u_j, $\tilde{u}_1$ and $\tilde{u}_2$, which are only coupled through the non-linear terms, and are written

$$\frac{\partial u_j}{\partial t} = \mathcal{F}_j\left[-(\mathbf{u}\cdot\nabla)\mathbf{u}\right]_z - \frac{\partial p_j}{\partial z} + \frac{1}{Re}\left(\nabla^2_{rz} - \frac{m^2 j^2}{r^2}\right)u_j, \tag{2.30}$$

$$\frac{\partial \tilde{u}_1}{\partial t} = \tilde{\mathcal{F}}_j\left[-(\mathbf{u}\cdot\nabla)\mathbf{u}\right]_r - \left(\frac{\partial}{\partial r} - \frac{mj}{r}\right)p_j + \frac{1}{Re}\left(\nabla^2_{rz} - \frac{(mj+1)^2}{r^2}\right)\tilde{u}_1, \tag{2.31}$$

$$\frac{\partial \tilde{u}_2}{\partial t} = \tilde{\mathcal{F}}_j\left[-(\mathbf{u}\cdot\nabla)\mathbf{u}\right]_\theta - \left(\frac{\partial}{\partial r} + \frac{mj}{r}\right)p_j + \frac{1}{Re}\left(\nabla^2_{rz} - \frac{(mj-1)^2}{r^2}\right)\tilde{u}_2, \tag{2.32}$$

where the non-linear terms are given by

$$\begin{aligned}\tilde{\mathcal{F}}_j\left[-(\mathbf{u}\cdot\nabla)\mathbf{u}\right]_r &= \mathcal{F}_j\left[-(\mathbf{u}\cdot\nabla)\mathbf{u}\right]_r + \mathrm{i}\mathcal{F}_j\left[-(\mathbf{u}\cdot\nabla)\mathbf{u}\right]_\theta \\ &= \mathcal{F}_j\left[-\tilde{u}_1\left(\frac{\partial u_j}{\partial z}+\frac{\partial v_j}{\partial r}+\frac{\mathrm{i}mjw_j}{r}\right)\right], \qquad (2.33)\\ \tilde{\mathcal{F}}_j\left[-(\mathbf{u}\cdot\nabla)\mathbf{u}\right]_\theta &= \mathcal{F}_j\left[-(\mathbf{u}\cdot\nabla)\mathbf{u}\right]_r - \mathrm{i}\mathcal{F}_j\left[-(\mathbf{u}\cdot\nabla)\mathbf{u}\right]_\theta \\ &= \mathcal{F}_j\left[-\tilde{u}_2\left(\frac{\partial u_j}{\partial z}+\frac{\partial v_j}{\partial r}+\frac{\mathrm{i}mjw_j}{r}\right)\right]. \qquad (2.34)\end{aligned}$$

In the computations, the z–derivative terms are evaluated in Fourier space, and the non-linear terms are evaluated in physical space for reasons of computational efficiency (see Karniadakis 1990). Only the modes corresponding to positive wavenumbers ($j \geq 0$) are retained in the computations, as the modes possess the symmetry $\mathbf{u}_j = \mathbf{u}_{-j}$. The $J/2$ mode is assigned a value of zero to permit the upper and lower modes in the computations to match, which is necessary to extract the real velocity components.

The present formulation does not explicitly take account of aliasing due to the non-linear substep, which is instead done in real space. Generally, this does not present a problem for computations of low-Reynolds-number flows, as viscosity acts to limit the highest modes (which correspond to the smallest scales) observed in the flow.

2.2 Formulation of the Ring Models

In the introduction, a conceptual representation of the flow system was presented (refer to figure I). In this section, the application of the computational method is described, and a thorough grid resolution and domain size study is presented.

The spectral-element method employed in this study requires a mesh of conforming quadrilateral macro-elements. The elements that comprise the grid are four-sided, and adjacent elements present their entire edge to each other.

Previous numerical studies of the flow past spheres and circular cylinders were used as a starting point for the development of the computational meshes for the present study. In particular, the meshes employed in the numerical stability analysis of the wake of a straight circular cylinder by Barkley & Henderson (1996), and the three-dimensional study by Henderson (1997), provided a helpful description of grid size and resolution for their spectral-element analysis. In order to compare with prior numerical studies of the wakes behind spheres, the meshes employed in the computational studies of Natarajan & Acrivos (1993), Tomboulides *et al.* (1993), Tomboulides & Orszag (2000), and Thompson *et al.* (2001a) were considered.

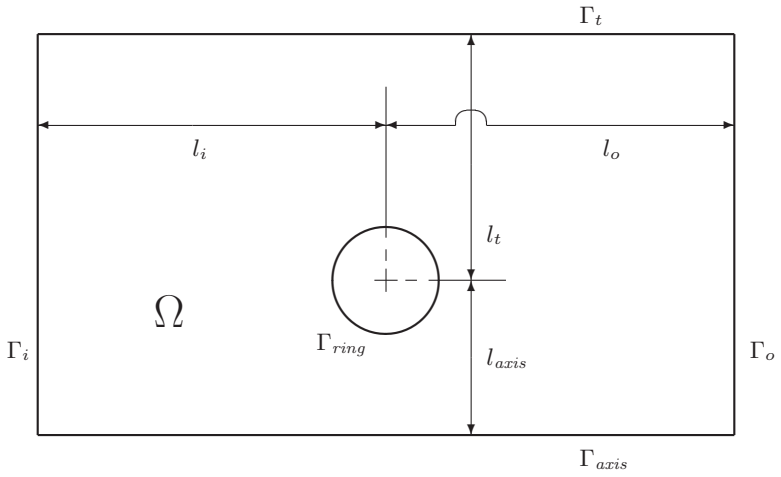

FIGURE 2.1: Diagram of computational domain Ω, with wall boundary and domain size nomenclature defined.

The computational meshes for all aspect ratios maintained consistent inlet, transverse and outlet domain lengths, and spatial element density. A rectangular domain was employed, with a zero normal velocity boundary condition imposed at the axis, a zero normal velocity gradient boundary at the outlet, and a constant velocity inlet condition imposed over the upstream inlet boundary and the outer transverse boundary to model the free stream fluid velocity U_∞. In figure 2.1, the computational domain is shown.

With the diameter of the ring cross-section scaled to unity, and the domain lengths l_i, l_t and l_o fixed for all aspect ratios, the aspect ratio may be varied by altering the length l_{axis}. The length l_{axis} is related to aspect ratio by

$$l_{axis} = \frac{Ar}{2}. \tag{2.35}$$

2.2.1 Grid-Resolution Study

A thorough grid-resolution study was performed to determine both an adequate domain size for the family of meshes created to model rings, and a sufficient spatial resolution to accurately and efficiently resolve all features of the flow field in the Reynolds number ranges under consideration in the study.

The determination of the inlet length (l_i), the transverse length (l_t), and the outlet length (l_o) is described in § 2.2.1.1. In § 2.2.1.2, a spatial resolution is selected for the meshes such that the requirements of computational accuracy and efficiency are

	Sphere studies		Circular cylinder studies			Square cylinder
	Mesh A	**Mesh B**	**Mesh C**	**Mesh D**	**Mesh E**	**Mesh F**
l_i	4.5	15	8	8	6	5.5
l_t	4.5	15	14	8	6	9
l_o	25	15	25	24	12	17.5

TABLE 2.1: Inlet, transverse and outlet computational domain lengths from numerical studies in the literature, normalised by the length scale, d. Sphere models include *Mesh A* from Tomboulides & Orszag (2000) and *Mesh B* from Johnson & Patel (1999), circular cylinder models include *Mesh C* from Barkley & Henderson (1996), *Mesh D* from Henderson (1997) and *Mesh E* from Zhang *et al.* (1995). *Mesh F* comes from a study of a square cross-section cylinder (Robichaux *et al.* 1999).

fulfilled.

2.2.1.1 Domain Size Study

As previously stated, the meshes generated for the present study were based on meshes used in similar numerical studies of wakes behind spheres and circular cylinders. The pertinent inlet, transverse and outlet domain lengths from some of these studies are provided in table 2.1.

An important point regarding the transverse domain size employed for a numerical study stems from an observation by Batchelor (1967) that in a cylindrical coordinate system (i.e. such as that employed for the present study), perturbations decay in proportion to $1/r^3$. This is one power of r faster than the corresponding decay rate in a Cartesian coordinate system, where transverse perturbations exhibit a rate of decay proportional to $1/y^2$. Based on previous experimental observations of the wake dynamics in the flow past rings by Leweke & Provansal (1995), the $1/y^2$ variation applies for the wakes behind rings with large aspect ratios, which scale on the cross-section diameter d. The flow visualisations of Monson (1983) suggest that the wakes behind rings with small aspect ratios scale with the outer ring diameter, $D + d$, and hence considering the $1/r^3$ variation would be more appropriate for these wakes. The maximum aspect ratio at which the wake behind a ring scales with the outer ring diameter must be considered when applying the $1/r^3$ law, to ensure that the models constructed for rings with intermediate aspect ratio are not subject to greater blockage restrictions than for the meshes of smaller and larger aspect ratios.

Presently, the exact maximum aspect ratio at which the wake behind a ring scales

with the outer ring diameter as opposed to the local ring cross section is unknown. Some guidance regarding this aspect ratio limit may be determined from the literature, with studies by Roshko (1954), Monson (1983) and Bearman & Takamoto (1988) observing that rings exhibit vortex shedding similar to the wake of a circular cylinder for aspect ratios $Ar \gtrsim 4$ to 6. A value of l_t for the ring models constructed for the present study must satisfy the $1/r^3$ law for $Ar \leq 6$, giving

$$\frac{1}{r^3} \lesssim \frac{1}{y^2}. \tag{2.36}$$

As $y = l_t$ and $r = l_t/l_{axis}$, it follows that

$$\begin{aligned} \frac{1}{(l_t/l_{\text{axis}})^3} &\lesssim \frac{1}{{l_t}^2} \\ \therefore (l_t/l_{\text{axis}})^3 &\gtrsim {l_t}^2. \end{aligned} \tag{2.37}$$

and substituting $l_{axis} = 3$ for $Ar = 6$, the minimum transverse domain length is determined by rearranging

$$\begin{aligned} \frac{{l_t}^3}{3} &\gtrsim {l_t}^2 \\ \therefore \frac{l_t}{27} &\gtrsim 1 \\ \therefore l_t &\gtrsim 27. \end{aligned} \tag{2.38}$$

A transverse domain length of $l_t > 27$, non-dimensionalised by the cross-section diameter, d, must be employed to ensure that errors due to the transverse domain are less than those of the circular cylinder for all aspect ratios.

A second, and largely independent, blockage consideration is the blockage (area) ratio, $R_{blockage}$. This is a ratio of the frontal projected area of the body to the frontal projected area of the entire domain. Tomboulides & Orszag (2000) employed a grid with a blockage ratio $R_{blockage} = 1.2\%$ to compute the wake behind a sphere. For the ring meshes, equation 2.39 gives the relationship describing $R_{blockage}$.

$$R_{blockage} = \begin{cases} \frac{(l_{axis}+\frac{1}{2})^2}{(l_{axis}+l_t)^2} & \text{for } 0 \leq Ar < 1, \\ \frac{2l_{axis}}{(l_{axis}+l_t)^2} & \text{for } Ar \geq 1. \end{cases} \tag{2.39}$$

Equation 2.39 describes an increase in $R_{blockage}$ with an increase in l_{axis} (and hence with an increase in Ar). This is due to an increase in the projected area of the ring with an increase in aspect ratio more rapidly than an increase in the projected area of the domain. This increase continues until $Ar = 2l_t$, where $l_t = l_{axis}$, and the blockage ratio is equivalent to the blockage of a circular cylinder mesh with the same l_t. Hence

	DS_1	DS_2	DS_3	DS_4	DS_5	DS_6	DS_7	DS_8
M_{elem}	356	356	378	291	447	330	486	538
l_i	15	8	25	15	15	15	15	15
l_t	20	20	20	20	20	10	20	30
l_o	25	25	25	15	35	25	25	25

TABLE 2.2: Domain length parameters defining the meshes DS_1 to DS_8. M_{elem} is the number of elements, and l_i, l_t and l_o describe the inlet, transverse and outlet domain sizes, respectively.

a value of l_t that satisfies the blockage of a circular cylinder grid, and the $l_t > 27d$ requirement imposed by the $1/r^3$ law will be satisfactory for all ring aspect ratios.

The inlet boundary condition imposes a constant inlet velocity parallel to the axis at the free-stream velocity U_∞. The length l_i must be sufficiently large to minimise the difference between the upstream flow conditions and the uniform inlet velocity. Table 2.1 shows that inlet lengths are generally relatively small compared to the transverse and outlet domain lengths, with values varying between $4.5d$ and $15d$. Similarly, there is variation in the outlet domain length, with l_o varying between $12d$ and $25d$.

The domain length study presented here employs a large family of meshes to allow independent variation of the domain lengths in question: l_i, l_t and l_o. For validation purposes, the pressure and viscous components of drag are monitored, as are the Strouhal frequency of vortex shedding, and the velocity magnitude at a point approximately $4d$ directly downstream of the ring cross-section.

Each group of meshes utilised in the grid-resolution study are shown in figure 2.2. For a summary of the domain lengths chosen for the domain length study, see table 2.2.

Axisymmetric computations were performed on meshes DS_1 to DS_5, as they modelled a ring with $Ar = 5$. A two-dimensional formulation of the spectral-element code was employed for the straight circular cylinder meshes DS_6 to DS_8. Initially, $N^2 = 49$ nodes per element was employed for the computations, at a Reynolds number of $Re = 100$, which was sufficiently large to produce periodic flows for all the meshes employed in the study. The parameters which were determined from these computations are provided in table 2.3.

Based on both the results of this study, and the blockage-related restriction on the transverse domain size (i.e. $l_t > 27d$), the models used throughout the investigation will employ $l_i = 15d$, $l_t = 30d$ and $l_o = 25d$.

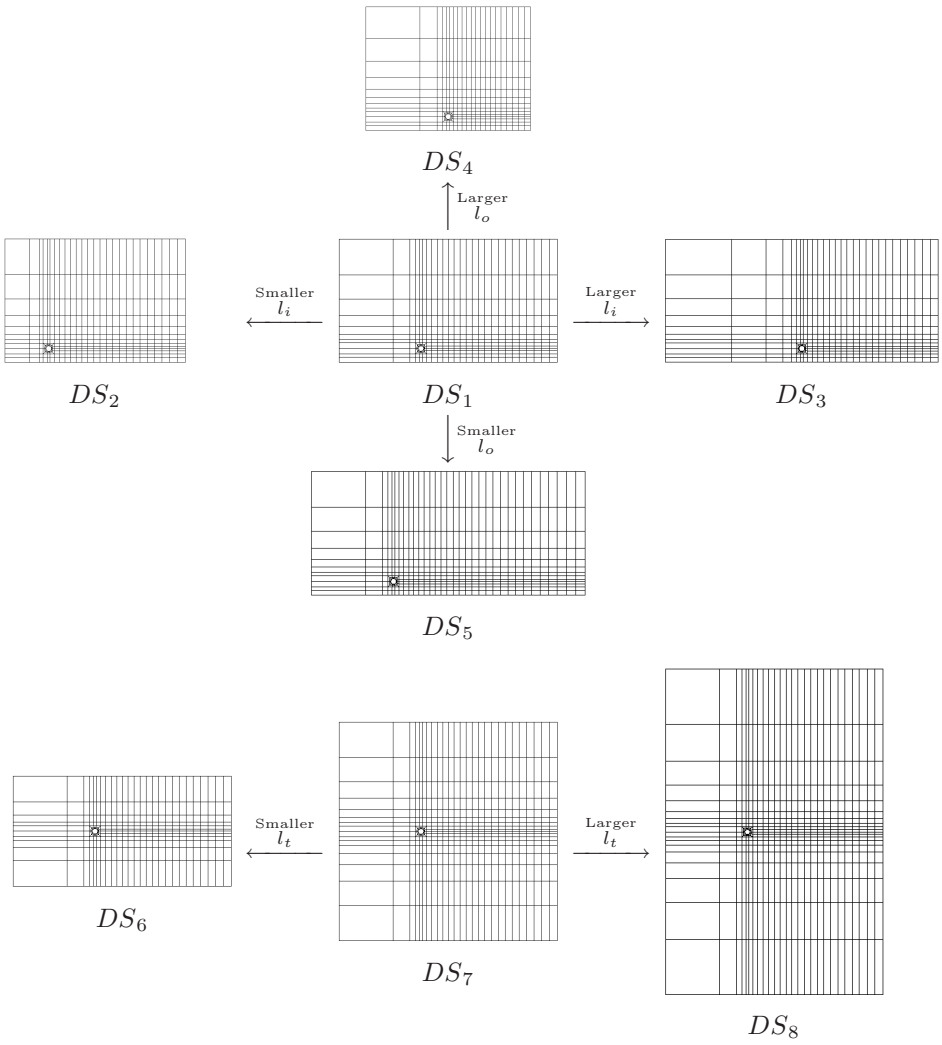

FIGURE 2.2: Groups of meshes used to test the effect of independently altering the parameters governing the domain lengths of the ring meshes. Note that meshes DS_1 to DS_5 define a ring with aspect ratio $Ar = 5$, for tests varying l_i and l_o. The meshes DS_6 to DS_8 define a straight circular cylinder to test the l_t length.

	l_i **variation**			l_o **variation**			l_t **variation**		
	DS_2	DS_1	DS_3	DS_4	DS_1	DS_5	DS_6	DS_7	DS_8
St	0.16433	0.15887	0.15769	0.15876	0.15887	0.15879	0.16905	0.16702	0.16671
C_{d_p}	0.9535	0.9035	0.8925	0.9028	0.9035	0.9035	1.0258	1.0096	1.0072
C_{d_ν}	0.3358	0.3226	0.3197	0.3224	0.3226	0.3226	0.3497	0.3455	0.3450
C_d	1.2893	1.2261	1.2122	1.2252	1.2261	1.2261	1.3755	1.3551	1.3522

TABLE 2.3: Convergence of global flow field parameters for the meshes used to determine suitable domain sizes for the meshes employed throughout this work.

N^2	4^2	5^2	6^2	7^2	8^2	9^2
St	0.15805	0.15847	0.15867	0.15867	0.15867	0.15867
C_d	1.2265	1.22111	1.22400	1.22419	1.22456	1.22465
C_{d_p}	0.9054	0.90049	0.90219	0.90200	0.90210	0.90209
C_{d_ν}	0.3212	0.32063	0.32181	0.32219	0.32246	0.32256

TABLE 2.4: Convergence of the flow field parameters at $Re = 100$.

2.2.1.2 Spatial Resolution Study

The spatial resolution study presented here varied the order of interpolation within each macro-element of a mesh based on the domain length parameters from the mesh domain size study of § 2.2.1.1. For consistency with the preceding domain size study, the mesh employed in the present study models a ring with aspect ratio $Ar = 5$.

Computations have been performed using the test mesh, with the number of nodes per element varying between $N^2 = 16$ and $N^2 = 81$. Computations with $N^2 = 100$ required a smaller time-step due to restrictions imposed by the Courant condition, and were therefore discarded. The macro-element distribution remains unchanged throughout the spatial resolution study. Two sets of computations are performed: one with $Re = 100$, and the other at $Re = 200$. It is clear from numerical stability analysis of the sphere wake (Natarajan & Acrivos 1993) and the circular cylinder wake (Barkley & Henderson 1996); as well as experimental studies of the wake behind the sphere (Magarvey & Bishop 1961b; Johnson & Patel 1999) and the circular cylinder (Williamson 1988a), that a transition to three-dimensionality occurs over the Reynolds number range $190 \lesssim Re \lesssim 210$. The experimental studies of the flow past a ring (Monson 1983; Leweke & Provansal 1995) suggest that the axisymmetric flow regime does not extend far beyond $Re \approx 200$. The spatial resolution study presented here covers a sufficient Reynolds number range to represent the axisymmetric flow regime for rings.

As with the domain size study, the global flow field parameters St, C_d, C_{d_p} and C_{d_ν} are recorded. Tables 2.4 and 2.5 show the convergence characteristics with an increase in polynomial order for the global flow field quantities.

The data shows a more rapid convergence of the flow field parameters for the computations at $Re = 100$ than at $Re = 200$, which is expected. An accuracy in the order of 0.1% is desired for the selected node resolution, which is achieved at $Re = 100$ with $N^2 \geq 7^2$. At $Re = 200$, a resolution of $N^2 = 8^2$ achieves a similar accuracy. For consistency, all axisymmetric computations employ a polynomial order $N^2 = 8^2$ in the

N^2	4^2	5^2	6^2	7^2	8^2	9^2
St	0.17951	0.18389	0.18485	0.18482	0.18492	0.18497
C_d	1.20487	1.22292	1.23404	1.23243	1.23442	1.23264
C_{d_p}	0.97018	0.98495	0.99497	0.99364	0.99516	0.99360
C_{d_ν}	0.23468	0.23797	0.23906	0.23880	0.23925	0.23904

TABLE 2.5: Convergence of the flow field parameters at $Re = 200$.

present study.

2.2.2 Details of Mesh Construction

The set of meshes constructed for this study maintained a remarkable similarity over the entire aspect ratio range. The domain parameters l_i, l_t and l_o were constant for all meshes, and the macro-element density was kept as consistent as possible. Some alteration in mesh density between the ring cross-section and the axis of symmetry was unavoidable, due to the variation in that particular domain length l_{axis} with aspect ratio. A uniform expansion in element size was adopted for the meshes in all directions away from the ring cross-section, to minimise computational expense. The ring cross-section was surrounded by a square ($2d \times 2d$) containing a mesh of between 12 and 14 elements around, and three elements deep. The innermost ring of elements are small enough in the radial direction (relative to the centre of the ring cross section) to capture the boundary layer around the cross section of the ring.

The thickness of the laminar boundary layer around the ring cross-section can be approximated from boundary layer theory (see White 1999, pages 428–429). It can be shown that at $Re = 200$, the idealised boundary layer thickness varies between $0d \leq \delta \leq 0.22d$ from the front to rear surface of the cross-section, with $\delta \approx 0.16d$ at the mid-point. The element polynomial order $N^2 = 8^2$ ensured that approximately 8 interpolation points were included within the boundary layer, even for the thinnest boundary layers considered.

The inlet, transverse and outlet domain regions consist of 3, 7 and 20 elements, respectively, between the square mesh surrounding the cross-section of the ring, and their respective boundaries Γ_i, Γ_t and Γ_o.

Special attention has to be given to the meshes created to model rings in the range of aspect ratios $0 \leq Ar < 2$, as no outer mesh is present between the square mesh surrounding the ring cross-section, and the axis of symmetry boundary Γ_{axis}. Several

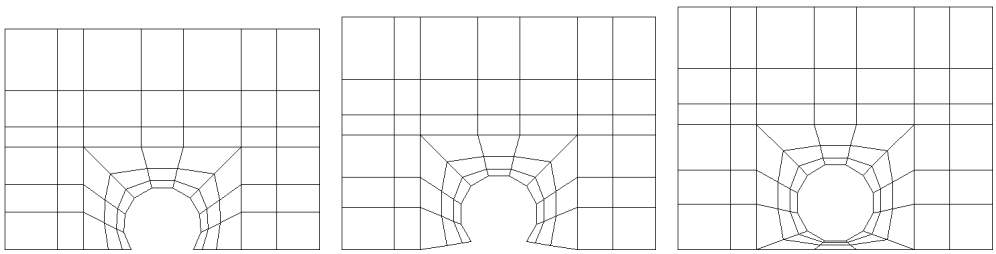

(a) $Ar = 0.6$ (b) $Ar = 0.9$ (c) $Ar = 1.2$

FIGURE 2.3: The various modifications of the standard mesh to accommodate rings with aspect ratios in the range $0 \leq Ar < 2$. Note that the macro elements around the in the vicinity of the ring cross-section boundary Γ_{ring} are displayed here without any curvature. Curvature was included in the computations, though, to accurately model the circular geometry.

different refinements to the meshes were employed to overcome the problems imposed by this situation. Figure 2.3 presents the mesh structure surrounding the cross-section of the ring for several aspect ratios; each requiring a different modification to model the aspect ratio.

For rings with aspect ratios $0 \leq Ar \lesssim 0.71$ (see figure 2.3(a)), the mesh structure is similar to meshes created to model a sphere (Natarajan & Acrivos 1993; Thompson *et al.* 2001a). As the aspect ratio increases over the range $0 \leq Ar \leq 1$, near to the axis, the ring develops sharp dimples upstream and downstream, as in cross section the ring shifts from a single circle to a pair of circles.

To maintain numerical stability over the aspect ratio range $0.71 \lesssim Ar \leq 1$, the numerical models required a modification that fundamentally altered the geometry. Due to this mesh alteration, only limited results were obtained over this aspect ratio range in the present work, and are considered qualitatively only.

For aspect ratios $0.71 \lesssim Ar \leq 1$ mesh elements near to the axis in the vicinity of the ring become too skewed to accurately model the flow. The modification displayed in figure 2.3(b) shows how this problem was overcome for meshes over this aspect ratio range. The zero normal velocity boundary at the axis of symmetry was diverted locally from the axis both upstream and downstream of the ring. This created computational conical stress-free surfaces tapering upstream and downstream of the body. It is clear that this mesh modification fundamentally alters the geometry being modelled, which will influence the surrounding flow field. The greatest geometric alteration was made

Mesh variable	Uncertainty ΔE_i	
	$Re = 100$	$Re = 200$
l_i	1.232%	
l_t	0.0504%	
l_o	0.238%	
N^2	0.115%	0.157%
Overall uncertainty	**1.64%**	**1.68%**

TABLE 2.6: Uncertainty estimates for axisymmetric computations using the proposed ring meshes at Reynolds numbers $Re = 100$ and $Re = 200$, employing an element polynomial order of $N^2 = 49$ and $N^2 = 64$, respectively.

for $Ar = 1$, with the diameter of the artificial conical surfaces reaching $0.59d$ at the point of intersection with the ring cross-section. To preserve the integrity of this study, results from rings with $0.71 \lesssim Ar \leq 1$ will only be referred to qualitatively throughout this work.

The meshes describing rings with aspect ratios $1 < Ar < 2$ require a minor modification. The distance between the inner surface of the ring cross-section and the axis is less than $d/2$. The elements in the quadrant between the ring surface and the axis are compressed in the transverse direction to accommodate this reduction.

2.2.3 Accuracy of the Ring Models

An estimation of the overall accuracy of the models employed in the present work is formulated in this section. Knowledge of the accuracy of the numerical modelling is paramount to the formation of solid conclusions from the study.

In keeping with standard scientific practices, an overall error (ΔE_{tot}) is evaluated as a summation of the $N_{\Delta E}$ relative uncertainties (ΔE_i) corresponding to each aspect of the study,

$$\Delta E_{tot} \cong \sum_{i=1}^{N_{\Delta E}} \Delta E_i. \tag{2.40}$$

Equation 2.40 was applied to determine estimates of the overall uncertainty for axisymmetric computations at both $Re = 100$ and $Re = 200$. These uncertainties are presented in table 2.6. An increase in the overall uncertainty is expected with an increase in Reynolds number, due to the convergence properties of the spectral-element method employed here (Patera 1984; Karniadakis 1990). Thus, through inference and extrapolation, an understanding of the uncertainty behaviour over the Reynolds number range $0 < Re \lesssim 200$ may be established.

The variation in the length of the inlet contributes the vast majority of the overall uncertainty of the computations at Reynolds numbers of both $Re = 100$ and $Re = 200$. The overall uncertainty is of the order $O(1\%)$, varying between approximately 1.6% and 1.7% over the Reynolds number range pertinent to the present study. Due to the consistent domain lengths employed between aspect ratios in the present study, an uncertainty of order $O(0.1\%)$ is expected when comparing results between rings, due only to the uncertainty in the spatial resolution.

2.3 The Landau Model and Non-Axisymmetric Transition Behaviour

The Landau model provides a means for studying the non-linear behaviour near the transition Reynolds number. It has been used widely in describing and classifying bluff body wake transitions previously: for example, the Hopf bifurcation of a circular cylinder wake (Provansal *et al.* 1987; Dušek *et al.* 1994; Zielinska & Wesfreid 1995); the three-dimensional Mode A and B transitions in the wake of a circular cylinder (Henderson 1997); and the non-axisymmetric transitions in the wake of a sphere (Provansal & Ormières 1998; Ghidersa & Dušek 2000; Thompson *et al.* 2001a).

Landau & Lifshitz (1976) proposed the Landau equation as a model to describe the growth and saturation of a perturbation post-transition. The governing equation is written

$$\frac{\mathrm{d}A}{\mathrm{d}t} = (\sigma + \mathrm{i}\omega)A - l(1 + \mathrm{i}c)|A|^2 A + \ldots, \tag{2.41}$$

where $A(t)$ is a complex variable representing the mode amplitude. A description of this equation, and its application to stability analysis, is provided in Provansal *et al.* (1987). Here, the characteristics of the model and the method of its application to the present study is discussed.

The complex variable $A(t)$ represents the amplitude of the perturbation mode from the base flow. The right-hand side of the equation gives the first two non-zero terms of a series expansion. Provided that l is positive, these first two terms should provide a good description of the non-linear behaviour in the neighbourhood of the transition, since the saturated amplitude should still be small. This is not true if l is negative; in that case, the cubic term accelerates the growth of the perturbation and quintic or even higher-order terms are required to describe saturation of the mode. Thus, the sign of l plays an important role in classifying the transition. Positive l means the transition is

supercritical (non-hysteretic), while negative l means it is subcritical (hysteretic). The parameter σ is the linear growth rate of the perturbation, and thus at the transition point, its value changes from negative to positive. Also, ω is the angular oscillation frequency during the linear growth phase, which is non-zero for a Hopf bifurcation. The parameter c is known as the Landau constant. It is a global quantity (unlike l) and hence does not vary with position in the flow. It modifies the oscillation frequency at saturation, and in addition, its size and magnitude determine global behaviour in related flow systems such as wake behaviour under external oscillatory forcing (Le Gal *et al.* 2001).

The usual way to manipulate the Landau equation (i.e. Dušek *et al.* 1994) is to write the complex amplitude variable as

$$A \equiv \rho \mathrm{e}^{\mathrm{i}\Phi}, \tag{2.42}$$

where $\rho = |A|$ is a real variable describing the mode amplitude, and Φ is a real variable providing the phase of the mode. The Landau equation can then be split into real and imaginary parts, giving

$$\frac{\mathrm{d}\log(\rho)}{\mathrm{d}t} = (\sigma - l\rho^2 + \ldots), \tag{2.43}$$

$$\frac{\mathrm{d}\Phi}{\mathrm{d}t} = (\omega - lc\rho^2 + \ldots). \tag{2.44}$$

Using equation 2.43 and noting that at saturation the (real) amplitude will not change in time, gives ${\rho_{sat}}^2 = \sigma/l$. In addition, since σ is necessarily proportional to the Reynolds number increment above critical in the neighbourhood of a simple transition, the energy in the mode (proportional to ρ^2) varies as $Re - Re_c$, where Re_c is the critical Reynolds number. This behaviour was verified numerically (e.g. Dušek *et al.* 1994) and experimentally (e.g. Ormières & Provansal 1999) for different supercritical wake transitions. The equation for the phase (equation 2.44) also provides useful information. If the flow reaches a periodic state at saturation, $\mathrm{d}\Phi/\mathrm{d}t$ becomes the constant angular frequency of oscillation (ω_{sat}). It takes the value $\omega_{sat} = \omega - lc{\rho_{sat}}^2 = (\omega + \sigma c)$. Hence, σc determines the shift from the oscillation frequency in the linear regime, as the flow saturates.

Provansal *et al.* (1987) showed that the viscous diffusion timescale (d^2/ν) is proportional to $(Re - Re_c)/\sigma$. Grouping these terms allows the constant of proportionality,

known as the Landau diffusivity constant, to be expressed

$$\eta_{diff} = \frac{(Re - Re_c)}{\sigma} \times \frac{\nu}{d^2}. \tag{2.45}$$

This constant was evaluated from experimental measurements for the Hopf transition of a circular cylinder wake by Provansal *et al.* (1987). They found a value of approximately $\eta_{diff} = 5$. Using the data presented in Thompson *et al.* (2001a), the Landau diffusivity constant may be computed for the Hopf transition of a sphere wake. At $Re = 280$ ($Re - Re_c \approx 7.8$), they predicted the Hopf transition to grow with $\sigma \approx 0.015$, and yielding $\eta_{diff} \approx 1.86$.

For regular (i.e. steady–steady) transitions, only the real component of the amplitude A need be considered, and hence equation 2.43 is applied. For transitions involving time-dependent flows, the phase of the amplitude is considered by applying equation 2.44.

Given equation 2.43, it is possible to determine the real parameters in the model from numerical computations by plotting $\mathrm{d}\log|A|/\mathrm{d}t$ against $|A|^2$. The y–intercept gives the linear growth rate σ and the gradient for small amplitudes near to the y–axis yields $-l$. For the truncated *cubic* Landau model to describe the transition well, equation 2.43 indicates the plot should be linear. Plotted this way, the time trajectory of the transition should start at the y–axis, and finish on the x–axis if the flow reaches a periodic or steady asymptotic state. If the slope of the curve is positive at the y–axis, the transition is subcritical and at least quintic terms are required in the Landau equation to describe the saturation process with any accuracy. The linear dependence of $\mathrm{d}\log|A|/\mathrm{d}t$ with $|A|^2$ for supercritical transitions was explained in a recent publication by Noack *et al.* (2003), in the context of low-dimensional Galerkin models for the viscous incompressible flow past a circular cylinder.

In the vicinity of the transition, it is possible to determine the Landau constant by measuring the oscillation frequency of the perturbation in the linear regime and at saturation, and by rearranging equation 2.44 to give

$$c = \frac{\omega_{sat} - \omega}{\sigma}. \tag{2.46}$$

From a numerical point of view, the derivative ($\mathrm{d}\log|A|/\mathrm{d}t$) can be accurately estimated using finite-differences. For transitions to a time-dependent final state, the signal at small times is initially sinusoidal multiplied by an exponential growth factor. At larger times, as the flow saturates, the amplitude envelope asymptotes to a

constant width and the sinusoidal oscillation frequency adjusts slightly according to equation 2.44. Thus, in the more complicated case of transition to a time-dependent final state, the derivative can be estimated by finite-differences by using the heights of the approximately sinusoidal peaks and troughs during the growth and saturation of the instability.

To proceed further, the amplitude variable A needs to be specified. Previous studies have taken different approaches. For example, Dušek *et al.* (1994), and Thompson *et al.* (2001a) used the transverse velocity component at a fixed point on the centreline of the circular cylinder wake. Zielinska & Wesfreid (1995) instead used the maximum transverse velocity component on the centerline. The position at which this occurs varies with Reynolds number. Henderson (1997) used the L_2 norm of spanwise velocity component for examining two-dimensional to three-dimensional transitions for the wake of a circular cylinder. However, because the numerical domain was necessarily truncated downstream before the mode amplitude decayed to zero, this also was not a unique global measure. For the analysis presented in chapter 5, the L_2 norm method, as described in Henderson (1997) and Thompson *et al.* (2001a), is employed. As the transitions studied in chapter 5 are non-axisymmetric transitions, an L_2 norm is computed based on an integration of the azimuthal velocity component of the wake, as follows:

$$|A| \equiv \left[\Psi_{cylinder} \int_V w^2 \mathrm{d}V \right]^{1/2}, \tag{2.47}$$

where $|A|$ is the amplitude of the mode in question, $\Psi_{cylinder}$ is a normalising coefficient set to unity for simplicity, V is the volume of the computational domain, and w is the azimuthal component of the velocity field.

2.4 Experimental Validation of the Flow past Rings

Despite comprising a small portion of this study, it is pertinent to divulge the experimental technique used in the present study for validation of selected numerical results.

Two techniques for experimental flow visualisation have been employed in previous studies for the wakes behind rings. Monson (1983) observed rings falling through a tank of water. The rings were coated with a dye that entrained into the wake, highlighting the flow structures present. This method has the advantage of not imparting any spurious perturbation on the wake due to the presence of tethers attached to the ring. A major drawback with the technique of Monson (1983) is the inability to maintain

a perpendicular orientation of the ring to the vertical direction of motion. This effect is especially noticeable for asymmetric wake visualisation, where the non-uniform distribution of drag around the ring incites an oscillatory wobble in the axial orientation of the ring. Leweke & Provansal (1995) overcame this difficulty by fixing their rings within a wind tunnel with an arrangement of fine tethers. The mounting of four tethers to the ring did not provide a noticeable effect on the wake, due to the large difference in scale between the tether diameter, and their placement around the circumference of the ring. The radial direction that these wire anchors were placed appeared to add no observable alteration of the wake structures in the flow visualisation images presented by Leweke & Provansal (1995).

The experimental method employed in the present study differed somewhat from those of these previous studies. Due to the desire to monitor the wakes behind rings with aspect ratios in the range $4 < Ar < 7$, a technique was developed whereby a buoyant ring coated in Fluorescein dye is dragged vertically downward into a tank. The tension of the tow line was maintained by the buoyancy of the ring, which had a density approximately half that of the water. The horizontal inclination of the ring was maintained by the attachment of three equi-spaced tethers positioned at the centre of the upstream surface of the ring. The three tethers were affixed to a tow line approximately $10d$ to $15d$ upstream of the ring. The tow line traversed a near-frictionless pulley system at the base of the tank, and returned to the surface near to a side wall of the tank, where it was wound onto a spool machined to a uniform diameter. The spool was driven at a constant velocity by a computer-controlled stepper motor which employed 40000 steps per revolution. The ring velocity was kept constant to a high degree of accuracy, which maintained a constant Reynolds number for the system. Regular temperature measurements ensured that an accurate estimation of the kinematic viscosity of the fluid was made for precise Reynolds number measurements. The ring was carefully machined from wood, and was sanded smooth with a fine-grit sandpaper. Surface roughness effects were not considered significant due to the low Reynolds number of the experiments. No surface treatment was performed in addition to sanding, as the ring was painted with dye prior to immersion in the water tank.

The experimental rig consisted of a vertical tank 550mm high, and 500mm square at the base. A schematic representation of the experimental apparatus setup is shown in figure 2.4. It should be noted that the distance over which the ring was towed during the

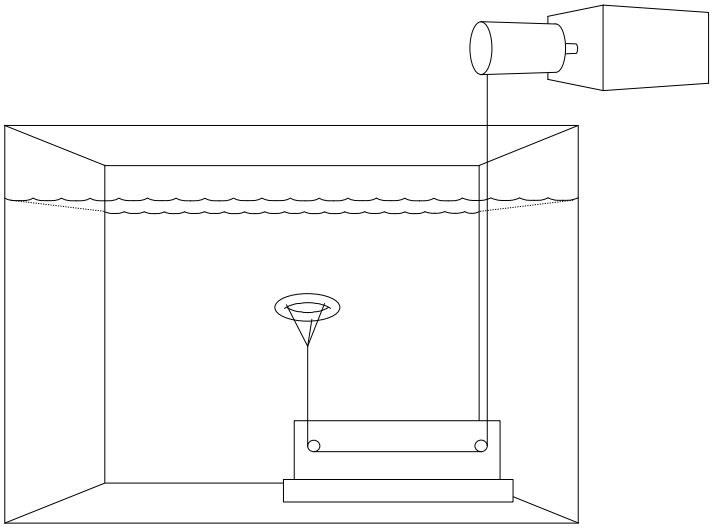

FIGURE 2.4: A schematic representation of the experimental apparatus employed to obtain wake flow visualisation images to validate the numerical predictions presented throughout this work.

experiments was approximately 450mm, or $56d$. For qualitative purposes, the annular vortex street was generally observed to saturate over between 200mm–250mm from the startup condition. Therefore, over at least the final $25d$ of the experimental run, the vortex street was qualitatively free of transients.

Flow visualisation was performed by illuminating the dye with a laser light source (wavelength 540nm). Images were captured with a Canon EOS 300 35mm SLR camera fitted with a 22–55mm $f/4.0$–$f/5.6$ USM zoom lens. 400 ASA colour film stock was employed, and the photographs were digitised with a Nikon Coolscan II 2700dpi film scanner.

The computer-controlled motion of the ring was initiated from a static position approximately 1cm below the surface of the tank, and buoyancy forces maintained a vertical alignment of the ring. Initially, a fast acceleration was applied to the ring, which resulted in the evolution of a uniform axisymmetric vortex street in the wake of the ring. This condition was fundamental to the evolution of linear asymmetric instability modes of the wake.

The mean inner and outer diameters of the ring used in the experiments were measured by digital calipers, with 31.88mm and 48.07mm being measured, respectively. These measurements provide the mean ring diameter $D = 39.98$mm and the mean

cross-section diameter $d = 8.095$mm. As an independent verification of these measurements, the cross section was also measured to be $d = 8.10\text{mm} \pm 0.03\text{mm}$. From these measurements, the aspect ratio of the ring employed in the experiments was determined to be $Ar = 4.94$ (actually closer to $Ar = 4.9382$).

The circumference along the ring centreline non-dimensionalised with respect to the ring cross-section (d) is $\pi D = 15.51d$. Numerical studies predict that the wake behind a ring with $Ar = 5$ will become unstable to a linear Mode C instability at $Re = 161$, followed by a Mode A instability at $Re = 194$. The respective azimuthal mode numbers of these instability modes are $m = 9$ and $m = 4$, respectively, corresponding to azimuthal wavelengths (non-dimensionalised with d) of $\lambda_d = 1.75d$ and $\lambda_d = 3.93d$.

The measured mean ring cross-section diameter was $d = 8.10 \times 10^{-3}$ m, and the assumed kinematic viscosity was $\nu = 1.01 \times 10^{-6}\text{m}^2\text{s}^{-1}$ based on a water temperature of 23.5°C. Therefore, the velocity (U) range that the ring was required to be towed at to achieve the Reynolds number range (above the critical Reynolds number for Mode C and below Mode A) was $2.01\ \text{cm}^1\text{s}^{-1} < U < 2.42\ \text{cm}^1\text{s}^{-1}$. Clearly, these velocities were extremely low, and left the experiment susceptible to slightly non-uniform conditions, such as convection within the tank, imperfections on the body of the ring, and the wake disruption imposed by the towing line upstream of the ring. These problems were overcome through careful machining of the geometry, the use of extremely fine thread to attach the ring to the tow line, and by allowing sufficient time before a run for the ring to reach a vertical equilibrium point in the tank, and the fluid to become motionless to the limit of observation.

2.5 Chapter Summary

In this chapter, the spectral-element method has been introduced. This computational technique is the sole method employed to solve the fluid flows associated with the flow past the rings studied in the present work.

The logical extensions of the axisymmetric (or two-dimensional) formulation of the spectral-element method to both a linear Floquet-type stability analysis technique, and a non-axisymmetric (or three-dimensional) method have been discussed.

Numerical meshes have been developed that model a wide range of ring aspect ratios, and a detailed grid-resolution study has been presented. The difficulty of modelling the sharp dimples located on the axis of the ring both upstream and downstream, as the

aspect ratio increases to $Ar \to 1$, and difficulty of modelling the constriction through the small hole at the axis when the aspect ratio is just greater than unity have been discussed.

The Landau model has been introduced, and the useful features of the model have been explored. The method by which the model will be applied in the current work was presented.

Finally, the experimental apparatus and methodology employed to validate the numerical fluid flow predictions for an intermediate aspect ratio of approximately $Ar \approx 5$ was discussed.

In the next chapter, axisymmetric wakes are computed for a range of aspect ratios. The axisymmetric separation and Hopf transitions are studied, and characteristics of the unsteady wakes produced following the Hopf transition are investigated. These include the Strouhal–Reynolds number variation, the wake structure, and the drag characteristics.

Chapter 3

Axisymmetric Flow past Rings

The axisymmetric flow past a sphere, and the two-dimensional flow past a circular cylinder have been investigated previously (Taneda 1956a,b), and are well understood. For the axisymmetric flow past rings, only the unsteady axisymmetric flow has been investigated (Leweke & Provansal 1994, 1995). The steady axisymmetric flow past rings at low Reynolds numbers is not yet well understood. In order to perform the linear stability analysis and non-axisymmetric computational studies presented in later chapters, the axisymmetric flow regimes for the flow past rings must be characterised and investigated.

This chapter presents an axisymmetric computational study of the flow past rings. In the next section, the results of computations are presented which identify low-Reynolds-number flow regimes characterised by attached flow, separated flow, and unsteady flow. The transition Reynolds numbers for flow separation and unsteady flow are determined for a wide range of rings. In the following section, the Strouhal–Reynolds number profiles for unsteady wakes behind rings are analysed, and a relationship is proposed for the Strouhal frequency of the axisymmetric wakes behind rings. A third section explores the drag properties of the flow past rings, drawing comparisons with the drag properties of the flow past both a sphere and a circular cylinder. Finally, a qualitative comparison between experimental and numerical flow visualisations is presented.

Some of the results in this chapter have previously been published in Sheard *et al.* (2003c).

3.1 Axisymmetric Transitions and Flow Regimes

A study of the flow past a sphere (Taneda 1956a) and a study of the flow past a circular cylinder (Taneda 1956b) both verify that at sufficiently small Reynolds numbers the flow remains steady and attached to these bodies. In cross-section, the attached flow past a sphere and a circular cylinder consists of a single upstream and a single downstream stagnation point. At some transition Reynolds number, the flow separates from the body due to an adverse (or increased) pressure gradient in the direction of flow, which creates a pair of separation points in the vicinity of the rear of the body beyond the separation transition. A steady recirculation bubble is located in the wake between the separation points, and its length increases with an increase in Reynolds number. At some higher Reynolds number, the steady recirculation bubble becomes unstable to two- or three-dimensional disturbances, depending on the geometry.

The characteristics and transition Reynolds numbers of these regimes in the flow past rings is currently unknown. To characterise these regimes, axisymmetric computations were employed to determine the transition Reynolds numbers for both flow separation and unsteady flow in the wakes behind rings, and to establish features of the structure of the wakes.

3.1.1 The Transition to Separated Flow

Two methods can be employed to determine the transition Reynolds number for separated flow: the wake length method and the separation angle method. The wake length method was employed in several experimental studies (including Taneda 1956b,a; Coutanceau & Bouard 1977a), and involves the extrapolation to zero of the measured variation in recirculation bubble length with Reynolds number. The separation angle method was employed by computational studies (Rimon & Cheng 1969; Tomboulides *et al.* 1993), and involves the extrapolation to zero of the computed variation in separation angle with Reynolds number. The separation angle is defined as the angle between lines through the separation points and the centre of the sphere or cylinder.

The wake length method is suitable for symmetrical flows, such as the flow past a sphere or a circular cylinder. However, for open rings ($Ar > 1$), the flow field around the ring cross-section is asymmetrical, and measurement of the wake length is difficult. The separation angle method was therefore applied in the present work.

Using the separation angle method, the transition Reynolds number for separated

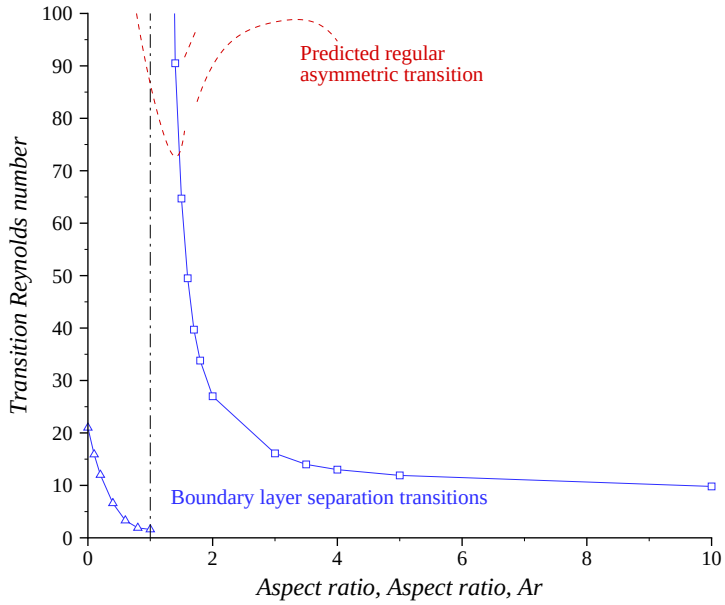

FIGURE 3.1: Reynolds numbers for the flow separation transition (Re_{T1}) versus aspect ratio for rings shown by blue lines. The dashed line indicates the emergence of the hole in the centre of the ring at $Ar = 1$, and the upper limit of the applicability of axisymmetric computations is indicated by the dotted red lines, which represent the predicted transition to non-axisymmetric flow discussed later.

flow was determined for the flow past rings of a wide range of aspect ratios, and for the flow past a sphere and a circular cylinder. For the flow past a sphere, the separation transition was found to occur at $Re_{S1} = 21$, and for the flow past a circular cylinder, the separation transition was found to occur at $Re_{C1} = 6$. These Reynolds numbers are within ± 0.5 Reynolds numbers of the accepted values from previous studies. For the flow past rings, a plot of the variation in separation transition Reynolds number (Re_{T1}) with aspect ratio is presented in figure 3.1.

Two distinct flow regimes can be identified from figure 3.1. For $0 \leq Ar \leq 1$, the transition Reynolds number for flow separation decreases from $Re_{T1} = 21$ at $Ar = 0$ to $Re_{T1} \approx 0$ at $Ar = 1$. For $Ar > 1$, the transition Reynolds number for flow separation decreases from a very large value over aspect ratios $1 < Ar \lesssim 3$, and approaches $Re_{T1} \approx 6$ as $Ar \to \infty$.

The flow separations that occur over these two regimes are distinct. For $0 \leq Ar \leq 1$, the separation transition forms a recirculation bubble located on the axis behind the

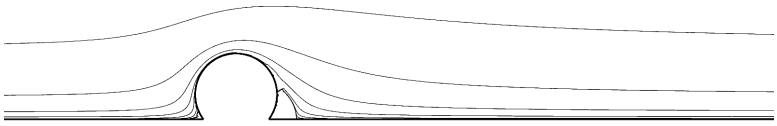

FIGURE 3.2: Flow streamlines around a ring of aspect ratio $Ar = 0.6$ at $Re = 10$, following the separation transition, illustrating the recirculating region behind the ring on the axis. Unevenly spaced streamline contour levels are used to elucidate relevant flow structures.

closed rings, as shown in figure 3.2. For $Ar > 1$, the separation transition forms an annular recirculation bubble located behind the cross-section of the open rings, as shown in figure 3.3. A steady flow was computed at all aspect ratios at the separation transition.

The variation in the separation transition Reynolds number with aspect ratio is best explained in terms of the structure of the computed wakes. For $0 \leq Ar \leq 1$, the transition Reynolds number for flow separation decreases with an increase in aspect ratio. For attached flow to be maintained at Reynolds numbers below Re_{T1}, the fluid that travels down the axis must divert from the axis upstream of the ring, remain attached around the body, and continue along the axis downstream. With an increase in aspect ratio from $Ar = 0$, the adverse pressure gradient towards the leeward side of the ring becomes more pronounced as $Ar \to 1$. At $Ar = 0$, the fluid must turn 90° from the rear of the ring to align with the axis. As $Ar \to 1$, the fluid must turn by more obtuse angles approaching 180°. Hence lower Reynolds numbers are required to maintain attached flow as the aspect ratio increases from $Ar = 0$ to $Ar \to 1$, and therefore the transition Reynolds number decreases over this aspect ratio range from $Re_{T1} \approx 21$ to $Re_{T1} \to 0$.

At $Ar = 1$, the separated flow condition is almost paradoxical. The conjecture that $Re_{T1} \to 0$ as $Ar \to 1$ implies that at $Ar = 1$, the separation transition occurs at $Re_{T1} = 0$. The Stokes flow condition at $Re = 0$ does not allow flow separation; however, separated flow exists for $Re > Re_{T1}$, and as $Re_{T1} \to 0$ as $Ar \to 1$, separated flow exists at $Ar = 1$ for all Reynolds numbers $Re > 0$. A close inspection of the transition Reynolds numbers in the vicinity of $Ar = 1$ in figure 3.1 shows that at $Ar = 1$, $Re_{T1} \approx 1$. In chapter 2 is was described that for the numerical meshes employed to model rings with $Ar = 0.8$ and 1, the extreme geometric constrictions at

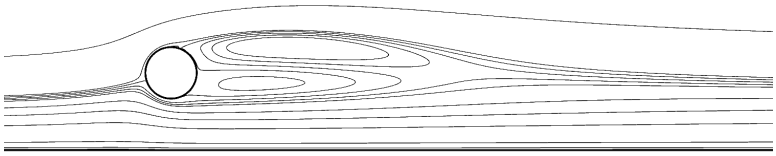

FIGURE 3.3: Flow streamlines around a ring with aspect ratio $Ar = 3$ at $Re = 100$, following the separation transition, illustrating the recirculating region behind the ring cross-section. Arbitrary contour levels are used to highlight the flow structures.

the axis were removed by adding artificial tapered slip-walls which diverted the flow away from the axis in the vicinity of the ring for computational stability. This mesh alteration slightly inflated the computed values of Re_{T1} in the vicinity of $Ar = 1$. If the Re_{T1} values at $Ar = 0.8$ and 1 are disregarded, an extrapolation of Re_{T1} from $Ar = 0$ to $Ar = 1$ yields $Re_{T1} \approx 0$.

For $Ar > 1$, the transition Reynolds number for flow separation increases as the aspect ratio decreases towards $Ar \to 1$. With a decrease in aspect ratio, the flow around the circular cross-section increases in asymmetry between the flow around the outer side of the ring, and the flow around the inner side of the ring. This asymmetry is imposed by the proximity of the axis at smaller aspect ratios. The rapid increase in the transition Reynolds number for $Ar \lesssim 3$ as $Ar \to 1$ is caused by a reduction in velocity of the fluid which passes through the hole of the ring. The velocity reduction causes a reduction in the local Reynolds number of flow, which amplifies the effective Reynolds number required to cause flow separation.

3.1.2 A Detached Axial Recirculation Bubble

For $1 < Ar \lesssim 3$, the attached flow at Reynolds numbers below the transition Reynolds number for flow separation exhibit an interesting structure. A detached axial recirculation bubble is located directly behind the ring, which corresponds to the attached axial recirculation bubble observed for $Ar \leq 1$. Examples of the detached recirculation bubble are provided in figure 3.4. The figure shows that the recirculation bubble increases in length with an increase in Reynolds number, which is consistent with the axial recirculation bubble computed in the wakes behind rings with $0 \leq Ar \leq 1$.

The detached recirculation bubble is located downstream of a stagnation point on the axis behind the open ring. The stagnation of flow is caused by an adverse pressure

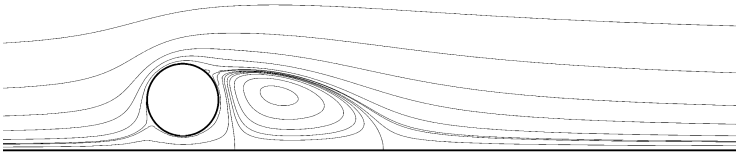

(a) $Re = 25$.

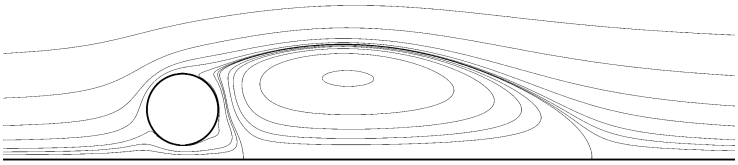

(b) $Re = 100$.

FIGURE 3.4: Flow streamlines around a ring with aspect ratio $Ar = 1.4$. In (a) the axial recirculation bubble located downstream of the ring is observed. In (b), this bubble is significantly larger, and a divergence of streamlines from the lower right surface of the ring cross-section may be observed, corresponding to boundary layer separation. Again, the contour levels of the streamline plots are arbitrary.

gradient along the axis, as the downstream side of the hole in the ring acts as a local expansion. The effect of the expansion is greatest at $Ar \approx 1$, and is negligible for $Ar \gtrsim 3$, where flow stagnation is no longer observed on the axis. This explains the absence of a detached recirculation bubble in the wake of the ring with $Ar = 3$ in figure 3.3.

Figure 3.4(a) shows a detached recirculation bubble downstream of a ring with $Ar = 1.4$ at $Re = 25$. The flow around the ring cross-section shows an upstream stagnation point on the inner upstream surface of the ring, and a downstream stagnation point on the outer downstream surface of the ring. Boundary layer separation had not occurred at this Reynolds number. The small closed streamline in the vicinity of the downstream stagnation point is an artefact of the streamline integration.

The flow around the ring cross-section in figure 3.4(b) differs from the flow in figure 3.4(a). On the inner downstream surface of the ring, a local divergence of the flow streamlines is observed. This divergence is due to the boundary layer separation that was computed to occur at $Re_{T1} = 91$ for a ring with $Ar = 1.4$.

The streamline plots in figure 3.4 show that with an increase in Reynolds number, a larger proportion of fluid passes through the hole of the ring due to viscous effects.

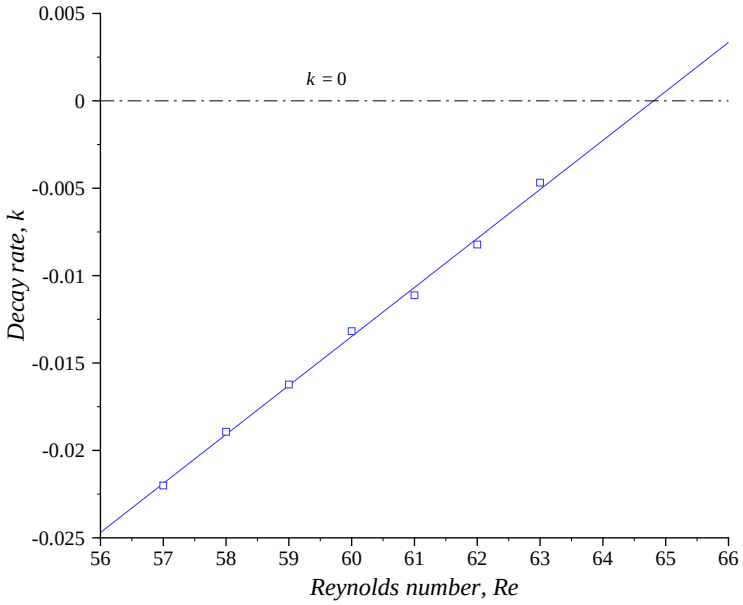

FIGURE 3.5: Unsteady transient decay rates for the flow past a ring with $Ar = 5$. Computed decay rates are shown as squares, and the solid line represents a linear fit to the data. The dashed line represents the neutral stability limit where the decay rate $k = 0$.

In figure 3.4(a), the upstream streamlines indicate that a column of fluid at the axis approximately $0.1d$ in diameter passes through the hole in the ring. In figure 3.4(b), the upstream streamlines indicate that a column of fluid at the axis approximately $0.4d$ in diameter passes through the hole in the ring. In other words, a Reynolds number of $Re = 100$ is required to provide a local velocity through the hole in the ring of approximately unity. At aspect ratios $Ar \gtrsim 3$, this can be achieved at far lower Reynolds numbers, which explains the rapid increase in Re_{T1} as the aspect ratio decreases towards $Ar \to 1$.

It is proposed from the observation of axial recirculation bubbles in the wakes of closed and open rings with $0 \leq Ar \lesssim 3$, and the observation of an annular recirculation ring in the wake of open rings with $Ar \gtrsim 3$, that the transition from closed to open rings at $Ar = 1$ does not discontinuously alter the wake dynamics. In relation to the scaling of the wakes, for $0 \leq Ar \lesssim 3$ the wake is observed to scale with the diameter of the ring $D + d$, whereas for $Ar \gtrsim 3$ the wake is observed to scale with the cross-section diameter d.

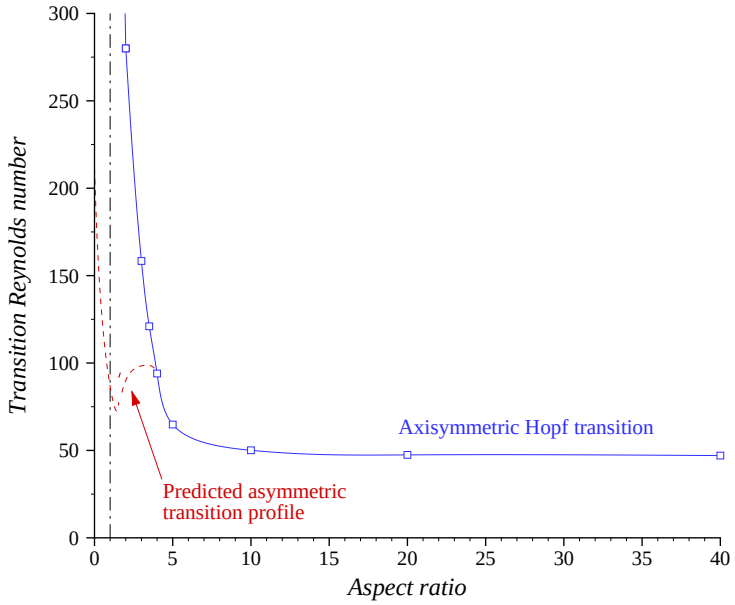

FIGURE 3.6: Reynolds numbers for the Hopf transition versus aspect ratio for rings obtained from axisymmetric computations (blue line). The dashed line indicates $Ar = 1$, where the hole first appears in the ring at the axis, and the predicted non-axisymmetric transition profiles are included as dotted red lines.

3.1.3 The Transition to Unsteady Flow

The critical Reynolds numbers for the transition from steady to periodic flow were found for a range of aspect ratios with $Ar > 1$. To determine the critical Reynolds number, the decay rates of unsteady velocity transients in the wake were measured at Reynolds numbers below the transition Reynolds number. Extrapolation of the decay rate variation with Reynolds number to zero yielded the neutral stability limit for unsteady transients in the wake, which corresponded to the critical Reynolds number for the transition to unsteady flow, Re_{T2}. An example of the linear trend in measured decay rates in the vicinity of the unsteady flow transition is presented in figure 3.5, for the wake behind a ring with $Ar = 5$.

In figure 3.6, a plot of the variation in Re_{T2} with aspect ratio is presented. Unsteady flow was not able to be computed for rings with $Ar \lesssim 1$ over the Reynolds number range $0 < Re \lesssim 400$. This was expected, as studies of the flow past spheres and discs (Natarajan & Acrivos 1993; Johnson & Patel 1999; Tomboulides & Orszag 2000) show that the steady axisymmetric wakes become unstable to non-axisymmetric flow at lower

Reynolds numbers than a for a transition to unsteady flow. In chapter 4, results of a linear stability analysis are presented which predict that a regular non-axisymmetric wake transition will precede the axisymmetric Hopf bifurcation in the wake for aspect ratios $Ar \lesssim 3.9$. The present results from the axisymmetric study are presented here in their entirety, and the predicted non-axisymmetric transition boundaries are included to indicate the physical limits of these results.

At the large-aspect-ratio limit, the critical Reynolds number for the transition to unsteady flow past rings asymptotes to the critical Reynolds number for the transition to unsteady flow past a circular cylinder, $Re_{T2} \to Re_{C2} \approx 47$. This result is expected based on the studies by Monson (1983) and Leweke & Provansal (1995). For an increase in aspect ratios over $Ar \gtrsim 5$, the critical Reynolds number for the transition to unsteady flow decreases slowly from $Re_{T2} \approx 65$ towards $Re_{T2} \approx 47$. For a decrease in aspect ratios from $Ar \approx 5$ towards $Ar \to 1$, the critical Reynolds number for the transition to unsteady flow increases rapidly. At $Ar = 2$, for example, $Re_{T2} \approx 280$.

It is known that the Hopf transition in the wake of a circular cylinder is caused by an instability of the shear layers in the wake, which manifests itself through transverse oscillations of the recirculation bubble (Provansal *et al.* 1987; Dušek *et al.* 1994). The dramatic increase in Re_{T2} as the aspect ratio decreases towards $Ar = 1$ follows the similar increase in Re_{T1}, with the instability of the annular recirculation bubble occurring with $Re_{T2} > Re_{T1}$ for $Ar > 1$.

The flow past rings with small aspect ratios is an axisymmetric analogy to the flow past a circular cylinder near to a slip-wall, or free surface of high Froude number. Various works have treated this subject (Bearman & Zdravkovich 1978; Sheridan *et al.* 1997; Reichl *et al.* 1998, 2001a,b; Reichl 2001; Hourigan *et al.* 2002). Through these studies it was noticed that vortex shedding was suppressed at $Re = 180$ for gap ratios less than $0.1d$. In the present work, a ring with $Ar = 1.2$ has a similar gap ratio between the axis and ring cross-section, but no vortex shedding was computed in the wakes behind rings with $Ar \lesssim 2.7$ at $Re = 180$. The higher solidity of the ring about the axis may have provided a greater constraint on the transition to unsteady flow than the analogous circular cylinder near to a slip-wall. Therefore greater Reynolds numbers were required to induce vortex shedding, although the mechanism which inhibited the unsteady transition was the same.

3.1.4 Axisymmetric Vortex Shedding

At Reynolds numbers beyond Re_{T2}, the transition to unsteady flow results in an axisymmetric vortex street in the flow past rings. This observation is consistent with the experiments of Leweke & Provansal (1995), who observed that for rings with $10 \lesssim Ar \lesssim 31.7$ at Reynolds numbers beyond the transition to unsteady flow, vortex rings were shed into the wake. In figure 3.7, contour plots of vorticity are presented for the flow past a range of rings, and the flow past a circular cylinder, at $Re = 200$. In figure 3.7(a–b), a steady wake was computed, as at these aspect ratios $Re_{T2} > 200$.

For aspect ratios $Ar \geq 5$, presented in figure 3.7(c–e), the vortex rollers were shed at an angle to the flow. A decrease in the shedding angle was observed for an increase in aspect ratio. In keeping with observations by Monson (1983) and Leweke & Provansal (1995), the vortex street in the flow past rings approaches the vortex street in the flow past a circular cylinder (in figure 3.7(f)) as the aspect ratio increases, as indicated by the reduction in shedding angle.

3.1.4.1 The Strouhal–Reynolds Number Profile for Rings

Leweke & Provansal (1995) provided Strouhal number measurements for the flow past rings, and they observed that with an increase in aspect ratio, the Strouhal–Reynolds number profiles for the flow past rings approached the Strouhal–Reynolds number profile of the flow past a circular cylinder. Lower Strouhal numbers were measured for rings with smaller aspect ratios at a given Reynolds number. In the present study, Strouhal–Reynolds number profiles were obtained from axisymmetric computations of the periodic flow past rings with aspect ratios over the range $3 \leq Ar \leq 40$. The Strouhal–Reynolds number profile for the flow past a circular cylinder was also computed. In figure 3.8, the computed Strouhal–Reynolds number profiles are presented.

As the aspect ratio increases, the computed Strouhal–Reynolds number profiles for the flow past rings approach the Strouhal–Reynolds number profile computed for the flow past a circular cylinder, in agreement with the behaviour observed by Monson (1983), and measured by Leweke & Provansal (1995). An increase in critical Reynolds number for the onset of periodic flow is observed with a decrease in the aspect ratio, which verifies the critical Reynolds number profile in figure 3.6.

A significant drop in Strouhal number was computed for rings with $3 \lesssim Ar \lesssim 5$. The experimental studies of Roshko (1954), Monson (1983), Bearman & Takamoto

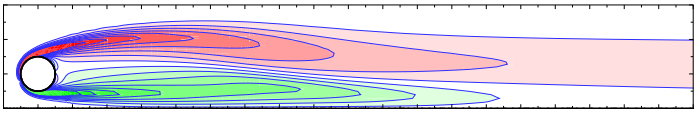

(a) $Ar = 2$.

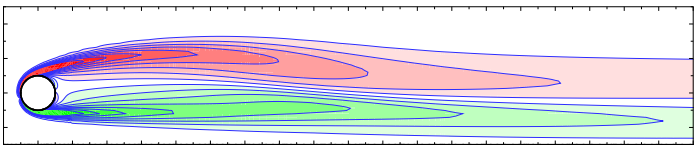

(b) $Ar = 3$.

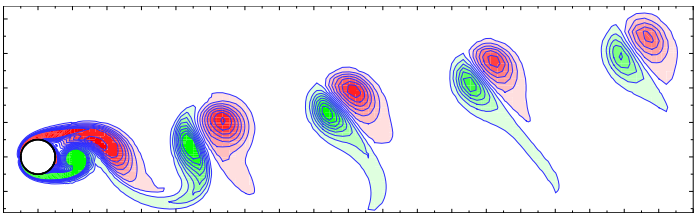

(c) $Ar = 5$.

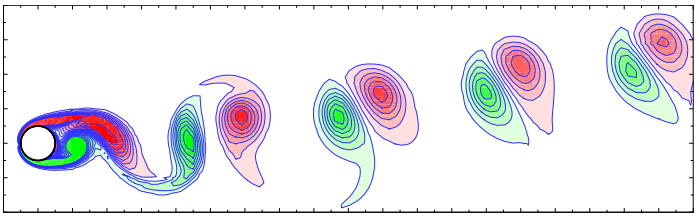

(d) $Ar = 10$.

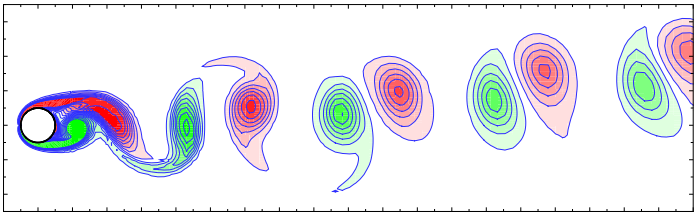

(e) $Ar = 20$.

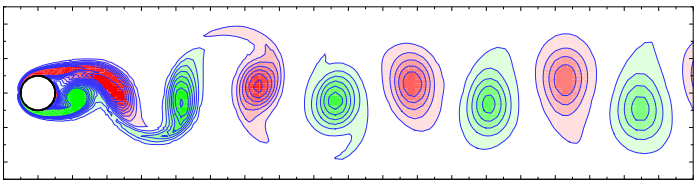

(f) Circular cylinder.

FIGURE 3.7: Vorticity contour plots of axisymmetric wakes of rings and the two-dimensional wake of a circular cylinder, at $Re = 200$. 16 contour levels are displayed between $-3 \leq \omega_z \leq 3$, with red and green contours representing negative and positive vorticity, respectively.

(1988) and Miau *et al.* (1992) all report a change in behaviour of the wake over a similar range of aspect ratios, in the wakes behind rings with various cross-sections. In chapters 4 and 5, the reason for the observed change in the characteristics of the wake is investigated.

3.1.4.2 The Relationship Between the Strouhal–Reynolds Number Profile and Aspect Ratio

A relationship for the Strouhal number of the flow past rings as a function of both the Reynolds number and aspect ratio was proposed by Leweke & Provansal (1995). The relationship that they proposed was extended from a relationship for the laminar Strouhal–Reynolds number relationship for the unsteady flow past a circular cylinder proposed by Williamson (1988a). Williamson showed that the product of the Strouhal number and the Reynolds number in the two-dimensional regime was approximated closely by a quadratic function

$$Re\,St = A\,Re^2 + B\,Re + C\,, \tag{3.1}$$

where A, B and C are real coefficients determined empirically. Fey *et al.* (1998) proposed an alternative functional form for the Strouhal–Reynolds number relationship, where St was a function of $1/\sqrt{Re}$. By choosing appropriate values of the coefficients for the flow regimes which included laminar parallel shedding, three-dimensional transition regimes, the Kelvin–Helmholtz shear-layer instability regime and the subcritical regime, a good approximation of the experimentally measured profile was obtained over a wide Reynolds number range $47 < Re < 2 \times 10^5$. As the present study aims to extend the circular cylinder and ring Strouhal–Reynolds number relationships proposed by Williamson (1988a) and Leweke & Provansal (1995), a functional form similar to the Williamson and Leweke & Provansal relationships is employed here.

The relationship proposed by Leweke & Provansal introduced a ring curvature $K = 2/Ar$, and was written as

$$St(Re, K, \theta) = St_0(Re, K = 0) - a\,[Re - Re_c(K = 0)]\,K\cos(\theta), \tag{3.2}$$

where θ specified the angle between the vortex rollers and the ring for oblique shedding modes, and St_0 was the Strouhal frequency of parallel shedding in the wake of a circular cylinder. Leweke & Provansal determined from experimental measurements that the coefficient $a = 0.0002134$.

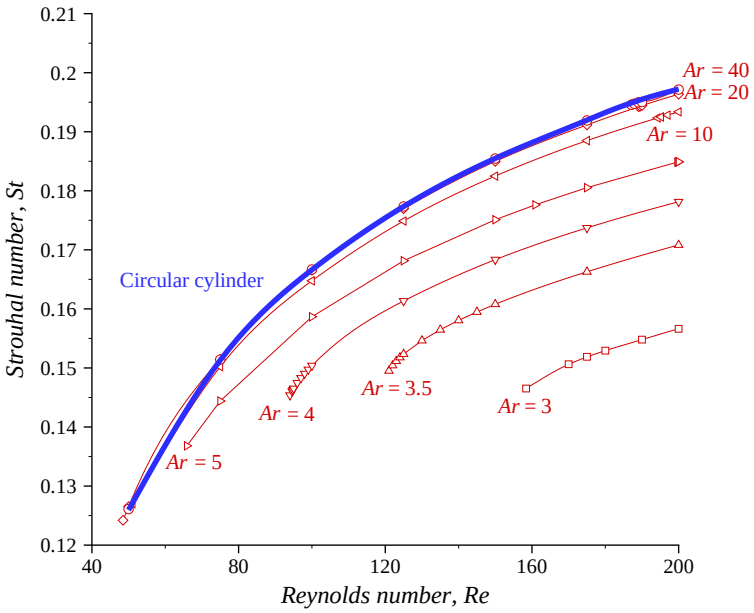

FIGURE 3.8: Computed Strouhal–Reynolds number profiles for the two-dimensional axisymmetric flow past rings (red lines). The blue line represented the circular cylinder Strouhal number profile for reference.

The relationship proposed by Leweke & Provansal was adapted to the Strouhal–Reynolds number profiles computed in the present study. A simplification to the relationship was made by taking $\cos(\theta)$ to be unity, as the axisymmetric computations that were employed suppressed oblique shedding modes. The validity of the relationship proposed by Leweke & Provansal for the wider range of aspect ratios considered in the present study was determined by the application of a correction to the present computations for zero curvature. For the relationship to be applicable, the Strouhal–Reynolds number profiles for the flow past rings should collapse onto the Strouhal–Reynolds number profile for the flow past a circular cylinder. In figure 3.9, a plot of the corrected profiles from the present computations is shown. The plot shows that the relationship proposed by Leweke & Provansal breaks down for aspect ratios $3 \leq Ar \lesssim 10$. In the formulation of the relationship, a linear dependence of the Strouhal number shift with K was assumed. The relationship which they proposed was of the form $St = St_0 - g(Re)K$, where the function $g(Re)$ was a linear function of Re independent of K, which represented $|\Delta St_0/\Delta K|$, where ΔSt_0 was the difference between the Strouhal numbers at a given Reynolds number for the flow past rings and a circular cylinder.

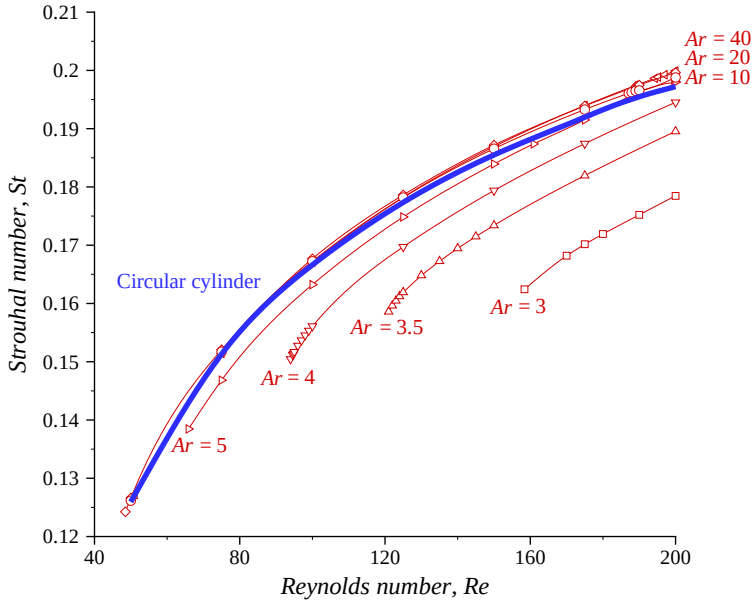

FIGURE 3.9: Strouhal–Reynolds number profiles of the current data extrapolated to zero curvature using the curvature correction formula developed by Leweke & Provansal (1995). Line colours and symbols are as per figure 3.8.

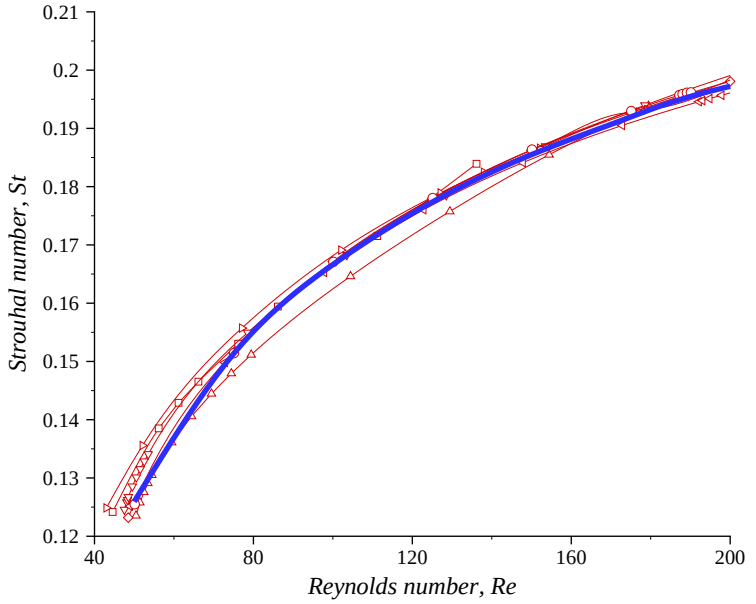

FIGURE 3.10: Ring Strouhal–Reynolds number profiles corrected to zero curvature using the proposed relationship. Line colours and symbols are as per figure 3.8.

An alternative functional dependence is proposed, whereby the Strouhal–Reynolds number profiles all exhibit a similar profile when translated to the same starting point and scaled by a factor that varies with aspect ratio. This relationship takes the form

$$St(Re, Ar) = St_c + [St_0(Re - Re_{T2} + Re_{C2}) - St_{C2}]/A, \tag{3.3}$$

where $St(Re, Ar)$ is the Strouhal number for a given Re and Ar, Re_{T2} is the critical Reynolds number for the onset of unsteady flow at a given Ar, St_c is the Strouhal number at Re_{T2} for a given Ar, $St_0(Re)$ is the Strouhal–Reynolds number relationship for a straight circular cylinder, Re_{C2} is the critical Reynolds number for unsteady flow in the wake of a straight circular cylinder, St_{C2} is the Strouhal number at the critical Reynolds number for the circular cylinder and A is the factor by which the Strouhal frequencies differ, as a function of Ar.

Relationships were determined for these coefficients as functions of K from the computed wakes. The relationship forms were chosen to minimise the discrepancy between computed and estimated values of the coefficients to less than 1%.

$$\begin{aligned}
St_c &= -1.14786K^5 + 0.59433K^4 + 0.34015K^3 - 0.12845K^2 + 0.0188K + 0.124 \\
St_0 &= 0.0000452401Re + 0.213346098 - 4.9434288783/Re \\
Re_{T2} &= 414.405922K^3 - 16.516256K^2 - 2.411304K + 46.51112 \\
Re_{C2} &= 46.51112 \\
St_{C2} &= 0.124 \\
A &= 14.032351K^3 - 4.842855K^2 + 0.72144K + 1.0
\end{aligned}$$

The new relationship provides an excellent description of the Strouhal–Reynolds number profiles over the entire aspect ratio range investigated here. A plot of the present Strouhal–Reynolds number data, corrected for zero curvature, is presented in figure 3.10. An excellent collapse onto the Strouhal–Reynolds number profile of the circular cylinder is achieved. The maximum deviation of any one point from the corresponding Strouhal number for the flow past a circular cylinder is approximately 5%, but generally the deviation is much less than 2%. The fit provided by Leweke & Provansal (1995) is accurate to within 1% for rings with aspect ratios $Ar \geq 10$, however for aspect ratios in the range $3 \leq Ar \lesssim 10$ the discrepancy can be as high as 15%. Over this aspect ratio range, the relationship derived by Leweke & Provansal typically predicts Strouhal frequencies with a discrepancy an order of magnitude greater than the current

expression. It is pertinent to note that in the linear stability analysis reported in chapter 4, it is predicted that the wakes behind rings with aspect ratios $Ar \lesssim 4$ undergo a non-axisymmetric transition prior to the predicted Hopf transition. Even for an aspect ratio $Ar = 4$, the present formula still exceeds the accuracy of the Leweke & Provansal relationship.

3.1.4.3 Experimental and Computational Comparison

Limited attempts to capture flow visualisation of axisymmetric vortex shedding in the wakes behind rings have been reported. Some dye visualisation was presented for the flow past a flat ring in Takamoto & Izumi (1981), which showed an annular vortex street in the wake. The visualisations presented in the experimental work by Monson (1983) captured the entire wake region behind freely falling rings in a liquid. The use of dye and the camera positioning occluded the internal wake structure, although some evidence of parallel Kármán type vortex shedding was observed for rings with low solidity (i.e. large aspect ratio).

In the experimental study by Leweke & Provansal (1995), images of oblique and parallel modes of vortex shedding were captured with a smoke-visualisation method for the wakes behind rings with $Ar \gtrsim 10$. The study was primarily concerned with Strouhal number measurements and dynamical modelling of the various unsteady modes, so no attempt was made to study the localised wake structure in the vicinity of the cross-section of the rings.

As part of the present study, both an experimental dye visualisation technique and a computational simulated-particle visualisation technique were employed to study the axisymmetric vortex street in the wake behind a ring with $Ar = 4.94$. The study was performed to validate the results of the numerical computations for intermediate aspect ratios, as limited data was available in the literature to validate the computational results obtained in the present study for the flow past rings with $Ar < 10$. In the experiments performed as part of this study, the vortex street in the wake was visualised by the illumination of a Fluorescein dye with a thin laser sheet through the centreline of the ring and the wake. The entrainment of the dye into the wake provided a cross-sectional view of the process of vortex shedding into the wake. Computations were performed to provide a comparison with the experimental dye visualisations. The computed wake was visualised by computing the entrainment of simulated particles

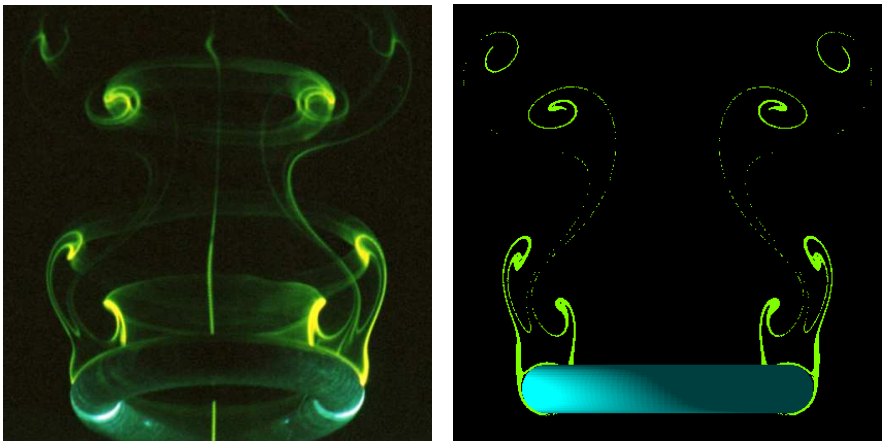

(a) Comparison 1. Left: Experimental dye visualisation. Right: Simulated-particle visualisation.

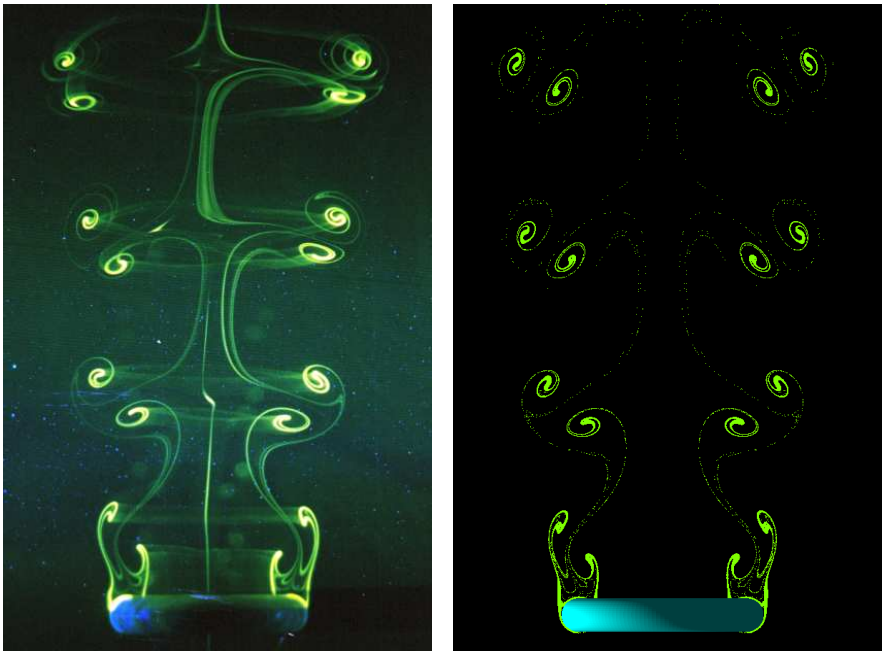

(b) Comparison 2. Left: Experimental dye visualisation. Right: Simulated-particle visualisation.

FIGURE 3.11: Comparisons between experimental and numerical observations of an axisymmetric vortex street in the wake of a ring with $Ar = 4.94$ at $Re = 100$.

into the wake from the cross-section of the ring. The simulated-particle computations included 50 particle injection points distributed around the cross-section of the ring. The injection point of the particles was $0.04d$ from the surface of the ring, which facilitated a rapid entrainment of particles into the wake. In a postprocessing step, the particle positions were reflected about the wake centreline to mimic the experimental dye visualisations.

Experiments were carried out at $Re = 100$ to capture an axisymmetric vortex shedding street. At this Reynolds number, the vortex street in the wake saturated rapidly, as it was significantly greater than the critical Reynolds number for the transition to unsteady flow in the wake ($Re_{T2} \approx 65$). A rapid evolution of the vortex street was required, as a relatively small tank was employed for the experiments. An upper limit on the Reynolds number chosen for the experiments was imposed by the development of non-axisymmetric instabilities in the wake, and preliminary investigations determined that $Re = 100$ provided a satisfactory compromise between the need for a rapid vortex street evolution, and the need to avoid non-axisymmetric flows.

Two comparisons are presented in figure 3.11 at different stages in an experimental run. Figure 3.11(a) shows a comparison near the beginning of an experimental run, which shows the rapid formation of the vortex street. The corresponding simulated-particle computation employed a saturated axisymmetric wake at the same Reynolds number. Notice the good agreement in the structure of the forming vortices in the near wake, which indicates that the experimental run was near to saturation at that early stage. The inclination of the ring in the dye visualisation image is indicative of the early stage of the experimental run, as the ring had yet to travel to the centre of the frame of the camera. The inclination corresponded to approximately 10° of parallax error in the plane of the laser sheet, which was not considered significant for the purposes of qualitative comparison.

Figure 3.11(b) shows a comparison from the same experimental run as figure 3.11(a), almost exactly two shedding cycles later. At this time, the ring is located at the centre of the frame of the camera, and is viewed directly side-on in both the experimental and computational visualisations. An excellent agreement between the experimental and numerical visualisations is observed in the near-wake region, within $2d$ of the ring, and the shed vortex roller pair, which is located approximately $4d$–$5d$ downstream. The strength, position, orientation, size, shape, and dye/particle distribution are all

consistent. Further downstream, a discrepancy is observed for the two vortex roller pairs located farthest downstream in figure 3.11(b). The vortex pairs are aligned in a streamwise direction in the experimental dye visualisation, convecting radially outwards, whereas the vortex pairs are aligned diagonally in the numerical simulated-particle visualisation, convecting upstream and radially outwards. These are the same vortex pairs as the shed and forming vortex pairs from figure 3.11(a). As these vortex pairs were the first two pairs of vortices shed in the experimental run, they are influenced by transient conditions in the wake prior to saturation, which explains the observed discrepancy.

The vortex street visualisations of the wake behind a ring presented in figure 3.11 highlight several differences between the vortex street in the wakes behind rings of moderate aspect ratio and the classic vortex street that forms in the wake behind a circular cylinder. The vortex street in the wake behind a ring increases in diameter further downstream of the ring. Upon closer inspection, it is apparent that relative to the cross-section of the ring, the vortices that comprise the vortex street are shed into the wake at an inclined angle to the direction of motion. The inclination of the vortex street is caused by the pairing of the inner to the outer vortex roller over each shedding cycle. The vortex street therefore comprises pairs of counter-rotating vortex rollers, which are known to convect in a direction normal to a plane though the vortex cores (see Marshall 1992; Garten *et al.* 1998; Leweke & Williamson 1998; Ortega *et al.* 2003, for further discussions on the dynamics of vortex pairs).

The effects of this convection of the vortex roller pairs on the wake is displayed with clarity in the experimental dye visualisation of figure 3.11(b). A small amount of dye is present in the braid region between each vortex pair. The inner braid regions are swept radially inwards towards the axis. These bands of dye are connected to the rear of each vortex pair, giving them the appearance of mushrooms sprouting out from the axis. This illuminates the direction of motion of the convecting pairs. It is also interesting to compare the dye distribution in the wake cross-section for the flow past the ring in figure 3.11(b) with the dye distribution in the wake for the antiphase shedding in the flow past a pair of circular cylinders which was presented earlier in figure 1.9(a), from Williamson (1985a). A similar distribution of vorticity is observed in both cases. Importantly, no dye is transferred from one side of the wake to the other, which verifies that the vortex street was axisymmetric in the experimental work.

An increase in the curvature of the ring increases the inclination of the local centre-line of the vortex street with respect to the direction of flow. This causes a deviation from a reflective wake symmetry of the vortex street local to the ring cross-section, when compared to the wake of a straight circular cylinder. This has ramifications for the stability characteristics of the vortex street to non-axisymmetric modes, which will be investigated in chapter 4.

3.2 Axisymmetric Computation of Drag on a Ring

Drag and lift coefficients are non-dimensional parameters for the drag and lift forces acting on a body which is in motion through a fluid. The total force imposed on a body by a fluid in motion comprises components which result from both viscous shear and pressure. It is convenient to consider these forces in directions both parallel to, and normal or transverse to the direction of flow (i.e. drag and lift, respectively).

The axisymmetry of a ring is such that transverse (or radial) forces imposed on the body by the surrounding fluid sum to zero when the flow is axisymmetric. Hence lift forces due to contributions of pressure (F_{l_p}) and viscosity (F_{l_ν}) that act in the radial direction are of little interest for the wake flows described here. The drag force (F_d) is significant, as it acts in the axial direction, and will be considered in this study.

Many previous studies have calculated the lift and drag coefficient variation for the flow past both a sphere (e.g. Mittal 1999a; Johnson & Patel 1999) and a circular cylinder (e.g. Henderson 1995, 1997), but there is very little known about the drag coefficient variation in the flow past rings. In the literature, only Bearman & Takamoto (1988) provide results of force measurements for the flow past rings. Their experiments were performed on a flat ring, with a axial width 2% of its outer diameter, and aspect ratio variation was achieved through variation in the ring hole size, and measured drag coefficients for rings with $Ar = 1$, 4, 6 and 10, at a constant speed, providing Reynolds numbers varying with aspect ratio $6.8 \times 10^4 > Re > 1.3 \times 10^4$. The measured drag coefficients varied continuously over this aspect ratio range from $C_d \approx 1.1$ to $C_d \approx 2.0$.

No previous studies have reported drag coefficient measurements over a Reynolds number range consistent with the present study. A comprehensive study of the variation in drag coefficient with both Reynolds number and aspect ratio for the flow past rings was performed as part of the present study. Constant drag coefficients were computed for steady flows past rings, and mean drag coefficients were computed for unsteady flows

past rings. In addition, drag coefficients were computed for the flow past a sphere and a circular cylinder. The variation in the drag coefficient was monitored with respect to both the Reynolds number of the flow, and the aspect ratio of the rings. Comparisons are drawn between the computed drag coefficients of the flow past a sphere and a circular cylinder, and previous measurements of the drag coefficients of the flow past a sphere and a circular cylinder.

3.2.1 The Drag Coefficient

The drag force is a dimensional measure of the total force imparted in the axial direction by the fluid on the ring. In order to gain a better understanding of the relative variation in the drag force for all aspect ratios, the drag coefficient (C_d) is considered. The drag coefficient is a non-dimensionalised representation of the drag force, and is expressed by the relationship

$$C_d = \frac{F_d}{\frac{1}{2}\rho A_{frontal} {U_\infty}^2}, \tag{3.4}$$

where ρ, $A_{frontal}$ and U_∞ are the fluid density, the projected frontal area of the ring, and the free-stream velocity of the fluid, respectively. The drag force (F_d) consists of both a pressure contribution, and a viscous contribution such that $F_d = F_{d_p} + F_{d_\nu}$, where F_{d_p} and F_{d_ν} are the contributions of the pressure drag force and the viscous drag force, respectively.

From a numerical perspective, the pressure drag force (F_{d_p}) is computed by integrating the pressure over the axial projection of the surface of the ring. The viscous drag force (F_{d_ν}) is computed by integrating the shear force at the ring surface acting in the axial direction over the surface area of the ring. The shear force is determined from the spatial velocity gradients at the ring surface, and the kinematic viscosity of the fluid. Equation 3.4 is simplified in the present numerical formulation, as ρ and U_∞ are non-dimensionalised. Furthermore, the frontal area is expressed as a function of aspect ratio if the length is non-dimensionalised with respect to the cross-section diameter d, written as

$$A_{frontal} = \begin{cases} \frac{\pi}{4}(Ar^2 + 2Ar + 1) & \text{for } 0 \leq Ar \leq 1, \\ \pi Ar & \text{for } Ar > 1. \end{cases} \tag{3.5}$$

Substitution of equation 3.5 into equation 3.4 provides simplified non-dimensional relationships for the drag coefficient as a function of both the aspect ratio and the drag

force,

$$C_d = \begin{cases} \frac{8F_d}{\pi(Ar^2+2Ar+1)} & \text{for } 0 \leq Ar \leq 1, \\ \frac{2F_d}{\pi Ar} & \text{for } Ar > 1. \end{cases} \tag{3.6}$$

These equations were used to calculate the drag coefficients for the flow past rings in the present study.

3.2.2 Drag Coefficients for the Flow past Spheres and Circular Cylinders

The computed drag coefficients for the axisymmetric flow past a sphere and the two-dimensional flow past a circular cylinder are presented in figure 3.12.

The computed drag coefficients for the flow past a sphere in figure 3.12(a) are within 1% of the measured and computed data from other studies. The computed drag coefficients for the flow past a circular cylinder in figure 3.12(b) are generally within 10% of the measured and computed data from other studies. A number of studies of the low-Reynolds-number flows past a circular cylinder discuss the effect on measured parameters such as C_d of experimental conditions such as end-effects (Leweke & Provansal 1995; Williamson 1996c) and the associated wake dynamics such as vortex dislocations (Williamson 1992) and oblique shedding modes (Williamson 1989). These effects add to the uncertainty of the experimental measurements, and are suppressed in the two-dimensional computations.

The computed drag coefficients for the flow past a sphere are compared in figure 3.12(a) to the computed data from Tomboulides *et al.* (1993), Johnson & Patel (1999) and Mittal (1999a), experimental measurements from Roos & Willmarth (1971), and an experimental collocation from Clift *et al.* (1978). The computed drag coefficients for the flow past a circular cylinder are compared in figure 3.12(b) to the computed data from Henderson (1995) and Henderson (1997), and experimental measurements from Wieselberger (1921).

As shown in figure 3.12(a), the present numerical results are consistent with the experimentally obtained C_d values beyond the non-axisymmetric transition Reynolds number of approximately $Re_c \approx 211$. This is despite the employment of axisymmetric computations, which exclude the evolution of non-axisymmetric modes in the wake. By contrast, as observed in figure 3.12(b), the present two-dimensional drag coefficients for the flow past a circular cylinder and those from Henderson (1995) increase from $C_d \approx 1.4$ at $Re = 100$ to $C_d \approx 1.5$ at $Re = 1000$, whereas the experimental measurements from

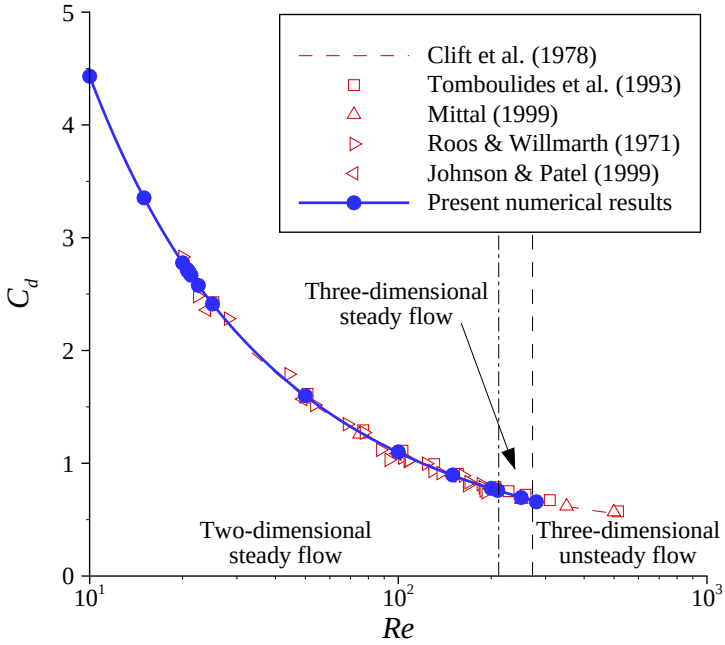

(a) The wake of a sphere.

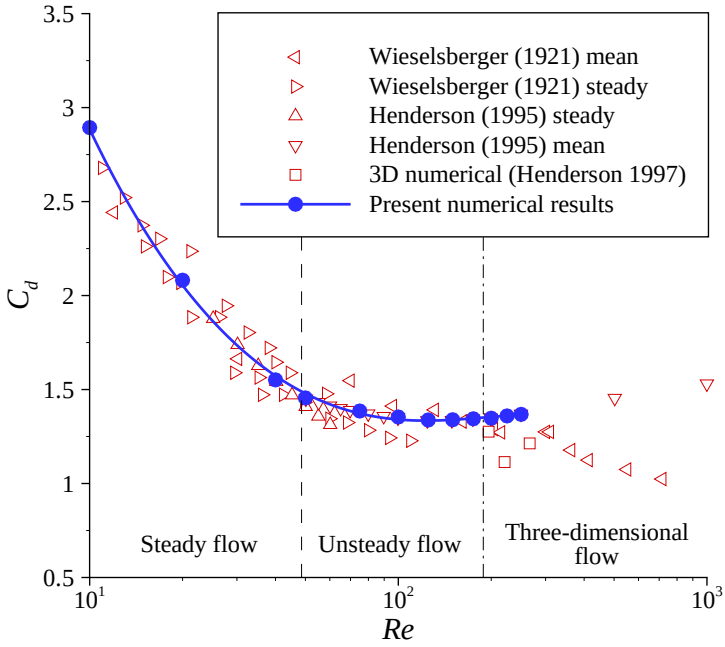

(b) The wake of a circular cylinder.

FIGURE 3.12: Comparison between computed drag coefficients from the present study with existing experimental and numerical data. The present data is coloured blue, and the data from previous studies are coloured red.

Wieselberger (1921) and the three-dimensional computations from Henderson (1997) decrease from $C_d \approx 1.4$ at the onset of three-dimensional flow at $Re_c \approx 188.5$, to $C_d \approx 1$ at $Re = 1000$.

3.2.3 Drag Coefficients for the Flow past Rings

The drag coefficients for the flow past rings were computed, and are analysed here. In figure 3.13, the computed drag coefficients for the flow past rings are compared with the computed drag coefficients for the flow past a sphere and a circular cylinder. The figure includes a plot of both C_d versus $\log Re$ and $\log C_d$ versus $\log Re$ for clarity.

The profiles presented in figure 3.13(a) show a significant decrease in C_d with an increase in Reynolds number for the flow past rings and the flow past a sphere and a circular cylinder. The decrease in the computed drag coefficients is attributed to the decrease in the viscous component of the drag as the Reynolds number increases. Interestingly, there is a significant difference between the computed drag coefficient profile for the flow past a sphere and the flow past rings with $Ar \geq 1$. For the flow past a ring with $Ar = 1$, the drag coefficient profile is similar in gradient, but is significantly smaller in magnitude than the drag coefficient profile for the flow past a sphere. At first inspection this result appears surprising, but it may be explained in terms of the Reynolds number length scale. The Reynolds number for the computations was based on the cross-section diameter, d, and not the projected frontal diameter, $D + d$, which effectively shifts the drag coefficient profiles for rings with $1 \lesssim Ar \lesssim 3$ to the left in figure 3.13. From the computed results, the computed drag decreases for a given Reynolds number as the aspect ratio is increased from $Ar = 0$ to $Ar = 1$.

Figure 3.13 shows that at Reynolds numbers $Re \lesssim 5$, a decrease in the computed drag coefficient is found for an increase in aspect ratio from $Ar = 1$ to $Ar \approx 3$. An increase in the computed drag coefficient towards the drag coefficient computed for the flow past a circular cylinder is found for an increase in aspect ratio from $Ar \approx 3$ to $Ar \to \infty$. At higher Reynolds numbers ($Re \gtrsim 20$), the computed drag coefficients that were obtained for $Ar = 1$ were the smallest obtained for any aspect ratio included in the study. It can be observed in figure 3.13(b) that for $Re \gtrsim 20$, the drag coefficients–Reynolds number profiles computed for the flow past rings with $Ar > 1$ approach constant values. For $Ar \geq 5$, the computed drag coefficients reach a minimum of $C_d \approx 1.2$. This is interesting, as for unsteady wakes the drag coefficient does not

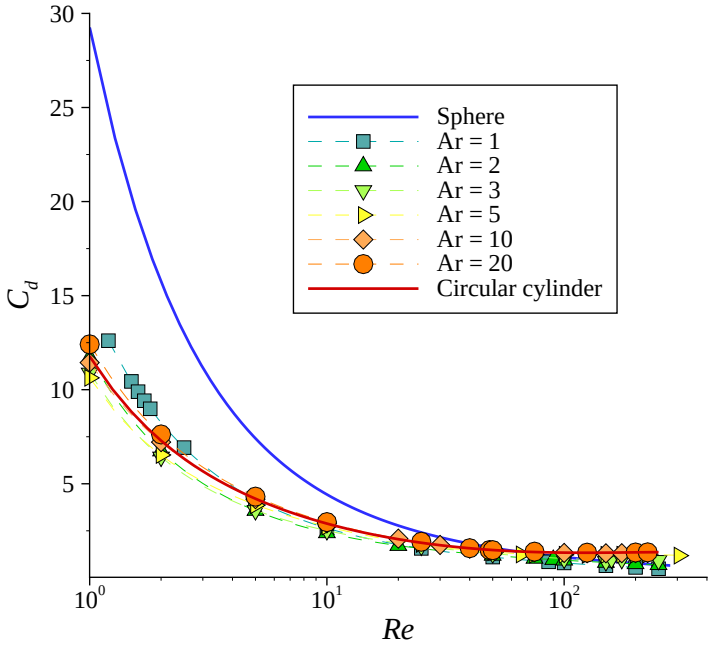

(a) C_d versus $\log Re$.

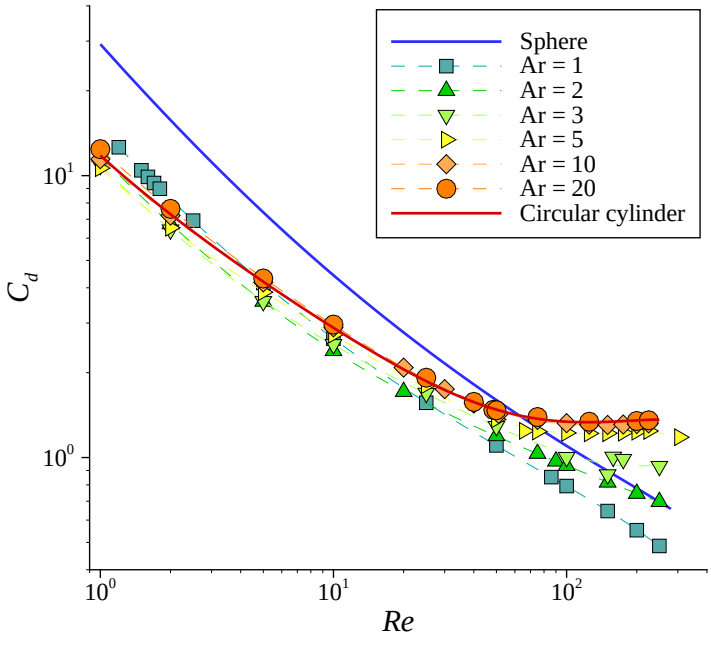

(b) $\log C_d$ versus $\log Re$.

FIGURE 3.13: Computed drag coefficients for the flow past a sphere and a circular cylinder (blue and red lines, respectively) compared with the computed drag coefficients for the flow past rings (coloured symbols and dotted lines).

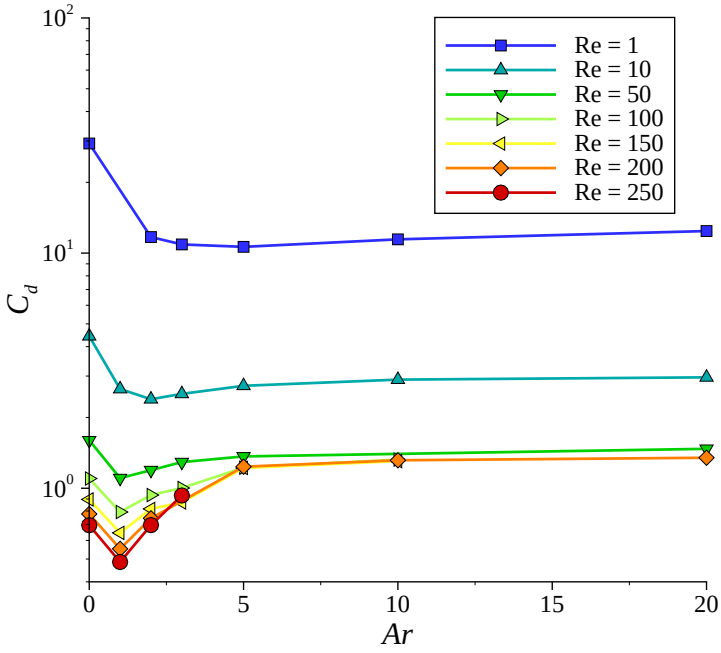

FIGURE 3.14: Constant Reynolds number variation in C_d versus Ar. Colours are chosen to show a smooth variation between the low Reynolds numbers ($Re = 1$ is blue) and high Reynolds numbers ($Re = 250$ is red).

continue to decrease with an increase in Reynolds number; instead, it reaches some near-constant value.

To develop an understanding of the drag coefficient variation with aspect ratio for a given Reynolds number for the flow past rings, the computed drag coefficients are presented in figure 3.14. The plot reveals some striking features of the drag of rings. As previously discussed, the computed drag coefficients decrease in magnitude as the Reynolds number is increased. For aspect ratios $Ar \geq 5$, the drag profiles for all Reynolds numbers remain approximately constant, which suggests that the wake dynamics of the flow past rings over this range of aspect ratios is consistent with the wake dynamics of the flow past a circular cylinder. It is pertinent to note that for all Reynolds numbers $Re \geq 50$ over the range of aspect ratios $Ar \geq 5$, the computed drag coefficient profiles are almost equal. This corroborates the previous observations of the mean drag coefficient measurements of the unsteady flow past a circular cylinder (see figure 3.12(b)), which showed limited variation in total drag for Reynolds numbers $Re \gtrsim 50$.

An additional point of interest occurs in the small aspect ratio regime. For all

Reynolds numbers, a minimum in the computed drag coefficient is found over the range of aspect ratios $0 < Ar \leq 5$. At $Re = 1$, the minimum computed drag coefficient is found for the flow past a ring with an aspect ratio $Ar = 5$. At $Re = 10$, the minimum computed drag coefficient is found for the flow past a ring with $Ar = 2$. For all Reynolds numbers $Re \geq 50$, the minimum computed drag coefficient is found for the flow past a ring with $Ar = 1$. This observation is interesting, as an open ring with an aspect ratio in the vicinity of $Ar = 1$ is similar to a vented bluff body. Drag reductions in the order of 40% have been obtained for the flow past spheres with an axial vent aligned with the direction of flow, even with vent diameters as small as $0.02d$ (e.g. see Lu *et al.* 1999; Grosche & Meier 2000; Grosche *et al.* 2003).

3.2.4 Pressure and Viscous Components of the Drag Coefficient for the Flow past a Circular Cylinder

The pressure and viscous components of the drag coefficient of the flow past a circular cylinder from both steady and unsteady two-dimensional computations was studied by Henderson (1995). He showed that beyond the transition to unsteady flow ($Re \approx 48.6$), the mean pressure component of the drag coefficient increased, whereas the mean viscous component of the drag coefficient decreased. The reduction in the total drag coefficient due to the decrease in the viscous component continued beyond $Re \approx 1 \times 10^2$. For $Re \gtrsim 200$, the total mean drag coefficient increased, as the pressure drag increase outweighed the viscous drag decrease. In figure 3.15, the computed mean pressure and viscous components of the drag coefficient for the flow past a circular cylinder are presented. These are compared with the reported pressure and viscous components of the drag coefficient for the flow past a circular cylinder computed by Henderson (1995). An excellent agreement is obtained. The present computed values adhere to the steady profiles for $Re \lesssim 48$, and for $Re \gtrsim 48$, the present values are consistent with the mean profiles computed by Henderson.

3.2.5 Pressure and Viscous Components of the Drag Coefficient for the Flow past Rings

The contribution of pressure and viscous components to the drag coefficient of the flow past a circular cylinder has been discussed in § 3.2.4. The contribution of these components to the drag coefficients of the flow past rings is examined in this section.

The pressure and viscous components of the drag coefficients for the flow past rings

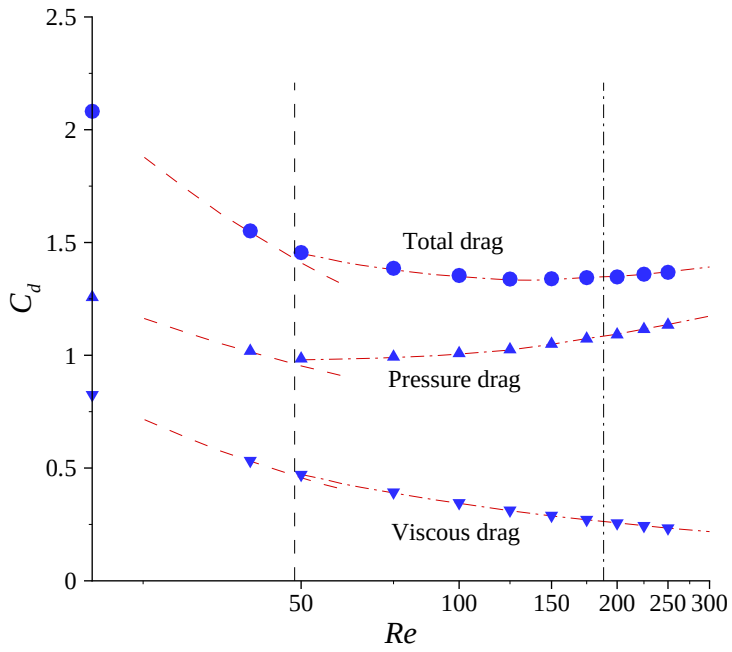

FIGURE 3.15: Pressure and viscous components of the total drag on a circular cylinder. Blue circles and triangles represent the present numerical values for the total drag and the components, respectively. Red lines denote the profiles obtained by Henderson (1995). Dashed lines represent the steady wake regime and drag profiles, and "dash–dot" lines represent the unsteady wake regime and drag profiles.

were calculated, and are plotted in figure 3.16. The pressure contribution is presented in figure 3.16(a), and the viscous contribution is presented in figure 3.16(b).

A plot of the pressure component of the drag coefficients of the flow past rings is presented in figure 3.16(a). Aside from the C_{d_p} profile of the wake of a sphere (whose large deviation from the ring with $Ar = 1$ due to effective length scaling has already been discussed), all the C_{d_p} profiles exhibit similar behaviour. At Reynolds numbers $Re \approx 4$, the ring with $Ar = 3$ has the lowest pressure component of the drag coefficient of the rings considered, with $C_{d_p} \approx 1.9$. At $Re = 4$, the ring with $Ar = 1$ has $C_{d_p} \approx 2.1$, which decreases more rapidly than the pressure component of the drag coefficient for the other rings as the Reynolds number is increased. For Reynolds numbers $Re \gtrsim 20$, the profile of the pressure component of the drag coefficient is consistent with the profile of the pressure component of the drag coefficient in the flow past a sphere. At a Reynolds number of $Re = 250$, the pressure component of the drag coefficient of the flows past both a sphere and a ring with $Ar = 1$ are as low as $C_{d_p} \approx 0.35$. The ring with $Ar = 2$

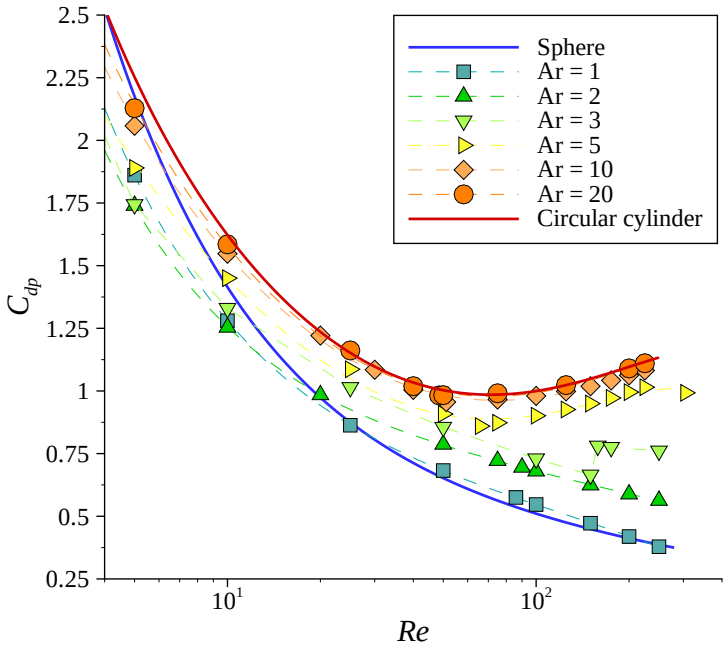

(a) Pressure drag component, C_{d_p}.

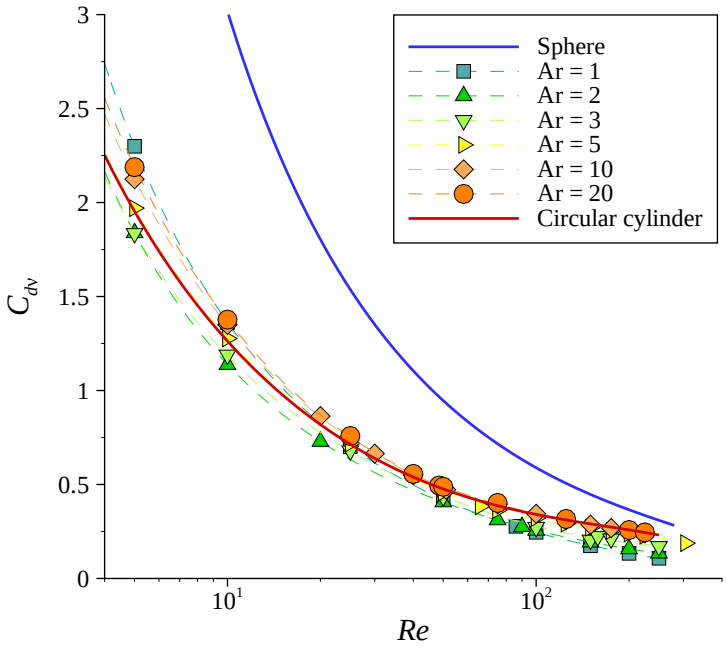

(b) Viscous drag component, C_{d_ν}.

FIGURE 3.16: Components of C_d for the wakes behind rings. Results for the sphere and the circular cylinder are included for comparison. Symbols and colours are as per figure 3.13.

decreases in a similar fashion to $C_{d_p} \approx 0.6$ at $Re = 250$.

At $Re = 4$, the pressure component of the drag coefficients for the flow past rings with aspect ratios $Ar \geq 5$ vary with an increase in aspect ratio over the range $2.1 \lesssim C_{d_p} \lesssim 2.5$. At $Re \approx 50$, the flows become unsteady, and as in the study of the drag coefficient of the flow past a circular cylinder by Henderson (1995), the pressure component of the drag coefficient reaches a minimum, and increases with an increase in Reynolds number for $Re \gtrsim 50$. Figure 3.16(a) shows this increase, with the pressure component of the drag coefficients for the flow past rings with $Ar \geq 5$ and a circular cylinder computed between $0.85 \lesssim C_{d_p} \lesssim 1.0$ at $Re \approx 50$, and between $1.0 \lesssim C_{d_p} \lesssim 1.15$ at $Re = 200$. For a ring with $Ar = 3$, the pressure component of the drag coefficient increases with an increase in Reynolds number beyond $Re \gtrsim 150$. In contrast to the larger aspect ratios discussed previously, the pressure component increase is more pronounced for the drag coefficient for the flow past a ring with $Ar = 3$, as it increases from $C_{d_p} \approx 0.7$ at $Re = 150$ to $C_{d_p} \approx 0.8$ at $Re \approx 158$.

A plot of the viscous component of the drag coefficients of the flow past rings is presented in figure 3.16(b). A large difference can be observed between the profiles of the viscous component of the drag coefficient for the flows past rings with $Ar = 0$ and $Ar = 1$, which follows the wake length scale issue discussed earlier. The minimum viscous component of the drag coefficient for the flow past rings is computed for the flow past a ring with $Ar = 3$. At $Re = 5$, for example, $C_{d_\nu} \approx 1.8$ for the flow past a ring with $Ar = 3$, whereas $C_{d_\nu} \approx 2.3$ for the flow past a ring with $Ar = 1$ and $C_{d_\nu} \approx 2.2$ for the flow past a ring with $Ar = 20$. Interestingly, the viscous component of the drag coefficient for the flow past a circular cylinder is a little lower for $Re \lesssim 5$, with $C_{d_\nu} \approx 2.0$. A possible explanation for this computed discrepancy is due to the difference between the formulation of the axisymmetric and two-dimensional models for rings and a circular cylinder. The meshes employed to model rings have a unit velocity condition imposed at the outer boundary $30d$ from the ring cross-section, which is consistent with the mesh employed to model a circular cylinder. However, the meshes employed to model rings have a zero normal velocity condition imposed at the inner boundary. For the mesh employed to model a ring with $Ar = 20$, the inner boundary is merely $10d$ from the ring cross-section. For higher Reynolds numbers, where viscous effects are not significant, these boundary effects are less significant (as can be observed in figure 3.16(b) where the viscous component of the drag coefficients for the flow past a

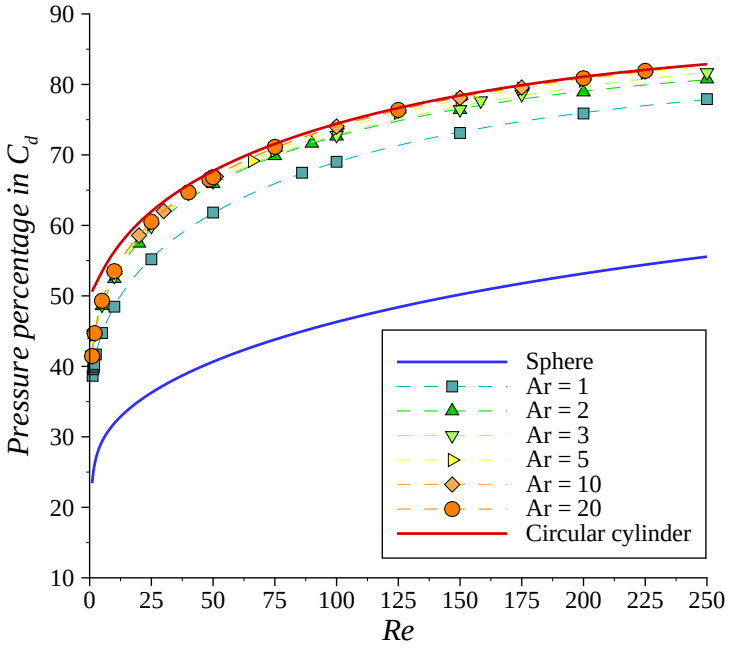

FIGURE 3.17: Percentage contribution of C_{d_p} to C_d varying with Reynolds number for various rings. Symbols and colours are as per figure 3.13.

circular cylinder and a ring with $Ar = 20$ align closely at higher Reynolds numbers).

An alternative representation of the contribution of pressure and viscosity to the total drag of rings is presented in figure 3.17, in which the percentage contribution of the pressure component of the total drag coefficient is plotted with Reynolds number for each of the aspect ratios considered in the present study.

Two important points should be drawn from the plot in figure 3.17. Firstly, the pressure drag component percentages for all rings vary in a similar manner to those computed for both the flow past a sphere and a circular cylinder, despite some variation in the magnitude of the percentage contribution. Secondly, the magnitude of the percentage contribution at any given Reynolds number increases with an increase in aspect ratio. The minimum percentage contribution of the pressure component of the drag coefficient was computed for the flow past a sphere, and the maximum percentage contribution of the pressure component of the drag coefficient was computed for the flow past a circular cylinder.

This completes the analysis of the drag of rings from axisymmetric wakes. In chapter 4, results of a linear stability analysis are presented, in which the critical Reynolds

numbers for the onset of non-axisymmetric modes in the wakes behind rings were determined. As part of the non-axisymmetric computations which are presented in chapter 5, the drag coefficients of non-axisymmetric flows past rings were computed. It is interesting to compare the drag coefficients that have been calculated from both axisymmetric and non-axisymmetric flows past rings.

3.3 Chapter Summary

In this chapter, the axisymmetric flow past rings has been examined in detail. Previous studies have reported the transition Reynolds number for separation in the flow past a sphere and a circular cylinder. For the first time, the variation in the separation transition Reynolds number with aspect ratio has been established for the flow past a ring.

The structure of the steady wakes behind rings has not previously been studied in detail. In the present work, plots of the flow streamlines have been presented, which have allowed a detailed analysis of the low-Reynolds-number flow past rings to be conducted. For aspect ratios $0 \leq Ar \lesssim 3$, the wakes behind rings have been shown to comprise a large recirculation bubble on the axis. This bubble is attached to the rear of the closed rings with aspect ratios $0 \leq Ar \leq 1$, and is detached in the wakes behind rings with aspect ratios $1 < Ar \lesssim 3$. For aspect ratios $Ar \gtrsim 3$, the wakes behind rings consist of an annular recirculation bubble attached to the rear of the open rings.

Previous studies established that the steady wake behind a circular cylinder becomes unstable to unsteady flow at $Re_{C2} \approx 46$. Following this transition, a wake consisting of a Kármán vortex street is formed. An analogous annular vortex street has been observed in the wakes behind rings with large aspect ratios (Monson 1983; Leweke & Provansal 1995). However, the aspect ratio variation in the critical Reynolds number for this transition in the flow past rings was only previously studied for aspect ratios $Ar \gtrsim 10$. For the first time, the precise variation in the unsteady flow transition in the flow past rings has been computed over a wide range of aspect ratios ($Ar \gtrsim 2$).

In previous studies, the flow past rings was reported to approach the flow past a circular cylinder with an increase in aspect ratio (Monson 1983; Leweke & Provansal 1995). Vorticity contour plots are presented in the present study, which verify this observed phenomenon with striking clarity. Vortex streets are computed at a $Re = 200$, and with an increase in aspect ratio the vortices shed from alternate sides of the ring

cross-section become more symmetrical, which results in a reduction in the inclination of the vortex street to the flow direction.

A previous study (Leweke & Provansal 1995) has proposed a relationship for the Strouhal–Reynolds number profile of the flow past rings as a function of aspect ratio. In this chapter, the previous relationship has been shown to be valid only for aspect ratios in the range $Ar \gtrsim 10$. A new relationship has been proposed in this study, and evidence has been presented which shows that the new relationship accurately describes the Strouhal–Reynolds number profiles for the flow past rings for a range of aspect ratios $Ar \gtrsim 3$.

In the present study, detailed measurements of the drag coefficient have been made for the flow past rings for the first time. The use of computational methods has permitted the precise measurement of the viscous friction and pressure components of the drag force, which have been analysed with respect to the total drag. This has enabled a solid understanding of the relationship between the pressure and viscous components of the drag coefficient to be determined for the flow past rings. In addition, the Reynolds number variation in the drag coefficient has been computed for the flow past a sphere and a circular cylinder, with an excellent agreement being found with previous experimental and computational measurements. This favourable comparison verified that the numerical method employed in this study accurately computes the drag coefficient.

Previous studies did not attempt to visualise the cross-section of the annular vortex street in the wakes behind rings. Instead, experimental dye visualisation was employed to capture the global wakes behind rings. The vortex street cross-section has been captured experimentally in the present work. This was achieved by illuminating dye in a plane through the centre of the wake with a thin laser sheet. To compare with the experimental dye visualisations, a computation of the wake was performed. The computation included simulated particles, which were injected into the flow field in order to mimic the entrainment of dye into the wake behind the ring. The computed and experimentally obtained wake visualisations confirmed the similarity between the vortex street in the wake behind a circular cylinder, and the annular vortex street in the wake behind a ring.

In the next chapter, results of a stability analysis of the axisymmetric flow past rings to non-axisymmetric instabilities is presented.

Chapter 4

Non-Axisymmetric Instabilities in the Flow past Rings

The detailed dye visualisation experiments of the wake of a sphere by Magarvey & Bishop (1961b,a), Magarvey & MacLatchy (1965) and Johnson & Patel (1999), indicate that the axisymmetric wake becomes unstable at $Re_{S2} \approx 210$. This instability was shown to lead to the development of a non-axisymmetric wake beyond this critical Reynolds number, which in turn was shown to undergo a further transition to unsteady flow at $Re_{S3} \approx 270$. Likewise, experiments have shown that the two-dimensional vortex street in the wake of a circular cylinder becomes three-dimensional beyond $Re_{C3} \approx 180$ (Williamson 1988a,b, 1996b).

Experimental observations of the flow past rings (Monson 1983; Miau *et al.* 1992) indicate that similar non-axisymmetric transitions occur in these flows. To date no computational studies have been reported in the literature for the flow past rings.

Previously, the classic linear stability analysis studies by Natarajan & Acrivos (1993) and Barkley & Henderson (1996) successfully predicted the critical Reynolds numbers and symmetry characteristics of the non-axisymmetric and three-dimensional instabilities in the wake of a sphere and a circular cylinder, respectively. In this chapter, a similar stability analysis technique (described in § 2.1.3) is employed to predict the non-axisymmetric instabilities in the flow past rings. The results of this study are presented in the following section. In addition, a detailed analysis of a previously unreported instability mode is included in this chapter.

Some of the results in this chapter have been published in Sheard *et al.* (2001, 2003c).

4.1 A Linear Stability Analysis of the Flow past Rings

Prior to presenting the results of the linear stability analysis, the applicability of predicted secondary instabilities to the physical flows around bluff bodies is discussed. The results of the stability analysis are presented over the remaining sections. In the first section, the stability of axisymmetric vortex streets is analysed, with results presented for rings with aspect ratios Ar = 4, 5, 10, 20 and 40. In the second section, the stability of steady wakes over the aspect ratio range $0 \leq Ar \lesssim 4$ is examined. A third section presents the results of a non-axisymmetric computational study used to determine the secondary non-axisymmetric transitions in the wakes behind rings in the range $0 \leq Ar \lesssim 4$.

4.1.1 A Comment on Predicted Secondary Instabilities

Secondary instabilities are instabilities which are predicted to occur at higher Reynolds numbers than the first-occurring (or primary) instability in a wake. The critical Reynolds numbers predicted for secondary instabilities should be considered qualitative estimates at best, as the evolution of the primary instability alters the flow from the axisymmetric base flow employed in the stability analysis. Barkley & Henderson (1996) offer a useful discussion of the limitations of linear stability theory. To understand these limitations in relation to the present work, the predictions of secondary instabilities in the wakes of a circular cylinder and a sphere are discussed below.

With an increase in the Reynolds number, the first-occurring three-dimensional mode in the flow past a circular cylinder was predicted to be Mode A by Barkley & Henderson (1996). At a higher Reynolds number, they predicted a secondary instability, Mode B. The topological predictions of the Mode B transition from the stability analysis compared favourably with experimental flow visualisations of the saturated mode (Williamson 1988b, 1996b) in terms of both the spanwise wavelength of the three-dimensional structures and their spatio-temporal symmetry. Despite the accurate predictions relating to the structure of this second instability, experimental observations (Williamson 1988b) show evidence of Mode B structures in the wake at Reynolds numbers as low as Re = 230, 11% below the predicted transition Reynolds number from the stability analysis (presumably due to the discrepancy between the two-dimensional base flow and the actual three-dimensional wake).

A discrepancy between the prediction of the secondary three-dimensional transition

for the flow past a sphere and computations of the non-axisymmetric wake can also be shown. Stability analysis performed by Natarajan & Acrivos (1993) highlights a second mode following the initial steady three-dimensional transition in the wake of the sphere. This transition, from a steady three-dimensional flow to an unsteady three-dimensional flow, was predicted to occur at $Re_{S3} = 277.5$. Recent numerical computations of the flow past a sphere by Thompson *et al.* (2001a) computed $Re_{S3} \approx 272$. The topology of the transition was in agreement with the stability analysis, however the critical Reynolds number for the transition was 2% lower in the computed wake than the Reynolds number predicted from the stability analysis. It may be inferred that the topology of secondary modes in the wake of the ring will be predicted accurately by the stability analysis, however only qualitative estimates of the critical Reynolds numbers relating to secondary transitions can be made, generally accurate to within 15% of the actual values as determined from non-axisymmetric computations.

Non-axisymmetric instability modes of the wakes behind rings with aspect ratio $Ar \geq 5$ are presented in the next section. Later, smaller aspect ratios will be considered, where the non-axisymmetric instabilities evolved from steady base flows.

4.1.2 Instabilities of the Vortex Street for $Ar \geq 5$

The spanwise wavelengths and critical Reynolds numbers of the Mode A and B transitions for the flow past a circular cylinder (Barkley & Henderson 1996) were used as a guide for the present stability analysis. Barkley & Henderson predicted that the Mode A instability had a spanwise wavelength of $\lambda_d \approx 3.96d$, and became unstable at $Re_c \approx 188.5$. They also predicted that the Mode B instability had a spanwise wavelength of $\lambda \approx 0.822d$, and became unstable at $Re_c \approx 259$. In the present study, Floquet multipliers were calculated at Reynolds numbers in the vicinity of the critical transitions of the dominant modes, and polynomial interpolation was used to refine the predicted critical Reynolds numbers and spanwise wavelengths of the instabilities.

Following a comprehensive computational study, three real instability modes were identified in the vortex streets behind rings with $4 \leq Ar \leq 40$. Two of these modes agreed favourably with the Mode A and Mode B instabilities in the wake of a circular cylinder (Barkley & Henderson 1996), in terms of the dominant azimuthal wavelengths, spatio-temporal symmetries, and critical Reynolds numbers of the instability modes. The third mode, referred to as Mode C in this study, had interesting symmetry proper-

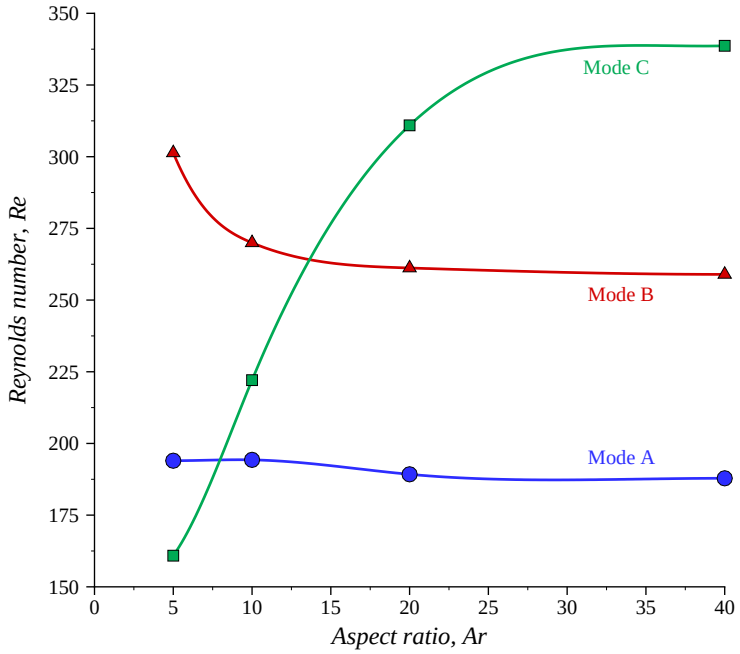

FIGURE 4.1: Critical Reynolds numbers for the transitions to the asymmetric vortex shedding modes for rings with aspect ratios $Ar \geq 4$. The Mode A transition is coloured blue, the Mode B transition is coloured red, and the Mode C transition is coloured green. For guidance, cubic splines are fitted to the computed data points.

ties that will be discussed later. Profiles of the predicted transition Reynolds numbers for these non-axisymmetric instability modes of the vortex streets in the wakes behind rings as a function of aspect ratio are shown in figure 4.1.

For the flow past rings with aspect ratios $Ar \gtrsim 4$, the fastest-growing modes for the predicted Mode A and B transitions had azimuthal wavelengths which corresponded closely with the respective wavelengths for the corresponding instability modes in the flow past a circular cylinder. However, the fastest-growing mode of the predicted Mode C instability had an azimuthal wavelength in the range $1.6d \lesssim \lambda_d \lesssim 1.7d$. The variation in Floquet multiplier with azimuthal wavelength in the vicinity of the critical Reynolds numbers for the three wake instabilities is presented in figure 4.2, for the wake behind a ring with $Ar = 10$.

The symmetry and structure of these three predicted instability modes is analysed over the following sections.

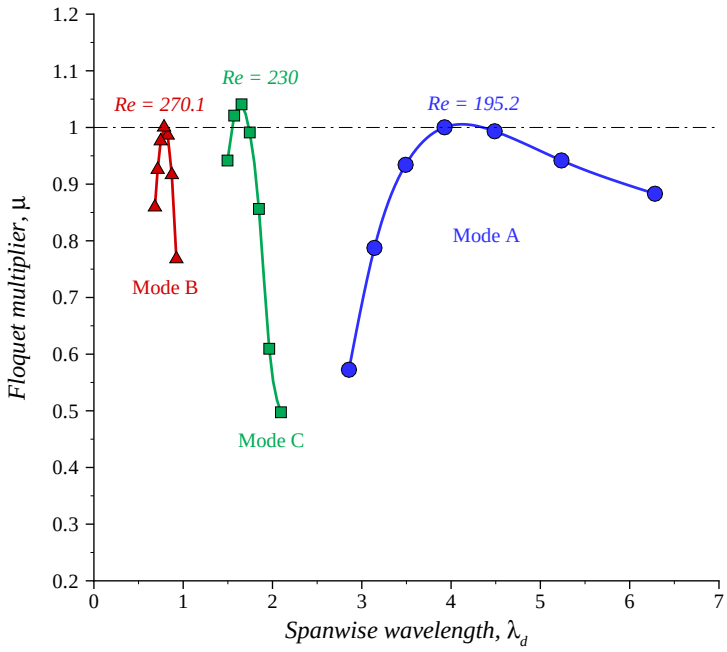

FIGURE 4.2: Floquet multiplier profiles at Reynolds numbers in the vicinity of the critical Reynolds numbers for each of the instabilities in the wake behind a ring with $Ar = 10$. The modes are coloured as per figure 4.1.

4.1.2.1 The Mode A Instability

The numerical stability analysis of the flow past a circular cylinder by Barkley & Henderson (1996) predicted that the spanwise wavelength of the Mode A instability was $3.96d$. The fastest-growing azimuthal wavelength of the corresponding Mode A instabilities for the flow past rings with $Ar = 20$, 40, 100 and 1000 was within 1.1% of the straight circular cylinder wavelength. At $Ar = 5$, however, the predicted wavelength was $4.5d$, which is 14.5% larger than the wavelength of the Mode A instability in the flow past a circular cylinder. In addition, at $Ar = 4$, the predicted wavelength was $4.2d$. Each of these rings became critically stable in the Reynolds number range $188 \leq Re \leq 194$. The predicted critical Reynolds number for the Mode A instability in the flow past rings with $Ar \geq 20$ was within 1.0% of the critical Reynolds number in the flow past a circular cylinder. The critical Reynolds number increased with a decrease in aspect ratio until at $Ar = 5$ it occurred at a Reynolds number 3% higher than the critical Reynolds number for the flow past a circular cylinder. Visualisation of the streamwise vorticity of the perturbation fields of the dominant Floquet modes

for these wakes (figure 4.3(a) for $Ar = 5$ and figure 4.4(a) for $Ar = 20$) reveal identical topology and time-symmetry, and show a similar distribution of vorticity to the Mode A instability predicted by Barkley & Henderson (1996). The perturbation field of the instability maintained the same single-period ($1T$) symmetry as the Mode A wake, and much of the perturbation streamwise vorticity is present within the vortex cores of the base flow vortex street.

4.1.2.2 The Mode B Instability

For the flow past rings with $Ar \geq 5$, an instability was predicted which had characteristics consistent with the Mode B instability in the flow past a circular cylinder. The critical Reynolds number for this instability was predicted to occur at $Re = 301$ for the flow past a ring with $Ar = 5$, and for the flow past rings with $Ar \geq 20$, the critical Reynolds number was predicted to occur at $Re \approx 258$, which is within 1% of the critical Reynolds number for the Mode B instability in the flow past a circular cylinder. For the flow past rings with $Ar \geq 5$, the azimuthal wavelength of the Mode B instability was within 2.5% of the spanwise wavelength of the Mode B instability in the flow past a circular cylinder.

The Strouhal–Reynolds number profiles for rings found in experiment by Leweke & Provansal (1995) are continuous over the range of Reynolds numbers for which the Mode B instability occurs in the wake of a circular cylinder. However, they do observe a change in gradient of the Strouhal–Reynolds number profiles in the Reynolds number range $255 < Re < 310$ consistent with critical Reynolds numbers for the Mode B instability in the present study.

The symmetry of the Mode B instability is again of the $1T$ type, consistent with the predictions of Barkley & Henderson (1996) and Robichaux *et al.* (1999). Figure 4.3(b) and figure 4.4(b) show plots of the streamwise vorticity of the Mode B instability for rings with aspect ratios $Ar = 5$ and $Ar = 20$, respectively. Small portions of the plots in figure 4.3(b) and figure 4.4(b) appear slightly under-resolved, owing to the interpolation of the computed vorticity over the mesh during post-processing. Despite the relatively high Reynolds number for the computation, and the higher spatial resolution required to resolve the perturbation field, the overall structure of the vorticity field is well defined, indicating good convergence of the computations.

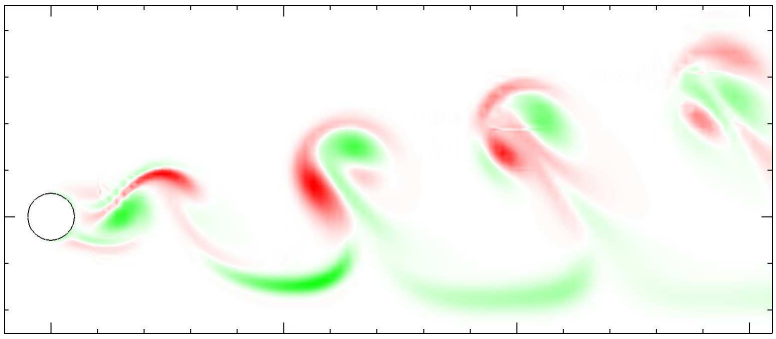

(a) Mode A: $Re = 200$ and $\lambda_d \approx 3.93d$.

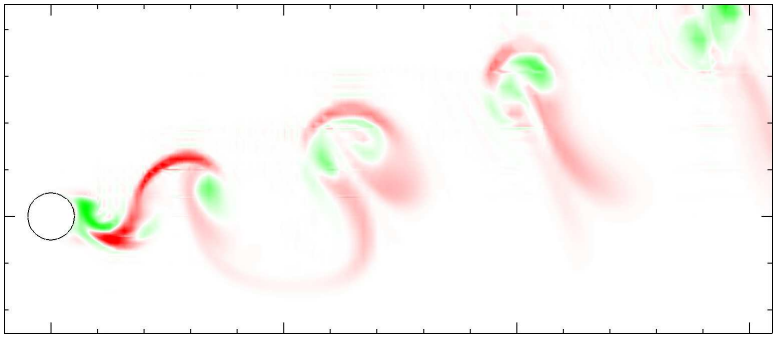

(b) Mode B: $Re = 305$ and $\lambda_d \approx 0.785d$.

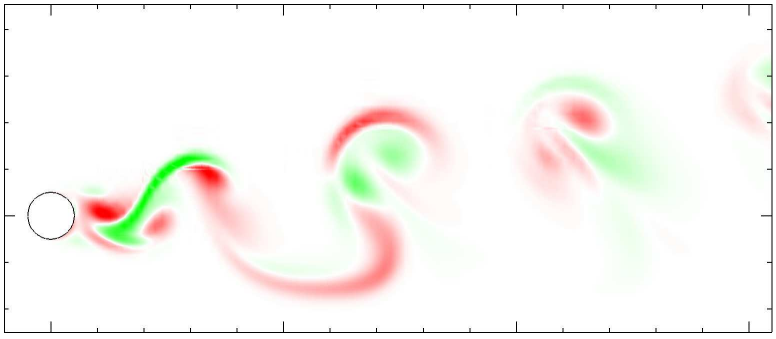

(c) Mode C: $Re = 175$ and $\lambda_d \approx 1.57d$.

FIGURE 4.3: Streamwise vorticity of the perturbation fields of the dominant azimuthal modes in the flow past a ring with $Ar = 5$. A portion of the z–r plane of the flow field is shown, and the circular ring cross-section is located at the left of each frame. The axis of symmetry is located below each frame, the direction of flow is from left to right, and the streamwise vorticity contours are between -0.5 (red) and 0.5 (green).

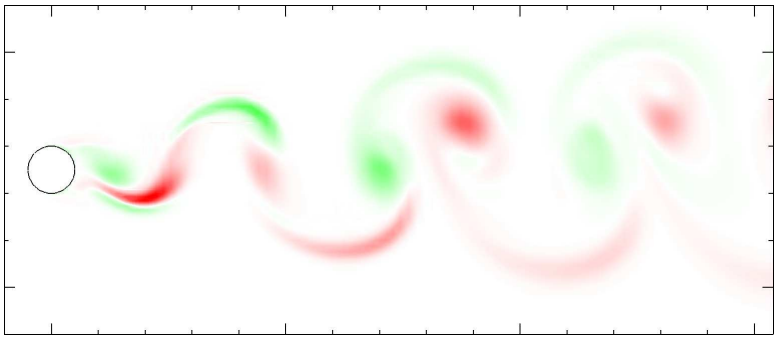

(a) Mode A: $Re = 200$ and $\lambda_d \approx 3.93d$.

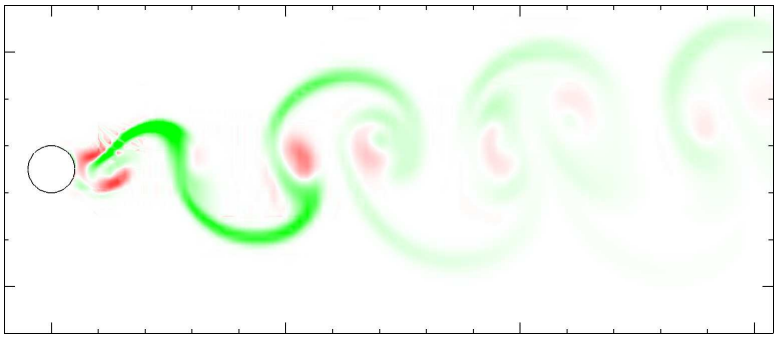

(b) Mode B: $Re = 265$ and $\lambda_d \approx 0.795d$.

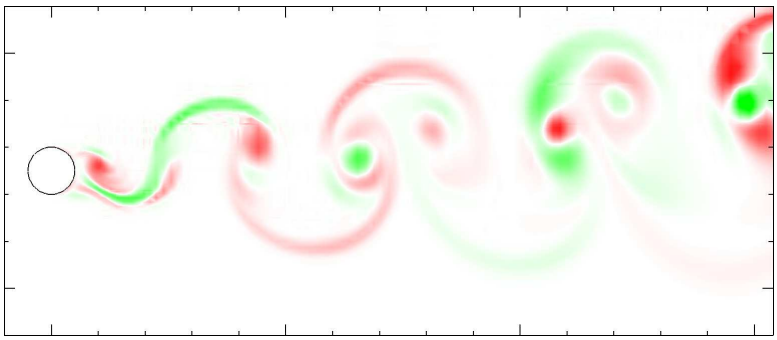

(c) Mode C: $Re = 325$ and $\lambda_d \approx 1.65d$.

FIGURE 4.4: Streamwise vorticity of the perturbation fields of the dominant azimuthal modes in the wake behind a ring with $Ar = 20$. The orientation of the plots and the streamwise vorticity contour shading are as per 4.3.

4.1.2.3 The Mode C Instability

The fastest-growing azimuthal wavelength of the predicted Mode C instability was computed to lie between $1.6d$ and $1.7d$ for the flow past rings with $4 \leq Ar \leq 40$. Figure 4.1 shows that this mode is predicted to occur at higher Reynolds numbers as the ring aspect ratio is increased. For rings with $Ar \lesssim 8$, it is predicted to be the first-occurring non-axisymmetric transition mode in the wake. Figure 4.1 shows that at $Ar = 5$, the Mode C transition is the primary non-axisymmetric instability, at $Ar = 10$ it is the secondary non-axisymmetric instability, and at $Ar = 20$ it is the tertiary non-axisymmetric instability.

Streamwise vorticity plots of the perturbation field of the Mode C instability are presented in figure 4.3(c) and figure 4.4(c) for the flow past rings with $Ar = 5$ and $Ar = 20$, respectively. These plots show that the mode is characterised by a two-period ($2T$) symmetry, with the sign of the perturbation field vorticity alternating between each successive vortex roller pair that convect downstream. The observation of this $2T$ symmetry, combined with the converged Floquet multipliers obtained for the Mode C instability, suggest that the instability is a real subharmonic Floquet mode.

The predicted azimuthal wavelength of the Mode C instability that was computed for the flow past rings corresponds to the predicted wavelengths of the complex-conjugate Floquet modes in the wakes of both square cylinders (Robichaux *et al.* 1999; Blackburn & Lopez 2003), and the perturbed wakes of circular cylinders (Zhang *et al.* 1995). The spanwise wavelength of the instability predicted by Zhang *et al.* (1995) was approximately $2d$, which is 17% greater than the present result. Similarly, however, they also over-predicted the wavelengths for the Mode A and Mode B instabilities by between 10% and 20%.

The wavelength of the complex-conjugate Mode S instability in the wake of a square cylinder (Robichaux *et al.* 1999) was around 50% greater than the present value. They based their length scale on the side length of the square cross-section of the cylinder, whereas the predicted Mode A and B instabilities and the vortex street scaled with the diagonal length. The spanwise wavelength of their predicted Mode S instability is within 10% of the Mode C instability predicted in the present study for the flow past rings if their mode is scaled with the diagonal length. Despite these similarities in wavelength, the present Mode C instability and the Mode S instability in the square cylinder wake evolve from fundamentally different Floquet modes, which will be discussed later.

With a decrease in aspect ratio, the asymmetry between the inner and outer vortex rollers of the underlying vortex street is increased. This results in a loss of the reflective symmetry of the vortex street (i.e. the two-dimensional vortex street in the wake of a circular cylinder at a given time is identical to the same wake shifted in time by half a period, and reflected about the wake centreline). The Mode C instability is predicted to become more unstable with an increase in the asymmetry of the vortex street. This topic is treated in depth in § 4.2, but it should be noted that as part of the present study an attempt was made to find a real instability mode in the wake of a circular cylinder corresponding to the Mode C instability. Despite a careful investigation of the wavelengths in the vicinity of the Mode C instability, only complex-conjugate modes were obtained, consistent with the analysis of Blackburn & Lopez (2003).

4.1.3 Primary Instabilities in the Wakes for $0 \leq Ar < 4$

In this section, the wakes of numerous rings with aspect ratios over the range $0 \leq Ar < 4$ are studied. Careful investigation reveals that at a critical aspect ratio of $Ar \approx 3.9$, the critical Reynolds numbers for the primary Hopf and non-axisymmetric transitions in the flow past rings intersect. Thus for aspect ratios in the range $0 \leq Ar \lesssim 3.9$, the transition to non-axisymmetry occurs at a lower Reynolds number than does the transition to unsteady flow.

The stability of several azimuthal mode numbers was computed for the flow past rings to ascertain the dominant azimuthal mode number of the non-axisymmetric instability at each of the aspect ratios considered. The predictions of the critical Reynolds numbers of these instabilities were refined by polynomial interpolation. In figure 4.5, the computed critical Reynolds numbers are plotted against aspect ratio for the flow past rings with $Ar \lesssim 4$. The critical Reynolds number profiles in figure 4.5 show that three distinct flow regimes exist over the aspect ratio range $0 \leq Ar < 4$. As labelled in the figure, these regimes are hereafter referred to as Mode I, Mode II and Mode III, and occupy the aspect ratio ranges $0 \leq Ar \lesssim 1.6$, $1.6 \lesssim Ar \lesssim 1.7$ and $1.7 \lesssim Ar \lesssim 3.9$, respectively.

The properties of the instabilities in each flow regime are unique to each flow regime, and will be discussed in the following sections. In figure 4.6, plots of the streamwise vorticity of the perturbation fields of the instability modes are presented for each of the flow regimes under consideration.

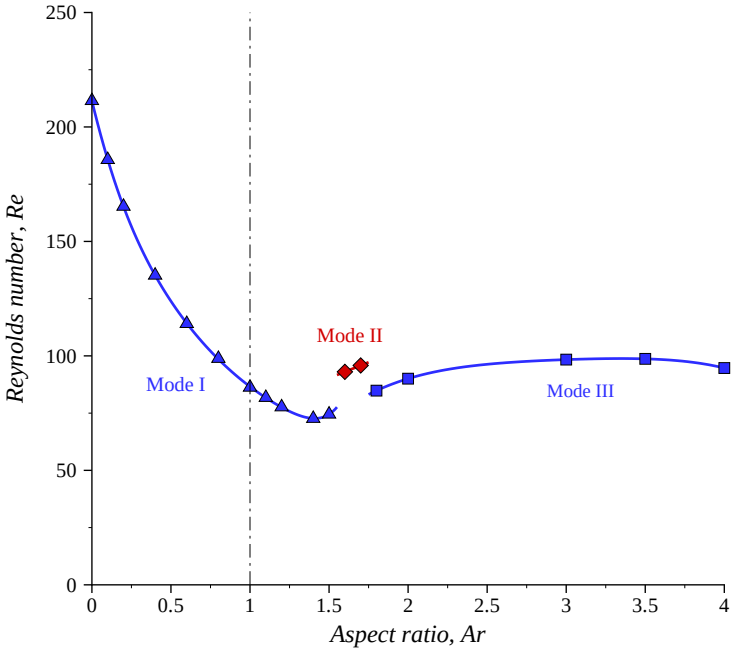

FIGURE 4.5: Asymmetric transition profile for rings with aspect ratios $0 \leq Ar < 4$. The point at which the axial hole appears is marked by the vertical dashed line at $Ar = 1$. The regular Mode I and mode III transitions are coloured blue, and are represented by triangles and squares, respectively. The Hopf Mode II transition is coloured red, and is represented by diamonds.

4.1.3.1 The Mode I Flow Regime ($0 \leq Ar \leq 1.5$)

The Mode I regime consists of a regular (i.e. steady–steady) transition, followed by a Hopf transition at higher Reynolds numbers. The stability analysis formulation employed to compute these modes suppressed all but the dominant mode of a given wavelength. Therefore the secondary Hopf transitions were determined by measurement of the unsteady transient decay from non-axisymmetric computations, which are presented later.

The perturbation field corresponding to the regular Mode I instability is analogous to the regular non-axisymmetric transition mode in the flow past a sphere. In figure 4.6(a), the regular Mode I transition in the flow past a sphere is presented, which corresponds favourably with the predicted mode from Natarajan & Acrivos (1993) and Tomboulides *et al.* (1993). In figures 4.6(b) and 4.6(c), plots which show both a closed and an open ring, respectively, in the Mode I regime are included. The perturbation field is almost identical between figures 4.6(a–c).

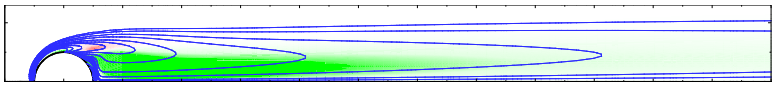

(a) Sphere wake regular Mode I transition ($Ar = 0$, $Re = 211.5$).

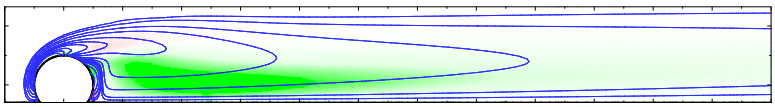

(b) Regular Mode I transition (closed ring, $Ar = 0.6$, $Re = 114$).

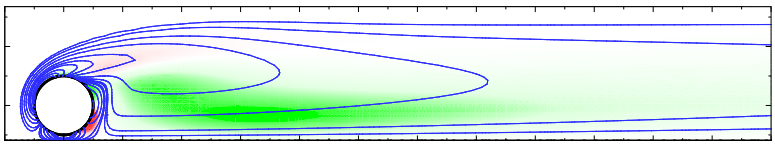

(c) Regular Mode I transition (open ring, $Ar = 1.2$, $Re = 77.7$).

FIGURE 4.6: Plots of the base flow vorticity (arbitrary blue contour lines), and the streamwise vorticity of the perturbation field (red negative and green positive vorticity) of the primary instability for rings with $0 \leq Ar \leq 3$.

Throughout the aspect ratio range of the Mode I regime, a rapid decrease in transition Reynolds number is experienced with an increase in aspect ratio. The minimum critical Reynolds number reached is $Re = 72.6$ at $Ar = 1.4$. The steady decrease in the critical Reynolds number from $Re = 212$ at $Ar = 0$ indicates that the mode scales on the outer ring diameter $D + d$ rather than the cross-section diameter d. For example, the critical Reynolds number for the regular Mode I transition in the flow past a ring with $Ar = 1.4$ based on a length scale $D + d$ is $Re_{D+d} \approx 174$, which is within 18% of the critical Reynolds number for the regular transition in the flow past a ring with $Ar = 0$.

The critical Reynolds number variation of the regular Mode I transition in figure 4.5 is continuous through $Ar = 1$. This shows that the emergence of the axial hole for open rings, and the subsequent detachment of the recirculation bubble have no discontinuous influence on the transition, as shown by the similarity between the perturbation fields in figures 4.6(b) and 4.6(c). This continuity is observed as the size and position of the downstream recirculation region remain consistent as the aspect ratio is increased through $Ar = 1$. The large scale of the recirculation bubble when compared to the small scale of the axial ring hole explains this computed behaviour. Experiments show that for

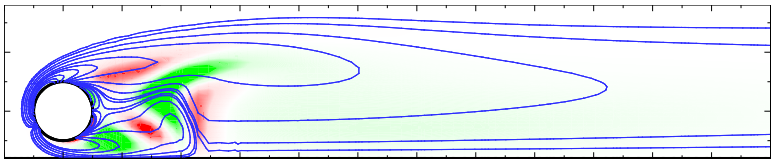

(d) Hopf Mode II transition ($Ar = 1.6$, $Re = 93.0$).

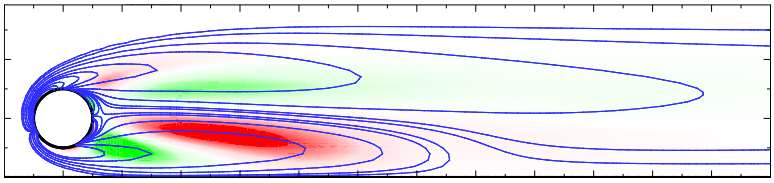

(e) Regular Mode III transition ($Ar = 2$, $Re = 90.1$, $m = 1$).

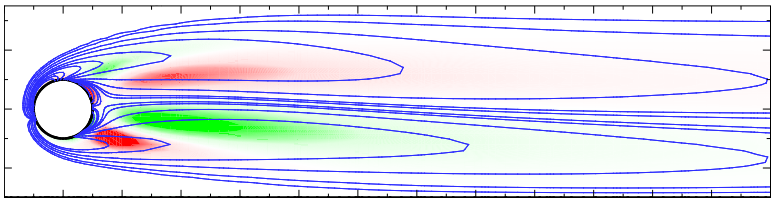

(f) Regular Mode III transition ($Ar = 3$, $Re = 98.4$, $m = 2$).

FIGURE 4.6: Continued.

the flow past a sphere, the recirculation bubble becomes unstable to non-axisymmetric perturbations. This instability shifts the recirculation bubble in a transverse direction from the axis of symmetry in the flow, which creates the classic double-threaded wake (Magarvey & Bishop 1961b; Johnson & Patel 1999; Thompson *et al.* 2001a).

4.1.3.2 The Mode II Flow Regime ($1.6 \leq Ar \leq 1.7$)

In the Mode II regime, a single non-axisymmetric Hopf transition was predicted. A plot of the perturbation field for the instability is presented in figure 4.6(d). The explanation for the suppression of a regular transition over this small range of aspect ratios, which allows the steady axisymmetric wake to experience such a curious spontaneous transition to an unsteady non-axisymmetric wake, is linked to the increased influence of the hole in the ring for an increase in aspect ratio.

The effect of the axial hole on the transitions becomes apparent at aspect ratios $Ar \geq 1.6$, when the size of the hole is of the same order as the cross-section of the ring. The base flow field is steady at this transition, and the perturbation field is also steady to about $1d$ downstream of the ring cross-section. Further downstream a gentle

oscillation of the perturbation field was observed, in the form of vorticity being shed from the tail of the wake. This oscillation had a Strouhal frequency $St = 0.00705$ at the critical Reynolds number for the transition. The experimentally measured Strouhal frequency for the vortex-loop shedding from a sphere by Magarvey & Bishop (1961a) was found to be approximately 12 times this value.

The suppression of a regular mode in the Mode II regime is best explained in terms of the base flow wake structure. The base flow vorticity contours lines for the Mode II Hopf transition in figure 4.6(d) indicate that the fluid passing through the hole travels a complex path downstream, due to the strong inner vortex within $2d$ of the ring. In fact, the initially trajectory of the fluid is aligned with the axis, however it recirculates back up to the leeward surface of the ring, before being deflected around the axial recirculation bubble, which is displaced approximately $2d$ downstream. Over the Mode II aspect ratio range, the attached vortex located downstream of the ring hole has altered the wake to the extent that the regular Mode I transition is suppressed. The vortex is not sufficiently large in the Mode II regime to permit the regular Mode III instability to occur (as discussed in the next section). Hence no regular modes appear prior to the critical Reynolds number for the non-axisymmetric Mode II Hopf transition.

In order to understand the nature of the Mode II transition, a study of the stability of the flow past a ring with $Ar = 1.6$ is discussed, and a plot of the Floquet multipliers for the fastest-growing $m = 1$ mode, which were computed in the wake with Reynolds number, is presented in figure 4.7. The axisymmetric base flow is absolutely stable to the primary Floquet mode (a real mode corresponding to a regular asymmetric transition of the wake). The highest Floquet multiplier for this mode is $\mu \approx 0.92$, for $Re \approx 70$, always below the neutral stability limit (i.e. $\mu < 1$). A complex-conjugate pair of Floquet multipliers (corresponding to a non-axisymmetric Hopf transition) is the first Floquet mode to become unstable (i.e. $\mu > 1$). This mode is unstable for $Re \gtrsim 94$, and is characterised by a periodic perturbation field. The plot in figure 4.7 confirms that the Mode II transition occurs through a non-axisymmetric Hopf transition.

4.1.3.3 The Mode III Flow Regime ($1.8 \leq Ar < 4$)

The regular Mode III transition arises when the recirculating vortex ring from the rear of the body becomes unstable, as shown in figures 4.6(d–e). This transition occurs over the aspect ratio range $1.8 \lesssim Ar \lesssim 3.9$.

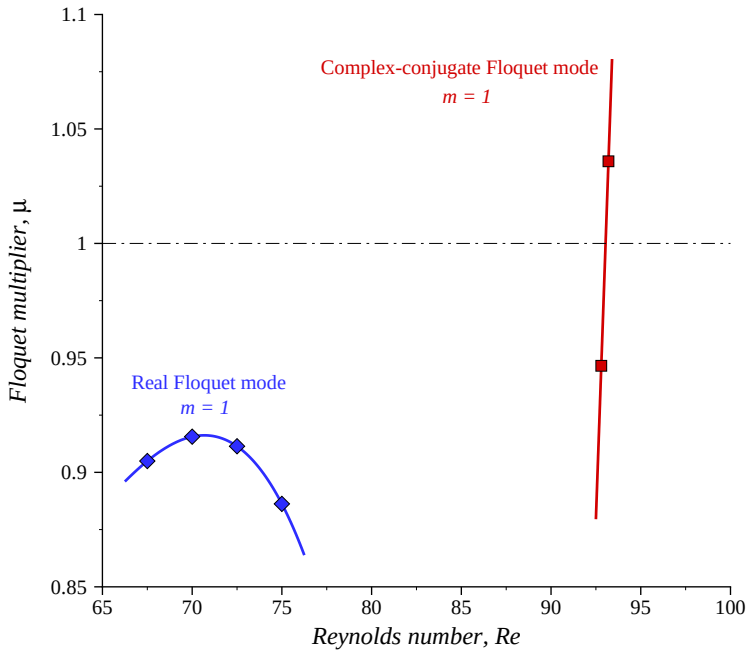

FIGURE 4.7: The two dominant non-axisymmetric Floquet modes with $m = 1$ for the flow past a ring with $Ar = 1.6$ with an increase in Reynolds number. The absolutely stable real mode is represented by blue diamonds, and the complex-conjugate pair Floquet mode (unstable for $Re \gtrsim 94$) is represented by red squares. The neutral stability limit is indicated by a dotted line.

The azimuthal mode number of the regular Mode III transition at $Ar = 2$ and $Ar = 3$ are $m = 1$ and $m = 2$, respectively. These transitions are both classified on the regular Mode III transition branch, as the corresponding axisymmetric base flow scales on the ring cross-section (rather than the outer ring diameter as per the Mode I transition). Hence, the azimuthal wavelength of the Mode III instability also scales with the cross-section diameter d, and the azimuthal mode number increases with aspect ratio to maintain the azimuthal wavelength. It is important to point out that in terms of the classification of the mode, the perturbation fields are consistent between the flows with $Ar = 2$ and 3, despite the different mode numbers $m = 1$ and 2 of the instability. In figure 4.6(e), the perturbation field of the regular Mode III transition with $Ar = 2$ and $m = 1$ is presented, and in figure 4.6(f), the perturbation field of the regular Mode III transition with $Ar = 3$ and $m = 2$ is presented.

The dominant azimuthal mode numbers of the instabilities at different aspect ratios are summarised in table 4.1. Both the primary asymmetric instability and the secondary

Aspect ratio range	Primary instability m	Secondary instability m
$0 \leq Ar \leq 2$	$m = 1$	$m = 1$
$3 \leq Ar \leq 3.5$	$m = 2$	$m = 2$

TABLE 4.1: Predicted azimuthal mode number of transition modes in the wakes behind rings with $Ar < 4$.

instability are included.

4.1.4 Secondary Instabilities in the Wakes for $0 \leq Ar < 4$

The critical Reynolds numbers for the secondary instabilities in the Mode I and III regimes were determined by computing the decay rate of unsteady transients in non-axisymmetric computations. In this respect, the critical Reynolds numbers that have been obtained over aspect ratios $0 \leq Ar < 1.6$ and $1.7 < Ar \lesssim 3.9$ correspond to the computed transition to unsteady non-axisymmetric flow, and not the predicted critical Reynolds number based on the stability of an axisymmetric base flow.

The computed critical Reynolds numbers for the secondary transition in the flow past rings in the Mode I, III regimes are presented in figure 4.8. The secondary transitions are computed to be Hopf transitions, and hence the predicted critical Reynolds numbers in Mode II regime are included. For reference, the predicted critical Reynolds numbers for the regular Mode I and III transitions are also provided in the plot. For the flow past a sphere, a critical Reynolds number for the Hopf transition of $Re_{S3} = 272.2$ was obtained, in close agreement with previous studies (Johnson & Patel 1999; Tomboulides & Orszag 2000; Ghidersa & Dušek 2000; Thompson *et al.* 2001a).

The plot of the regular and Hopf transitions in the flow past rings with $0 \leq Ar \leq 4$ in figure 4.8 confirms that the intersection between the non-axisymmetric and Hopf transitions occurs for $Ar \approx 3.9$.

4.2 The Subharmonic Instability: Mode C

In this section, the Mode C instability will be closely examined to verify that it is a subharmonic instability, and a detailed description of the evolution of the instability over two periods of the base flow will be provided to ascertain the mechanism responsible for the subharmonic behaviour of the instability.

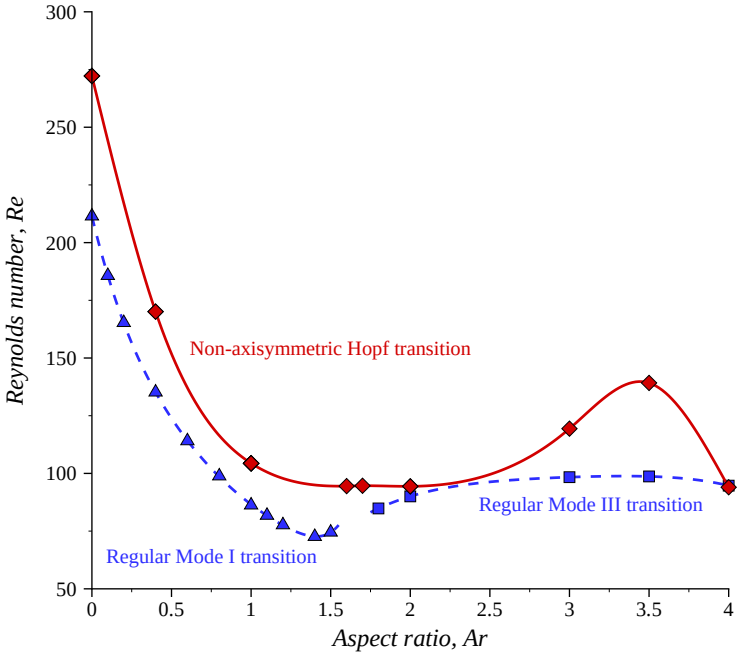

FIGURE 4.8: Critical Reynolds number profile of the secondary non-axisymmetric Hopf transition in the wakes of rings with $Ar < 4$, represented by a red line. The regular Mode I and Mode III transitions are indicated by blue dashed lines for reference.

4.2.1 Evidence Supporting Subharmonic Classification

Results are presented here from a stability analysis that was undertaken for the flow past a ring with $Ar = 5$ at $Re = 170$. The perturbation field for a mode with $m = 10$ symmetry (giving $\lambda_d \approx 1.6d$) was computed to saturation, where the Floquet multipliers had converged to better than 7 significant figures. Figure 4.9 provides evidence to support the observation that the Mode C instability is a subharmonic mode. Recall that a subharmonic mode exists when the dominant Floquet mode of the system occurs with $\mu = -1$. This means that the mode alternates in sign every period, which results in a doubling of the period of the mode. The absence of any oscillation of the computed Floquet multipliers around a mean value also suggests that the mode was real (i.e. the Floquet mode contains no imaginary component, see Blackburn & Lopez 2003). This explains the observations in figure 4.9, where both an absolutely convergent Floquet multiplier is observed for the Mode C instability, and perturbation fields obtained exactly one base flow period apart are opposite in sign.

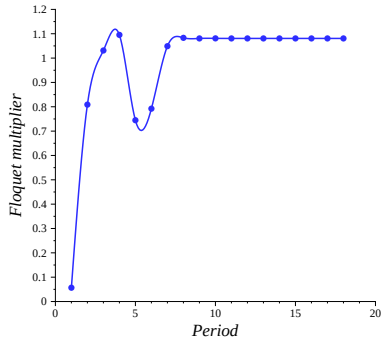

(a) Floquet multiplier convergence for the Mode C instability.

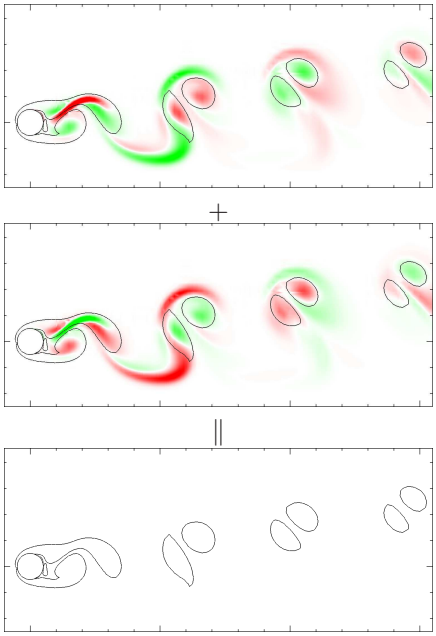

(b) Summation of the perturbation fields at arbitrary times t_i and $t_i + T$, which results in a zero-velocity perturbation field.

FIGURE 4.9: Verification that the Mode C instability is subharmonic. In (a), the convergence of the Floquet multiplier suggests that the mode has no imaginary component, and in (b), the perturbation field is observed to alternate in sign from one period to the next.

4.2.2 Perturbation Field Evolution Characteristics

In this section, plots of the spanwise vorticity of the perturbation field of the Mode C instability computed in the flow past a ring with $Ar = 5$ are analysed over two periods of the base flow, to determine the mechanism responsible for the formation of a subharmonic instability in the wake.

In figure 4.10, the variation in the instantaneous growth rate is plotted over two base flow periods. The base flow period T_{2D} is abbreviated to T in the present work. It is useful to compare the instantaneous growth rate with the perturbation fields at various times, which are presented in figure 4.11. Consistent with a subharmonic instability, the growth rate variation is periodic with the base flow, whereas the perturbation field of the instability alters in sign each period.

The base flow vorticity contours in figure 4.11 show that the asymmetry induced on the vortex street by the curvature of the ring has the effect of pairing each lower vortex

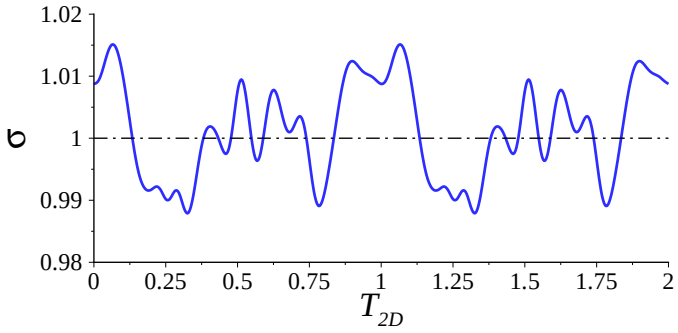

FIGURE 4.10: Variation in the growth rate over two base flow periods for the Mode C instability in the wake behind a ring with $Ar = 5$ at $Re = 170$.

roller to a previously shed upper roller. This phenomenon was observed in studies of the vortex shedding behind rings (Monson 1983; Leweke & Provansal 1995), and relates to the asymmetry induced by the curvature of the ring.

The pairing of the shed vortex rollers is driven by the extended attachment duration of the upper vortex roller (with negative vorticity) to the ring body, and a streamwise elongation of the vortex. A rapid evolution of a strong (positive vorticity) lower vortex roller occurs over a time $0.5T \lesssim t \lesssim 0.8T$. At this time, the pair of vortices is shed downstream, with the lower vortex closely following the upper vortex.

Initially, the strain field of the flow deforms both the upper and lower vortices that are shed (observe the pair of vortex rollers located approximately $3d$ downstream in figure 4.11(c) at $t = 0.5T$). As this pair of vortex rollers convect downstream (from $t = 0.5T$ to $t = 1T$), in figures 4.11(c–e), the upper vortex (further downstream) acquires a more circular shape, while the lower vortex (further upstream) remains strained in an elliptical shape. For times $t \gtrsim 0.5T$, elliptic instabilities evolve in this vortex pair. These elliptic instabilities may be identified by the counter-rotating perturbation field vortices within the enclosed elliptical vortex rollers (for a detailed discussion of elliptic instabilities of strained vortices refer to Bayly 1986; Landman & Saffman 1987; Williamson 1996b; Thompson *et al.* 2001b). A stronger elliptic instability persists in the lower vortex roller than in the upper vortex roller as the pair of cores convect downstream, due to this higher strain (see figures 4.11(d–f)).

At $t \approx 0.5T$ in figure 4.11(c), an elliptic instability may be observed in the elliptical core of the forming upper vortex roller, located within approximately $1d$ of the cross-section of the ring. The lower vortex roller strengthens to $t \approx 0.75T$ in figure 4.11(d),

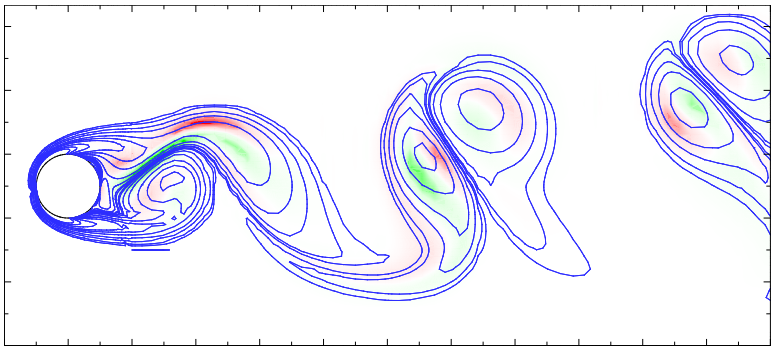

(a) $t = 0.0T$.

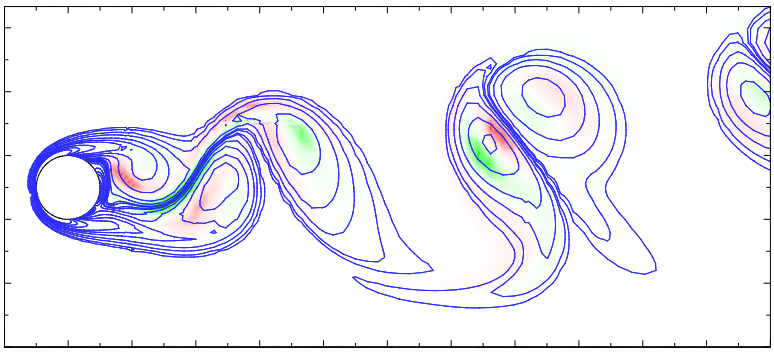

(b) $t = 0.25T$.

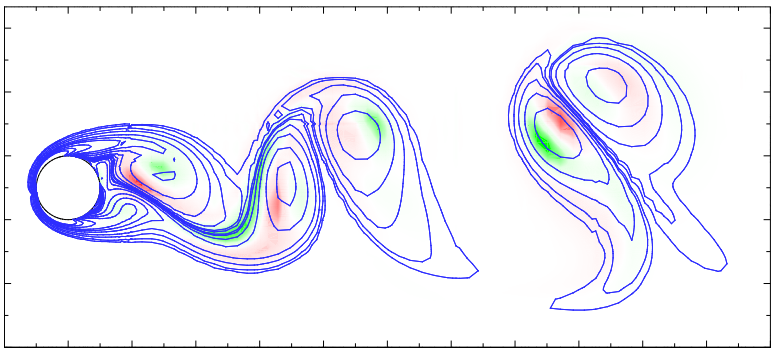

(c) $t = 0.5T$.

FIGURE 4.11: Evolution of the Mode C instability ($1T$ = one base flow period). The included graphs plot the instantaneous growth rate of the instability over time. Arbitrary blue contour levels show the base flow vorticity, and positive and negative spanwise vorticity of the perturbation is represented by green and red contours, respectively.

which causes the elliptic instability perturbations to shear in the upper vortex core, as the core loses its elliptical shape. A local clockwise rotation of the perturbation field occurs, and the negative component of spanwise vorticity is drawn between the upper and lower vortex cores.

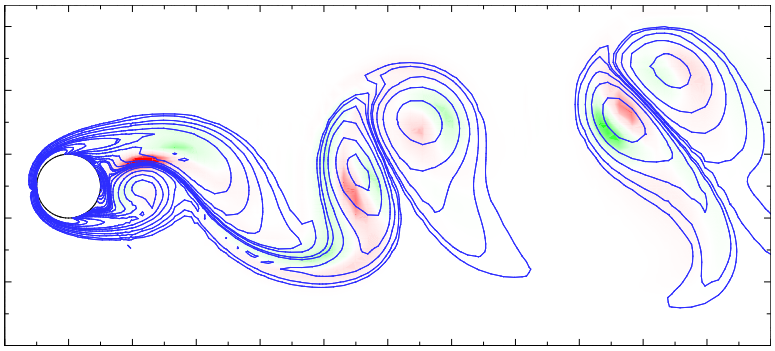

(d) $t = 0.75T$.

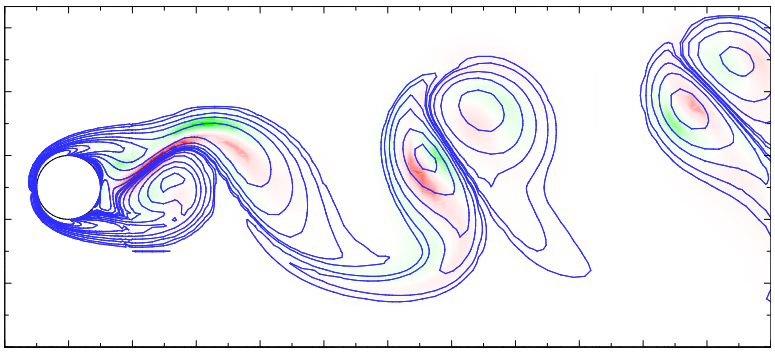

(e) $t = 1.0T$.

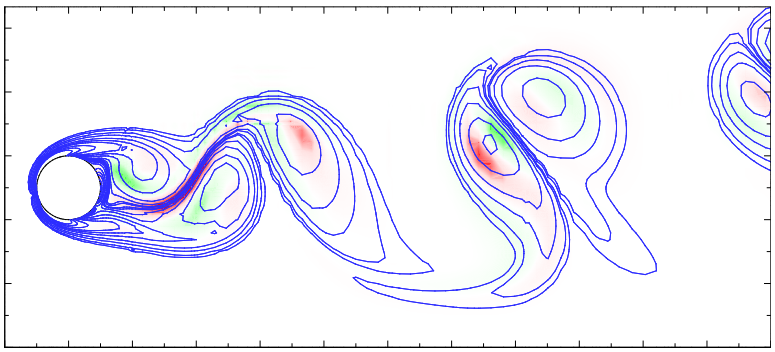

(f) $t = 1.25T$.

FIGURE 4.11: Continued.

As $t \to 1T$, the lower vortex roller increases in strength and detaches. Through this detachment, which may be observed over figures 4.11(e–f), the negative perturbation vorticity from the upper core that was forced between the upper and lower cores is stretched in an approximately diagonal direction between the cores. The corresponding positive perturbation field vorticity from the elliptic instability in the upper vortex core is also stretched alongside the band of negative vorticity. The positive vorticity band is located above the negative vorticity band, and hence is still contained within the upper

vortex core. As the upper vortex roller is shed, this positive vorticity band stretches from the upper side of the core of the shed roller, to the lower side of the newly forming upper vortex. As the base flow evolves, this band of perturbation field vorticity splits into two local regions of vorticity, with one contained in the shed upper vortex, and the other located within the newly forming upper vortex roller.

The location of this region of positive perturbation field vorticity corresponds to the location of the negative vorticity component of the elliptical instability that evolved in the upper roller from the previous shedding cycle of the base flow. Thus the sign of the perturbation field vorticity alternates for the second period, as the elliptical instability evolves through $t \approx 1.25T$, and hence a subharmonic instability is sustained, as can be observed by comparing the signs of the perturbation vorticity between figures 4.11(b) and 4.11(f), which are exactly one base flow period apart.

The instantaneous growth rate of the Mode C instability is highest at $t \approx 0.1T$. At this time the near-wake perturbation field consists of strong vorticity between the core of the shed lower vortex roller, and the newly forming upper vortex roller. A weak elliptical instability is present in the lower vortex at this time, and the band of perturbation field vorticity from the upper vortex roller is splitting prior to the formation of the evolution of the elliptical instability in the forming upper vortex.

4.3 The Limitations of Linear Stability Analysis

Thus far only axisymmetric computations and linear non-axisymmetric stability analysis have been performed. The stability analysis suggests that these axisymmetric wakes are unstable to non-axisymmetric disturbances in the flow beyond certain critical Reynolds numbers. Chapter 5 seeks to verify this prediction through non-axisymmetric computations employing a restricted computational domain in the azimuthal direction to isolate these pure non-axisymmetric modes. For rings with aspect ratios $Ar \leq 2$, computations will necessarily include the entire ring, as the azimuthal symmetry of the dominant non-axisymmetric modes for these rings is $m = 1$.

In this fashion, the extrinsic non-axisymmetric instabilities that are expected to exist in the wakes behind rings of larger aspect ratio, namely oblique vortex shedding modes and vortex dislocations (as observed by Leweke & Provansal 1995; Williamson 1989) are excluded from the non-axisymmetric computations. A study which employs computations with larger azimuthal domain sizes to include these effects is presented

in Chapter 6.

4.4 Chapter Summary

In this chapter, a linear stability analysis technique was employed to predict the previously unknown non-axisymmetric instabilities in the flow past rings.

A previous stability analysis was reported for the axisymmetric flow past a sphere by Natarajan & Acrivos (1993). Their study predicted that the wake behind a sphere is unstable to a non-axisymmetric instability with an azimuthal mode number $m = 1$, which was predicted to occur through a regular bifurcation at $Re = 210$. They also predicted a secondary non-axisymmetric instability with an azimuthal mode number $m = 1$, which was predicted to occur through a Hopf bifurcation at $Re \approx 277.5$.

Likewise, a stability analysis was reported for the flow past a circular cylinder by Barkley & Henderson (1996). Their study predicted that the wake behind a circular cylinder is unstable to a regular Mode A instability, with a spanwise wavelength of $\lambda \approx 3.96d$ at $Re = 188.5$. A second regular instability, Mode B, was predicted to occur with a spanwise wavelength of $\lambda \approx 0.822d$ at $Re \approx 259$.

Prior to the present study, no computations of the flow past rings have been reported. In the stability analysis reported in this chapter, three flow regimes were identified for the flow past rings over the aspect ratio range $0 \leq Ar \lesssim 3.9$. This range of aspect ratios represents flows which are predicted to experience a non-axisymmetric instability at Reynolds numbers below the Hopf transition Reynolds number for axisymmetric vortex shedding. These three flow regimes have been classified as Mode I, II and III. The predicted bifurcation scenarios and characteristics of the instability modes are unique to each flow regime. In the Mode I regime, a predicted regular non-axisymmetric transition is followed by a Hopf transition, due to instabilities of the axisymmetric recirculation bubble in the wake. In the Mode II regime, a non-axisymmetric Hopf transition is predicted to occur. In the Mode III regime, a predicted regular non-axisymmetric transition is followed by a Hopf transition, due to instabilities of the annular recirculation bubble behind the open ring.

In contrast to the flow regimes predicted in the flow past rings with aspect ratios $0 \leq Ar \lesssim 3.9$, the annular vortex streets in the flow past rings with aspect ratios $Ar \gtrsim 4$ are predicted to be unstable to non-axisymmetric perturbations. In the present study, two real instability modes are predicted which have characteristics consistent with the

Mode A and Mode B instabilities in the wake of a circular cylinder. An additional mode has been discovered, which is referred to as Mode C in the present study. The Mode C instability is predicted to occur through a subharmonic bifurcation, and its critical Reynolds number increases with an increase in aspect ratio.

In previous studies, the Mode A and B instabilities in the wake of a circular cylinder have been analysed in detail. These studies predict that the Mode A instability evolves primarily from an elliptic instability in the shed vortex rollers. Conjecture exists regarding the instability mechanism for Mode B, with a hyperbolic instability of the braid region of the vortex street being suggested. As the subharmonic Mode C instability has not previously been reported, a detailed analysis of the perturbation field of the instability over a shedding cycle is presented. This analysis shows that the asymmetric shedding of the annular vortex street is responsible for inciting the subharmonic instability. Perturbation field vorticity evolves in the attached outer vortex behind the ring through an apparent elliptic instability. This vorticity convects into the region between the vortex rollers during the detachment phase of the shedding process. The alternation in sign from period to period which characterises a subharmonic instability occurs as remnants of opposite-sign vorticity which evolved from the previous period are located in the vicinity of the elliptic instability of the attached outer vortex.

In the next chapter, a non-axisymmetric computational study is reported, in which the wakes that evolve beyond the critical Reynolds numbers for the non-axisymmetric instabilities predicted in this chapter are computed.

Chapter 5

Non-Axisymmetric Modes in the Flow past Rings

Previous chapters have investigated the axisymmetric wakes behind rings, and a stability analysis has been presented which provides predictions for the transitions to non-axisymmetric flow in the wakes behind rings.

This chapter aims to verify the existence of all the transition modes predicted by the stability analysis presented in Chapter 4. Furthermore, coefficients of the Landau model will be calculated for each of the transition modes to ascertain the non-linear characteristics of the transition modes. In the vicinity of the transitions, an L_2 norm of the computed non-axisymmetric flow past rings is monitored to verify the hysteretic transition properties predicted by the Landau model.

Two methods are employed to determine the amplitude $|A|$ of the Landau model from the non-axisymmetric computations. For the regular transitions in the Mode I and Mode III regimes, and the non-axisymmetric vortex shedding modes, the instabilities evolve from an axisymmetric wake which corresponds to a mode amplitude of $|A| = 0$. For these modes, $|A|$ in the Landau model is determined directly from the L_2 norm of the non-axisymmetric flow. For the Hopf transitions in the Mode I, II and III regimes, the instabilities evolve from a steady flow to an unsteady flow. For these modes, $|A|$ in the Landau model is determined from the envelope of the L_2 norm of the unsteady non-axisymmetric flow.

Some of the results included in this chapter may be found in Sheard *et al.* (2002, 2003b, 2004a,b).

5.1 Wake Transitions at Small Aspect Ratios ($0 \leq Ar \lesssim 3.9$)

In this section, results from computations of the flow past rings with $0 \leq Ar \lesssim 4$ are presented. The study included computations of the flow past rings in each of the three flow regimes (Mode I, II and III). For the Mode I regime, the flow past a closed ring with $Ar = 0.6$, and the flow past an open ring with $Ar = 1.2$ were computed. For the Mode II regime, the flow past a ring with $Ar = 1.6$ was computed, and for the Mode III regime, the flow past rings with $Ar = 2$ and $Ar = 3$ were computed. Isosurface plots of the flow fields from these computations were constructed.

The Landau model coefficients were determined from the evolution of non-axisymmetric flow past rings with $Ar = 0.6$, $Ar = 1.6$ and $Ar = 2$. As described previously, the Landau model is assumed to describe the growth and saturation of the non-axisymmetric modes in the flow past rings at Reynolds numbers near to the transition point. The coefficients that were determined from the computations are compared with studies which applied the Landau model to the flow past a sphere (Ghidersa & Dušek 2000; Thompson *et al.* 2001a).

5.1.1 The Mode I Regime ($0 \leq Ar < 1.6$)

In this section, the non-axisymmetric transitions in the wakes behind rings in the Mode I regime are studied. Flow visualisation and Landau model predictions of the regular transition and the Hopf transition are presented, followed by a discussion of the non-axisymmetric bifurcations in the Mode I regime.

5.1.1.1 The Regular Transition

Isosurface plots of the saturated non-axisymmetric wakes that were computed at Reynolds numbers beyond the critical Reynolds number for the regular Mode I transition are presented in figure 5.1. For comparison, the regular non-axisymmetric mode in the flow past a sphere was also computed, and is included in the figure. It is apparent from these isosurface plots that a plane of symmetry exists in the wake through the centre of the ring. This symmetry has also been observed for the steady non-axisymmetric flow past a sphere (Johnson & Patel 1999; Tomboulides & Orszag 2000). Furthermore, the wakes display an $m = 1$ azimuthal symmetry, which corresponds to an azimuthal wavelength which spans the azimuthal domain (2π). The similarity between figures 5.1(b) and

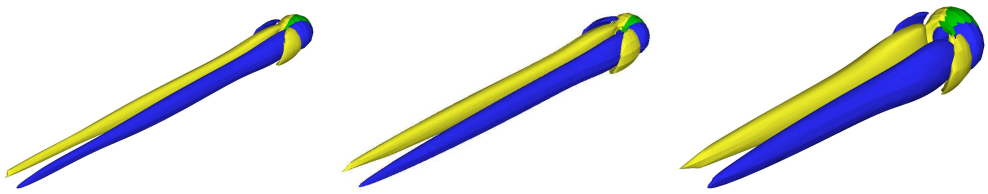

(a) $Ar = 0$, $Re = 270$. (b) $Ar = 0.6$, $Re = 130$. (c) $Ar = 1.2$, $Re = 85$.

FIGURE 5.1: Isosurface plots of streamwise vorticity which show the non-axisymmetric structure of the wakes behind rings after the Mode I transition. Blue and yellow represent positive and negative streamwise vorticity, respectively. The ring, coloured green, is located at the upper right corner of each frame, and flow is from the top right to bottom left.

5.1(c) indicate that the wakes are both produced by the growth and saturation of the predicted regular Mode I instability. The similarity between the figures also confirms that flow through the hole in the ring in this aspect ratio regime does not affect the transition process in the Mode I regime. The wakes comprise bands of streamwise vorticity located immediately behind the ring, which are wrapped around an opposite-sign counter-rotating pair of streamwise vortical tails which extend far downstream. These tails correspond to the classic "double-threaded wake" observed in the wake of the sphere (Magarvey & Bishop 1961b,a; Tomboulides & Orszag 2000; Thompson *et al.* 2001a) at Reynolds numbers greater than the critical Reynolds number for the regular non-axisymmetric wake transition.

Due to the similarity between the non-axisymmetric wake structures of the regular Mode I wake throughout the Mode I regime, only one aspect ratio ($Ar = 0.6$) is used to study the non-linear transition characteristics.

Figure 5.2 shows the non-linear evolution behaviour of the regular Mode I transition. The negative slope near to the y–axis in figure 5.2(b) indicates that the transition occurs through a supercritical bifurcation. This prediction suggests that no hysteresis will be observed in the vicinity of the critical Reynolds number of the transition. This is in agreement with the work by Ghidersa & Dušek (2000) and Thompson *et al.* (2001a), who identify similar behaviour for the regular non-axisymmetric transition in the wake of a sphere.

The critical Reynolds number of the regular Mode I transition in the flow past a ring with $Ar = 0.6$ was determined from the variation in growth rate (σ) with

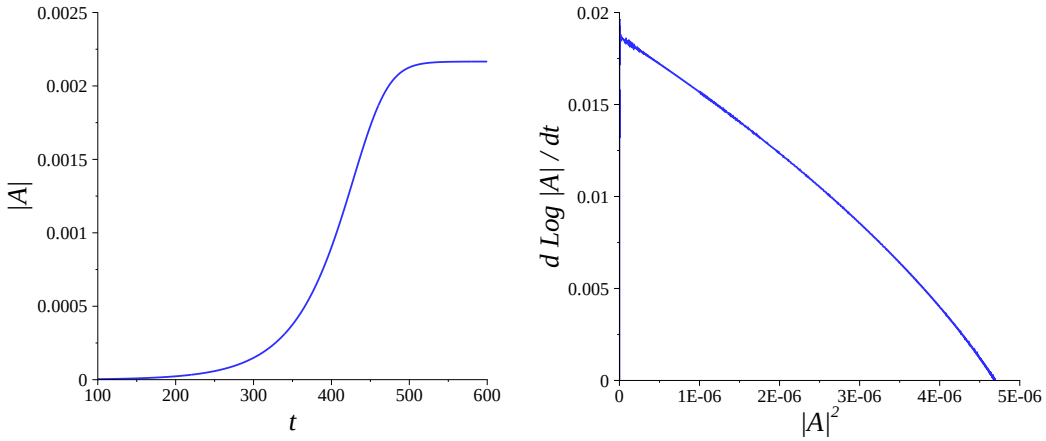

(a) Time history of the regular Mode I transition amplitude evolution.

(b) Derivative of the amplitude logarithm versus amplitude squared plot.

FIGURE 5.2: Plots used to determine the coefficients of the Landau model for the regular Mode I transition in the flow past a ring with $Ar = 0.6$ at $Re = 120$. In (b), the y–axis intercept gives growth rate (σ) and the gradient close to y–axis gives saturation term, l. The negative slope and linear behaviour near the y–axis indicate that the transition is supercritical.

Reynolds number. The computed critical Reynolds number matched the predicted transition Reynolds number from chapter 4 to within 0.5%, in which case $Re_c = 114$ was ascertained. Figure 5.3 gives the variation in the computed growth rate of non-axisymmetric flow with Reynolds number for the flow past a ring with $Ar = 0.6$. Both the stability analysis from

chapter 4 and an independent quadratic fit to the current data verify that the critical Reynolds number was $Re_c = 114$ for the regular non-axisymmetric transition in the wake.

Landau model theory (e.g. see Provansal *et al.* 1987; Dušek *et al.* 1994) predicts that for transitions which are described by a cubic truncation of the Landau model, a linear variation in $|A|^2$ with $Re - Re_c$ is obtained in the vicinity of the transition. Conversely, subcritical transitions will not exhibit a linear variation in $|A|^2$ with $Re - Re_c$ in the vicinity of the transition.

In figure 5.4(a), a plot of $|A|^2$ versus $Re - Re_c$ is presented for the regular transition in the flow past a ring with $Ar = 0.6$. The linear profile near to the transition ($Re - Re_c = 0$) supports the prediction that the transition is supercritical. Furthermore, the critical

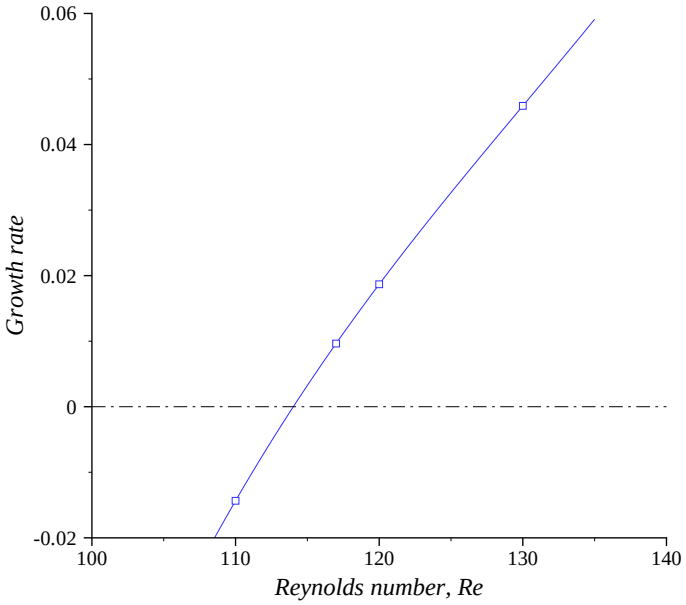

FIGURE 5.3: Computed growth rate in the vicinity of the Mode I transition for the flow past a ring with $Ar = 0.6$. Cubic interpolation gives $Re_c = 114$.

Reynolds number of the regular transition is verified to be $Re_c \approx 114$.

5.1.1.2 The Hopf Transition

Over the aspect ratio range $0 \leq Ar < 1.6$, the regular Mode I transition is followed by a Hopf transition to unsteady flow at higher Reynolds numbers. For the flow past a sphere, this transition occurs at $Re = 272$ (Johnson & Patel 1999; Thompson *et al.* 2001a), and produces a planar-symmetric wake with an $m = 1$ azimuthal symmetry. Numerical visualisation of the vortical wake structure typically shows hairpin shaped vortex loops shedding alternately from opposite sides of the axis (Johnson & Patel 1999; Tomboulides & Orszag 2000; Thompson *et al.* 2001a), whereas experimental flow-visualisation can indicate hairpins aligned on one side of the axis only (Magarvey & Bishop 1961b,a), depending on the location of the dye injection point.

Interestingly, the wakes computed at Reynolds numbers above the Hopf transition are remarkably similar in structure to the unsteady wake behind a sphere. Figure 5.5(a–c) shows isosurface plots of the vortical structure of the wakes behind a sphere, and rings with aspect $Ar = 0.6$ and $Ar = 1.2$, respectively. The plots show that the hairpin vortex structures, the vertical plane of symmetry, and the $m = 1$ azimuthal symmetry

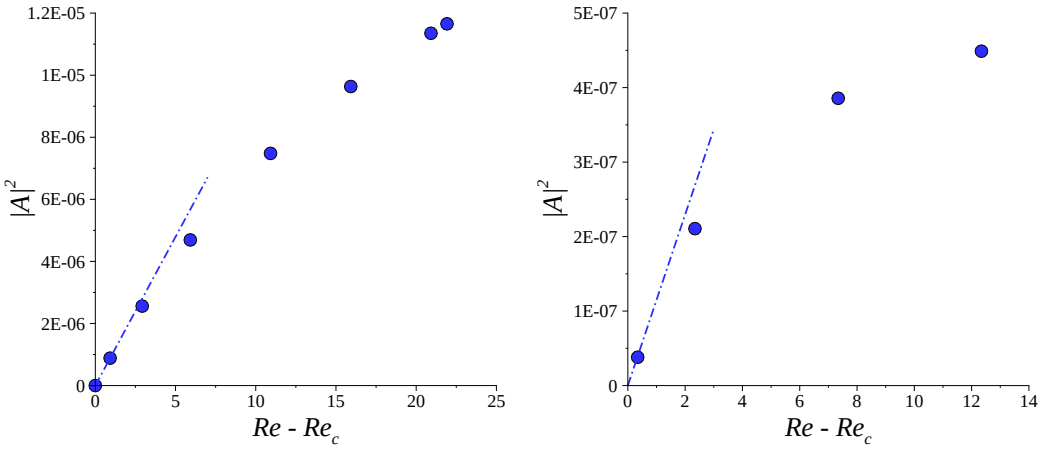

(a) Non-hysteretic behaviour of the regular Mode I transition with $Re_c = 114$.

(b) Non-hysteretic behaviour of the Mode I Hopf transition with $Re_c = 138$.

FIGURE 5.4: Plots of $|A|^2$ with $Re - Re_c$ in the vicinity of the transition for both the regular (a) and Hopf (b) transitions in the flow past a ring with $Ar = 0.6$ in the Mode I flow regime. The dots represent the measured amplitudes, and the lines provide a linear fit to the data through $Re - Re_c = 0$.

of the wakes are consistent throughout the Mode I regime.

The non-linear evolution of the Hopf transition in the Mode I regime is presented in figure 5.6. The negative slope in figure 5.6(b) indicates that the Hopf transition occurs through a supercritical bifurcation, which again suggests that no hysteresis will be observed in the vicinity of the critical Reynolds number for the transition. The wiggles near to the y–axis result from transients in the flow after a Reynolds number shift at the beginning of the computation from a Reynolds number below the Hopf transition to a Reynolds number above the Hopf transition. The prediction of supercritical flow is in agreement with previous studies of the flow past a sphere, which predicted that the Hopf transition that follows the regular non-axisymmetric transition is supercritical (Thompson *et al.* 2001a).

In figure 5.4(b), a plot of $|A|^2$ versus $Re - Re_c$ is presented which shows the envelope of the Hopf transition as the non-axisymmetric wake saturates in the flow past a ring with $Ar = 0.6$. The linear profile in the vicinity of $Re - Re_c = 0$ supports the Landau model prediction that the transition occurs through a supercritical bifurcation. The critical Reynolds number for this transition is $Re_c \approx 137.7$.

The Landau constant, c, was calculated in the vicinity of the secondary transition

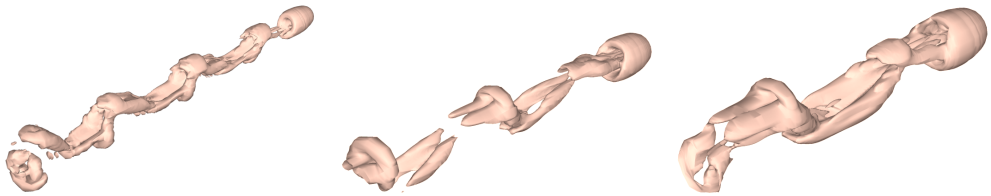

(a) $Ar = 0$, $Re = 300$. (b) $Ar = 0.6$, $Re = 160$. (c) $Ar = 1.2$, $Re = 120$.

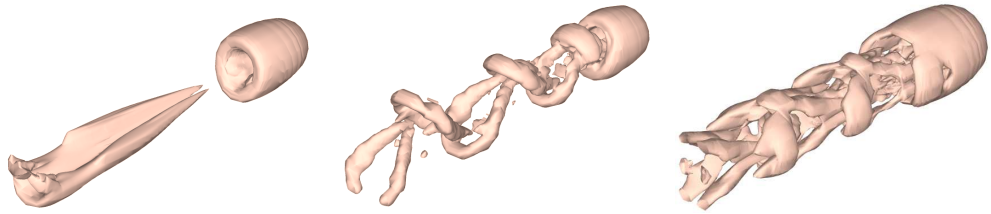

(d) $Ar = 1.6$, $Re = 100$. (e) $Ar = 2$, $Re = 150$. (f) $Ar = 3$, $Re = 138$.

FIGURE 5.5: Isosurface plots of the unsteady wakes observed following the Hopf transition over the Mode I (a–c), Mode II (d) and Mode III (e–f) regimes. The method of Jeong & Hussain (1995) is used to capture the vortical structure of the wakes. Note the plane of symmetry through centre of each ring, and similar vortical structure of the wakes. Flow is from top right to bottom left of each frame.

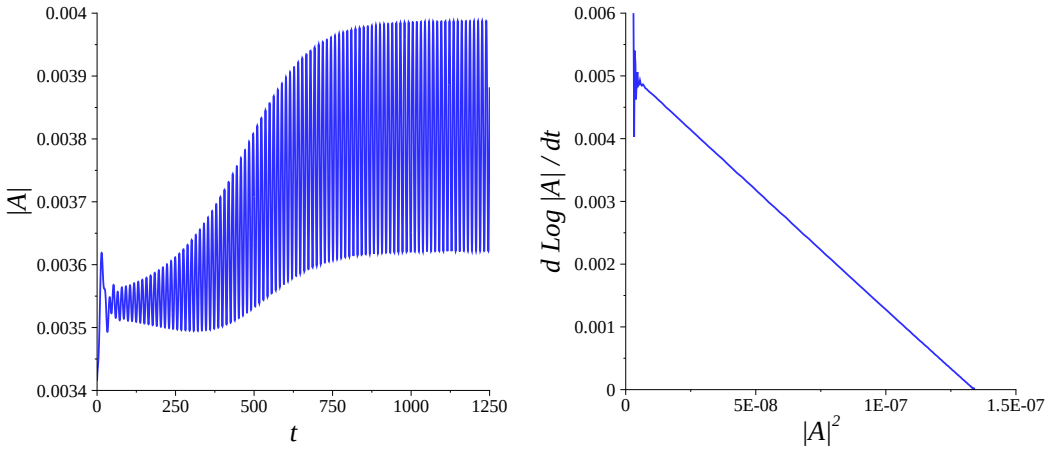

(a) Time history of the Mode I Hopf transition amplitude evolution.

(b) Derivative of the amplitude logarithm versus amplitude squared plot.

FIGURE 5.6: Plots used to determine the coefficients of the Landau model for the regular Mode I transition in the flow past a ring with $Ar = 0.6$ at $Re = 139$. In (b), the negative slope and linear behaviour near the y–axis indicate that the transition is supercritical.

for the ring with $Ar = 0.6$. The value of the Landau constant was approximately $c = -0.50 \pm 0.05$. For comparison, the Landau constant for the Hopf transition in the flow past a sphere was found to be $c = -0.55$ (Ghidersa & Dušek 2000; Thompson *et al.* 2001a), which is close to the value found for the Hopf transition in the flow past a ring with $Ar = 0.6$. This result supports the classification of these transitions in the Mode I regime.

5.1.1.3 Mode I Regime Bifurcations

To verify the predicted hysteretic properties of the regular and Hopf transition modes in the Mode I regime, saturated amplitudes were computed at several Reynolds numbers close to the transitions. For the unsteady wakes that evolved beyond the Hopf transition Reynolds number, maximum and minimum amplitudes were obtained to determine the envelope of the amplitude.

In figure 5.7, a plot of the non-axisymmetric mode amplitude over a Reynolds number range which encompasses the regular and Hopf transitions in the flow past a ring with $Ar = 0.6$ is presented. The figure shows that both the regular and Hopf transitions occur through supercritical bifurcations, as no hysteresis is computed in the vicinity of either transition. This is consistent with the predictions of the Landau model in previous sections.

5.1.2 The Mode II Regime ($1.6 \leq Ar \leq 1.7$)

The non-axisymmetric Hopf transition in the wake behind a ring in the Mode II regime is studied here. Following flow visualisation and Landau model predictions of the post-transition wake, a discussion of the non-axisymmetric bifurcation scenario of the Mode II regime is presented.

5.1.2.1 The Hopf Transition

The flow past a ring with $Ar = 1.6$ was computed at a Reynolds number greater than the critical Reynolds number for the Mode II Hopf transition to model the growth and saturation of the transition with the Landau model. An isosurface plot of the wake structure is presented in figure 5.8. The plot shows that the non-axisymmetric structure of the near wake in the Mode II regime is similar to the structure of the near wake in the Mode I regime, after the evolution of the regular transition. However, in this case the wake comprises wings of streamwise vorticity of opposing sign wrapped around longer

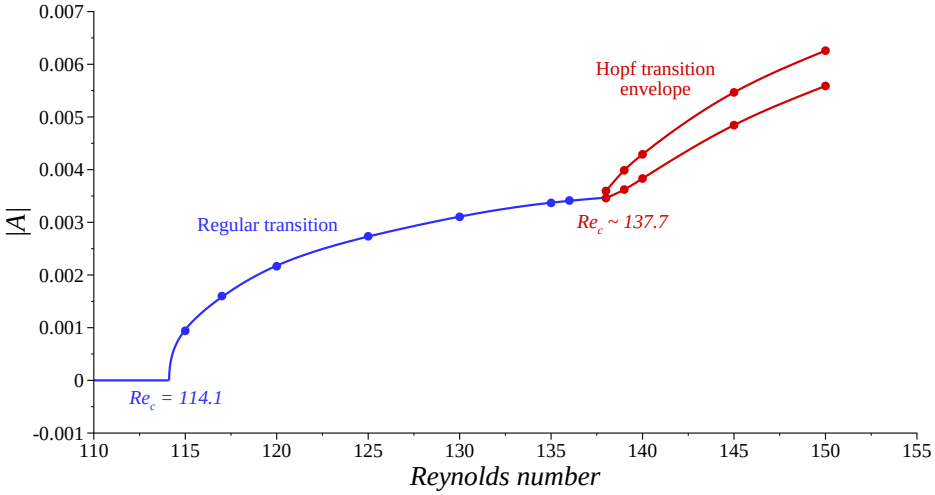

FIGURE 5.7: Non-axisymmetric regular and Hopf mode bifurcations of the wake behind a ring with $Ar = 0.6$. Blue dots represent the computed mode amplitudes for the regular transition, and red dots show the maximum and minimum computed mode amplitudes of the envelope of oscillation of the Hopf transition. Lines show the likely transition branches.

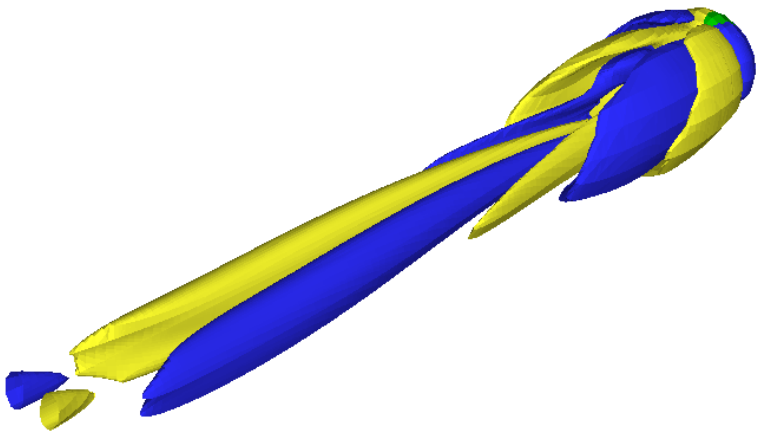

FIGURE 5.8: Streamwise vorticity isosurface plot of the wake behind a ring with $Ar = 1.6$ at $Re = 100$, after the saturation of the Mode II transition. Isosurface contours and flow direction are as per figure 5.1.

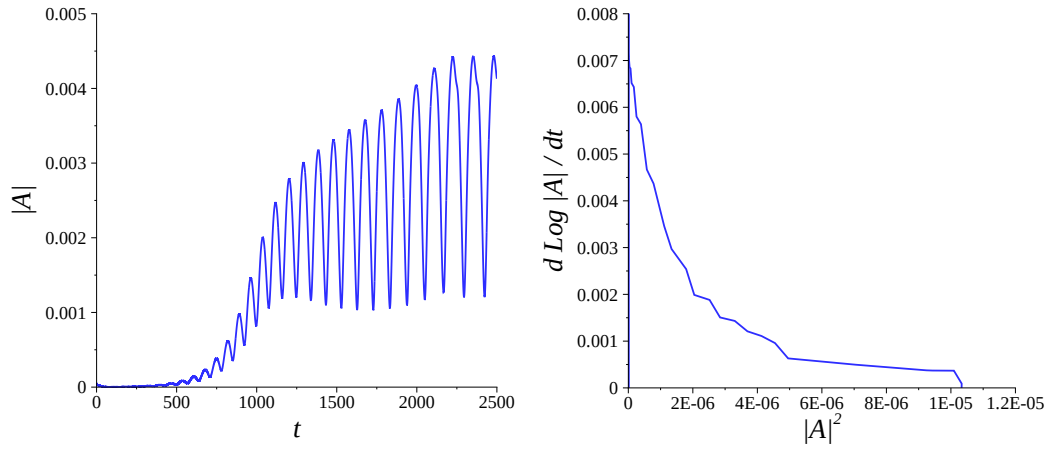

(a) Time history of the Mode II Hopf transition amplitude evolution.

(b) Derivative of the amplitude logarithm versus amplitude squared plot.

FIGURE 5.9: Plots used to determine the coefficients of the Landau model for the Mode II Hopf transition in the flow past a ring with $Ar = 1.6$ at $Re = 98$. In (b), the negative slope near the y–axis indicate that the transition is supercritical.

tails of streamwise vorticity which extend downstream. The computed vortex tails were unsteady, and were observed to convect downstream with a Strouhal frequency of $St \approx 1 \times 10^{-2}$. This observed behaviour was in agreement with the behaviour of the Mode II transition predicted by the linear stability analysis in chapter 4. The stability analysis predicted that the dominant Floquet mode of the Mode II instability was complex, which suggested that the transition occurred through a spontaneous non-axisymmetric Hopf bifurcation. The planar symmetry and the $m = 1$ azimuthal symmetry which were observed for the flows in the Mode I regime are preserved in the Mode II regime.

The vortical structure of the computed flow past a ring with $Ar = 1.6$ is also presented in figure 5.5(d). In figure 5.5, the wake structure is compared to the unsteady wakes behind rings in the Mode I and III regimes. The Mode II wake differed from the unsteady wakes computed in the Mode I and Mode III regimes in that the saturated wake had a Strouhal frequency which was approximately 30% of the Strouhal frequency of the saturated wakes behind rings in the Mode I and III regimes. Structurally, the Mode II wake was different to the other wakes which evolved from Hopf transitions. Instead of a vortex-loop wake structure, with vortex loops shed on alternating sides of the axis, long bands of vorticity were observed to be cast into the wake on one side of the axis only.

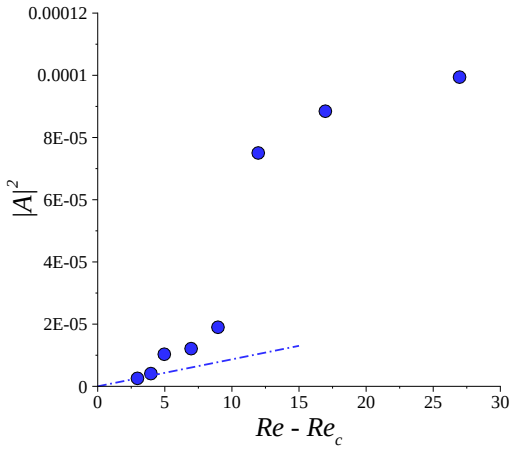

(a) Amplitude squared versus $Re - Re_c$.

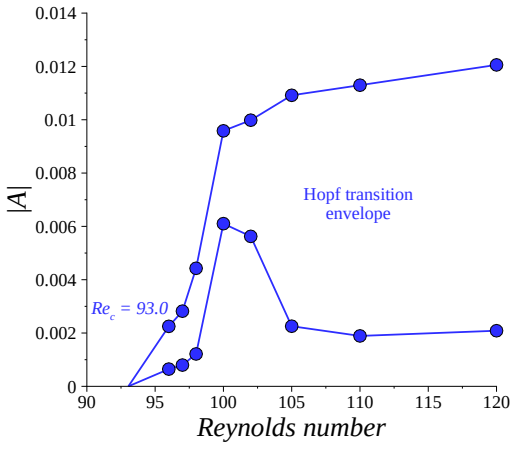

(b) Amplitude envelope versus Reynolds number.

FIGURE 5.10: Plots of the evolution of the Mode II transition in the wake behind a ring with $Ar = 1.6$. In (a) the dash-dot line shows a possible linear fit to the data in the vicinity of $Re - Re_c = 0$, and dots show the computed data points. In (b), dots represent the maximum and minimum computed mode amplitudes at a given Reynolds number, and lines approximate the maximum and minimum limits to the oscillation envelope of the mode amplitude.

To model the non-linear behaviour of the Mode II transition, the envelope of the oscillation of the L_2 norm was calculated. Figure 5.9 shows the non-linear evolution of the non-axisymmetric Hopf transition in the wake behind a ring with $Ar = 1.6$, at $Re = 98$.

The negative slope observed near to the axis in figure 5.9(b) indicates that the Mode II transition occurs through a supercritical bifurcation. The evolution of the mode in figure 5.9(a) shows that despite the large period of oscillation, sufficient data points have been obtained to predict the transition bifurcation type. The Landau constant measured within the vicinity of the Mode II transition was found to be $c = -0.60$. This value was obtained at $Re - Re_c = 3.5$, for the flow past a ring with $Ar = 1.6$, and was measured from the velocity signal at a point in the wake approximately $4d$ downstream of the ring cross-section. The variation in the Landau constants which were computed at different aspect ratios is discussed in § 5.2.

5.1.2.2 Mode II Regime Bifurcations

The evolution of a non-axisymmetric and unsteady wake in the Mode II regime is highlighted by the plots in figure 5.10. Figure 5.10(a) shows the variation of the envelope of the amplitude with $Re - Re_c$, and verifies that the Landau model correctly predicts that the Mode II transition occurs through a supercritical bifurcation. Figure 5.10(b) shows the variation in $|A|$ with Reynolds number, and again shows the supercritical nature of the transition, with both the maximum and minimum amplitude profiles observed to become non-zero ($|A| \geq 0$) continuously with an increase in Reynolds number through $Re_c \approx 93$. The absence of a region of steady non-axisymmetric flow for $Re > Re_c$ supports the prediction in chapter 4 that the first-occurring non-axisymmetric instability in the Mode II regime has a complex-conjugate Floquet mode.

5.1.3 The Mode III Regime ($1.7 \lesssim Ar \lesssim 3.9$)

The computed wakes that evolve from the non-axisymmetric regular and Hopf transitions in the flow past rings in the Mode III regime is presented here. Firstly, flow visualisations and Landau model predictions of the computed wakes is presented. Following this, the non-axisymmetric bifurcation scenario in the Mode III regime is discussed.

5.1.3.1 The Regular Transition

Isosurface plots of the computed wakes that evolve from the regular Mode III transition in the flow past rings in the Mode III regime are presented in figure 5.11. The computed wakes have a different structure to the steady non-axisymmetric wakes computed in the Mode I regime. The long tails of streamwise vorticity which were observed in the wakes behind rings in the Mode I regime are not observed in the wakes behind rings in the Mode III regime. The wakes behind rings in the Mode III regime consist of bands of vorticity which are localised in the wake directly downstream of the ring body.

The computations in the Mode III regime suggest that the regular Mode III transition occurs in the flow past rings with $1.8 \lesssim Ar \lesssim 3.9$. In the flow past rings with larger aspect ratios ($Ar \gtrsim 3.9$) the non-axisymmetric transition is preceded by a Hopf bifurcation to a periodic axisymmetric wake, which is similar to the von Kármán vortex street in the flow past a circular cylinder. The $m = 1$ azimuthal symmetry of the instability associated with the Mode III transition is not maintained throughout the Mode III regime ($1.8 \leq Ar \lesssim 3.9$). In chapter 4, stability analysis predicted that the flow past

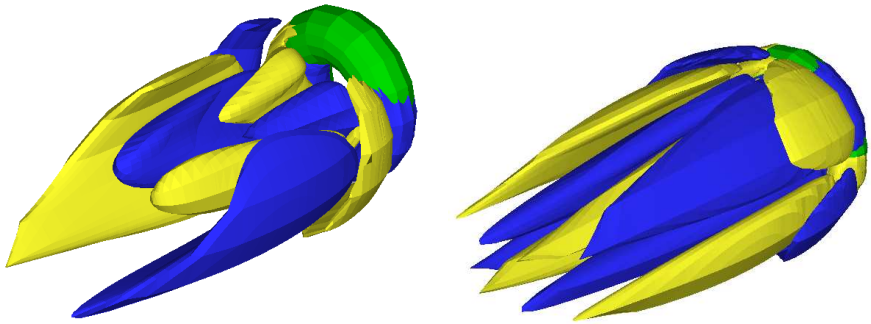

(a) $Ar = 2,\ Re = 90.$ (b) $Ar = 3,\ Re = 115.$

FIGURE 5.11: Streamwise vorticity isosurface plots of the asymmetric wakes following the Mode III transition. Note the difference in azimuthal symmetry between the two aspect ratios. Isosurface contours as per figure 5.1.

a ring with $Ar = 3$ was unstable to an azimuthal mode with $m = 2$ symmetry, which is consistent with the symmetry of the non-axisymmetric wake structure in figure 5.11(b). The $m = 2$ azimuthal symmetry is associated with perpendicular planes of symmetry which intersect along the axis. The wake structures in figure 5.11(a) corresponds to an instability with $m = 1$ symmetry.

The wake structures presented in figure 5.11 do not appear to be consistent with a common instability mode. A better indication of the consistency between the wakes is achieved if the wakes are viewed from directly behind the ring, as shown in figure 5.12. If an imaginary cut is made through the top of the ring in figure 5.12(a), and the ring and wake are bent outwards into a semicircle, then the wake structures are similar to the wake structures present in the bottom half of the ring in figure 5.12(b). This observation confirms that the wakes behind these rings were both correctly identified as regular Mode III transitions in the Mode III regime. Furthermore, the observation suggests that the mode scales with a length scale based on the cross-section of the ring (d), rather than the outer diameter of the ring ($D + d$).

In the computation of the evolution of the regular Mode III transition to saturation in the flow past a ring with $Ar = 2$ at $Re = 93$, the amplitude of the non-axisymmetric wake was recorded. Plots of the growth and saturation of the amplitude are presented in figure 5.13. In figure 5.13(b), the distinct non-linearity and positive gradient at the y–intercept suggest that the Mode III transition occurs through a subcritical bifurcation. This indicates that higher-order terms are required for the Landau model to completely

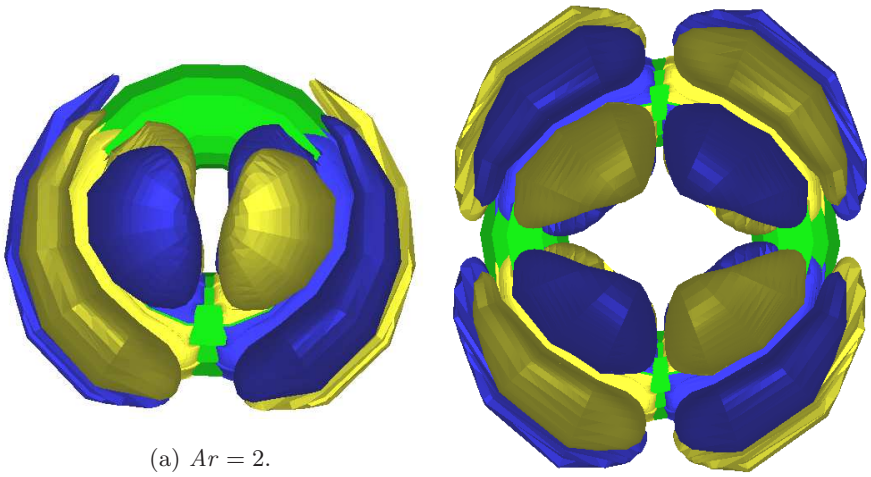

(a) $Ar = 2$.

(b) $Ar = 3$.

FIGURE 5.12: Isosurface plots of streamwise vorticity indicating $m = 1$ and $m = 2$ azimuthal symmetry of the Mode III transition. The flow is viewed from directly behind the rings, and isosurface shading is as per figure 5.1.

describe the saturation of this transition.

To verify that the regular Mode III transition occurs through a subcritical bifurcation, a plot of $|A|^2$ versus $Re - Re_c$ is provided in figure 5.14(a). It is clear that the mode amplitude does not approach zero as $Re - Re_c \to 0$. The plot shows that a steady non-axisymmetric wake was computed at $Re - Re_c = -1$, which verifies that the onset of the regular transition in the Mode III regime is hysteretic.

5.1.3.2 The Hopf Transition

The flow past rings with $Ar = 2$ and $Ar = 3$ were computed at Reynolds numbers greater than the critical Reynolds numbers for the Mode III Hopf transition. Isosurface plots which show the vortical structure of the computed wakes are presented in figure 5.5(e–f). The plots show that for the Hopf transition in the Mode III regime, a change in symmetry with an increase in aspect ratio is observed, which maintains the azimuthal symmetry properties of the regular Mode III transition that was discussed earlier. Azimuthal symmetries of $m = 1$ and $m = 2$ are observed in the wakes behind rings with $Ar = 2$ and $Ar = 3$, respectively. A hairpin structure and wake symmetry is observed in figure 5.5(e), which is analogous to the post-Hopf transition wakes computed in Mode I regime. A more complex vortex-loop structure is observed in fig-

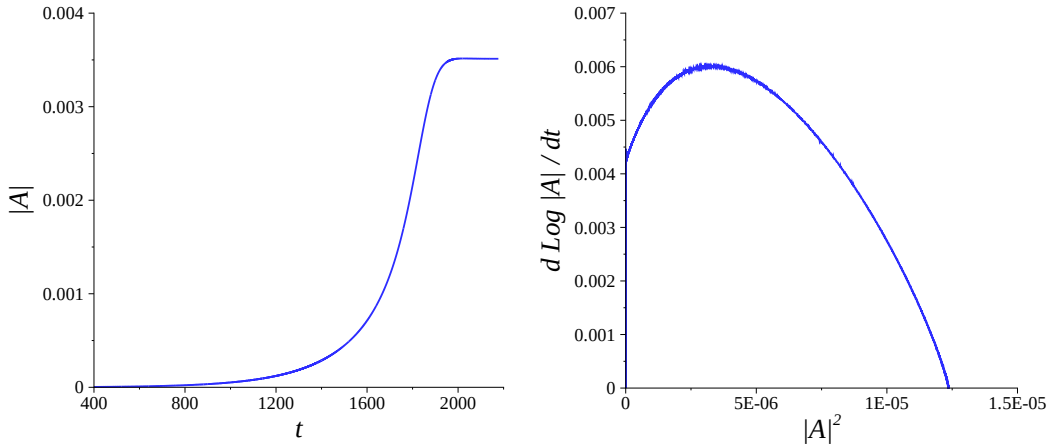

(a) Time history of the regular Mode III transition amplitude evolution.

(b) Derivative of the amplitude logarithm versus amplitude squared plot.

FIGURE 5.13: Plots used to determine the coefficients of the Landau model for the regular Mode III transition in the flow past a ring with $Ar = 2$ at $Re = 93$. In (b), the non-linear profile and positive slope near the y–axis indicate that the transition is subcritical.

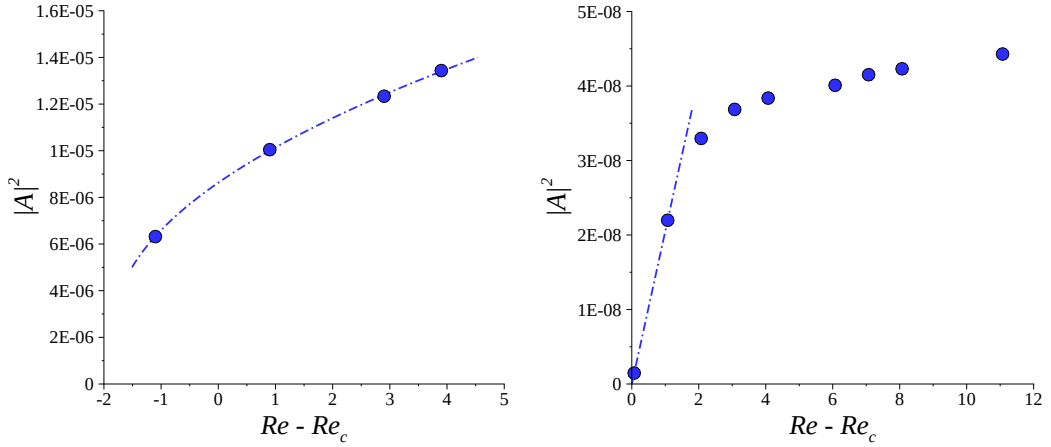

(a) Hysteretic behaviour of the regular Mode III transition with $Re_c = 90.1$.

(b) Non-hysteretic behaviour the Mode III Hopf transition with $Re_c = 94$.

FIGURE 5.14: Plots of $|A|^2$ with $Re - Re_c$ in the vicinity of the transitions for both the regular (a) and Hopf (b) transitions in the wake behind a ring with $Ar = 0.6$ in the Mode I flow regime. The dots represent the measured amplitudes, and the lines provide a linear fit to the data through $Re - Re_c = 0$.

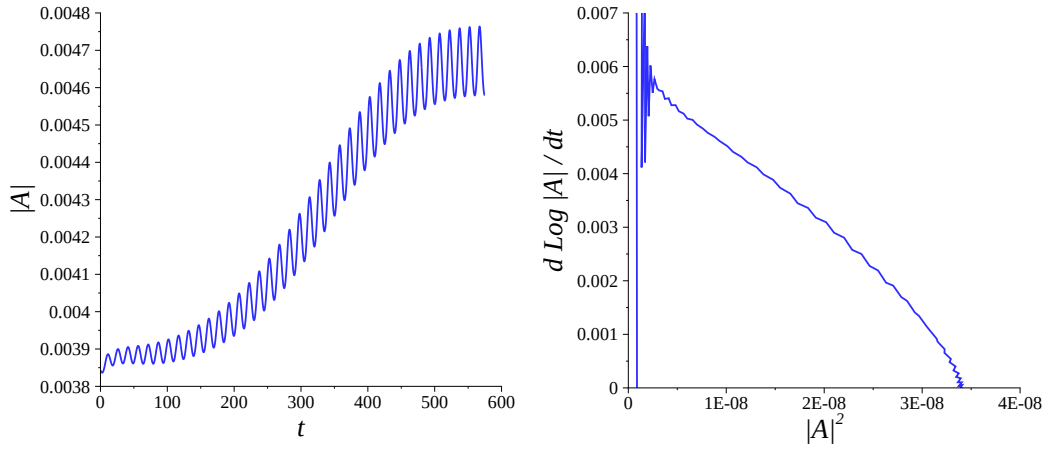

(a) Time history of the Mode III Hopf transition amplitude evolution.

(b) Derivative of the amplitude logarithm versus amplitude squared plot.

FIGURE 5.15: Plots used to determine the coefficients of the Landau model for the Mode III Hopf transition in the flow past a ring with $Ar = 2$ at $Re = 96$. In (b), the linear profile and negative slope near the y–axis indicate that the transition is supercritical.

ure 5.5(f), which shows a symmetry consistent with an $m = 2$ instability, with both horizontal and vertical planes of symmetry. Interestingly, miniature hairpin structures are also observed near to the core of the wake, which are shed from the inner surface of the ring, and appear to increase in prominence with an increase in the size of the hole in the ring.

In the previous sections, the Hopf transitions in the Mode I and II regimes were shown to occur through supercritical bifurcations. The evolution of the non-axisymmetric mode that evolved from a Hopf transition in the Mode III regime for a ring with $Ar = 2$ is presented in figure 5.15(a). The real coefficients of the Landau model are determined from figure 5.15(b), which shows behaviour consistent with a supercritical bifurcation. The wiggles present in the vicinity of the y–axis in figure 5.15(b) are an artefact of the initial conditions for the computation, where a steady-state non-axisymmetric flow field computed just below the unsteady transition Reynolds number ($Re = 93 < Re_c \approx 94$) was employed.

In figure 5.14(b) a plot of $|A|^2$ versus $Re - Re_c$ is presented. The plot shows a linear evolution of the square of the mode amplitude envelope with $Re - Re_c$. The continuous mode evolution is consistent with a supercritical bifurcation, which supports the Landau model prediction that the transition is supercritical.

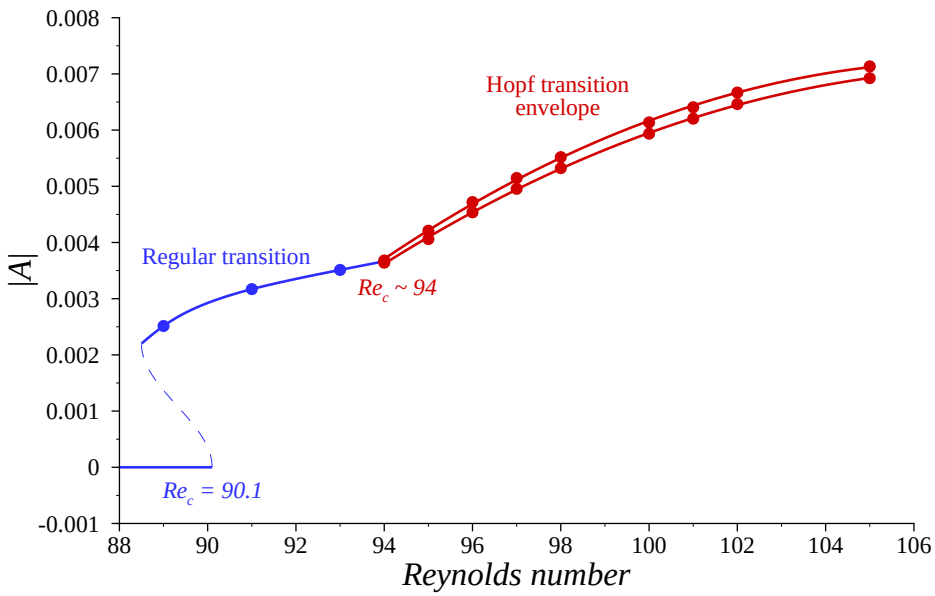

FIGURE 5.16: Mode amplitude variation versus Reynolds number for the non-axisymmetric transitions for a ring with $Ar = 2$. The dashed line highlights the hysteretic onset of the regular transition, and solid lines show the regular and Hopf transition branches. Computed data points for the regular transition branch, and the Hopf transition envelope are represented by blue and red dots, respectively.

The Landau constant was calculated for the Hopf transition in the Mode III regime at aspect ratios of $Ar = 2$ and $Ar = 3$. For the flow past a ring with $Ar = 2$, the Landau constant was calculated to be $c = -0.92$, and for the flow past a ring with $Ar = 3$, the Landau constant was calculated to be $c = -4.1$. See § 5.2 for a discussion of these computed Landau constants.

5.1.3.3 Mode III Regime Bifurcations

The non-axisymmetric bifurcations in the Mode III regime are the most interesting of the three regimes presented so far. Figure 5.16 shows the variation in non-axisymmetric mode amplitude with Reynolds number for the flow past a ring with $Ar = 2$. From the present computations it was observed that a regular non-axisymmetric mode evolved in the wake for $Re > Re_c$, where $Re_c \approx 90.1$. A region of hysteresis was observed for a small range of Reynolds numbers below Re_c, which supports the Landau model prediction that the regular Mode III transition occurs through a subcritical bifurcation.

The steady non-axisymmetric wake became unstable to a Hopf transition for Rey-

nolds numbers beyond $Re \approx 94$. With a reduction in Reynolds number, the unsteady wake decayed to a steady wake for all Reynolds numbers below the transition Reynolds number, which confirmed the prediction that the Hopf transition is supercritical in the Mode III regime.

5.2 Variation of Landau Model Constants with Aspect Ratio

The previous section presented the calculated Landau constant (c) values that were obtained for the first-occurring Hopf transition for rings with aspect ratios in the range $0 \lesssim Ar \lesssim 3.9$. In this section, the results of calculations of c for the axisymmetric Hopf transition in the flow past rings with $Ar \gtrsim 3.9$ are presented. Specifically, Landau constants were calculated for the Hopf transitions in the flows past rings with $Ar = 4$, 5, 10, 20 and 40.

In addition, the Landau diffusivity constant (η_{diff}) was evaluated for the Hopf transitions in the flow past rings over the entire aspect ratio range considered in the present study. Previously, a Landau diffusivity constant of $\eta_{diff} \approx 5$ was calculated for the Hopf transition in the flow past a circular cylinder by Provansal *et al.* (1987). A Landau diffusivity constant of $\eta_{diff} \approx 1.86$ can be calculated for the Hopf transition in the flow past a sphere using data provided in Thompson *et al.* (2001a).

A complete profile of the variation in the Landau constant with aspect ratio is presented in figure 5.17(a), for the Hopf transition in the flow past rings. The values calculated from the computed unsteady transition in the flow past rings with $Ar = 6$ and $Ar \geq 5$ are consistent with known values of the Landau constant for the Hopf transition in the flow past a sphere ($c = -0.55$) and a circular cylinder ($-3.0 < c < -2.6$), respectively. The most interesting feature of the Landau constant variation is the large magnitude of the Landau constant at $Ar = 4$ when compared with the Landau constant at other aspect ratios. The flow past a ring with $Ar = 4$ is in the vicinity of the crossover point in aspect ratio parameter space for the Hopf and non-axisymmetric transitions. The large amplitude resulted from a combination of a larger frequency shift as the mode saturated, as well as a smaller growth rate of the instability, than were measured at other aspect ratios.

For $Ar \gtrsim 4$, where the Hopf transition occurs prior to the non-axisymmetric transition, a small variation in the measured Landau constant was observed. This is con-

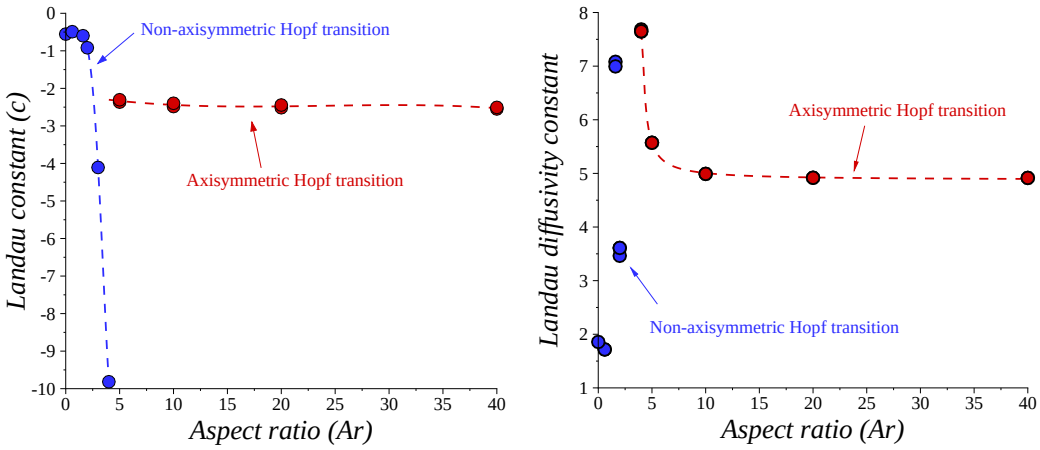

(a) Landau constant (c) variation with Ar.

(b) Landau diffusivity constant (η_{diff}) variation with Ar.

FIGURE 5.17: Variation of Landau model constants with aspect ratio for the first Hopf transition in the wakes behind rings. Blue dots represent the Hopf transition of the non-axisymmetric wakes behind rings with small aspect ratios, and red dots represent the Hopf transition of the axisymmetric wakes behind rings with large aspect ratios. The constants are calculated in the vicinity of the primary Hopf transition of the wake at each aspect ratio.

sistent with the observed similarity in the Strouhal–Reynolds number profiles and the critical Reynolds numbers for the transition to unsteady flow described in chapter 3. For $Ar \lesssim 4$, the structures of the post-Hopf transition wakes differ greatly, and it is therefore unsurprising that a large variation in the Landau constant is computed in the $Ar \lesssim 4$ regime, when compared with the Landau constants computed in the $Ar \gtrsim 4$ regime.

Figure 5.17(a) shows that for the Hopf transition in the flow past rings with $0 \leq Ar \lesssim 4$, the Landau constant decreases from $c = -0.554$ to $c = -9.8$. For the Hopf transition in the flow past rings with $Ar \gtrsim 4$, the Landau constant asymptotes towards a constant, with a decrease from $c \approx -2.37$ at $Ar = 5$ to $c \approx -2.55$ at $Ar = 40$.

Figure 5.17(b) shows the variation in η_{diff} with aspect ratio. The computed constants rapidly asymptote with an increase in aspect ratio over the axisymmetric Hopf transition range $Ar \gtrsim 4$ to $\eta_{diff} \approx 5$. There is no clear trend in the computed constants for the non-axisymmetric Hopf transition rage $Ar \lesssim 4$, with $\eta_{diff} \approx 1.8$, $\eta_{diff} \approx 7$ and $\eta_{diff} \approx 3.5$, computed in the Mode I, II and III regimes, respectively. A proposed explanation for the lack of a trend in the Landau diffusivity constant for $Ar \lesssim 4$ is that the

Ar	First mode	Second mode	Third mode
5	Mode C ($Re_c \approx 163.3$)	$\star$ Mode A ($Re_c \approx 194.0$)	Mode B ($Re_c \approx 301.4$)
10	Mode A ($Re_c \approx 194.3$)	Mode C ($Re_c \approx 222.1$)	Mode B ($Re_c \approx 270.0$)
20	Mode A ($Re_c \approx 189.2$)	Mode B ($Re_c \approx 261.2$)	$\star$ Mode C ($Re_c \approx 310.9$)

TABLE 5.1: The order in which the non-axisymmetric instabilities are predicted to occur in the flow past the rings selected for the present study. Predicted critical Reynolds numbers from Floquet analysis are also provided. Modes marked with a "$\star$" are not included in the present study as pure modes could not be computed.

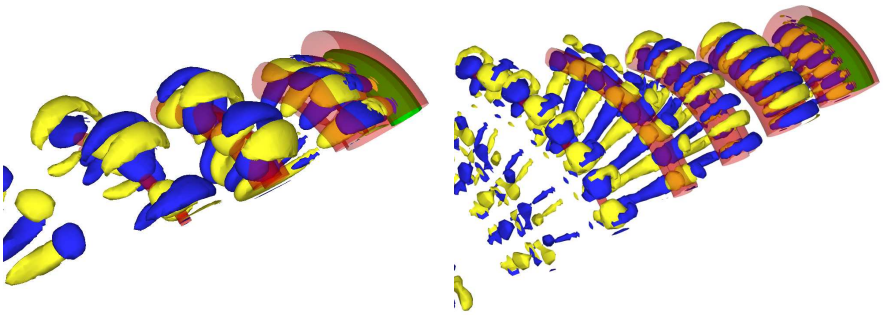

(a) Mode C: $Re = 170$, $\lambda_d \approx 1.7d$. Two azimuthal periods are shown.

(b) Mode B: $Re = 310$, $\lambda_d \approx 0.8d$. Four azimuthal periods are shown.

FIGURE 5.18: Vortex structure of the saturated non-axisymmetric wakes of a ring with $Ar = 5$ following the Mode C (a) and Mode B (b) instabilities. Blue and yellow contours represent positive and negative streamwise vorticity, respectively. A pressure level of -0.1 is represented by a translucent red isosurface, which shows the rollers in the vortex street. The ring is coloured green, and is located at the upper right corner of each frame, with the flow direction towards the lower left corner.

Hopf transitions evolve from different wakes in each of the Mode I, II and III regimes. A pleasing result was achieved for the Hopf transition in the Mode I regime. For the flow past a ring with $Ar = 0.6$, a constant of $\eta_{diff} \approx 1.72$ was obtained, which is similar to the constant of $\eta_{diff} \approx 1.86$ that has been determined for the flow past a sphere.

5.3 Wake Transitions at Large Aspect Ratios ($Ar \gtrsim 3.9$)

The existence of non-axisymmetric instability modes in the vortex streets behind rings was predicted by the stability analysis presented in chapter 4. Experimental Strouhal profiles have also indicated the presence of transitions in the vicinity of the critical Reynolds number for the Mode A and Mode B transitions for the circular cylinder

(Leweke & Provansal 1995). The results of non-axisymmetric computations are presented here to verify the predictions of the earlier stability analysis, and to classify the structural and hysteretic properties of the modes.

Rings with $Ar = 5$, 10 and 20 were chosen to study the non-axisymmetric vortex shedding modes in the flow past rings. These aspect ratios were selected as the predicted order in which the instabilities occur with an increase in Reynolds number differs for the flow past each of the rings. The different orders of the instability modes result from the wide variation in the critical Reynolds number for the onset of the Mode C instability, which varies between $Re_c = 163.3$ at $Ar = 5$ to $Re_c = 310.9$ at $Ar = 20$. Table 5.1 summarises the order in which the instabilities are predicted to occur for the rings chosen for the non-axisymmetric computations.

It is desired that only pure modes be considered in the present study, to assist in calculating the Landau model coefficients. The azimuthal domain size of the computations are therefore limited to the predicted dominant wavelength of the instability being modelled. It is not useful to attempt to compute transition modes where a shorter-wavelength instability exists at a lower Reynolds number, as the desired mode will be contaminated even if it does develop. The wakes behind rings with aspect ratios $Ar = 5$ and 20 both contain such "impure" modes, as highlighted in table 5.1.

5.3.1 Instability Mode Path C-A-B ($Ar = 5$)

In this section, isosurface plots and Landau model predictions are presented for the pure Mode C and Mode B wakes computed in the flow past a ring with $Ar = 5$. A bifurcation diagram which shows the respective evolution of the two modes is also provided, and the variation in drag coefficient through the pure bifurcations is investigated.

5.3.1.1 The Mode C Transition

The first non-axisymmetric mode to occur in the vortex street behind a ring with $Ar = 5$ is Mode C. An isosurface plot which shows the structure of a Mode C wake is provided in figure 5.18(a). The Mode C instability is interesting in that it is not observed in the circular cylinder wake (Barkley & Henderson 1996; Williamson 1996b), and it is predicted to be associated with a subharmonic Floquet mode.

The structure of the Mode C instability presented here highlights some interesting features of the saturated non-axisymmetric wake. Notice firstly that pairs of broad bands of opposite-sign streamwise vorticity are located above each vortex roller. Sig-

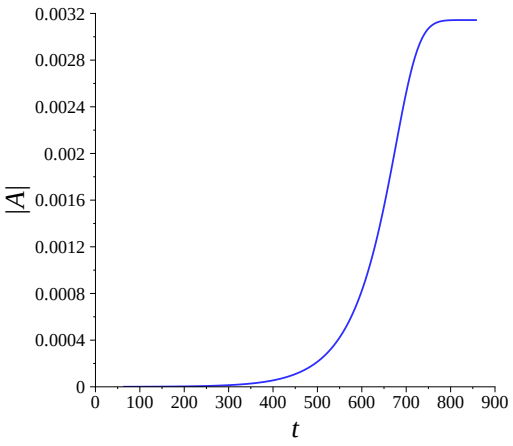

(a) Time history of the Mode C instability amplitude evolution.

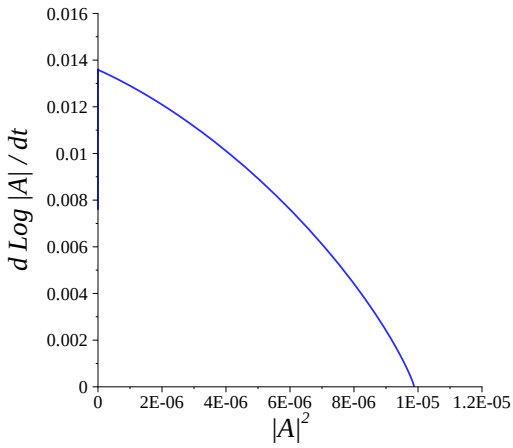

(b) Derivative of the amplitude logarithm versus amplitude squared plot.

FIGURE 5.19: Plots used to determine the coefficients of the Landau model for the Mode C transition in the flow past a ring with $Ar = 5$ at $Re = 170$. In (b), the negative slope near the y–axis indicates that the transition is supercritical.

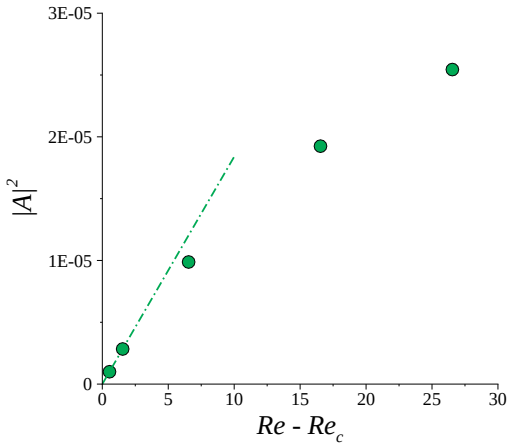

(a) Non-hysteretic behaviour of a pure Mode C instability with $Re_c = 163.3$.

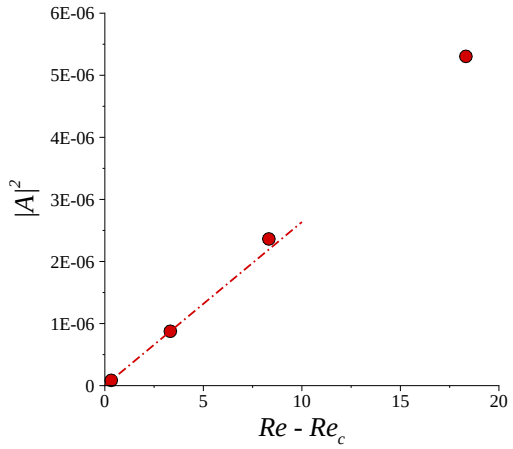

(b) Non-hysteretic behaviour of a pure Mode B instability with $Re_c = 301.4$.

FIGURE 5.20: Plots of $|A|^2$ with $Re - Re_c$ in the vicinity of the transitions for both the pure Mode C (a) and Mode B (b) instabilities in the wake behind a ring with $Ar = 5$. The dots represent the measured amplitudes, and the lines provide a linear fit to the data through $Re - Re_c = 0$.

nificantly, the sign of these vorticity bands alternates from one shedding cycle to the next. The vortex rollers are deformed into a wavy shape by the development of the streamwise vorticity. However, at every shedding cycle the axial direction of deformation alternates with the sign of the vortex structures. The high curvature of a ring with $Ar = 5$ (relative to larger aspect ratios) alters the shape of the corresponding streamwise vortices which form on the underside of the wake, however, an identical sign alternation takes place, with the same sign vorticity observed in the streamwise structures located above and below the wake centreline.

The azimuthal wavelength of the saturated Mode C wake is approximately $1.7d$. This is consistent with the most unstable wavelength of the Mode C instability predicted earlier.

Consistent with previous applications of the Landau model, an L_2 norm is computed for the evolution of the non-axisymmetric vortex shedding modes. In figure 5.19(a), the evolution of the amplitude of Mode C at $Re = 170$ is shown. Figure 5.19(b) is used to determine the cubic coefficients of the Landau model. The negative gradient at the y–axis suggests that the Mode C transition occurs here through a supercritical bifurcation. The variation in $|A|^2$ is non-linear over the entire range, suggesting that at least fifth-order terms need to be included for the Landau model to better describe the evolution of this Mode C instability.

The amplitude of the saturated Mode C instability was computed at several Reynolds numbers in the vicinity of the transition for the flow past a ring with $Ar = 5$. Figure 5.20(a) is a plot of $|A|^2$ against $Re - Re_c$ for the Mode C transition. The amplitude of the instability approaches zero with $Re - Re_c$, again indicating that the transition in non-hysteretic and occurs through a supercritical bifurcation.

5.3.1.2 The Mode B Transition

The saturated flow associated with the Mode B instability has also been computed for $Ar = 5$. An isosurface plot of the computed wake is presented in figure 5.18(b). Two features of this wake that are immediately identifiable as being consistent with the Mode B instability observed in a circular cylinder wake (Thompson *et al.* 1996; Henderson 1997) are the azimuthal wavelength of the instability (approximately $0.8d$), and the spatio-temporal symmetry of the non-axisymmetric structures in the wake.

The orientation of the isosurface plot allows the spatio-temporal symmetry charac-

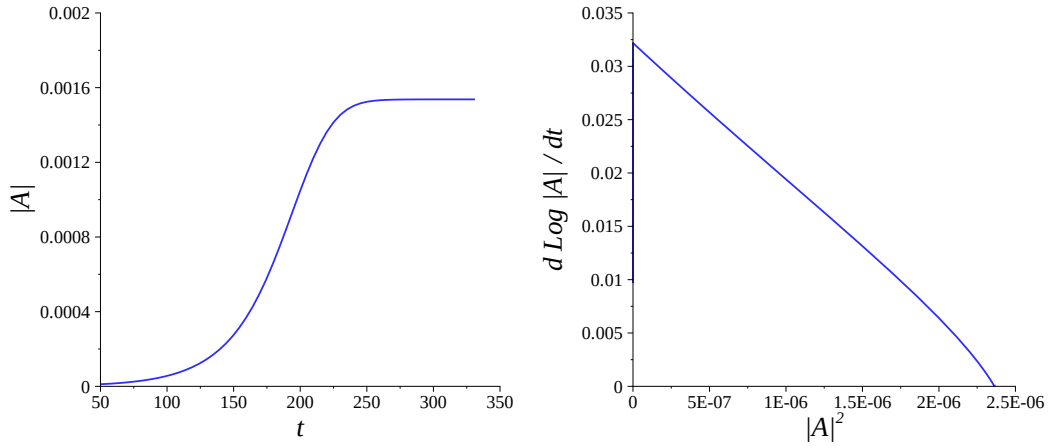

(a) Time history of the Mode B instability amplitude evolution.

(b) Derivative of the amplitude logarithm versus amplitude squared plot.

FIGURE 5.21: Plots used to determine the coefficients of the Landau model for the Mode B transition in the flow past a ring with $Ar = 5$ at $Re = 310$. In (b), the linear profile and negative slope near the y–axis indicate that the transition is supercritical.

teristics of the wake to be observed. The far wake (the lower end of the image) shows that the sign of the streamwise vortical braid structures above and below the wake are identical, whereas the sign alternates in the azimuthal direction. This particular vorticity distribution means that the following *qualitative* spatio-temporal symmetry applies to the velocity field: a wake shifted by a half-period in time, and by a half-span in the azimuthal direction is (approximately) identical to the same wake reflected about the wake centreline. Note however that the absence of a reflective symmetry about the wake centreline due to the curvature inherent in the ring geometry renders it impossible for the Mode B wake here to *exactly* satisfy a phase-shifted reflective symmetry about the wake centreline. Qualitatively, the spatio-temporal symmetry observed here for the Mode B wake is consistent with the symmetry described by Barkley & Henderson (1996) for the Mode B instability in the wake of a circular cylinder.

In figure 5.21(a), the evolution of the amplitude of the Mode B instability during linear growth and saturation at $Re = 310$ is shown. Figure 5.21(b) is used to determine the Landau model coefficients. The approximately linear profile and negative gradient in figure 5.21(b) indicate that the Mode B transition occurs through a supercritical bifurcation.

To verify that the transition is supercritical, a plot of $|A|^2$ versus $Re - Re_c$ is

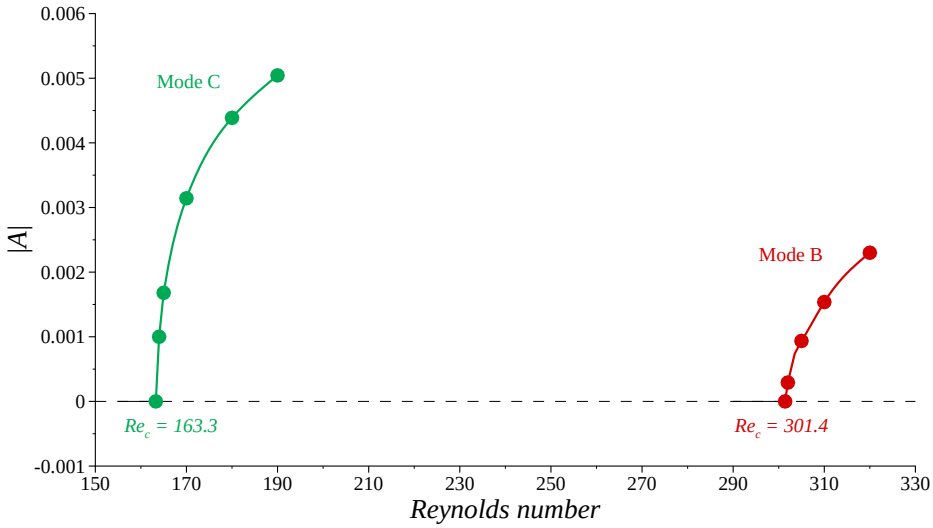

FIGURE 5.22: Mode amplitude $|A|$ versus Reynolds number plot which shows the pure mode bifurcations in the wake behind a ring with $Ar = 5$. Mode A is not included as it is preceded by the shorter-wavelength Mode C instability. Solid lines indicate the pure mode branches, and the dashed lines relate the solution branches. Circles show the computed data points, with Mode C and Mode B coloured green and red, respectively, consistent with preceding chapters.

presented in figure 5.20(b) for the Mode B transition. There is a high degree of linearity present in the vicinity of the transition, and the amplitude of Mode B tends to zero with $Re - Re_c$, indicating that the transition is non-hysteretic, confirming that the transition occurs through a supercritical bifurcation.

5.3.1.3 Non-Axisymmetric Mode Bifurcations

A bifurcation diagram for the non-axisymmetric transitions for $Ar = 5$ is presented in figure 5.22. The continuous supercritical evolution of the Mode C and Mode B transitions is apparent. It is interesting to note the relative magnitude of the two modes, with the longer wavelength Mode C wake reaching approximately twice the magnitude of the shorter wavelength Mode B wake over the same distance from the critical transition Reynolds number.

5.3.1.4 Drag of Non-Axisymmetric Wakes

As an extension to the analysis of the drag coefficients for the axisymmetric flow past rings which was presented in chapter 3, drag coefficients were computed for the non-

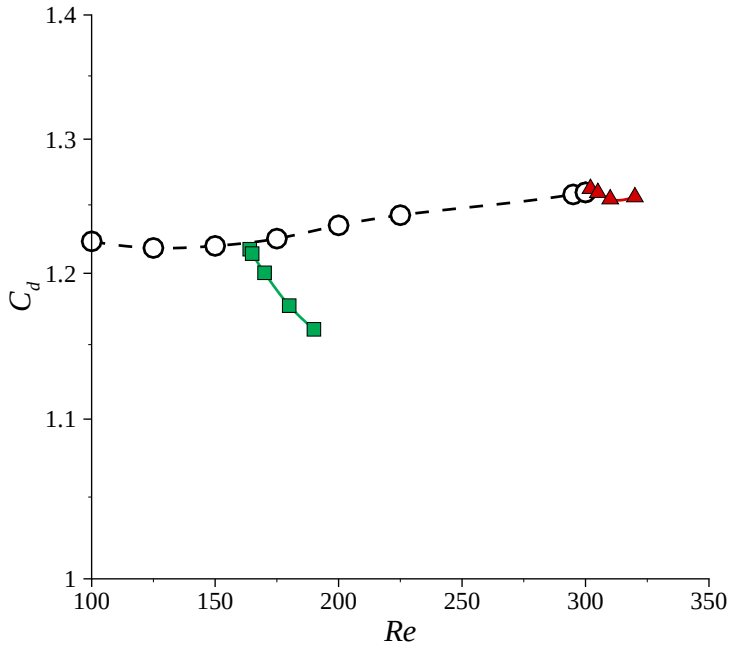

(a) Total drag (C_d).

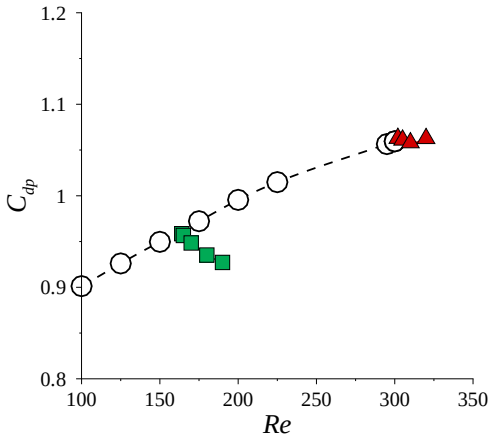

(b) Pressure component (C_{dp}).

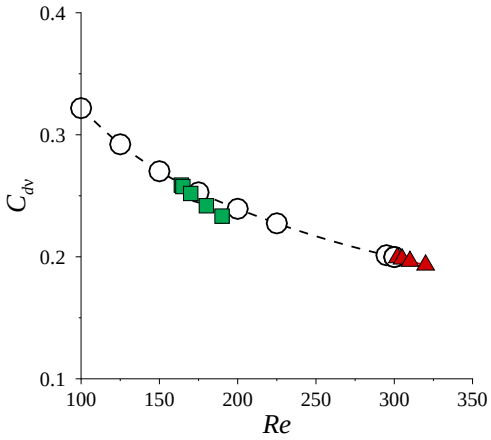

(c) Viscous component ($C_{d\nu}$).

FIGURE 5.23: Total and component drag coefficients computed for the non- axisymmetric bifurcations in the flow past a ring with $Ar = 5$. The previous axisymmetric drag profiles are represented by white circles. The Mode C bifurcation is represented by green squares, and the Mode B bifurcation is represented by red triangles, for consistency with earlier figures.

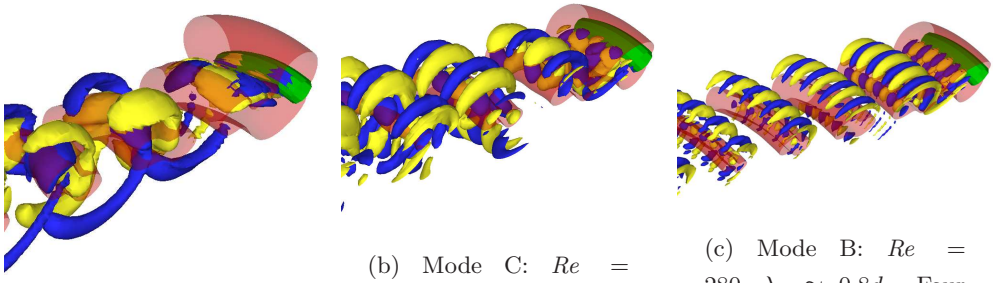

(a) Mode A: $Re = 200$, $\lambda_d \approx 4.0d$.

(b) Mode C: $Re = 235$, $\lambda_d \approx 1.7d$. Two azimuthal periods are shown.

(c) Mode B: $Re = 280$, $\lambda_d \approx 0.8d$. Four azimuthal periods are shown.

FIGURE 5.24: Vortex structure of the saturated non-axisymmetric wakes of a ring with $Ar = 10$ following the pure Mode A (a), Mode C (b) and Mode B (c) instabilities. Contour shading is as per figure 5.18.

axisymmetric bifurcations in the flow past rings as part of the present study.

In figure 5.23, the total drag coefficient (a) and the pressure (b) and viscous (c) components of the drag coefficient are presented, which show the deviation in the computed drag coefficient from the axisymmetric profile of the drag coefficient as the non-axisymmetric modes evolve in the wake. With an increase in Reynolds number, the computed drag for the wakes following the Mode C and Mode B instabilities decrease continuously from the axisymmetric drag profiles. This is consistent with the previous analysis of the modes, which suggested that these instabilities occur through continuous supercritical bifurcations.

Notice that the deviation from the axisymmetric drag profile in figure 5.23 is more pronounced following the Mode C instability than the Mode B instability. As the Mode B instability evolves over a shorter azimuthal wavelength, viscous diffusion limits the non-axisymmetry of the saturated wake. Therefore there is only a small difference between the non-axisymmetric Mode B wake and the axisymmetric wake, in terms of the physical structure and drag coefficient properties. It must be stressed that these computations pertain to the *pure* non-axisymmetric transition modes. The influence of the Mode C wake on the development of the Mode B instability, and the subsequent effect on the drag characteristics is the subject of work presented in chapter 6.

It is clear from the plots of the components of the drag coefficient in figure 5.23(b) and figure 5.23(c) that the evolution of the non-axisymmetric modes alters the pressure

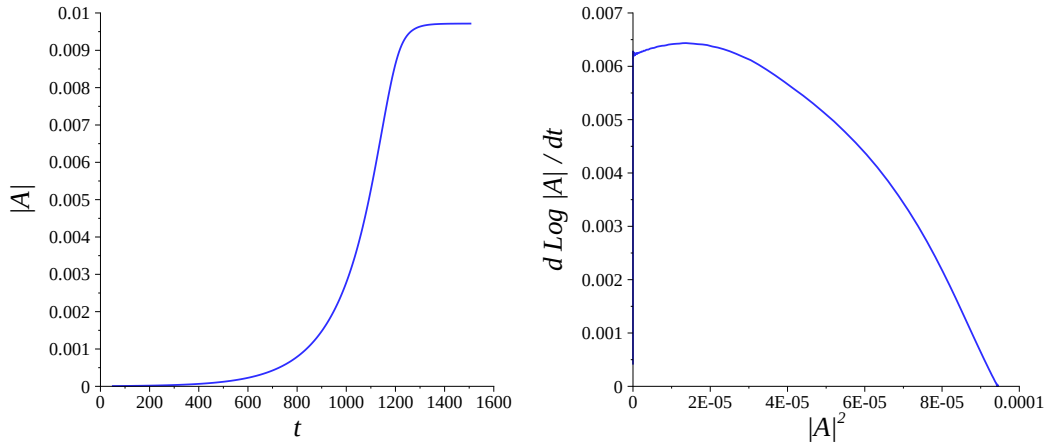

(a) Time history of the Mode A instability amplitude evolution.

(b) Derivative of the amplitude logarithm versus amplitude squared plot.

FIGURE 5.25: Plots used to determine the coefficients of the Landau model for the Mode A transition in the flow past a ring with $Ar = 10$ at $Re = 200$. In (b), the non-linear profile and positive slope near the y–axis indicate that the transition is subcritical.

component of the total drag coefficient far more significantly than the viscous component. This is not unexpected, as the base pressure coefficient (C_{pb}) has been shown to be sensitive to the vortex shedding phenomenon and the development of three-dimensional transitions in the flow past a circular cylinder by Williamson & Roshko (1990). Useful reviews on the subject are also included in Roshko (1993), Norberg (1994) and Williamson (1996c).

5.3.2 Instability Mode Path A-C-B ($Ar = 10$)

In this section, isosurface plots and Landau model predictions are presented for the pure Mode A, C and B instabilities in the flow past a ring with $Ar = 10$. A bifurcation diagram which shows the respective evolution of the modes is also included, and the variation in drag coefficient through the bifurcations is investigated.

5.3.2.1 The Mode A Transition

In figure 5.24, an isosurface plot illustrates the structure of the Mode A wake in the flow past a ring with $Ar = 10$. Features in common with the Mode A wake in the flow past a circular cylinder (Thompson *et al.* 1996; Barkley & Henderson 1996) that are readily identified here are the azimuthal wavelength of the instability of approximately

$4d$, the streamwise vorticity distribution, and the spatio-temporal symmetry.

The computed wake comprises spanwise vortex rollers which are deformed by the evolution of the non-axisymmetric Mode A instability. Every half period, a counter-rotating pair of streamwise vortices are entrained into the braid region on one side of the wake centreline, from the vortex roller in which they first form. This in turn induces the deformation of the underlying rollers observed in the plot. This process is repeated on alternating sides of the wake, every half-period. This process is described in more detail in Williamson (1996b) for the Mode A wake in the flow past a circular cylinder. The sign of the streamwise vortices remains consistent from one period to the next, and are opposite to the sign of the pair of vortices that form on the opposite side of the wake centreline. Thus the spatio-temporal symmetry of the wake is qualitatively similar to the symmetry of Mode A in the wake of the circular cylinder (Barkley & Henderson 1996): namely a half-period shift in time and a reflection about the wake centreline yields an identical wake.

The evolution of the L_2 norm of the Mode A amplitude allows non-linear characteristics of the transition to be determined.

Figure 5.25 shows both the evolution of the amplitude of the Mode A instability, and the plot used to determine the cubic coefficients of a Landau model fit to the data in figure 5.25(a). The positive slope near to the y–axis in figure 5.25(b), and the approximately parabolic profile suggest that the transition occurs through a subcritical bifurcation.

In order to verify the Landau model prediction of a subcritical Mode A instability, a plot of $|A|^2$ versus $Re - Re_c$ is provided in figure 5.26(a). Saturated mode amplitudes were computed at several Reynolds numbers in the vicinity of the transition, which confirm that the amplitude of the Mode A instability does not approach zero as $Re - Re_c$ approaches zero. The onset of the transition is hysteretic, which is consistent with observations of the Mode A transition in the flow past a circular cylinder (Henderson 1997).

5.3.2.2 The Mode C Transition

The saturated wake which evolves from the Mode C instability in the flow past a ring with $Ar = 10$ is qualitatively similar in structure to the wake which evolves from the Mode C instability in the flow past a ring with $Ar = 5$ described previously. An

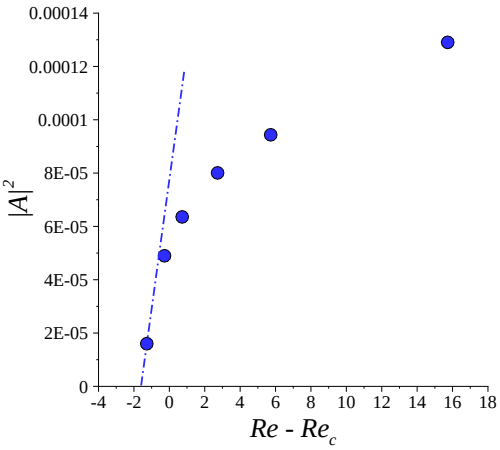

(a) Weakly hysteretic behaviour of a pure Mode A instability with $Re_c = 194.3$.

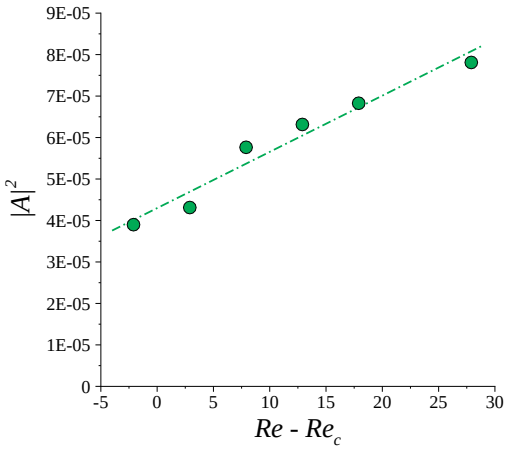

(b) Hysteretic behaviour of a pure Mode C instability with $Re_c = 222.1$.

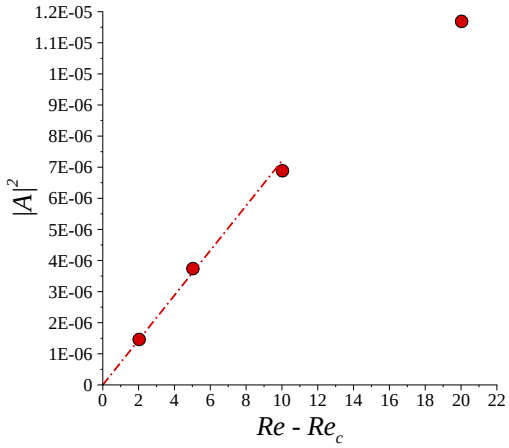

(c) Non-hysteretic behaviour of a pure Mode B instability with $Re_c = 270.0$.

FIGURE 5.26: Plots of $|A|^2$ with $Re - Re_c$ in the vicinity of the transitions for the pure Mode A (a), Mode C (b) and Mode B (c) instabilities in the wake behind a ring with $Ar = 10$. The dots represent the measured amplitudes, and the lines provide approximate fits to the data in the vicinity of $Re - Re_c = 0$.

isosurface plot of the Mode C wake is presented in figure 5.24(b). Again, the Mode C instability evolves with an azimuthal wavelength of approximately $1.7d$, and the spatio-temporal symmetry characteristics show that it is subharmonic. The distribution of streamwise vortical structures is consistent with the Mode C wake in the flow past a ring with $Ar = 5$, despite minor differences in orientation of the pairs of streamwise vortical structures with respect to the rollers of the vortex street. These differences are assumed to be due to the reduction in ring curvature with an increase in aspect ratio, which increases the symmetry between the vortex rollers shed from the inner and outer surface of the ring cross-section.

The L_2 norm of the amplitude of the Mode C instability is used to determine the coefficients of the Landau model for the growth and saturation of the transition. In figure 5.27(a) the growth and saturation of the Mode C instability at $Re = 230$ is shown. Figure 5.27(b) is used to estimate the cubic coefficients of the Landau model. Surprisingly, a positive gradient is observed near to the y–axis, and the plot is highly non-linear. This represents an acceleration in the growth as the instability evolves beyond the linear regime, which suggests that the transition occurs through a subcritical bifurcation. Recall that the Landau coefficients which were calculated for the Mode C transition in the flow past a ring with $Ar = 5$ suggested that the transition occurred through a supercritical bifurcation with fifth-order terms required to describe the transition to saturation. Here, the l–term of the Landau model has changed sign, which requires at least a fifth-order truncation of the Landau equation to describe the transition to saturation.

It is proposed that fifth-order terms are required to describe the evolution to saturation of both the subcritical and supercritical Mode C instabilities in the flow past rings, and that the cubic l–term changes in sign at some aspect ratio in the range $5 < Ar < 10$. It is probable that the Mode C instability is supercritical in the flow past rings with smaller aspect ratios (which includes $Ar = 5$), and subcritical in the flow past larger rings (which includes $Ar = 10$). The physical mechanism which is responsible for the change in hysteretic behaviour has not yet been determined, however, it may be associated with the increased asymmetry in the vortex street at smaller aspect ratios.

The variation in the square of the saturated Mode C amplitude ($|A|^2$) with $Re - Re_c$ is presented in figure 5.26(b). The hysteretic onset of the transition is clearly evident,

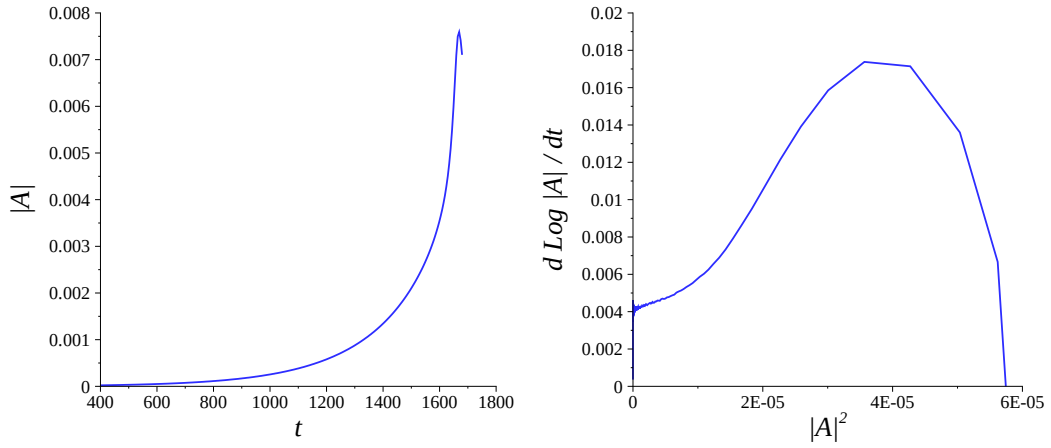

(a) Time history of the Mode C instability amplitude evolution.

(b) Derivative of the amplitude logarithm versus amplitude squared plot.

FIGURE 5.27: Plots used to determine the coefficients of the Landau model for the Mode C transition in the flow past a ring with $Ar = 10$ at $Re = 230$. In (b), the non-linear profile and positive slope near the y–axis indicate that the transition is subcritical.

with non-zero saturated amplitudes computed at Reynolds numbers $Re - Re_c \approx -2$.

5.3.2.3 The Mode B Transition

An isosurface plot which shows the non-axisymmetric structure of the saturated Mode B wake in the flow past a ring with $Ar = 10$ is presented in figure 5.24(c). Notwithstanding the alteration in wake trajectory due to the difference in aspect ratio, the wake is qualitatively similar to the Mode B wake in the flow past a ring with $Ar = 5$. The azimuthal wavelength of the instability (approximately $0.8d$), the spatio-temporal symmetry, and the distribution of non-axisymmetric vortical structures are all consistent with both the Mode B wake in the flow past a ring with $Ar = 5$, and previous experimental (Williamson 1988b) and numerical (Thompson *et al.* 1996; Henderson 1997) observations of the Mode B wake in the flow past a circular cylinder.

Coefficients of a cubic Landau equation are evaluated for the evolution of the Mode B instability for $Ar = 10$. Figure 5.28(a) shows the growth and saturation of the amplitude of the Mode B instability in the wake, and figure 5.28(b) shows the plot used to determine the coefficients of the Landau model. The negative gradient and approximately linear profile indicates that the transition occurs through a supercritical bifurcation. This prediction is consistent with both the Mode B wake in the flow past a

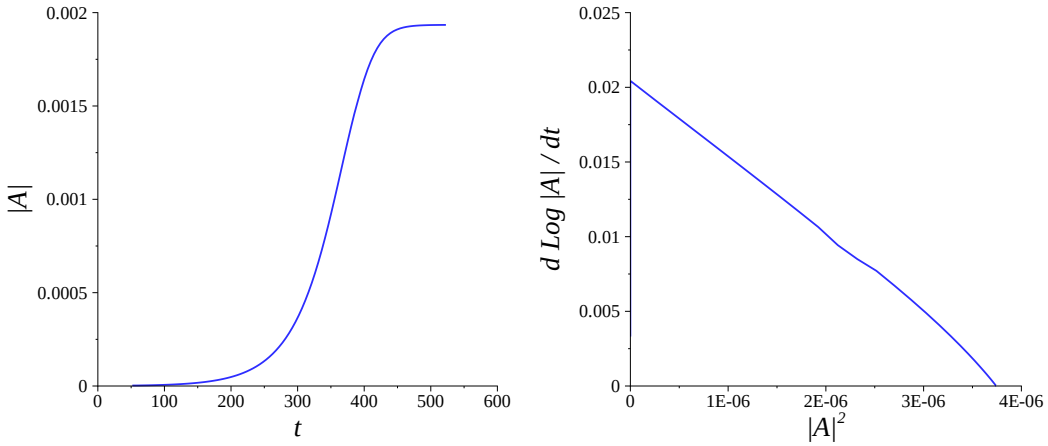

(a) Time history of the Mode B instability amplitude evolution.

(b) Derivative of the amplitude logarithm versus amplitude squared plot.

FIGURE 5.28: Plots used to determine the coefficients of the Landau model for the Mode B transition in the flow past a ring with $Ar = 10$ at $Re = 275$. In (b), the linear profile and negative slope near the y–axis indicate that the transition is supercritical.

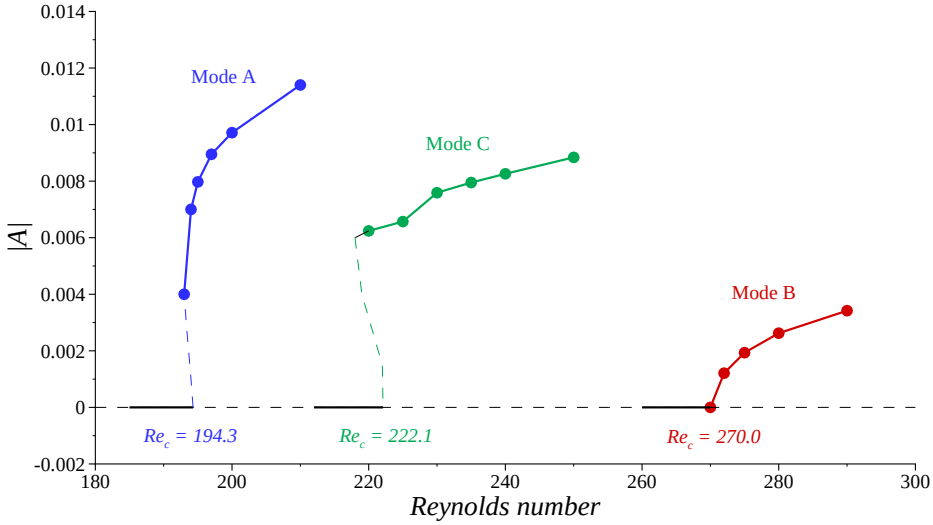

FIGURE 5.29: Mode amplitude $|A|$ versus Reynolds number plot which shows the pure mode bifurcations in the wake behind a ring with $Ar = 10$. Solid lines indicate the pure mode branches, and the dashed lines relate the solution branches. Circles show the computed data points, and are coloured as per figure 5.22, with Mode A represented by blue dots.

ring with $Ar = 5$ presented previously, and the Mode B wake in the flow past a circular cylinder (Henderson 1997).

5.3.2.4 Non-Axisymmetric Mode Bifurcations

A bifurcation diagram for the non-axisymmetric transitions for $Ar = 10$ is presented in figure 5.29. The plot is interesting, as the predicted weak hysteretic region at the onset of the Mode A transition is shown, as is the well defined region of hysteresis at the onset of the Mode C transition. The Landau model predictions are satisfied, as the Mode B transition is observed to bifurcate through a continuous supercritical transition.

5.3.2.5 Drag of Non-Axisymmetric Wakes

In figure 5.30, the total and component drag coefficients measured from the non-axisymmetric wakes that evolve from the Mode A, Mode C and Mode B instabilities in the flow past a ring with $Ar = 10$ are presented.

The drag coefficients for the three instability modes bifurcate from the axisymmetric drag profile towards smaller values. This observation, and the observation that the magnitude of the drag reduction increases with an increase in the azimuthal wavelength of the non-axisymmetric mode, are consistent with the previous non-axisymmetric drag measurements from the flow past a ring with $Ar = 5$. The Mode A instability displays a reduction in drag coefficient of approximately 5% over an increase in the Reynolds number of approximately $\Delta Re \approx 20$.

As with the earlier observations of the flow past a ring with $Ar = 5$, the majority of the drag coefficient reduction is a result of a decrease in the pressure component of the drag coefficient for the non-axisymmetric modes, shown in figure 5.30(b). The viscous component of the drag coefficient is almost unchanged between the axisymmetric and non-axisymmetric measurements in figure 5.30(c).

5.3.3 Instability Mode Path A-B-C ($Ar = 20$)

In this section, isosurface plots and Landau model predictions are presented for the pure Mode A and B instabilities in the flow past rings with $Ar = 20$. A bifurcation diagram which shows the respective evolution of the two modes is also included, and the variation in drag coefficient through the bifurcations is investigated.

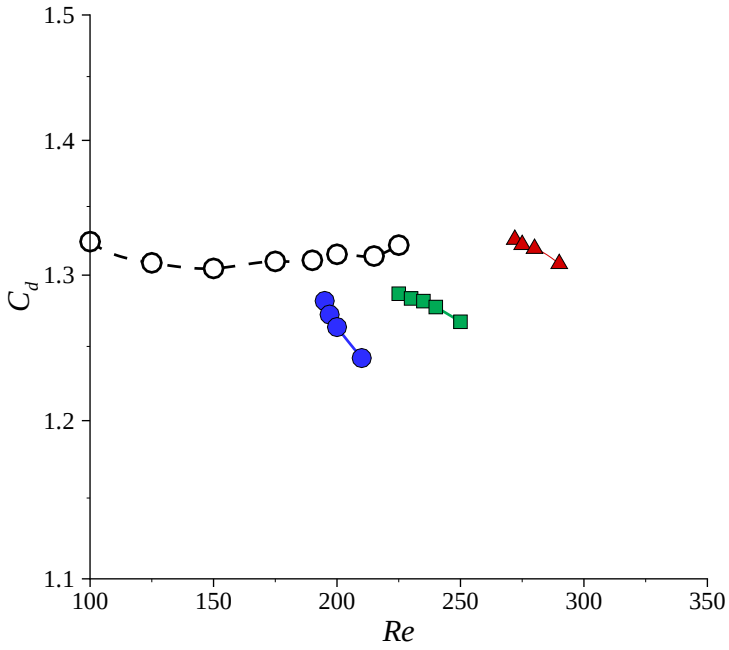

(a) Total drag (C_d).

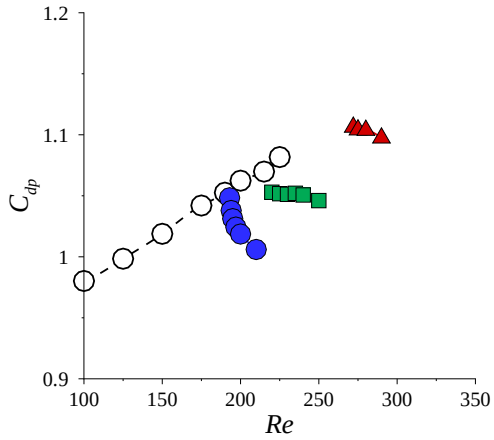

(b) Pressure component (C_{dp}).

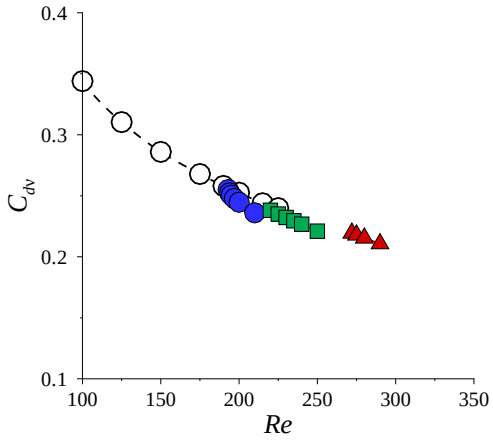

(c) Viscous component ($C_{d\nu}$).

FIGURE 5.30: Total and component drag coefficients computed for the non- axisymmetric bifurcations in the flow past a ring with $Ar = 10$. Colours and symbols are as per figure 5.23, with the additional drag measurements following the Mode A instability being represented by blue circles.

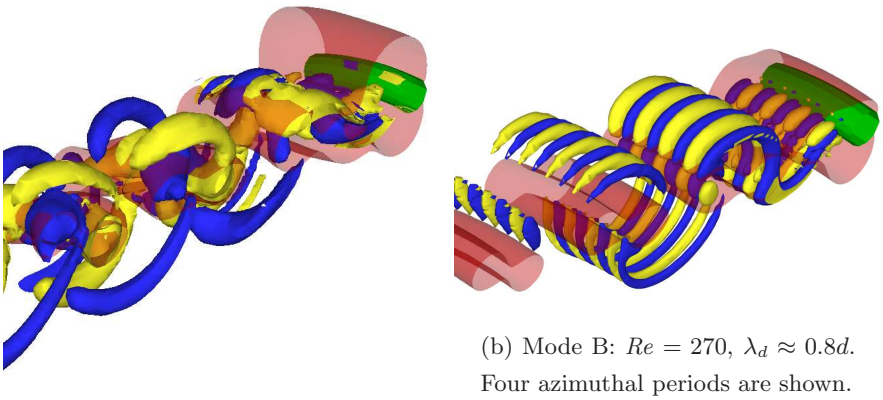

(a) Mode A: $Re = 200$, $\lambda_d \approx 4.0d$.

(b) Mode B: $Re = 270$, $\lambda_d \approx 0.8d$. Four azimuthal periods are shown.

FIGURE 5.31: Vortex structure of the saturated non-axisymmetric wakes of a ring with $Ar = 20$ following both the pure Mode A (a) and Mode B (b) instabilities. Contour shading is as per figure 5.18.

5.3.3.1 The Mode A Transition

The saturated wake from the evolution of the Mode A instability for a ring with $Ar = 20$ is presented in figure 5.31(a). It may be observed that the mode has an azimuthal wavelength of approximately $4d$, consistent with the corresponding Mode A wake behind a ring with $Ar = 10$. The dye visualisation experiments of Williamson (1988b) also observe a similar wavelength for the Mode A wake behind a circular cylinder, as do the computations of Thompson *et al.* (1994, 1996), and Henderson (1997).

The periodicity of the Mode A wake locked to the vortex street rollers is maintained, as are the spatio-temporal symmetry characteristics, and streamwise vorticity distributions described earlier for the Mode A wake for $Ar = 10$. The small body curvature of a ring with $Ar = 20$ enhances the similarity between the Mode A wake presented here, and the Mode A wake behind a circular cylinder. A useful comparison may be made with the isosurface plots of Mode A in the wake of a circular cylinder by Thompson *et al.* (1994, 1996), which use a similar colouring scheme.

The evolution of the Mode A wake at $Re = 195$ for $Ar = 20$ is monitored to evaluate the coefficients of the Landau model. Figure 5.32(a) shows the growth and saturation of the Mode A amplitude, and figure 5.32(b) shows the non-linear variation in growth rate with $|A|^2$ that is used to evaluate the pertinent coefficients of the Landau model.

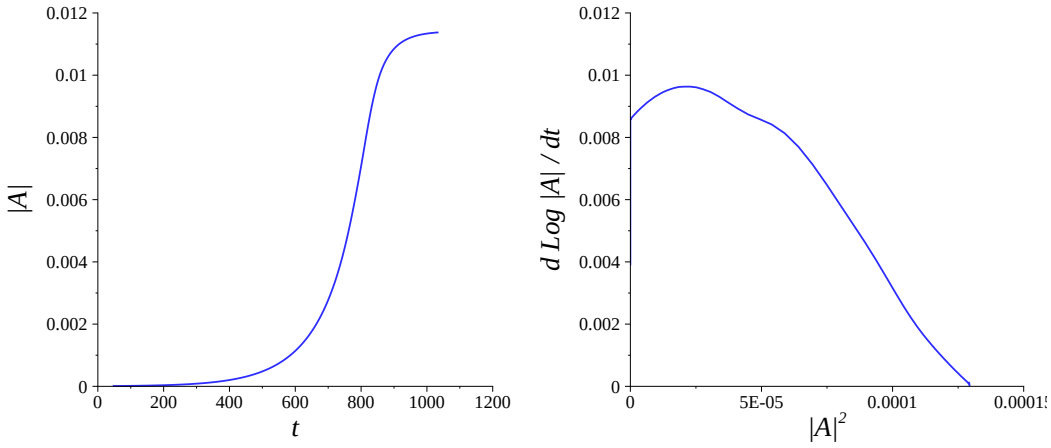

(a) Time history of the Mode A instability amplitude evolution.

(b) Derivative of the amplitude logarithm versus amplitude squared plot.

FIGURE 5.32: Plots used to determine the coefficients of the Landau model for the Mode A transition in the flow past a ring with $Ar = 20$ at $Re = 195$. In (b), the non-linear profile and positive slope near the y–axis indicates that the transition is subcritical.

The curve in figure 5.32(b) has a positive gradient in the vicinity of the y–axis, but over the range of $|A|^2$ is highly non-linear. These characteristics suggest that at least fifth-order terms are necessary for the Landau model to describe the saturation, and suggests that the transition occurs through a subcritical bifurcation.

A plot of $|A|^2$ against $Re - Re_c$ is presented in figure 5.33(a), and verifies the hysteresis of the Mode A transition as indicated by the previous analysis. The computed amplitudes do not display a linear trend towards zero as $Re - Re_c \rightarrow 0$, and hence the transition occurs through a subcritical bifurcation. The behaviour presented in (a) indicates that a small region of hysteresis is likely to be found in the vicinity of $Re - Re_c = 0$.

5.3.3.2 The Mode B Transition

The saturated Mode B wake computed for $Ar = 20$ is similar in structure to the Mode B wakes computed for rings with aspect ratios $Ar = 5$ and $Ar = 10$. An isosurface plot of the wake is presented in figure 5.31(b). The azimuthal wavelength of the mode (approximately $0.8d$) is maintained, as is the spatio-temporal symmetry and vorticity distribution described earlier.

The streamwise vortical structures dissipate more rapidly in figure 5.31(b) than for

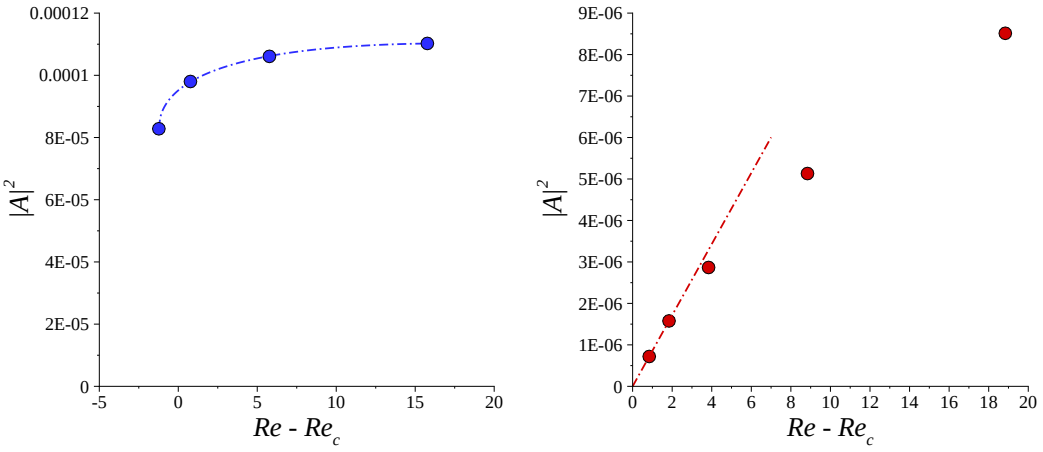

(a) Hysteretic behaviour of a pure Mode A instability with $Re_c = 186.3$.

(b) Non-hysteretic behaviour of a pure Mode B instability with $Re_c = 261.2$.

FIGURE 5.33: Plots of $|A|^2$ with $Re - Re_c$ in the vicinity of the transitions for both the pure Mode A (a) and Mode B (b) instabilities in the wake behind a ring with $Ar = 20$. The dots represent the measured amplitudes, and the lines provide approximate fits to the data.

the Mode B wakes observed for rings with $Ar = 5$ and $Ar = 10$. In fact the mode appears to be concentrated within approximately $10d$ of the ring cross-section. This is consistent with numerical computations of the Mode B wake behind a circular cylinder. Both Thompson *et al.* (1996) and Henderson (1997) show that Mode B structures decay rapidly after $8d$ to $10d$ downstream in the circular cylinder wake.

The evolution of the Mode B instability to saturation was monitored in the wake behind a ring with $Ar = 20$ to evaluate the coefficients of the Landau model. Plots which show the growth and saturation of the Mode B instability and the non-linear growth rate variation are presented in figure 5.34.

In figure 5.34(b), both a negative gradient in the vicinity of the y–axis and a linear profile throughout the $|A|^2$ range is observed. Based on this behaviour, the Landau model suggests that the transition occurs through a supercritical bifurcation.

The variation in $|A|^2$ with $Re - Re_c$, presented in figure 5.33(b), shows that the Landau model correctly predicts the supercritical behaviour of the Mode B transition. The continuous bifurcation from $|A|^2 = 0$ of $|A|^2$ beyond the transition Reynolds number ($Re - Re_c \geq 0$) is consistent with a supercritical bifurcation, and shows that no hysteresis exists for the Mode B transition.

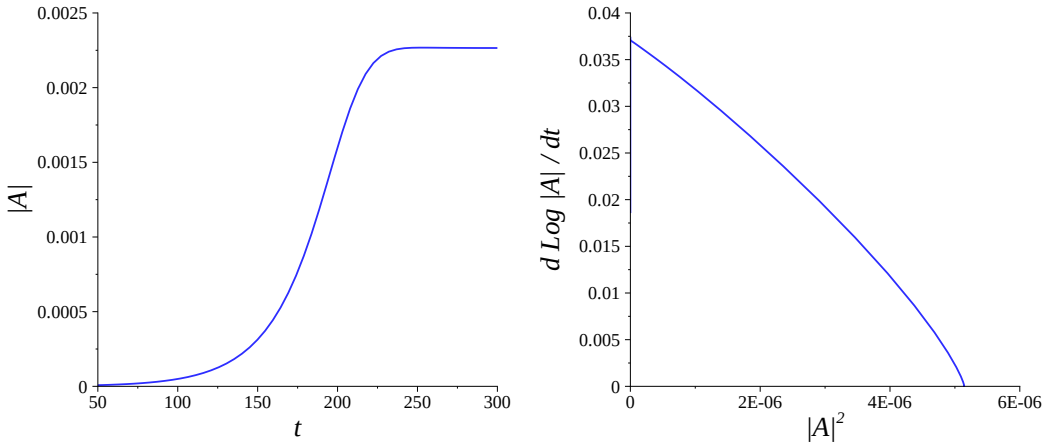

(a) Time history of the Mode B instability amplitude evolution.

(b) Derivative of the amplitude logarithm versus amplitude squared plot.

FIGURE 5.34: Plots used to determine the coefficients of the Landau model for the Mode B transition in the flow past a ring with $Ar = 20$ at $Re = 270$. In (b), the linear profile and negative slope near the y–axis indicates that the transition is supercritical.

5.3.3.3 Non-Axisymmetric Mode Bifurcations

A bifurcation diagram for the non-axisymmetric transitions in the wake behind a ring with $Ar = 20$ is presented in figure 5.35. The hysteretic region at the onset of the Mode A transition can be observed, which is in agreement with the prediction that this transition occurs though a subcritical bifurcation. Again, the Mode B instability adopts the familiar continuous supercritical bifurcation behaviour observed previously.

5.3.3.4 Drag of Non-Axisymmetric Wakes

In figure 5.36, the total and component drag coefficients measured from the non-axisymmetric wakes that evolve from the Mode A and B instabilities in the flow past a ring with $Ar = 20$ are presented.

Figure 5.36 shows that the Mode A instability in the wake behind a ring with $Ar = 20$ produces a sharp and discontinuous drop in the drag coefficient, owing to the subcritical nature of the transition. This reduction is approximately 7% over a Reynolds number range $\Delta Re \approx 10$. Likewise, the pure wake that evolves from the Mode B instability results in a reduction in drag. The supercritical nature of the Mode

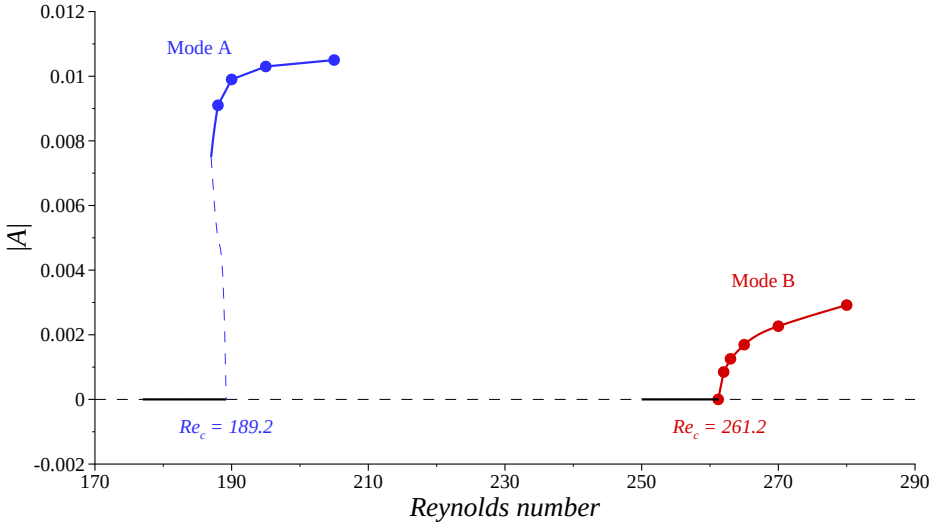

FIGURE 5.35: Mode amplitude $|A|$ versus Reynolds number plot which shows the pure mode bifurcations in the wake behind a ring with $Ar = 20$. Solid lines indicate the pure mode branches, and the dashed lines relate the solution branches. Circles show the computed data points, and are coloured as per figures 5.22 and 5.29.

B transition causes the non-axisymmetric drag profile deviate continuously from the axisymmetric profile. The subcritical nature of the Mode A transition is highlighted again in figure 5.36(b). Comparing against figure 5.36(c), it is again apparent that the drag reduction is caused by a loss of pressure drag, and that mean viscous drag losses are negligible.

5.4 Experimental Verification of the Existence of a Mode C Wake

Clearly, the most striking result to be obtained from the numerical computations performed in this chapter is the existence of a subharmonic wake that evolves from the intermediate-wavelength Mode C instability. In this section, an attempt is made to obtain experimental dye-visualisation images of the Mode C wake. The experimental setup is described in Chapter 2, however the variance between the numerical and experimental models used is treated here.

To gain a meaningful visual comparison with the numerical flow fields and the experimental dye visualisations achieved, the simulation of injected particles is performed, and the three-dimensional particle fields are post-processed to replicate the Fluorescein

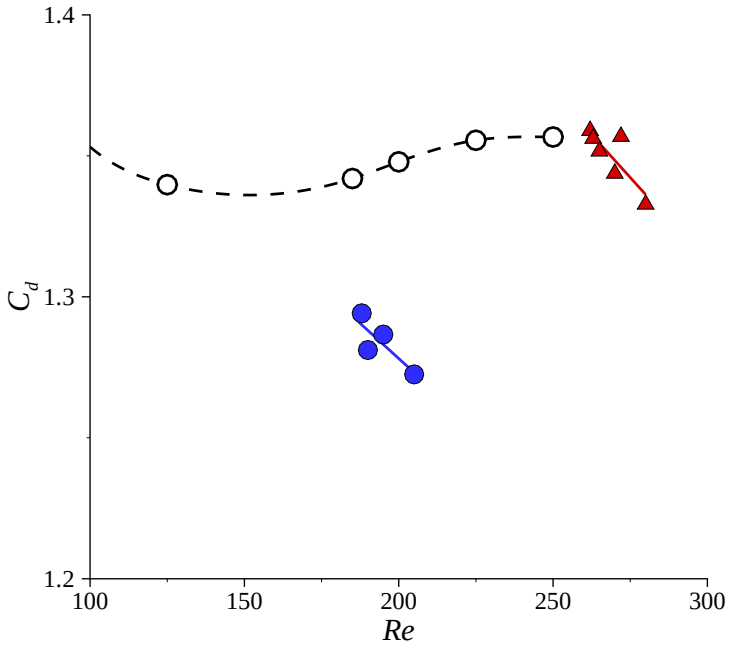

(a) Total drag (C_d).

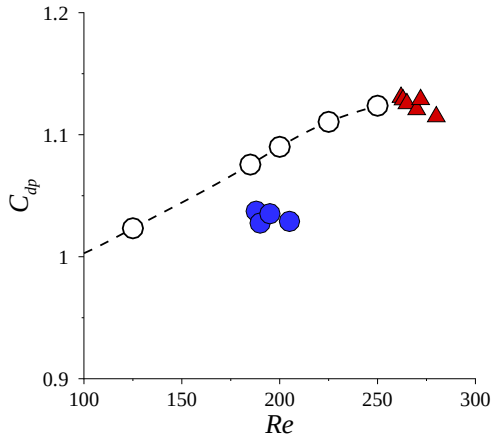

(b) Pressure component (C_{dp}).

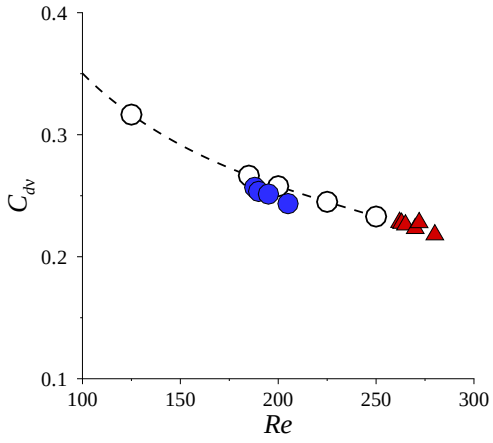

(c) Viscous component ($C_{d\nu}$).

FIGURE 5.36: Total and component drag coefficients computed for the non- axisymmetric bifurcations in the flow past a ring with $Ar = 10$. Colours and symbols are as per figure 5.23 and figure 5.30.

dye used in the experiments.

5.4.1 Comparison Between Experimental and Computational Results

The present experiments and numerical computations are limited to the aspect ratio $Ar = 4.94$, which was measured from the ring employed in the experiments performed for the present study. Although this aspect ratio is very close to $Ar = 5$, for which the flow has been computed throughout this work, a special mesh was created to model a ring with $Ar = 4.94$ to achieve the best possible consistency between the numerical and experimental cases. From a linear stability analysis of the axisymmetric flow past a ring with $Ar = 5$, presented in the preceding chapter, it was expected that the flow past a ring with $Ar = 4.94$ would exhibit vortex shedding for $Re \gtrsim 60$, and for Reynolds numbers $160 \lesssim Re \lesssim 195$ it was expected that a pure Mode C instability would evolve.

Experimental runs at Reynolds numbers exceeding the critical Reynolds number for the onset of the Mode C instability produced a variety of non-axisymmetric wake flows. These wakes included oblique (or helical) and transverse modes, where a transverse motion was imparted on the tethered ring, and parallel vortex shedding modes with wavelengths corresponding to both the Mode C and Mode A instabilities. The evolution of these wakes depended on the startup conditions within the tank, as the uniformity of the wakes was extremely sensitive to even small fluid motions within the tank, such as convection effects from the walls. Despite this, wake structures were observed during some experiments with an azimuthal wavelength consistent with the Mode C instability.

5.4.1.1 An Instability with an Azimuthal Wavelength which Corresponds to Mode C

Some experiments at both $Re = 200$ and $Re = 210$ produced a consistent parallel vortex shedding pattern, which developed non-axisymmetric instabilities which were periodic in the azimuthal direction, with an azimuthal wavelength of $1.5d \lesssim \lambda_d \lesssim 2d$. In figure 5.37 and figure 5.38, the experimental dye visualisations of these non-axisymmetric wakes are compared with the numerical particle trace computations of a saturated Mode C wake.

In figure 5.37, the experimental dye visualisation images show the presence of dye in the background from a previous run, and limited dye entraining into the wake. These images were captured as the ring was returning to the surface, and have been reproduced here upside-down for consistency with the other experimental dye visualisations

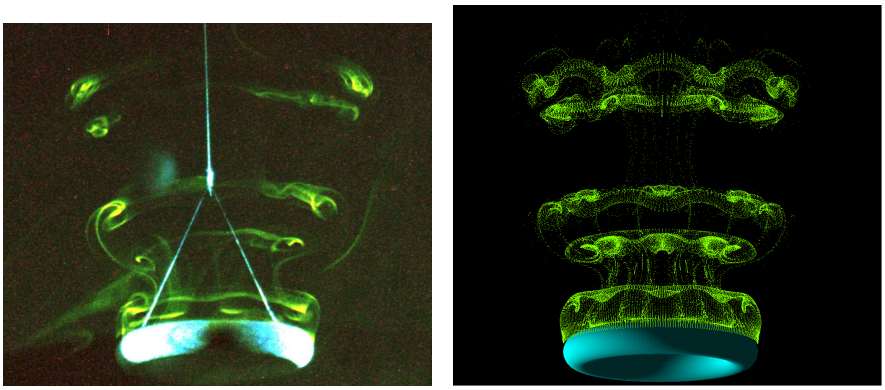

(a) Comparison 1. Left: Experimental dye visualisation. Right: Simulated-particle visualisation.

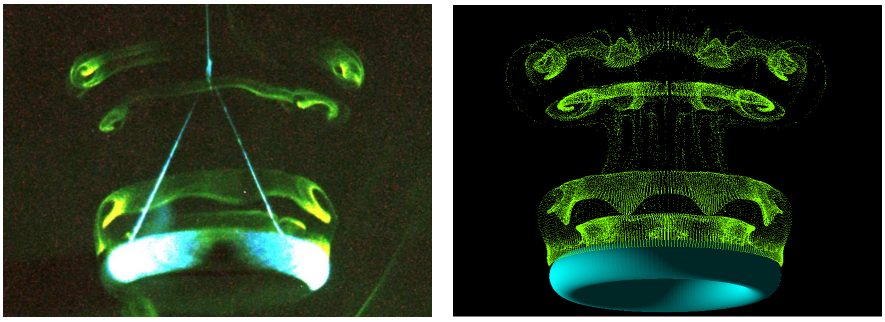

(b) Comparison 2. Left: Experimental dye visualisation. Right: Simulated-particle visualisation.

FIGURE 5.37: Comparisons between experimental observations of a non-axisymmetric disturbance with a Mode C wavelength, and a computed saturated Mode C wake. A ring with $Ar = 4.94$ at $Re = 200$ is considered.

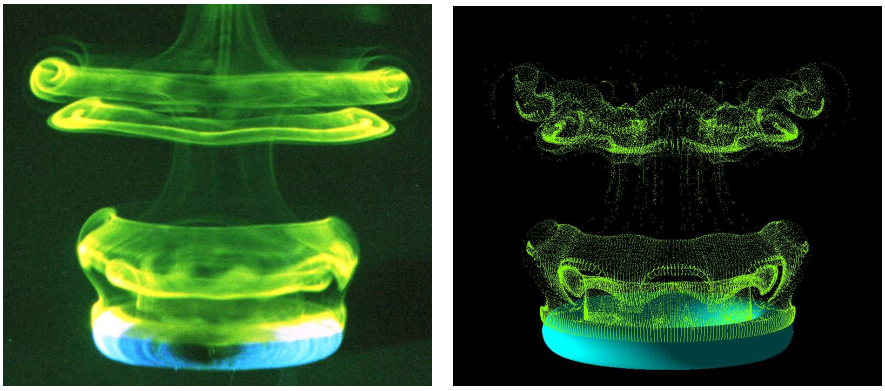

FIGURE 5.38: Comparison between experimental observations (left) of a non-axisymmetric disturbance with a Mode C wavelength, and a computed saturated Mode C wake (right). A ring with $Ar = 4.94$ at $Re = 210$ is considered.

displayed.

The closest consistency between the experimental and numerical visualisations that comprise figures 5.37 and 5.38 is found in the near-wake region, within $2d$–$3d$ downstream of the ring. The uniformity of the far wake was often lost due to non-uniformity of the flow in the tank. The important observations to make from these figures is that in the near-wake region, the azimuthal span of the repeating asymmetric structures, and the orientation of the wavy deformations of the vortex rollers suggests that a Mode C instability was captured in each case.

5.4.1.2 An Instability with an Azimuthal Wavelength which Corresponds to Mode A

As mentioned, the instabilities of the vortex street of the ring used in the present experiments are perturbed by non-uniformities such as slow convective cells in the tank. During some experimental runs, an instability with a wavelength similar to Mode A (approximately $4d$) was observed to develop in the wake. Numerical computations that are initiated from an axisymmetric wake are unable to capture this mode in the wake, as the Mode C instability evolves with a faster growth rate. To overcome this problem, an artificial startup condition was created by constructing a wake with a wavy deformation in the streamwise direction of approximately $1d$. This deformation decays over long times scales (hundreds of shedding cycles) to an axisymmetric wake. The images captured from simulated-particle computations for the comparison in figure 5.39 were obtained at an intermediate stage of the decay, and show a remarkable agreement with the experimental dye visualisation images presented.

5.4.2 Discussion with Regard to Mode C

A significant result from the numerical studies that comprise the majority of the present study is the discovery of the Mode C instability. The observation a subharmonic instability in a vortex shedding street without a reflective symmetry about the wake centreline is an important contribution to the present understanding of the three-dimensional bifurcation scenarios of a wake comprising a two-dimensional vortex street. It is with great satisfaction, therefore, that the numerical computations of a pure Mode C wake in this chapter are observed to be in excellent agreement with the dye visualisation images captured in the experiments.

Experimental runs at several Reynolds numbers provided a variety of interesting

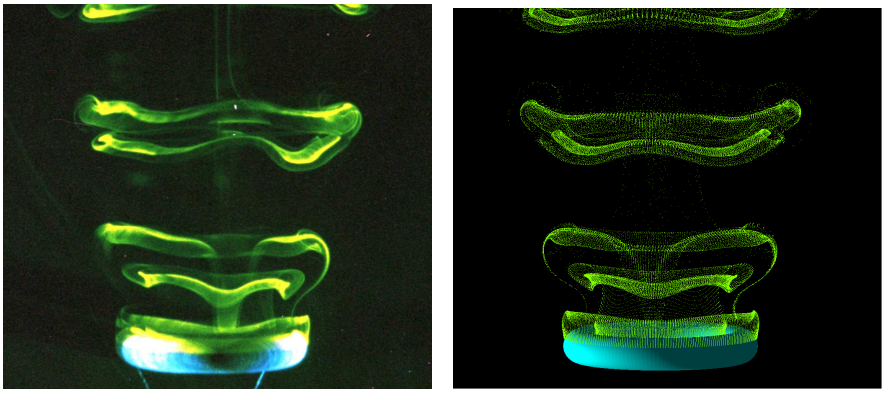

(a) Comparison 1. Left: Experimental dye visualisation. Right: Simulated-particle visualisation.

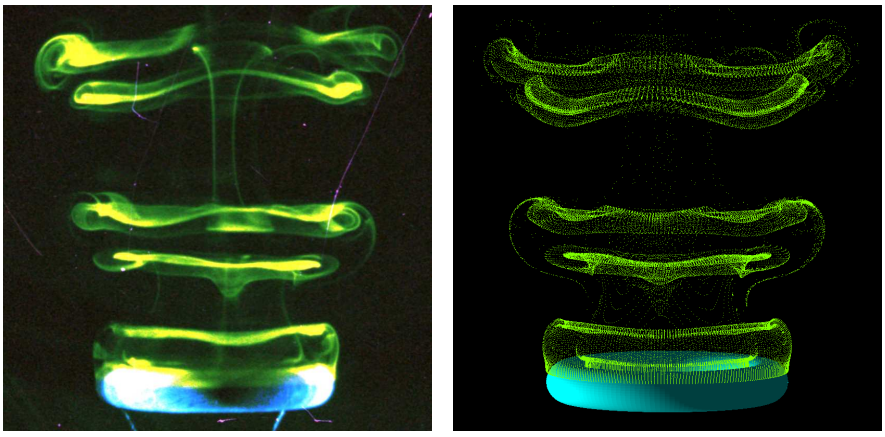

(b) Comparison 2. Left: Experimental dye visualisation. Right: Simulated-particle visualisation.

FIGURE 5.39: Comparisons between experimental observations of a non-axisymmetric disturbance with a Mode A wavelength, and a computed wake with an artificial perturbation of a similar wavelength. A ring with $Ar = 4.94$ at $Re = 200$ is considered.

observable wake structures. At Reynolds numbers $Re \geq 200$, non-axisymmetric deformations in the vortex rings shed into the wake were observed with wavelengths corresponding to both the azimuthal wavelength of the Mode A and Mode C instabilities.

These observations confirm that the Mode C instability exists, and can indeed evolve as the primary non-axisymmetric instability in the wakes behind rings with aspect ratios $Ar \approx 5$. Furthermore, the experiments show that the evolution of the vortex shedding instabilities is very sensitive to non-uniformities in the flow.

5.5 The Limitations of Azimuthal Computational Domain Size

Thus far, non-axisymmetric computations have employed a computational domain no greater than the azimuthal wavelength of the Mode A instability. It was shown that the Mode A instability has the longest azimuthal wavelength of the three asymmetrical vortex shedding modes of the ring (approximately $3.9d$ at the critical Reynolds number of the instability.

This restriction in the computational domain has excluded any longer-wavelength azimuthal modes to evolve in the wake. Linear stability analysis successfully showed in chapter 4 that the axisymmetric wake of the rings is absolutely stable to all longer-wavelength instability modes. The linear stability analysis technique employed in this work cannot be applied to irregular long-wavelength azimuthal disturbances such as vortex dislocations and oblique shedding modes, such as those that have been observed experimentally in the wake of the straight circular cylinder (Williamson 1989) and the ring (Leweke & Provansal 1995). Furthermore, the breakdown of the regular wake patterns of the primary three-dimensional instability as the Reynolds number is further increased (see Henderson 1997) for a study of the pattern breakdown of the wake of a circular cylinder), due to non-linear interaction with other instability modes cannot be described by a linear stability analysis technique.

In the chapter to follow, it is shown how the limitations of the analysis techniques applied thus far may be overcome. Computations are performed over a larger azimuthal domain, and a detailed analysis of the energy contributions of different azimuthal modes to the overall wake dynamics of the larger systems is presented.

5.6 Chapter Summary

This chapter presents, for the first time, numerical computations of the non-axisymmetric flow past rings. Flows have been computed for aspect ratios in the Mode I, II and III flow regimes, as well as for aspect ratios that have been chosen to capture the three vortex street instabilities in the flow past rings.

In the Mode I regime, the steady and unsteady wakes that evolve at Reynolds numbers above the critical transition Reynolds numbers have been computed, with the computed wakes displaying the double-threaded and vortex-loop wake structures,

respectively, which are consistent with the wakes observed in the flow past a sphere (Johnson & Patel 1999). In the Mode II regime, the unsteady wake that evolves beyond the critical transition Reynolds number was computed, with the computed wake structure comprising a stable near-wake region, and a long-timescale oscillation further downstream as vorticity is shed into the wake. In the Mode III regime, the steady and unsteady wakes that evolve at Reynolds numbers beyond the critical transition Reynolds numbers have been computed, with the steady wake displaying an asymmetry localised to the annular recirculation ring behind the ring, whereas the unsteady wake displayed a vortex-loop wake structure similar to the secondary instability in the Mode I regime.

Although non-axisymmetric vortex-loop shedding was observed behind some rings with aspect ratios corresponding to the Mode I–III flow regimes by Monson (1983), the results presented in this chapter provide a far more detailed description of the wake structure and bifurcation scenarios over this aspect ratio range.

An open question that remains to be answered is whether or not the vortex-loop wakes computed here are replaced by axisymmetric annular vortex streets at higher Reynolds numbers, as observed in the experiments of Bearman & Takamoto (1988).

The non-axisymmetric instability modes in the annular vortex streets behind rings have been computed for aspect ratios $Ar = 5$, 10 and 20. The variation in vortex street inclination angle with aspect ratio results in a variation in reflective asymmetry about the ring cross-section, which has enabled the first reported systematic study of the bifurcation scenario for vortex streets which lack a reflective wake symmetry to be completed in the study presented in this chapter. The Mode A and B instabilities have been successfully computed, and a non-linear analysis of the evolution of the modes has confirmed that these modes bifurcate through subcritical and supercritical transitions, respectively, consistent with the bifurcations in the vortex street behind a circular cylinder (Henderson 1997).

This study presents the first reported computations of the non-linear bifurcation properties of a subharmonic instability of a vortex street. This Mode C instability was shown in the present study to bifurcate through a supercritical transition at smaller aspect ratios, and to bifurcate through a subcritical transition at larger aspect ratios. Furthermore, it was established that at least fifth-order terms are required to describe the evolution of the Mode C instability with the Landau equation, for the aspect ratios

considered in the present study.

In the experimental study by Monson (1983), flow visualisation indicated the presence of a waviness in the annular vortex streets behind rings. In the present study, the non-axisymmetric instability modes are visualised with both simulated-particle computations and experimental dye visualisation. The wavy patterns that are observed in the vortex streets in these flow visualisations suggest that the waviness observed by Monson may have been due to the instabilities of the type computed in the present study.

Chapter 6

Route to Chaos in Vortex Streets in the Flow past Rings

In the previous chapters, axisymmetric computations have revealed features of the flow past rings such as flow separation and vortex shedding. With application of a linear stability analysis technique, and non-axisymmetric computations, predictions of the non-axisymmetric modes in the flow past rings have also been verified.

In a study by Henderson (1997), the flow past a circular cylinder was computed to determine the influence of longer-wavelength spanwise modes on the wakes associated with the Mode A and B instabilities. In that study, Henderson addressed the question as to the route to turbulence in a vortex street. Other studies had proposed that the route to chaos in a vortex street was through a period-doubling cascade. A study of an externally driven row of vortices by Braun *et al.* (1998) determined that the route to chaos occurred through a period-doubling cascade. A study of the flow past a circular cylinder by Tomboulides *et al.* (1992) determined that the route to chaos for a vortex street occurred through a period-doubling cascade. In that study, three-dimensional computations were employed with a spanwise domain of insufficient length to capture the Mode A instability in the wake. The suppression of the Mode A instability altered the three-dimensional bifurcation scenario, and called into question the accuracy of the proposal for the route to chaos. A period-doubling cascade involves a succession of doublings of the period of oscillation of a flow, which leads to a chaotic state with no clearly defined periodicity. That behaviour is consistent with flow characteristics at the onset of turbulence for a vortex street, where the periodicity of the wake breaks down (Henderson 1997).

Various attempts have been made to model a vortex street as a series of coupled os-

cillators, by applying the complex Ginzburg–Landau equation (e.g. Leweke & Provansal 1994, 1995). These systems can develop patterns through the development of spatio-temporal chaos, where irregularities evolve in both space and time. Leweke & Provansal modelled the vortex street in the flow past rings with aspect ratios $Ar > 10$ using the Ginzburg–Landau equation. It was determined that the uniform vortex street became unstable to long-wavelength spanwise disturbances in a manner consistent with the development of spatio-temporal chaos. Similarly, in computational studies of the flow past a long circular cylinder, Henderson (1997) observed behaviour consistent with spatio-temporal chaos. Spatio-temporal chaos is displayed by systems in which non-uniformities evolve in both space and time (see Henderson 1997).

As well as the breakdown of a uniform vortex street through spatio-temporal chaos, experimental studies of the flow past a circular cylinder have observed chevron patterns and oblique shedding modes (Williamson 1989; Hammache & Gharib 1991; Williamson 1996b,c). The vortex streets behind rings were shown to exhibit an analogous phenomenon at large aspect ratios (Monson 1983; Leweke & Provansal 1995), with the shedding of helical spirals into the wake.

These studies show that with an increase in Reynolds number or azimuthal domain length, vortex streets become unstable to longer-wavelength instabilities that are not predicted by linear stability analysis. As well as studying the route to turbulence in the vortex streets in the flow past rings through independent variation of both the azimuthal domain size and the Reynolds number, the phenomenon of oblique shedding will briefly be modelled in this chapter, as will transverse shedding modes in the flow past a tethered ring.

6.1 Methodology and Numerical Considerations

The non-axisymmetric formulation of the spectral-element code applied in chapter 5 is employed here. Extra consideration is given to the spatial resolution in both the azimuthal direction, and the z–r plane, to ensure that sufficient Fourier modes are included in the computations to resolve the non-axisymmetric wake, and that the elements of sufficiently high order are employed to capture all the fluid scales in the wake for the Reynolds number range considered ($Re \leq 320$). A spatial resolution study was performed to ascertain the optimum polynomial order for interpolation within the macro elements of the grid. The maximum time step and the accuracy of the computa-

N^2	St	% diff.	C_{d_p}	% diff.	C_{d_ν}	% diff.	C_d	% diff.
16	0.194939	7.416%	1.11310	2.353%	0.120066	0.490%	1.23317	2.083%
25	—	—	—	—	—	—	—	—
36	0.210479	0.036%	1.17795	3.336%	0.124825	4.473%	1.30277	3.444%
49	0.208449	1.000%	1.13895	0.085%	0.119961	0.402%	1.25892	0.038%
64	0.209611	0.448%	1.14279	0.252%	0.120143	0.554%	1.26294	0.281%
81	0.210309	0.116%	1.14023	0.027%	0.119462	0.016%	1.25970	0.024%
100	0.210554	0.0%	1.13992	0.0%	0.119481	0.0%	1.25940	0.0%

TABLE 6.1: Results of the spatial resolution study. N^2 represents the number of nodes per element, St gives the mean Strouhal number of the saturated wake, C_{d_p} is the pressure contribution of the drag coefficient, C_{d_ν} is the viscous component of the drag coefficient, C_d is the total drag coefficient. The percentage differences between the measured Strouhal number and drag coefficient for each N^2 are related to the most resolved model $N^2 = 100$.

tions throughout the Reynolds number range of the study ($170 \leq Re \leq 320$) were also evaluated, and the results of these studies are presented in the sections to follow.

6.1.1 Spatial Resolution

The highest Reynolds number at which computations were performed in this chapter was $Re = 320$. A spatial resolution study was performed for the mesh employed to model the flow past a ring with $Ar = 20$, and the results are summarised in table 6.1. The study computed a single span of the Mode B instability in the flow past a ring with $Ar = 20$ at $Re = 320$. The azimuthal mode number of this computation was $m = 79$, with eight Fourier planes employed to resolve three-dimensional modes of the flow field, corresponding to four azimuthal Fourier modes. The number of Fourier planes was sufficient to capture all the non-axisymmetric modes of the system that are not damped in the dissipative regime, which is discussed later.

6.1.1.1 Node Resolution Study

A maximum error of less than 0.5% was desired for the present study, to ensure confidence in the presented computations. Based on the results of the spatial resolution study which are presented in table 6.1, macro-elements of order $N^2 = 81$ were found to achieve sufficient accuracy, and were employed throughout the computations presented in this chapter.

The computations with element order $N^2 = 16$ and $N^2 = 25$ from the node resolution study require some discussion. The computations which employed elements with $N^2 = 16$ were stable, but the spatial resolution was so poor that no azimuthal

modes evolved in the wake, which rendered the solution axisymmetric to the limits of computational error. The computations which employed elements with $N^2 = 25$ diverged regardless of the size of the time step. A detailed analysis of these computations revealed that the non-axisymmetric modes in the flow grew exponentially until the computations diverged. It is likely that the solution was inadequately resolved to allow the non-axisymmetry in the flow to saturate. All computations that employed elements with $N^2 \geq 36$ converged to saturated non-axisymmetric wakes.

6.1.1.2 Azimuthal Fourier Modes and the Dissipative Regime

From Henderson (1997), the dissipative effects of viscosity dominate for azimuthal mode numbers m proportional to $Re^{1/2}$. The minimum number of Fourier modes (M_d) required to adequately resolve a flow field over an azimuthal span (λ_d) are therefore related by $M_d \sim \lambda_d Re^{1/2}/(2\pi)$. From this relationship, it was determined that the computations in the present study which employed an azimuthal span equal to the wavelength of a single Mode A instability ($\lambda_d = L_0 \simeq 4d$) required 32 Fourier planes which resolved the 16 Fourier modes which were outside the dissipative regime. Likewise, it was determined that computations in the present study which employed an azimuthal span equal to twice the wavelength of Mode A ($\lambda_d = 2L_0$) required 64 Fourier planes which resolved the 32 Fourier modes which were outside the dissipative regime.

6.1.2 Methodology of the Reynolds Number Variation Study

To study the effect of an increase in Reynolds number on the transitions which lead to turbulence in the wakes behind rings, computations were performed with an azimuthal domain chosen to compute a single period of the longest-wavelength instability mode of the system (Mode A), and the vortex street was computed at a Reynolds number greater than each of the critical Reynolds numbers for the non-axisymmetric instabilities in the wake that were predicted in chapter 4.

Two factors influenced the selection of suitable aspect ratios for this study. Firstly, consistent with the linear stability analysis of chapter 4, and the non-axisymmetric analysis comprising chapter 5, aspect ratios were required to capture the three possible non-axisymmetric transition paths with an increase in Reynolds number.

Secondly, the azimuthal symmetry of the ring limited the practical choice of azimuthal mode numbers (m) of the flows to integer values. Aspect ratios were chosen such that the dominant azimuthal mode number of the Mode A instability was a power

Aspect ratio	L_0 domain	$2L_0$ domain
5	$m = 4$	$m = 2$
10	$m = 8$	$m = 4$
20	$m = 16$	$m = 8$

TABLE 6.2: Azimuthal mode numbers of the computational domains employed in both the Reynolds number study (L_0), and the ($2L_0$) domain of the domain size study.

of 2 (i.e. $m = 2^n$ where $n = 0, 1, 2, \ldots$). This allowed a more precise study of the effect of an increase in the azimuthal domain length on the dynamics of the vortex streets in the flow past rings, which is presented in § 6.2.

From the analysis in previous chapters, it was found that aspect ratios $Ar = 5$, 10 and 20 satisfied these requirements. For the flow past a ring with $Ar = 5$, Reynolds numbers $Re = 190$, 220 and 320 were chosen to model the wake dynamics beyond the critical Reynolds numbers for each of the linear non-axisymmetric transitions. Similarly, for the flow past a ring with $Ar = 10$, Reynolds numbers $Re = 205$, 240 and 280 were chosen, and for the flow past a ring with $Ar = 20$, $Re = 205$, 280 and 320 were chosen.

6.1.3 Methodology of the Azimuthal Domain Variation Study

The final solutions from the highest-Reynolds-number computations from the Reynolds number variation study were used to construct an initial solution for computations with an azimuthal domain size $2L_0$, and for consistency, the Reynolds number remained unchanged.

The construction of the initial flow field resulted in a magnitude of zero for the odd-numbered Fourier modes of the wake. To facilitate a rapid evolution of these odd-numbered modes, a small random perturbation was added to the velocity field at the start of the computations.

The azimuthal mode numbers of the computational domains employed for the computations at each aspect ratio are summarised in table 6.2.

An important point must be made regarding the ring geometry in relation to the study of the variation of the azimuthal domain size. The ring is distinct from the straight circular cylinder in that the largest azimuthal domain is limited by the azimuthal symmetry of the ring. The longest-wavelength azimuthal mode that may be included in the wake is defined by the relationship $\lambda_{d_{max}} = \pi Ar$. It follows that the onset of long-wavelength non-axisymmetric modes in the wakes behind rings with smaller

aspect ratios may be delayed by the suppression of long-wavelength instabilities. This is consistent with the observations of Monson (1983) and Leweke & Provansal (1995), who observed helical shedding modes with higher mode numbers in the flow past large rings than in the flow past smaller rings.

6.2 Reynolds Number Variation Study

Some of the isosurface plots of streamwise vorticity presented in chapter 5 showed that wake structures corresponding to multiple linear instability modes can coexist simultaneously. In the computations presented in this study, the azimuthal wavelength of the computation is equal to the longest-wavelength linear instability predicted for each ring. A primary goal of this study is to determine if the subharmonic Mode C instability initiates a route to chaos through a period-doubling cascade. In § 6.2.1, the flow past a ring with $Ar = 5$ is considered, where Mode C is the primary non-axisymmetric instability. In § 6.2.2 the flow past a ring with $Ar = 10$ is considered, where Mode C is the secondary non-axisymmetric instability, and in § 6.2.3 the flow past a ring with $Ar = 20$ is considered, where Mode C is the tertiary non-axisymmetric instability.

For analysis of the computations, time histories of a point velocity approximately $4d$ downstream of the ring cross-section, and the drag force, were recorded. A time history of the azimuthal Fourier components of the velocity field at a point in the z–r plane approximately $4d$ downstream of the ring cross-section was also recorded, from which the energy corresponding to each azimuthal Fourier mode was monitored. In addition, the flow fields were stored for flow visualisation.

6.2.1 $Ar = 5$: A Primary Subharmonic Mode

The flow past a ring with $Ar = 5$ was computed at $Re = 190$, $Re = 220$ and $Re = 320$, to determine the wake transitions to turbulence with an increase in Reynolds number.

6.2.1.1 The Primary Instability: Mode C at $Re = 190$

The growth of the Mode C instability in computations of the flow past a ring with $Ar = 5$ at $Re = 190$ saturated within 700 time units. Figure 6.1 shows the saturation of the mean periodic kinetic energy components of the azimuthal modes commensurate with the Mode C instability. The modes incommensurate with the Mode C instability

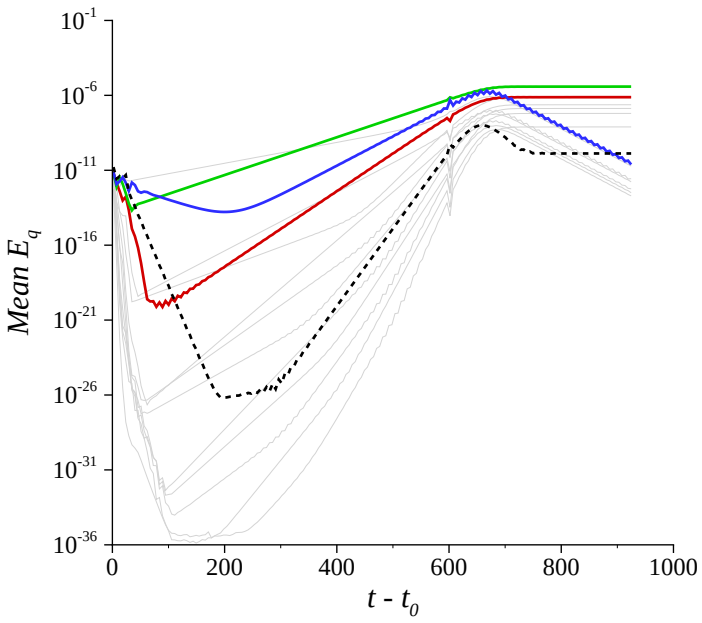

FIGURE 6.1: Evolution of the mean kinetic energy per period (E_q) for each azimuthal mode in the flow past a ring $Ar = 5$ with $Re = 190$. Measurements of E_q were taken at a point in the r–z plane approximately $4d$ downstream of the ring cross-section. Each azimuthal Fourier mode of the w–velocity was averaged over each shedding cycle. The fundamental Fourier mode is represented by a dotted black line, the modes which correspond to the wavelengths of Modes A, B and C are represented by blue, red and green lines, respectively. Shorter-wavelength modes are represented by light grey lines.

are observed to grow with the azimuthal modes of the Mode C instability over the first 700 time units of the computation. At the point of saturation of the azimuthal modes of Mode C, these modes are shown to decay at a constant rate. Figure 6.1 verifies that the non-axisymmetric wake structures correspond to the span of the Mode C instability, with an azimuthal wavelength of approximately $2d$ shown to dominate at saturation.

Figure 6.2 provides a striking verification of the effect of a subharmonic instability on the flow past a ring with $Ar = 5$. The frequency variation of the velocity at a point in the wake shows clearly that a bifurcation occurs from the single frequency of the axisymmetric wake ($t-t_0 < 200$) to two distinct frequencies in the wake that saturate for $t-t_0 \gtrsim 800$. The frequency of each successive oscillation in the wake alternates between the two frequency branches. This behaviour is consistent with a period-doubling of the wake, as the computed wake was periodic over two shedding cycles. Significantly, no

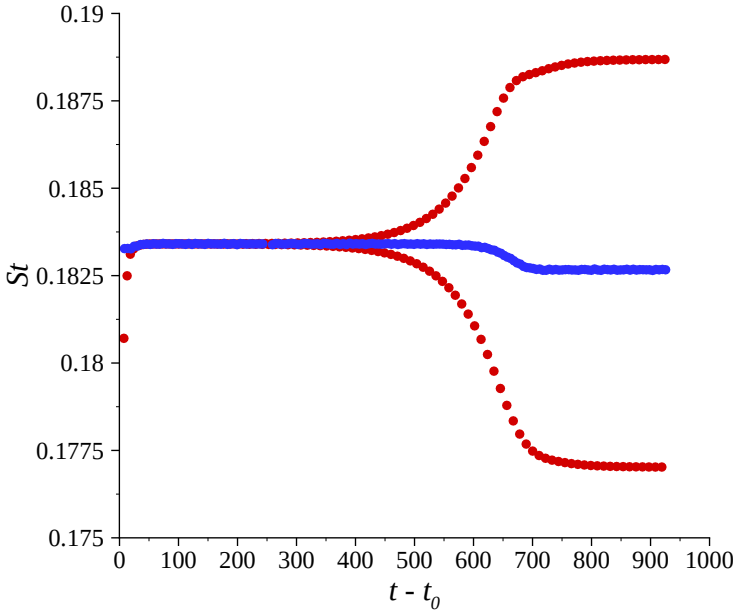

FIGURE 6.2: Time history of the variation in the Strouhal frequency for the flow past a ring with $Ar = 5$ at $Re = 190$. The Strouhal frequency was obtained from peak-to-peak measurements of the point velocity and drag force signals. Blue circles represent the Strouhal frequency variation determined from the drag force signal, and red circles represent the Strouhal frequency variation determined from the point velocity signal at a point in the wake approximately $4d$ downstream of the ring cross-section.

evidence of a period-doubling bifurcation is measured for the drag force on the ring. For practical purposes, this implies that regardless of the evolution of a subharmonic instability in the wake which causes a period-doubling bifurcation, no physical effect is encountered by the bluff body in question. A slight drop in frequency variation is observed for the computed drag force over $600 \lesssim t - t_0 \lesssim 700$, which is due to the saturation of non-axisymmetric flow in the wake.

The period-doubling in the wake is clearly presented in the point velocity spectrum presented in figure 6.3. In the figure, Fourier spectra of both the drag force and point velocity time histories are provided. The Fourier spectrum of the point velocity time history indicates clearly that a subharmonic frequency is present in the wake, with a small peak observed at $f/f_0 = 0.5$. There is no period-doubling peak observed for the Fourier spectrum of the drag force, which verifies the observed behaviour in the plot of the Strouhal frequency variation.

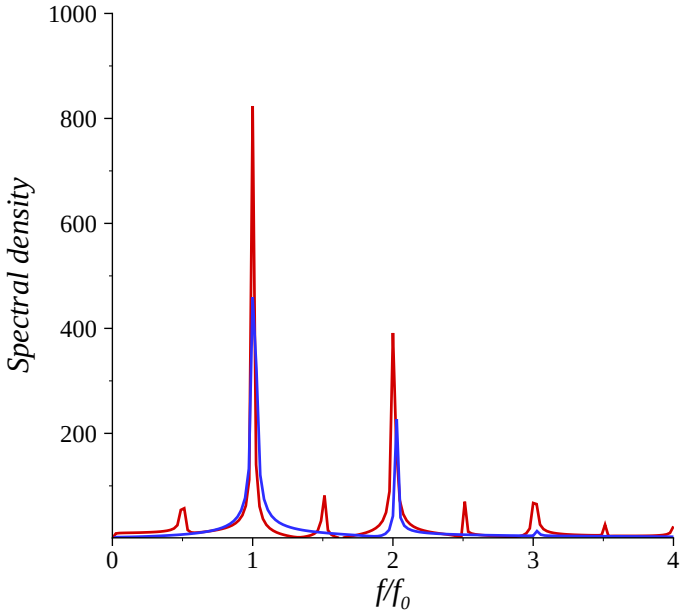

FIGURE 6.3: Fourier spectra of the computed time histories of both a point velocity (red line) and the drag force (blue line) for the flow past a ring with $Ar = 5$ at $Re = 190$. The spectral analysis was computed on data which was obtained after saturation of the non-axisymmetric flow. The computed frequency (f) is non-dimensionalised by the Strouhal frequency of the saturated flow ($St = f_0 = 0.1820$).

The large number of higher-frequency peaks in the spectrum of the point velocity are harmonics of the vortex shedding frequency. The drag force spectrum is more uniform than the point-velocity spectrum, as it is a global measurement of the properties of the wake, whereas the point velocity measurements are a local measurement of the properties of the wake.

The results presented here show that the onset of a primary subharmonic instability in a vortex street causes a period-doubling bifurcation in the wake. Computations at higher Reynolds numbers are required to ascertain whether the observed period-doubling is isolated, or in fact the first bifurcation of a period-doubling cascade.

6.2.1.2 The Secondary Instability: Mode A at $Re = 220$

A computation was performed at $Re = 220$ for the flow past a ring with $Ar = 5$, which was initiated using the saturated solution computed previously at $Re = 190$. The Reynolds number of the computation was approximately 10% greater than the critical

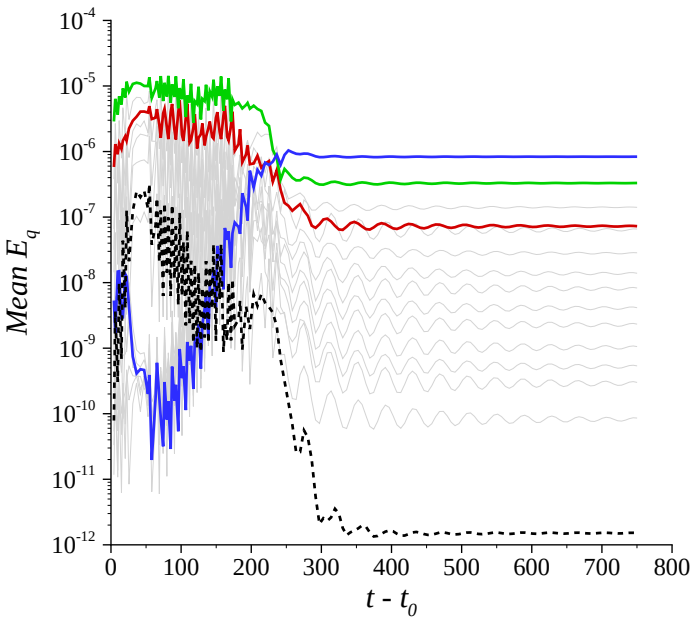

FIGURE 6.4: Evolution of the mean kinetic energy per period (E_q) for each azimuthal mode in the flow past a ring $Ar = 5$ with $Re = 220$. Axes and lines are as per figure 6.1.

Reynolds number for the linear Mode A instability, and a rapid saturation of the wake was observed, as shown in the plot in figure 6.4. The plot indicates that the wake structure was well organised at $t - t_o \approx 300$, and virtually all transients had decayed by $t - t_0 \approx 600$. Interestingly, the dominant wavelength of the wake at $Re = 220$ is consistent with the wavelength of a Mode A instability, which is a regular mode, not a subharmonic mode.

A plot of the frequency variation over time for the measured point velocity and drag force is presented in figure 6.5(a). For $t - t_0 < 200$, the twin branches associated with a subharmonic mode can be observed for the measured point velocity frequencies, as can the measured drag force frequency that bisects the point velocity frequency branches. The scatter of the measured frequencies over these times shows that the wake was unstable prior to saturation. After saturation, both sets of frequency measurements converge to a single frequency. The plot suggests that at $Re = 220$, the wake has reverted to a harmonic state, which has eradicated the period-doubling bifurcation caused by the primary Mode C instability.

The Fourier spectra measured for the flow past a ring with $Ar = 5$ at $Re = 220$ are

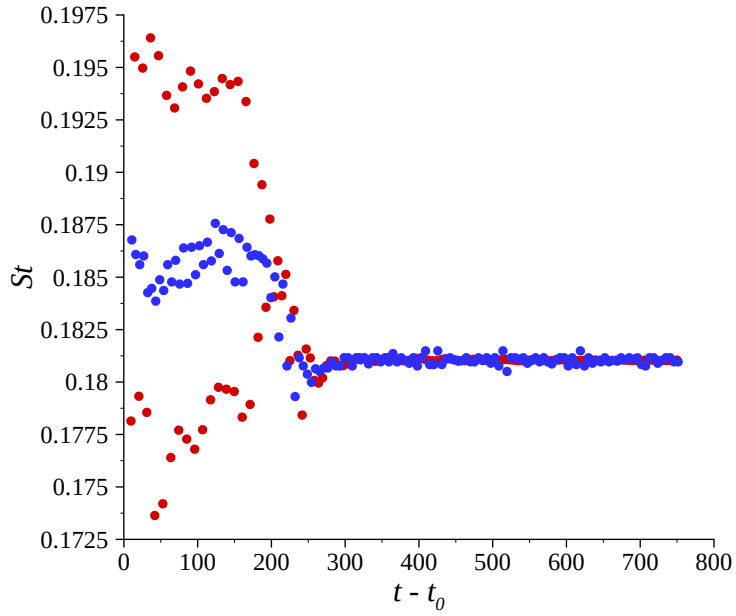

(a) Time history of the variation in the Strouhal frequency. Symbols are as per figure 6.2.

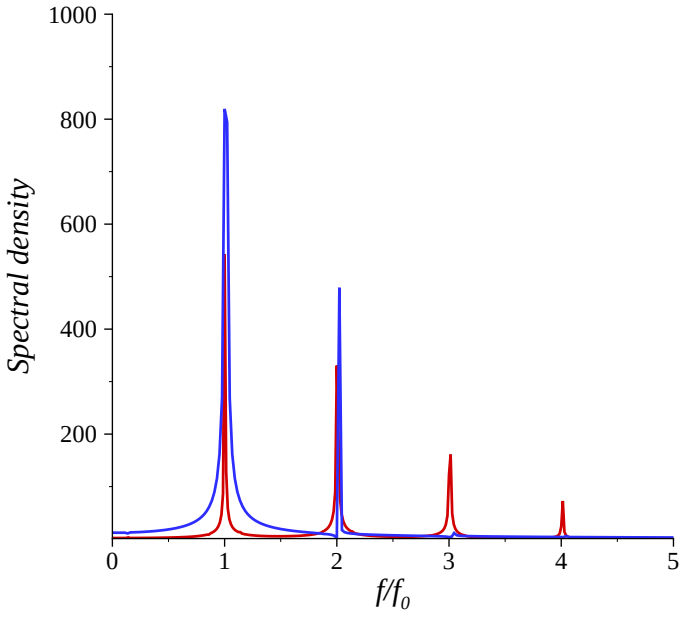

(b) Fourier spectra of the time histories of both a point velocity and the drag force. The chart lines and axes are as per figure 6.3, and the Strouhal frequency $St = f_0 = 0.1806$.

FIGURE 6.5: Strouhal frequency variation (a) and time history spectra (b) for the flow past a ring with $Ar = 5$ at $Re = 220$.

plotted in figure 6.5(b). The spectra are significant for several reasons. It is evident that the period-doubling bifurcation observed at $Re = 190$ is no longer present in the wake, with no peak observed in the vicinity of $f/f_0 = 0.5$. In addition, a peak in the drag force spectrum is observed at $f/f_0 = 2$. This is consistent with studies of the drag in the flow past a circular cylinder (Henderson 1995), which show that the drag force varies with twice the frequency of the shedding frequency. The asymmetry of the vortex street for the flow past rings means that an additional peak is observed at $f/f_0 = 1$, which is not measured in the flow past a circular cylinder. It follows that with an increase in aspect ratio, the asymmetry of the vortex street would decrease, and hence for an increase in aspect ratio, the peak at f/f_0 for the measured drag force would also decrease.

6.2.1.3 The Tertiary Instability: Mode B at $Re = 320$

A computation was performed at $Re = 320$ for the flow past a ring with $Ar = 5$, which was initiated using the saturated solution computed previously at $Re = 220$. The variation in mode energy for this Reynolds number is plotted in figure 6.6. In the plot, a markedly different behaviour is observed than for the corresponding plots at lower Reynolds numbers. The plot shows that after saturation at $t - t_0 \approx 80$, a chaotic variation in mode energy is observed for all modes.

Two points may be made regarding the mean mode energy plot in figure 6.6: Firstly, the modes corresponding to Mode A, Mode B and Mode C all contribute a similar amount of energy to the wake, with domination of one mode over the others observed for periods of up to 50 time units. This observed behaviour suggests that the structure of the wake is highly disordered. Secondly, the fundamental (zero frequency) azimuthal Fourier mode is observed to contribute significantly to the mode energy spectrum. In previous computations, the fundamental mode was consistently orders of magnitude smaller than the non-zero frequency modes of the system.

In figure 6.7, plots of the Strouhal frequency variation and the spectral density of the computed point velocity and drag force are presented. The plot of the Strouhal frequency variation in figure 6.7(a) shows a large scatter of the data. This is due to the emergence of small-scale structures in the wake, which cause small intermediate peaks to appear in the signals of the computed point velocity and drag force. The drag force is a global quantity, whereas the point velocity is a local quantity obtained at a point

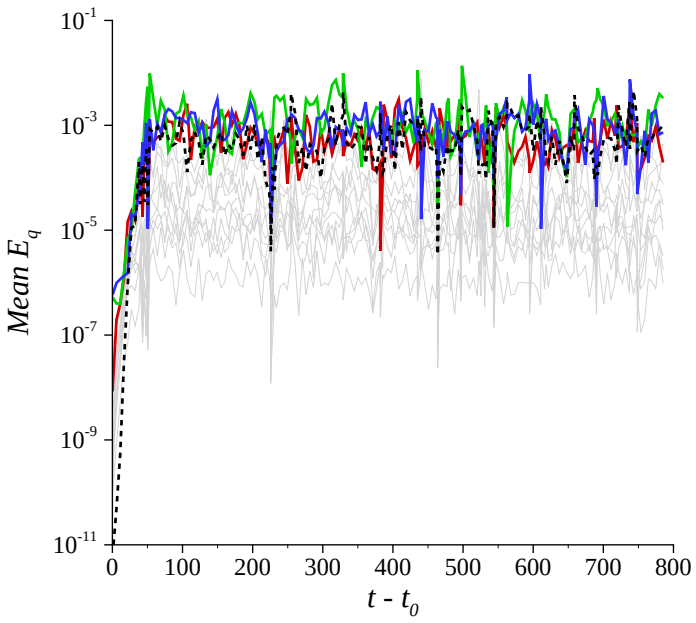

FIGURE 6.6: Evolution of the mean kinetic energy per period (E_q) for each azimuthal mode in the flow past a ring with $Ar = 5$ at $Re = 320$. Axes and lines are as per figure 6.1.

in the wake. Therefore, less scatter is observed in the data points for the Strouhal frequency variation in the drag force than for the Strouhal frequency variation in the point velocity. The plot in figure 6.7(a) shows that the majority of the computed drag force data points are grouped around three frequency bands, $St \approx 0.18$, $St \approx 0.32$ and $St \approx 0.43$. The point velocity data points are scattered in an almost random fashion throughout the plot.

The Fourier spectra corresponding to the time histories of a point velocity in the wake and the drag force for the flow past a ring with $Ar = 5$ at $Re = 320$ is provided in figure 6.7(b). The loss of periodicity of the computed wake at saturation highlights a limitation of the computations in the present study. The plot shows that the computed spectral density has a jagged profile, which was due to the relatively short sample time of the computation. Similar jagged profiles were observed in several of the spectral density plots to follow. Unfortunately, due to the high resolution of the computations, it was not feasible to extend the computations for sufficient time to smooth the jagged spectral density profiles. The plots do, however, provide useful information with regard to the peak and harmonic frequencies in the flow, and as the jagged effects are generally

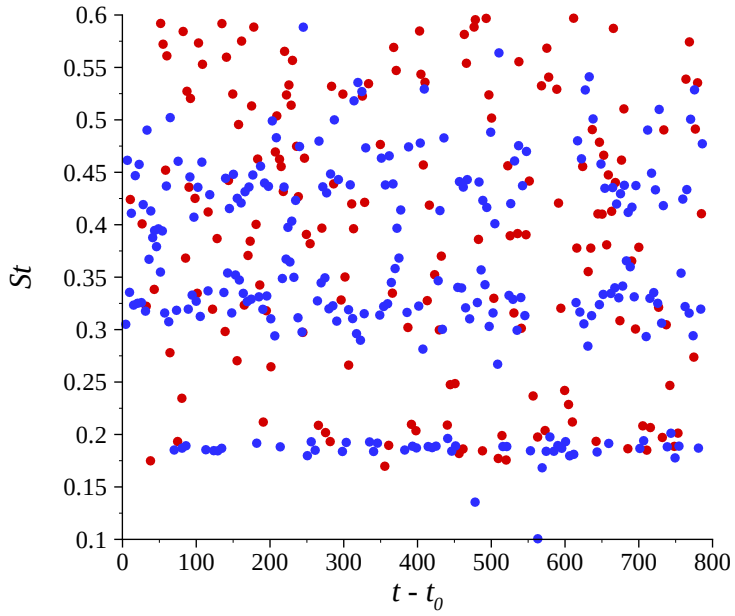

(a) Time history of the variation in the Strouhal frequency. Symbols are as per figure 6.2.

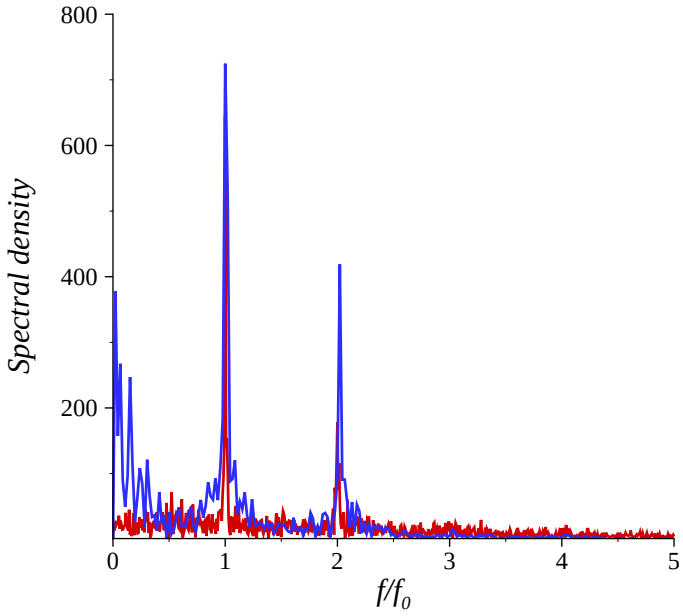

(b) Fourier spectra of the time histories of both a point velocity and the drag force. The chart lines and axes are as per figure 6.3, and the Strouhal frequency $St = f_0 = 0.1885$.

FIGURE 6.7: Strouhal frequency variation (a) and time history spectra (b) for the flow past a ring with $Ar = 5$ at $Re = 320$.

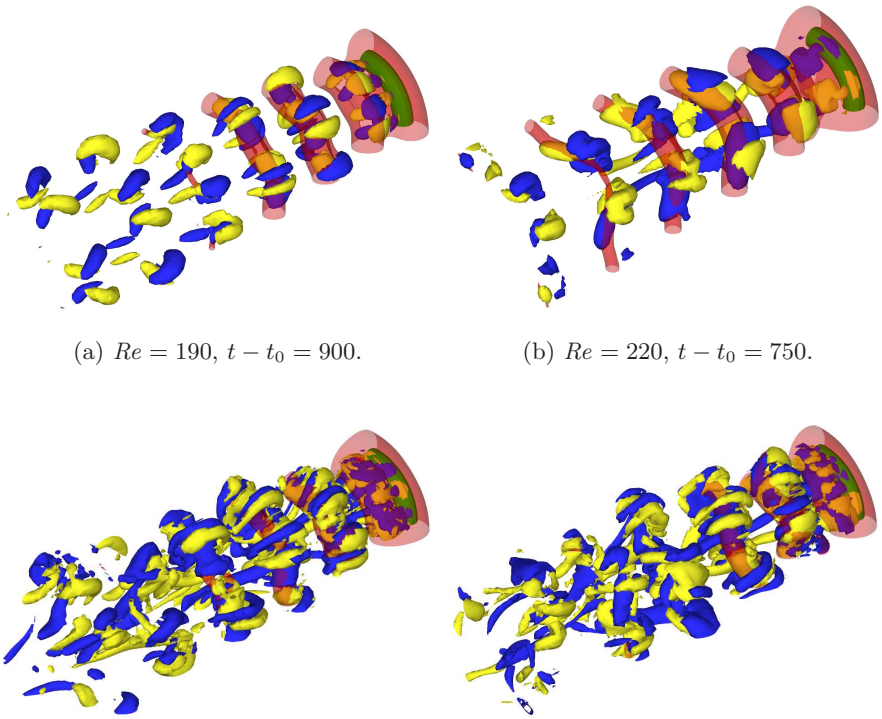

(a) $Re = 190$, $t - t_0 = 900$.

(b) $Re = 220$, $t - t_0 = 750$.

(c) $Re = 320$, $t - t_0 = 330$.

(d) $Re = 320$, $t - t_0 = 600$.

FIGURE 6.8: Isosurface plots of the saturated wake structures in the flow past a ring with $Ar = 5$ at various Reynolds numbers. The azimuthal domain size is $\lambda_d = L_0 \approx 4d$. Blue and yellow contours show positive and negative streamwise vorticity, highlighting non-axisymmetric wake structures. The translucent red isosurface represents a pressure contour to highlight the position of the rollers which comprise the vortex street. The ring is coloured green, and flow is from top right to bottom left in each frame.

isolated to regions of the spectrum with low energy, the plots were considered to be worthy of inclusion here.

The loss of periodicity of the saturated wake is shown in figure 6.7(b) by the shallow and narrow peaks at $f/f_0 = 1$ and 2, and the increased amount of high-frequency noise in the spectrum, when compared to the spectra presented previously for the lower-Reynolds-number flows. Despite the presence of a number of small jagged peaks over the frequency range $0 < f/f_0 < 1$, no evidence of a period-doubling bifurcation, or indeed a period-doubling cascade is observed in the flow.

Isosurface plots of the wakes computed as past of the present study of a ring with $Ar = 5$ are presented in figure 6.8. Plots of four wake states observed in the saturated regimes are provided. Figures 6.8(a) and (b) show the uniform saturated wakes

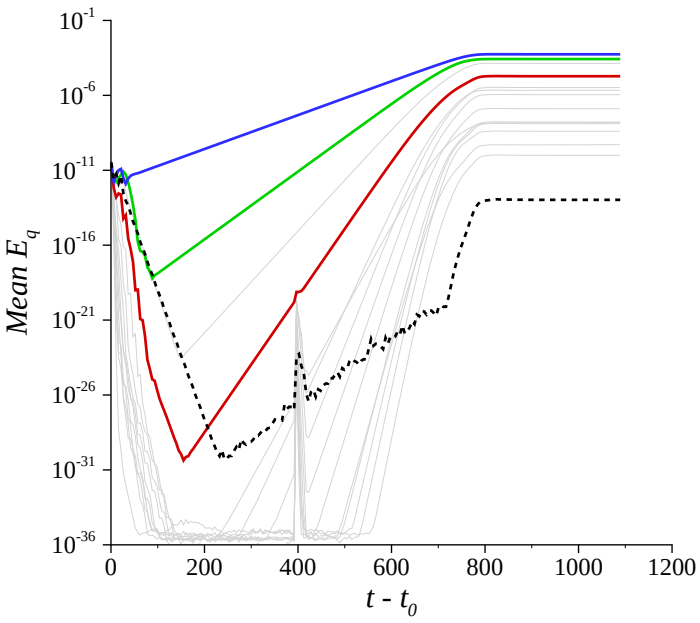

FIGURE 6.9: Evolution of the mean kinetic energy per period (E_q) for each azimuthal mode in the flow past a ring with $Ar = 10$ at $Re = 205$. Axes and lines are as per figure 6.1.

corresponding to the Mode C and Mode A instabilities at $Re = 190$ and $Re = 220$, respectively. The subharmonic nature of the Mode C wake in figure 6.8(a) is shown by the alternating sign of streamwise vortical structures from one shedding cycle to the next, and the alternating deformation of successive vortex streets (represented by red pressure contours). These aspects are not observed in the wake in figure 6.8(b), which clearly shows a periodic wake. Figures 6.8(c) and (d) show the disordered wake at $Re = 320$, for times $t - t_0 = 330$ and 600, respectively. Notice the localised regions in the wake with vortical structures consistent with each of the Mode A, Mode B and Mode C instabilities.

6.2.2 $Ar = 10$: A Secondary Subharmonic Mode

The flow past a ring with $Ar = 10$ was computed at $Re = 205$, $Re = 240$ and $Re = 280$, to determine the wake transitions to turbulence with an increase in Reynolds number.

6.2.2.1 The Primary Instability: Mode A at $Re = 205$

The flow past a ring with $Ar = 10$ was computed at $Re = 205$. Non-axisymmetry was computed to grow and saturate in the wake. In figure 6.9, the non-axisymmetric

modes are observed to saturate at $t - t_0 \approx 800$. At saturation, the dominant azimuthal wavelength in the wake is shown to be the wavelength associated with the Mode A instability. The spike in the low-energy modes at $t - t_0 \approx 400$ corresponds to a restart of the computations from a single-precision saved file. Note how the three modes that contain the most energy in the wake at this time remain unaffected by this restart condition, and even the fourth-highest energy mode contains an almost imperceptible kink in its linear profile. The linear continuation of the mode energy profiles after the spike indicate that these restart transients decayed rapidly, and did not influence the final saturation of the wake.

In figure 6.10(a), a plot of the Strouhal frequency variation is presented, which shows a shift in frequency as the flow evolves from an axisymmetric wake to a non-axisymmetric wake. The plot shows that non-axisymmetric wake retained the same periodicity as the axisymmetric wake, which is consistent with a transition to non-axisymmetric flow through a regular bifurcation. A high uniformity of the non-axisymmetric wake is suggested by the linear frequency profile observed at saturation for $t - t_0 \gtrsim 800$, and by the similarity between the Strouhal frequency for saturated flow from the time histories of the point velocity and the drag force.

The spectra presented in figure 6.10(b) emphasise the uniform nature of the saturated non-axisymmetric wake at $Re = 205$. In the plot, many harmonic peaks are observed in the point velocity spectrum, whereas little evidence of harmonic peaks is observed in the drag force spectrum for $f/f_0 > 2$.

6.2.2.2 The Secondary Instability: Mode C at $Re = 240$

A computation performed at a Reynolds number greater than the predicted critical Reynolds number for the secondary instability, Mode C, provides a striking and unexpected result. Computations were initiated from the saturated non-axisymmetric wake at $Re = 205$, and the Reynolds number was increased to $Re = 240$. A plot of the mode energy in figure 6.11 shows that the wake rapidly assumes a quasi-periodic state, which is characterised by a fluctuation in the azimuthal mode energy over a period of approximately 120 time units. The fluctuation is characterised by a linear growth of the longest wavelength azimuthal mode that contains the most energy, over approximately 60 time units. During this time, the lower-energy shorter-wavelength modes initially experience a decrease in energy over approximately 30 time units. The shorter-wavelength

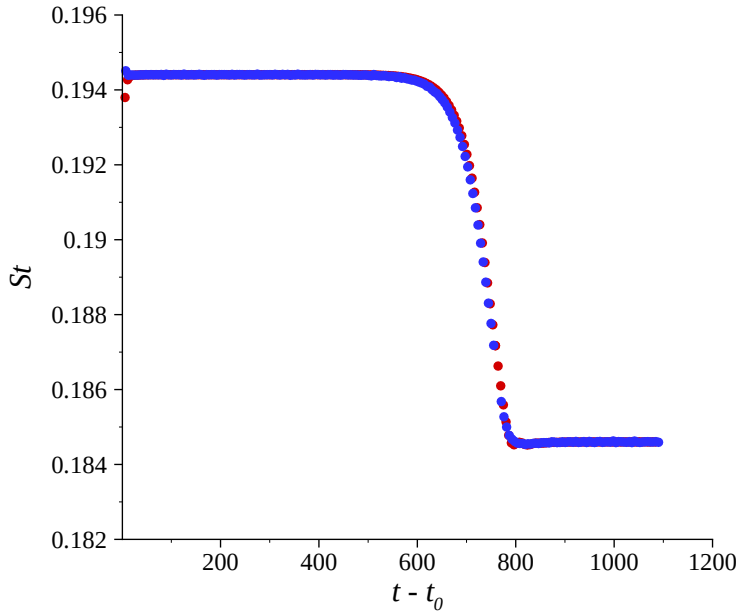

(a) Time history of the variation in the Strouhal frequency. Symbols are as per figure 6.2.

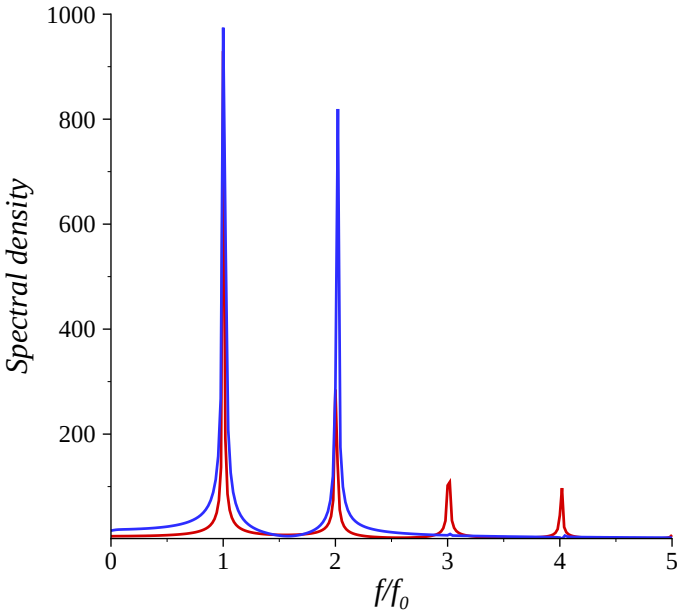

(b) Fourier spectra of the time histories of both a point velocity and the drag force. The chart lines and axes are as per figure 6.3, and the Strouhal frequency $St = f_0 = 0.1840$.

FIGURE 6.10: Strouhal frequency variation (a) and time history spectra (b) for the flow past a ring with $Ar = 10$ at $Re = 205$.

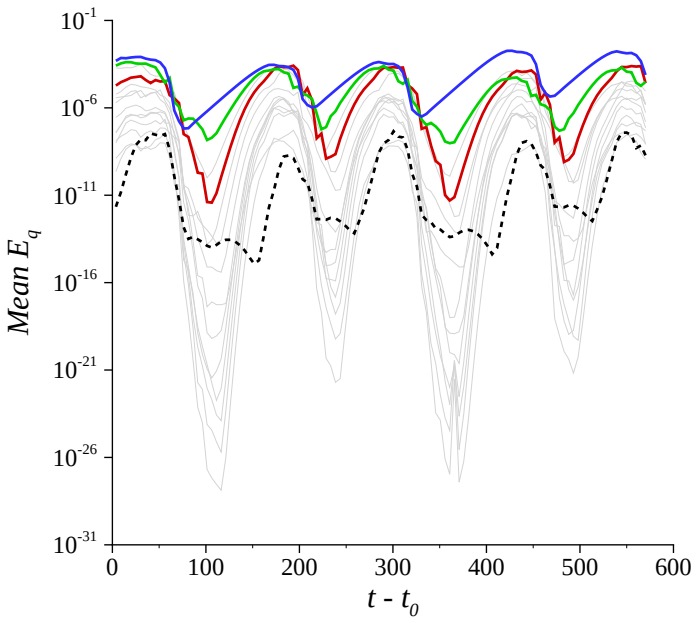

FIGURE 6.11: Evolution of the mean kinetic energy per period (E_q) for each azimuthal mode in the flow past a ring with $Ar = 10$ at $Re = 240$. Axes and lines are as per figure 6.1.

modes then grow at a faster rate than the dominant longest-wavelength mode. All of the modes reach a maximum energy at approximately 90 time units. At this time, the longest-wavelength mode rapidly loses energy, and reaches a minimum energy at approximately 120 time units. For a short time during this final phase, the longest-wavelength mode contains less energy than the shorter-wavelength modes, which decay more slowly between approximately 90 and 120 time units.

A plot of the Strouhal frequency variation is presented in figure 6.12(a). The plot provides additional information about the dynamics of the wake throughout the long-timescale fluctuations. The point velocity frequency data and the drag force frequency data are approximately equal, and show a cyclic change in the Strouhal frequency over a period of approximately 120 time units. The cycle was initially characterised by a Strouhal frequency of approximately $St = 0.2$. That frequency corresponded to the linear growth regime described for the first 60 time units of the cycle from the mode energy profiles of figure 6.11. The frequency rapidly decreased with the evolution of the non-axisymmetric flow in the wake. Instead of reaching a constant saturated frequency, the frequency then returned to $St \approx 0.2$, as the energy of the

non-axisymmetric modes in the wake decayed. A possible explanation for this is that the dominant non-axisymmetric mode is unstable, and is dissipated by the evolution of other competing modes in the wake.

An additional observation which may be drawn from the plots in figures 6.11 and 6.12(a) is that the cyclic mode evolution alternates between a deeper and more shallow decay every second cycle. The plot of the Strouhal frequency variation supports this observation, as the frequency associated with the linear high-frequency regime is sustained for more shedding cycles every second cycle of the non-axisymmetric mode evolution. This behaviour was observed at every second cycle, where the non-axisymmetric mode evolved from a flow with a smaller component of non-axisymmetry, when compared with the alternate cycles.

A plot of the Fourier spectra of the measured time histories of the point velocity and drag force are presented in figure 6.12(b). The plot exhibits broader peaks than are observed in the spectral density plot for the flow at $Re = 205$, which shows that the flow was not uniform and periodic at $Re = 240$. A low-frequency peak was also detected, with a frequency that corresponded to the frequency of the long-timescale cyclic mode energy fluctuation.

Figure 6.13 shows the non-axisymmetric wake structures that were computed at various stages throughout the cyclic mode energy fluctuations. The isosurface plots show the evolution of non-axisymmetric flow in the wake over one full cycle of the mode energy fluctuation. The plots correspond to the cycle from $t - t_0 \approx 180$ to $t - t_0 \approx 300$. The spatio-temporal distribution between the plots from successive peaks in the non-axisymmetric mode energy cycle in figures 6.13(a) and (e) indicates that the sign of the non-axisymmetric wake alternates every second cycle. Furthermore, it may be observed in figures 6.13(b–d) that between the peaks, the non-axisymmetric wake structures dissipate completely, before a subsequent evolution of the instability with a reversed sign. The computed wake structure shown in figures 6.13(a) and (e) is consistent with a Mode A instability. However, instead of the broad streamwise vorticity isosurfaces in the braid regions of the vortex street that are observed for a Mode A wake, pairs of co-rotating streamwise vortices are observed. This observed wake structure is consistent with the addition to the wake of vortical structures associated with the Mode B instability.

Although only five repetitions of the cyclic evolution of the non-axisymmetry in

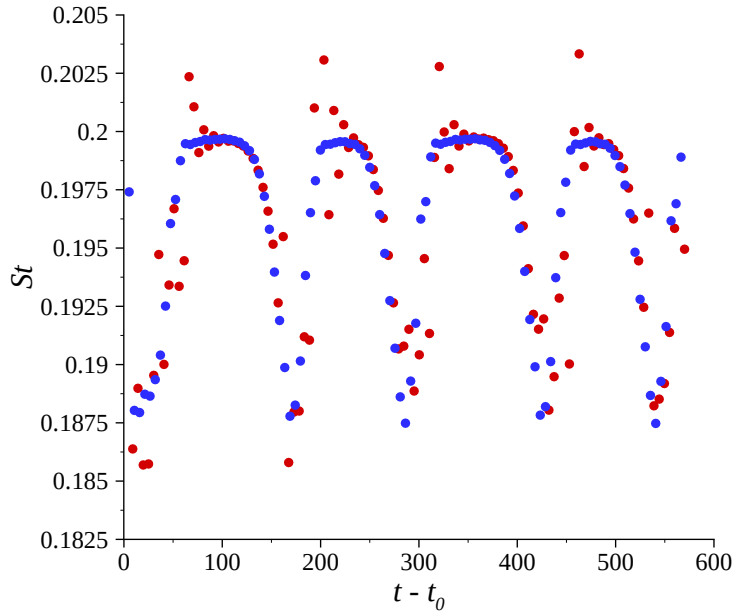

(a) Time history of the variation in the Strouhal frequency. Symbols are as per figure 6.2.

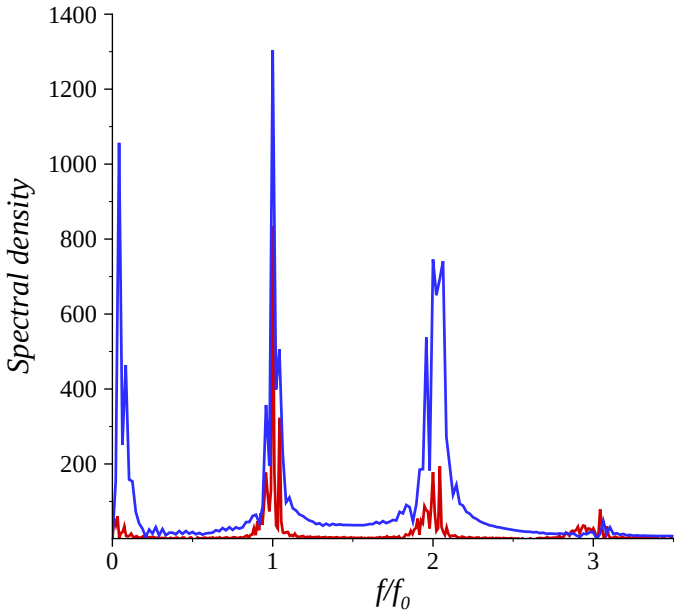

(b) Fourier spectra of the time histories of both a point velocity and the drag force. The chart lines and axes are as per figure 6.3, and the Strouhal frequency $St = f_0 = 0.1961$.

FIGURE 6.12: Strouhal frequency variation (a) and time history spectra (b) for the flow past a ring with $Ar = 10$ at $Re = 240$.

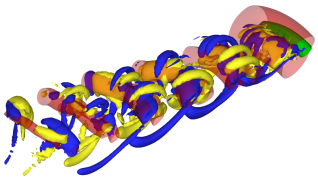

(a) $t - t_0 = 180$.

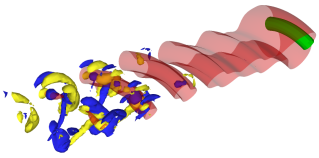

(b) $t - t_0 = 210$.

(c) $t - t_0 = 240$.

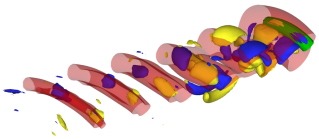

(d) $t - t_0 = 270$.

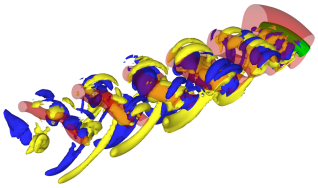

(e) $t - t_0 = 300$.

FIGURE 6.13: Isosurface plots of the saturated wake structures in the flow past a ring with $Ar = 10$ at $Re = 240$, at several times throughout the computation. The azimuthal domain size and contour shading are as per figure 6.8.

the wake at $Re = 240$ were computed, both the non-linear nature of the mechanism of non-axisymmetric mode destruction, and the long timescale of the phenomenon, lead to a conclusion that the cyclic evolution will not reach a periodic state. No further computations of the wake at $Re = 240$ were attempted, due to the high computational expense of the simulations.

6.2.2.3 The Tertiary Instability: Mode B at $Re = 280$

The flow past a ring with $Ar = 10$ at $Re = 280$ was computed. A plot of the variation in the non-axisymmetric mode energy is presented in figure 6.14. Saturation to a chaotic state occurred at $t - t_0 \approx 200$. The longest-wavelength azimuthal mode competes with the modes corresponding to the Mode B and Mode C wavelengths. Consistent with the flow past a ring with $Ar = 5$ at $Re = 320$, there are significant temporal regions that are dominated by modes other than the longest-wavelength mode (e.g. $360 < t - t_0 < 450$ and $580 < t - t_0 < 610$).

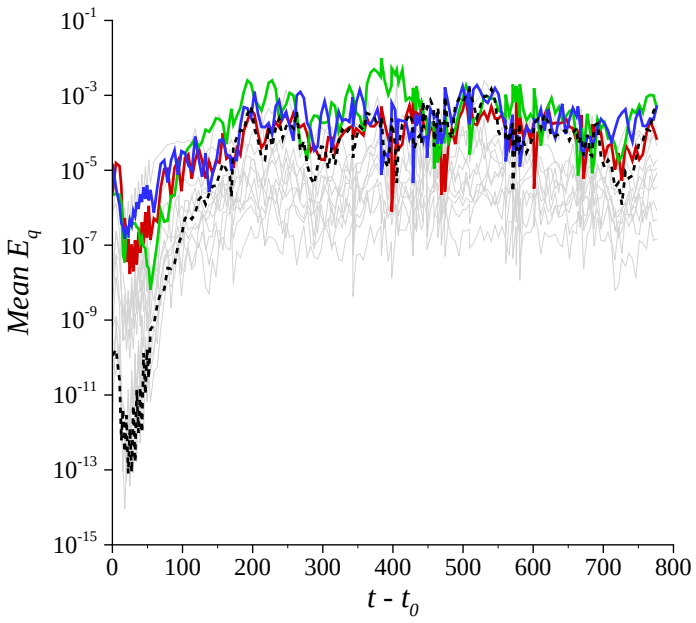

FIGURE 6.14: Evolution of the mean kinetic energy per period (E_q) for each azimuthal mode in the flow past a ring with $Ar = 10$ at $Re = 280$. Axes and lines are as per figure 6.1.

A plot of the Strouhal frequency variation is presented in figure 6.15(a). The plot shows that at saturation, oscillations occur over a frequency range of $0.191 < St < 2.04$ over times $t - t_0 > 200$.

The Fourier spectra for the flow past a ring with $Ar = 10$ at $Re = 280$ in figure 6.15(b) is similar to the spectra presented in figure 6.7(b) for the flow past a ring with $Ar = 5$ at $Re = 320$. The chaotic fluctuations in the wake contribute a broad spread of energy over a wide range of frequencies. In the plot, harmonic peaks are visible in the point velocity spectrum up to frequencies of $f/f_0 = 3$. For the flow past a ring with $Ar = 5$ at $Re = 320$, spectral peaks are only detected up to $f/f_0 = 2$, which further indicates that the computation at $Re = 320$ is more chaotic than the computation at $Re = 280$.

At $Re = 280$, the point velocity spectrum exhibits a small rise in the vicinity of the subharmonic frequency $f/f_0 = 0.5$. The absence of a well-defined peak at this frequency implies that it is improbable that the route to chaos for the flow past a ring with $Ar = 10$ occurs through a period-doubling cascade. Instead, the increase in the energy of incommensurate frequencies in the spectra with an increase in Reynolds

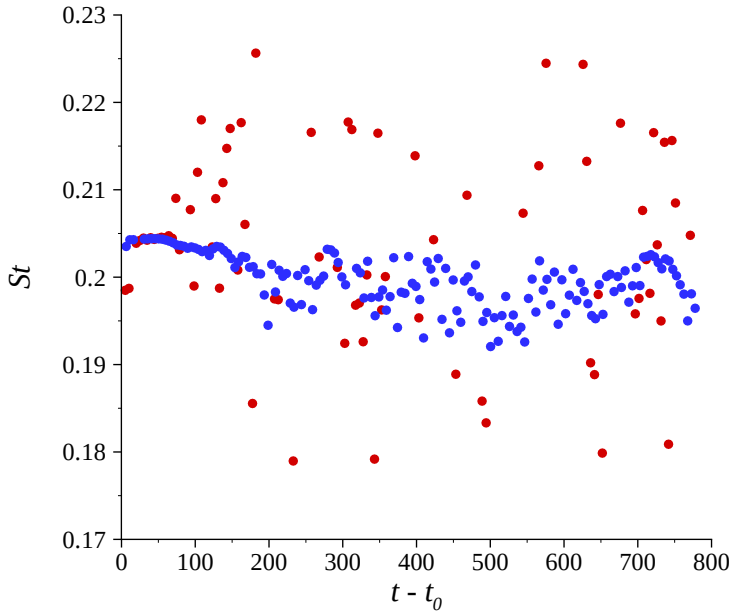

(a) Time history of the variation in the Strouhal frequency. Symbols are as per figure 6.2.

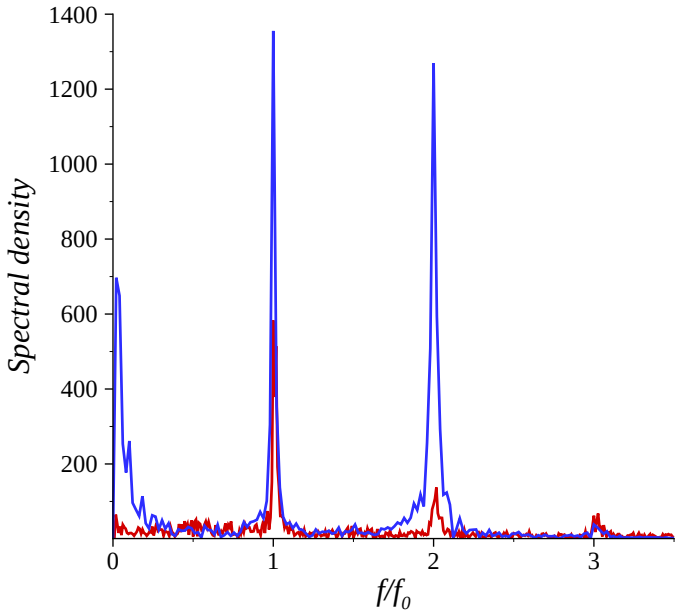

(b) Fourier spectra of the time histories of both a point velocity and the drag force. The chart lines and axes are as per figure 6.3, and the Strouhal frequency $St = f_0 = 0.1974$.

FIGURE 6.15: Strouhal frequency variation (a) and time history spectra (b) for the flow past a ring with $Ar = 10$ at $Re = 280$.

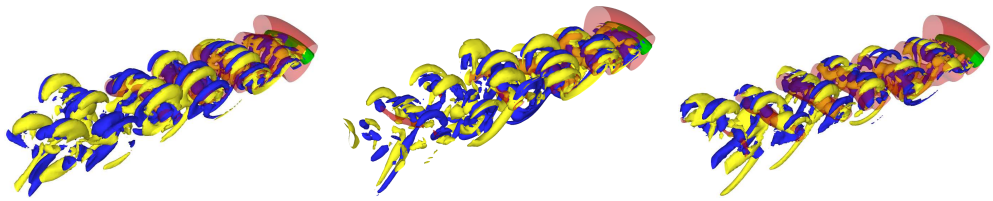

(a) $t - t_0 = 390$. (b) $t - t_0 = 540$. (c) $t - t_0 = 720$.

FIGURE 6.16: Isosurface plots of the saturated wake structures in the flow past a ring with $Ar = 10$ at $Re = 280$, at several times throughout the computation. The azimuthal domain size and contour shading are as per figure 6.8.

number suggests that the route to chaos is through the development of small scales in the wake. This behaviour is consistent with the observed behaviour in the flow past a ring with $Ar = 5$ with an increase in Reynolds number.

Three velocity fields were captured during the computation of the flow past a ring with $Ar = 10$ at $Re = 280$. Isosurface plots of these flow fields are presented in figure 6.16.

The flow visualisation plots presented in figure 6.16 show some interesting characteristics. It may be observed from figures 6.16(a–c) that the wake structures approximately $4d$ and further downstream of the ring cross-section are dominated by wake structures consistent with the Mode C instability. In figure 6.16(a), the near wake is dominated by wake structures consistent with the Mode B instability. In figure 6.16(b), the near-wake Mode B structures are not observed, and in figure 6.16(c), the near-wake Mode B structures are only observed over half of the azimuthal span of the computation. The Mode C wake structures observed further downstream are non-uniform, due to the competing longer-wavelength azimuthal mode in the computation, which in figure 6.14 is shown to dominate the wake for a significant proportion of the computation. The plot in figure 6.16(c) appears to be the most disordered of the three plots. The fundamental azimuthal mode had the highest energy of the non-axisymmetric modes in the wake at the time at which the flow field of the plot was captured.

6.2.3 $Ar = 20$: A Tertiary Subharmonic Mode

The flow past a ring with $Ar = 20$ was computed at $Re = 205$, $Re = 280$ and $Re = 320$, to determine the wake transitions to turbulence with an increase in Reynolds number.

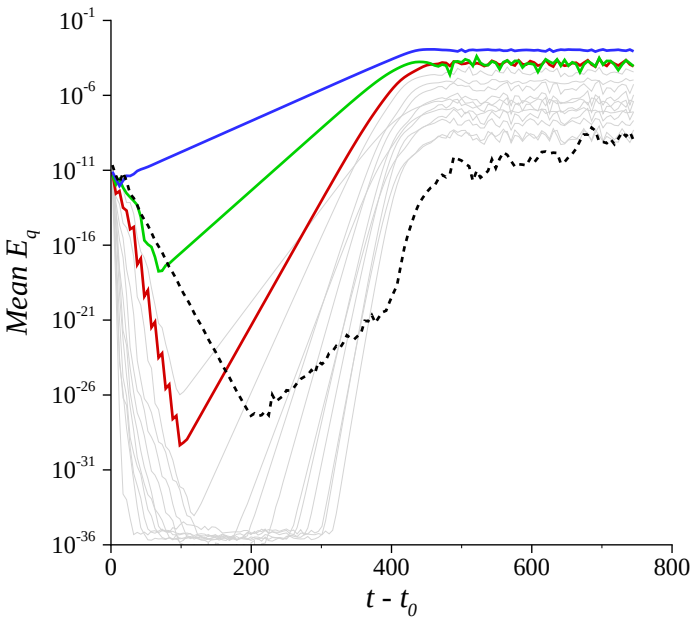

FIGURE 6.17: Evolution of the mean kinetic energy per period (E_q) for each azimuthal mode in the flow past a ring with $Ar = 20$ at $Re = 205$. Axes and lines are as per figure 6.1.

6.2.3.1 The Primary Instability: Mode A at $Re = 205$

The computed flow past a ring with $Ar = 20$ at $Re = 205$, with an azimuthal domain size $\lambda_d = L_0$, saturated at $t - t_0 \approx 470$, as shown in figure 6.17. The plot shows that the saturated state for the primary non-axisymmetric mode is dissimilar to the primary modes that evolve in the wakes of rings with $Ar = 5$ and $Ar = 10$, in that an equilibrium is not reached, which corresponded to a small variation in the computed Strouhal frequency in the wake. Figure 6.17 shows that after saturation of the non-zero azimuthal modes, the fundamental azimuthal mode of the system continues to evolve.

The effect of the aforementioned fundamental azimuthal mode evolution on the non-axisymmetric wake pattern is shown in figure 6.18, which presents isosurface plots of the wake when saturation of the azimuthal modes first occurs at $t - t_0 = 450$ in figure 6.18(a), and when the fundamental mode had evolved considerably at $t - t_0 = 750$ in part (b). The wake structures in part (a) are observed to be similar to both the computed Mode A wake for the flow past a circular cylinder (Thompson *et al.* 1996), and the visualisation of the Mode A wake in the flow past rings with $Ar = 10$ and $Ar = 20$,

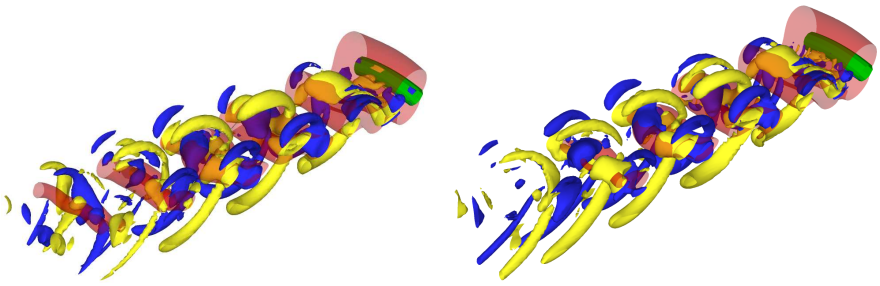

(a) $t - t_0 = 450$. (b) $t - t_0 = 750$.

FIGURE 6.18: Isosurface plots of the saturated wake structures in the flow past a ring with $Ar = 20$ at $Re = 205$, at the initial saturation point (a), and after the evolution of the fundamental azimuthal mode (b). The azimuthal domain size and contour shading are as per figure 6.8.

which were presented in chapter 5, figures 5.24(a) and 5.31(a). In figure 6.18(b), it is clear that the evolution of the fundamental azimuthal mode has altered the wake pattern from figure 6.18(a). A disruption of the $4d$ azimuthal symmetry of the mode is observed in the streamwise vortical structures stretching between the second pair of vortices downstream of the ring cross-section. Furthermore, the non-axisymmetric pattern is less defined, with the thickness of the streamwise vortical structures and their distribution being noticeably less uniform than in figure 6.18(a).

The time history of the Strouhal frequency variation for the flow past a ring with $Ar = 20$ at $Re = 205$ is presented in figure 6.19(a). Instead of a constant Strouhal frequency being computed at saturation, both the point velocity and drag force frequency measurements show that the Strouhal frequency varies considerably once the non-axisymmetric wake achieves saturation. The drag force oscillation measurements show that the wake oscillates over a narrow band of Strouhal frequencies $0.180 < St < 0.186$.

The Fourier spectra of both the point velocity measurements and the drag force measurements in figure 6.19(b) are indicative of the chaotic fluctuation of the wake at $Re = 205$. Despite the short sample time for the saturated flow, which resulted in the jagged spectral density profile, the shedding frequency $f/f_0 = 1$ and the first harmonic $f/f_0 = 2$ are both well-defined in the drag force spectrum.

The cause of the variation in the shedding frequency of the flow at saturation of the non-axisymmetric Mode A wake is unknown. Long-timescale computations would assist to determine if any equilibrium state is reached in the wake with regard to the

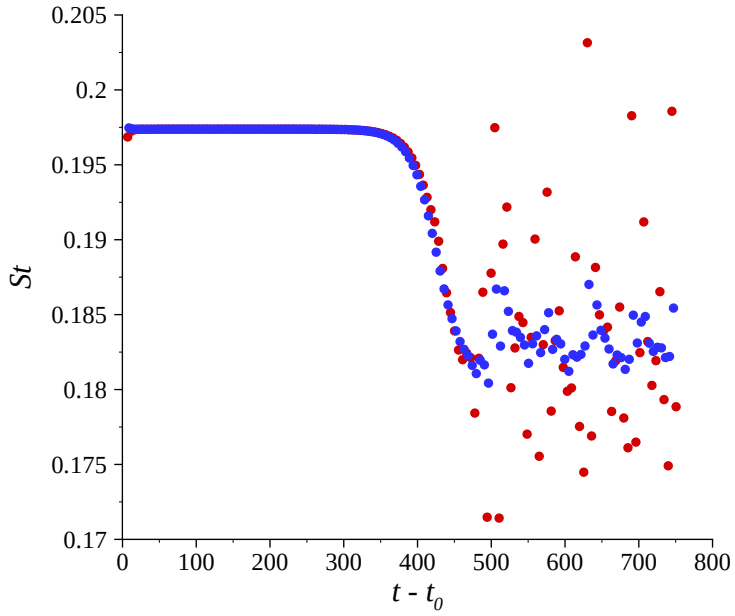

(a) Time history of the variation in the Strouhal frequency. Symbols are as per figure 6.2.

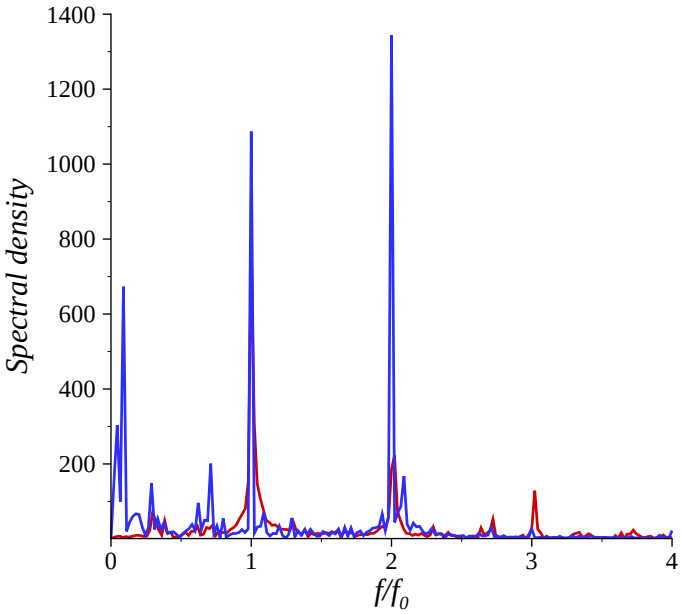

(b) Fourier spectra of the time histories of both a point velocity and the drag force. The chart lines and axes are as per figure 6.3, and the Strouhal frequency $St = f_0 = 0.1821$.

FIGURE 6.19: Strouhal frequency variation (a) and time history spectra (b) for the flow past a ring with $Ar = 20$ at $Re = 205$.

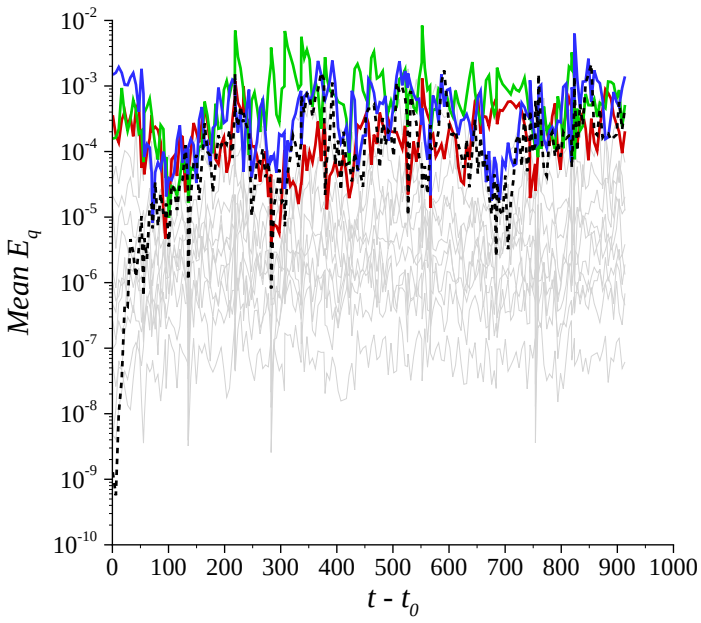

FIGURE 6.20: Evolution of the mean kinetic energy per period (E_q) for each azimuthal mode in the flow past a ring with $Ar = 20$ at $Re = 280$. Axes and lines are as per figure 6.1.

fundamental azimuthal mode, as it was still observed to increase when the computation was terminated. This underlying variation does not appear to correspond to an alternative non-axisymmetric instability mode, as the magnitude of the mean azimuthal mode energy corresponding to the wavelength of the Mode B and Mode C instabilities remains well below the energy of the azimuthal mode corresponding to the Mode A wavelength.

6.2.3.2 The Secondary Instability: Mode B at $Re = 280$

Figure 6.20 shows that the increase in Reynolds number from $Re = 205$ to $Re = 280$ has caused a significant change in the behaviour of the non-axisymmetric modes in the wake. The computation at $Re = 280$ saturated at $t - t_0 \approx 300$. For brief periods, an azimuthal wavelength which corresponds to the Mode C instability is observed to dominate in the wake for times $280 < t - t_0 < 380$, $430 < t - t_0 < 500$ and $600 < t - t_0 < 720$.

The Strouhal frequency variation of the flow past a ring with $Ar = 20$ at $Re = 280$ in figure 6.21(a) shows an increase in frequency of approximately 10% from the saturated Mode A wake at $Re = 205$. This is consistent with experimental observations of the flow past a circular cylinder (Williamson 1988b, 1996b), and the flow past a ring

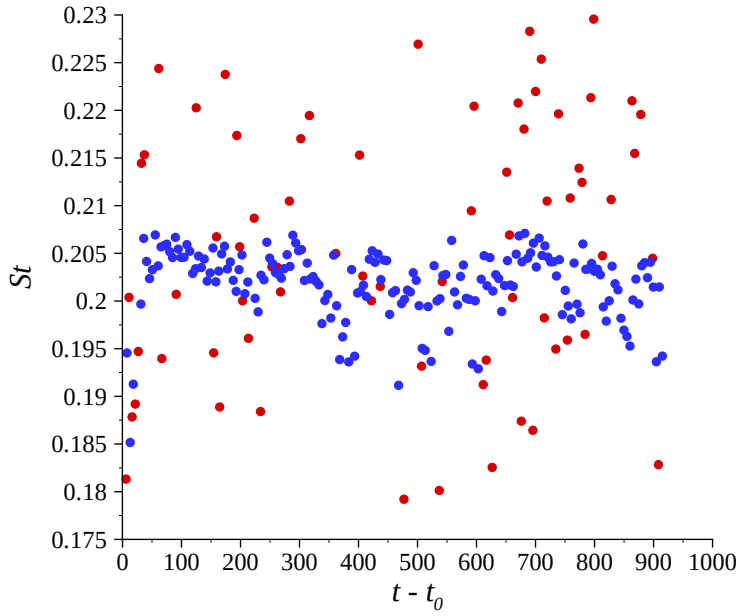

(a) Time history of the variation in the Strouhal frequency. Symbols are as per figure 6.2.

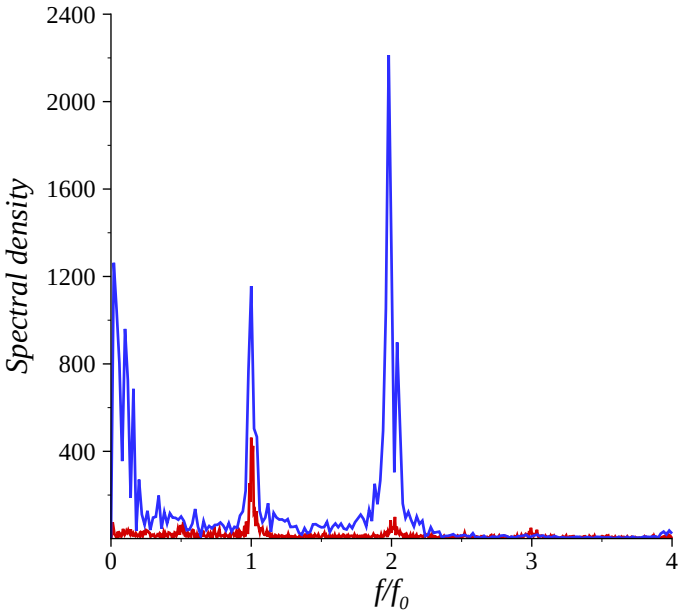

(b) Fourier spectra of the time histories of both a point velocity and the drag force. The chart lines and axes are as per figure 6.3, and the Strouhal frequency $St = f_0 = 0.2010$.

FIGURE 6.21: Strouhal frequency variation (a) and time history spectra (b) for the flow past a ring with $Ar = 20$ at $Re = 280$.

(Leweke & Provansal 1995), which both show a reduction in Strouhal number as the non-axisymmetric Mode A wake saturates at $Re \approx 190$, as well as a subsequent rise in Strouhal number as the secondary non-axisymmetric instability evolves for $230 \lesssim Re \lesssim 260$. The Strouhal frequencies at $Re = 280$ are scattered over the range $0.191 < St < 0.207$, with the majority of frequencies in the range $0.197 < St < 0.207$. As with the majority of examples presented here, the point velocity measurements of the Strouhal frequency variation are far more widely scattered, due to local oscillations from small-scale wake structures.

The point velocity and drag force spectra presented in figure 6.21(b) show a similar distribution of spectral density to the flow past a ring with $Ar = 10$ at $Re = 280$, and the flow past a ring with $Ar = 5$ at $Re = 320$, with two significant exceptions. These exceptions include a stronger drag force peak at $f/f_0 = 2$, and a small rise in the point velocity spectrum at $f/f_0 = 0.5$.

The previous discussion of the frequency of the drag force oscillation described how the drag force peak at $f/f_0 = 1$ vanishes as $Ar \to \infty$, with the curvature-induced asymmetry of the vortex street. Hence, with an increase in aspect ratio, the peak at $f/f_0 = 2$ grows as the wake approaches the wake behind a circular cylinder. For the spectrum obtained from the flow past a ring with $Ar = 20$, this effect is more apparent than for the smaller aspect ratios considered. In this case, the peak at $f/f_0 = 2$ is higher and more broad than the peak at $f/f_0 = 1$.

The second observation of interest pertains to the presence of a small rise in the vicinity of the subharmonic frequency $f/f_0 = 0.5$ in the point velocity spectrum. This observation is significant, as it is the strongest evidence presented thus far to suggest the influence of a subharmonic instability on a non-axisymmetric wake. Only the spectrum of the flow past a ring with $Ar = 5$ at $Re = 190$ presents a more well-defined subharmonic spectral peak, however, in that case the subharmonic Mode C instability was the only unstable non-axisymmetric mode. Here the Reynolds number is greater than both the critical Reynolds numbers of the linear Mode A and Mode B instabilities, and is still less than the critical Reynolds number of the Mode C instability. As the difference between the saturated non-axisymmetric wake at this Reynolds number, and the corresponding axisymmetric wake used for the linear stability analysis calculations is significant, it is not surprising that evidence of the tertiary non-axisymmetric vortex shedding mode in the flow past a ring with $Ar = 20$, Mode C, is observed at Reynolds

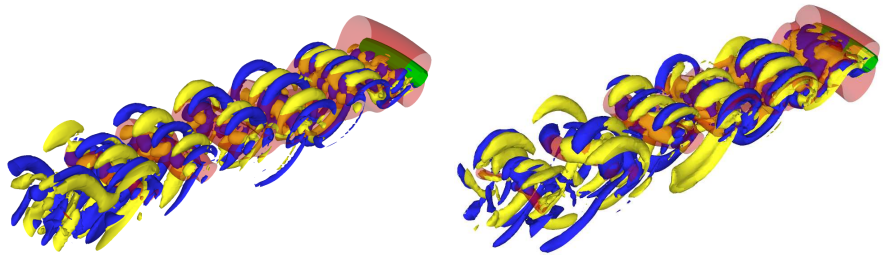

(a) $t - t_0 = 690$. (b) $t - t_0 = 840$.

FIGURE 6.22: Isosurface plots of the saturated wake structures in the flow past a ring with $Ar = 20$ at $Re = 280$, with the Mode C wavelengths dominating the wake (a), and where Mode A, Mode B and Mode C contribute a similar amount of energy to the wake (b). The azimuthal domain size and contour shading are as per figure 6.8.

numbers below the critical Reynolds number of the instability.

In figure 6.22, isosurface plots of the wakes computed for the flow past a ring with $Ar = 20$ at $Re = 280$ are presented. An attempt to visualise the different wake patterns that emerge throughout the saturated regime was made by analysing the mean azimuthal mode energy plot (figure 6.20). Two wake flow fields were captured, at times $t - t_0 = 690$, and $t - t_0 = 840$, corresponding to a wake that was dominated by a Mode C wavelength mode, and a wake where the wavelengths corresponding to the three non-axisymmetric instability modes contribute a comparable amount of energy.

The isosurface plot in figure 6.22(a) is consistent with the mean azimuthal mode energy plot, with well-ordered subharmonic wake patterns observed with both symmetry and azimuthal wavelength consistent with the Mode C instability in the far wake, and in the near wake (within $4d$ to $5d$ of the ring cross-section), shorter-wavelength streamwise vortical structures which correspond to the Mode B instability are visible. The poor definition of the streamwise vortical structures associated with Mode B is probably due to the competition with the Mode C instability in the near wake.

The mode energy distribution at a time $t - t_0 = 804$ shows a competition between all three of the non-axisymmetric vortex shedding modes, and the isosurface plot of the non-axisymmetric wake at this time in figure 6.22(b) is consistent with this observation. Downstream of the ring cross-section, the computational domain shows five sets of streamwise vortical structures on the upper side of the wake, corresponding to the braid region between each set of vortex cores. The apparent azimuthal symmetry for each of

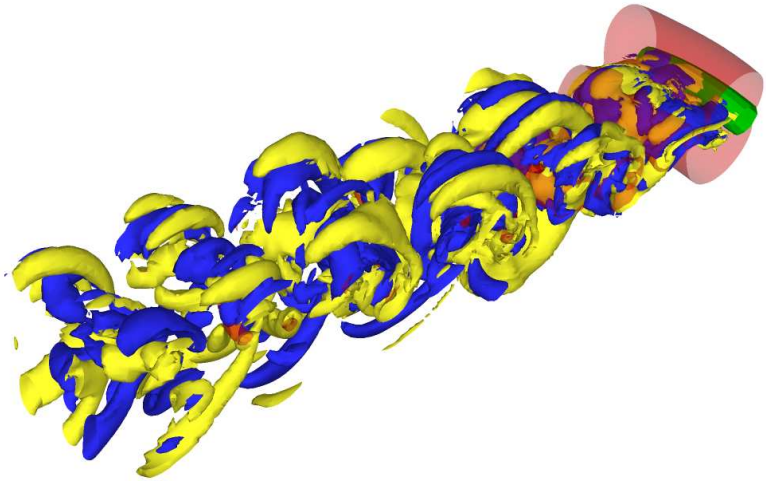

FIGURE 6.23: Isosurface plot of the saturated non-axisymmetric wake structures in the flow past a ring with $Ar = 20$ at $Re = 320$, at a time $t - t_0 = 510$. The azimuthal computational domain size and contour shading is as per figure 6.8.

these braid regions is as follows (upstream to downstream): Mode B, Mode A, Mode C, Mode A and Mode A. This behaviour in the wake reflects the competition between the azimuthal modes that is predicted from the mode energy plot from figure 6.20, and the irregularity of the wake over time is reflected in the Fourier spectra of time history presented in figure 6.21.

6.2.3.3 The Tertiary Instability: Mode C at $Re = 320$

To compare with the isosurface plot presented for the flow past a ring with $Ar = 20$ at $Re = 280$, an isosurface plot for the flow past the same ring at $Re = 320$ is presented in figure 6.23. The wake at $Re = 320$ shows the presence of smaller scales in the wake, which are visualised by both small-scale isosurfaces, and irregularities and inconsistencies in the larger-scale streamwise vortical structures. The asymmetry of the wake can be observed from the drastically deformed underlying vortex street, which in turn has disrupted the distribution of streamwise vortical structures in the wake.

A time history plot of the mean azimuthal mode energy for the flow past a ring with $Ar = 20$ at $Re = 320$ is presented in figure 6.24. The plot shows that the distribution of energy in the wake was similar to the flow past the same ring at $Re = 280$, which was presented in figure 6.20, with a chaotic energy fluctuation visible throughout the saturated regime. A distinction between this plot and the plot of computations at $Re = 280$ is the absence of temporal regions dominated by Mode C wavelengths. The plot

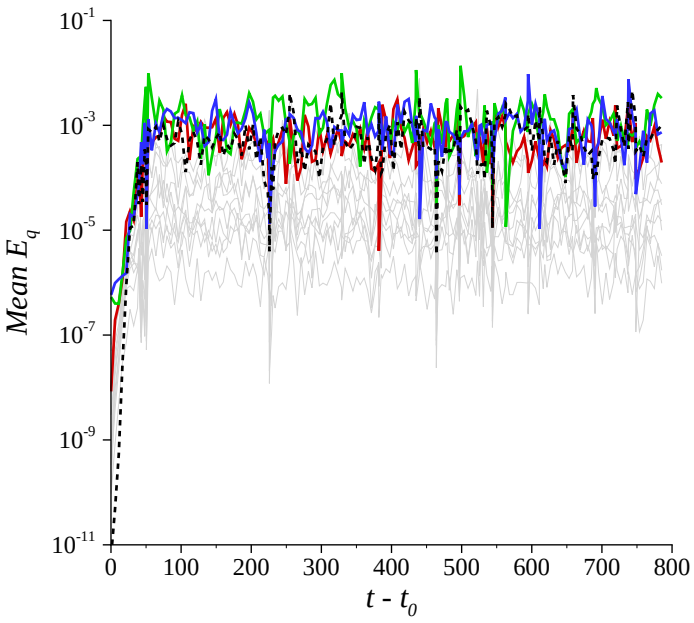

FIGURE 6.24: Evolution of the mean kinetic energy per period (E_q) for each azimuthal mode in the flow past a ring with $Ar = 20$ at $Re = 320$. Axes and lines are as per figure 6.1.

shows that at $Re = 320$, the three linear non-axisymmetric instability modes contain a similar proportion of the overall azimuthal energy in the wake. The fundamental azimuthal mode also contains a significant proportion of the azimuthal mode energy, indicating a lack of ordered patterns in the wake, in agreement with the wake isosurface visualisation presented in figure 6.23.

A plot of the Strouhal frequency variation in the flow past a ring with $Ar = 20$ at $Re = 320$ is presented in figure 6.25(a). The plot is remarkably similar to the plot for the flow past the same ring at $Re = 280$. In this plot, the Strouhal frequencies from drag force measurements are concentrated in the range $0.199 < St < 0.210$, whereas the Strouhal frequencies from point velocity measurements are scattered over a large range of frequencies.

Spectra of the point velocity and drag force time histories are presented in figure 6.25(b). The distribution of spectral density for both the drag force and the point velocity time histories is similar to the spectra presented for the flow past a ring with $Ar = 20$ at $Re = 280$. The drag force peak at $f/f_0 = 2$ is more strongly defined at $Re = 320$ than at $Re = 280$, which suggests a the reduction in the pairing of vortices

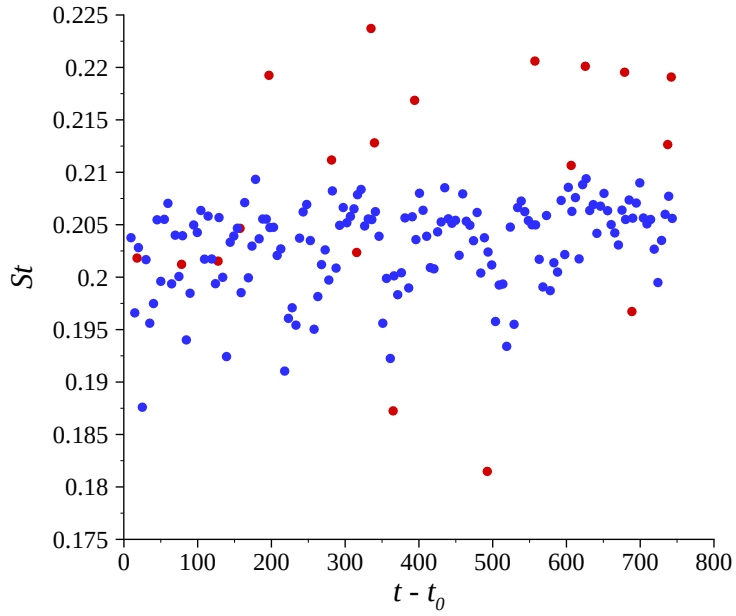

(a) Time history of the variation in the Strouhal frequency. Symbols are as per figure 6.2.

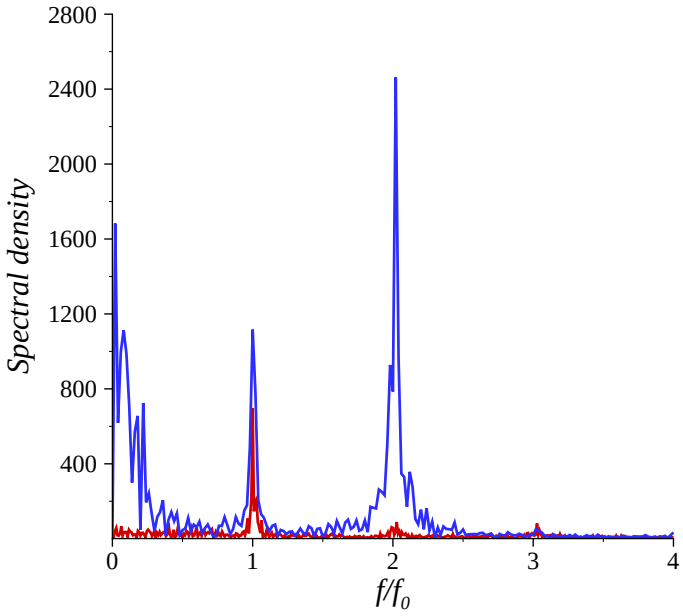

(b) Fourier spectra of the time histories of both a point velocity and the drag force. The chart lines and axes are as per figure 6.3, and the Strouhal frequency $St = f_0 = 0.2035$.

FIGURE 6.25: Strouhal frequency variation (a) and time history spectra (b) for the flow past a ring with $Ar = 20$ at $Re = 320$.

in the vortex street due to the ring curvature at this higher Reynolds number. The subharmonic peak in the point velocity spectrum at $f/f_0 = 0.5$ is absent, which is consistent with the absence of temporal regions dominated by subharmonic Mode C wavelengths in the mean azimuthal mode energy plot at $Re = 320$ in figure 6.24.

6.3 Azimuthal Domain Variation Study

Results are presented in this section from computations which were initiated from the computed flow fields obtained in the Reynolds number variation study. The Reynolds number from the computations of the tertiary instability regime is preserved for this study. To hasten saturation of the flow, the new modes introduced by the azimuthal Fourier expansion over the domain size $\lambda_d = 2L_0$ are perturbed by the addition of random noise at the commencement of the computations.

6.3.1 $Ar = 5$ with $\lambda_d = 2L_0$

The flow past a ring with $Ar = 5$ is computed to saturation at $Re = 320$, with an azimuthal domain size $\lambda_d = 2L_0$.

In figure 6.26 the mean azimuthal mode energy is presented for the flow past a ring with $Ar = 5$ at $Re = 320$, computed over a domain size $\lambda_d = 2L_0$. Saturation is observed occurring at $t - t_0 \approx 100$, and the computation is continued for approximately 550 further time units, providing over 100 vortex shedding cycles. The plot shows that upon saturation, a consistent random variation is present in the azimuthal energy of each mode, however individual modes only occupy a certain band of energies, and on average, it is the longer-wavelength azimuthal modes that contain the most energy in the saturated wake. Interestingly, in agreement with the findings of Henderson (1997) for the circular cylinder wake, the longest-wavelength mode ($\lambda_d \approx 8d$) was the highest-energy azimuthal mode in the present computation. Coupled with the significant amount of energy contained in the fundamental azimuthal mode, it is likely that the wake will exhibit a lack of coherence between any repeated non-axisymmetric wake structures in the azimuthal direction.

Isosurface plots which show the non-axisymmetric structure of the wake have been captured at times $t - t_0 = 300$ and $t - t_0 = 650$, and are presented in figure 6.27. It is obvious from the plots that there is little evidence of coherent non-axisymmetric wake patterns in the flow past a ring with $Ar = 5$. The near wake displays a distribution of

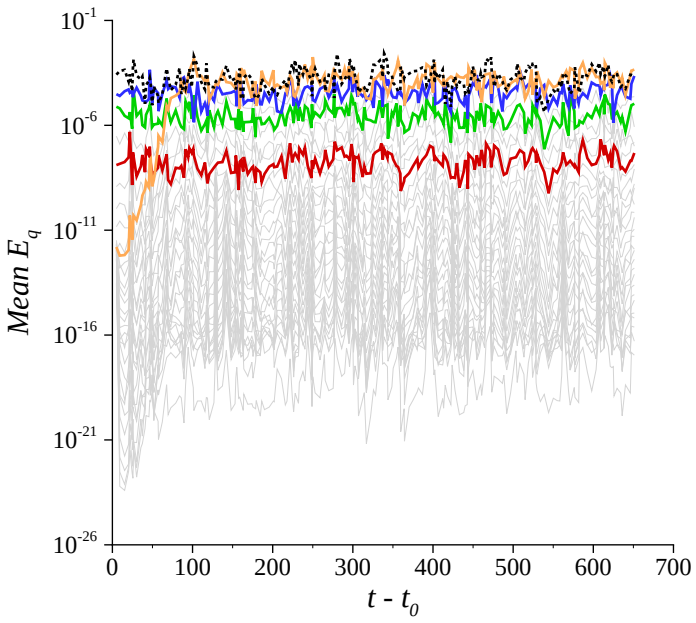

FIGURE 6.26: Evolution of the mean kinetic energy per period (E_q) for each azimuthal mode in the flow past a ring with $Ar = 5$ at $Re = 320$, with an azimuthal domain size $\lambda_d = 2L_0$. The fundamental Fourier mode is represented by a dotted black line, and the longest-wavelength azimuthal mode ($\lambda_d \approx 8d$) is coloured orange. The azimuthal modes which correspond to the wavelengths of the Mode A, B and C instabilities are represented by blue, red and green lines, respectively, and shorter-wavelength modes are coloured light grey.

Mode B wake structures in the near wake behind the ring cross-section at $t - t_0 = 300$. However, at $t - t_0 = 650$ these Mode B structures appear to break down at the azimuthal mid-point of the computational domain, in a fashion similar to the observed bursting of a Mode A wavelength wake structure among Mode B wake structures in the computed straight circular cylinder wake at $Re = 265$ (Henderson 1997) with a large spanwise computational domain.

Further downstream, isolated portions of the wakes at both times exhibit non-axisymmetric structures corresponding to either Mode B or Mode C type wake structures, however the high proportion of wake energy contained in the fundamental and longest-wavelength azimuthal modes destroy any large-scale repetitive wake patterns of these vortex shedding modes.

The Strouhal frequency variation measured from a point velocity time history and the drag force time history (see figure 6.28(a)) shows a high similarity to the Strouhal

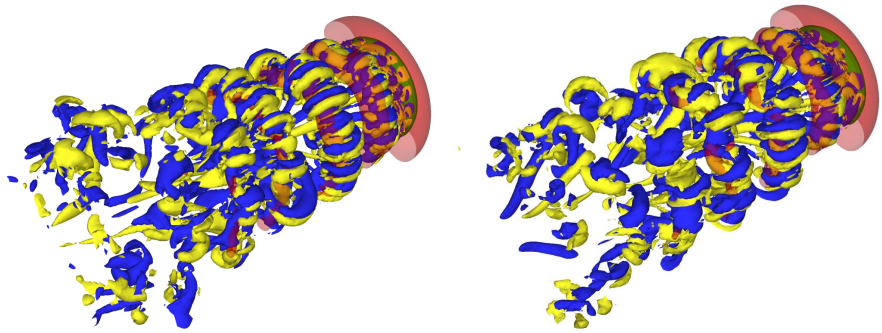

(a) $t - t_0 = 300$. (b) $t - t_0 = 650$.

FIGURE 6.27: Isosurface plots of the saturated wake structures in the flow past a ring with $Ar = 5$ at $Re = 320$. An azimuthal domain size of $\lambda_d = 2L_0$ was employed, and contour shading is as per figure 6.8.

frequencies determined from the corresponding computations with an azimuthal domain size $\lambda_d = L_0$, in that there is a wide scatter in the point velocity Strouhal frequencies, and the drag force Strouhal frequencies occupy three distinct frequency bands. A greater number of drag force frequencies occupy the shedding frequency band at approximately $St = 0.17$, while the harmonic frequency bands occupy frequencies $St \approx 0.325$ and $St \approx 0.45$.

Two significant alterations to the Fourier spectra of the saturated time histories of the point velocity and the drag force measurements shown in figure 6.28(b) have occurred when compared with the spectra obtained from computations with $\lambda_d = L_0$. Firstly, the drag force spectrum peaks have become broader, and higher frequencies contain a greater proportion of spectral density than for the drag force measurements over the shorter azimuthal domain. Secondly, the point velocity peak at $f/f_0 = 1$ is far smaller than for the point velocity peak obtained from the computations with $\lambda_d = L_0$, and the peak at $f/f_0 = 2$ is imperceptible. This agrees with the observation from figure 6.28(a) that shows no perceptible grouping of point velocity Strouhal frequencies near the base shedding frequency from the drag force measurements of $St \approx 0.17$.

The discrepancy between the point velocity and drag force Fourier spectra show that with the larger computational domain, and the induced breakdown of the regular patterns that correspond to non-axisymmetric vortex shedding modes, time histories recorded at a point in the wake will appear random due to the chaotic nature of the wake, whereas the drag force retains the shedding frequency information, as it is a

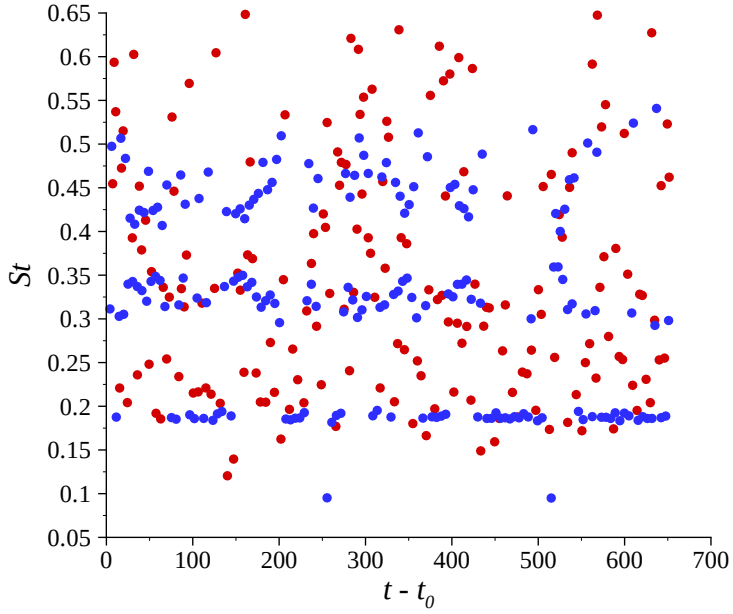

(a) Strouhal frequency variation. Axes and symbols are as per figure 6.2.

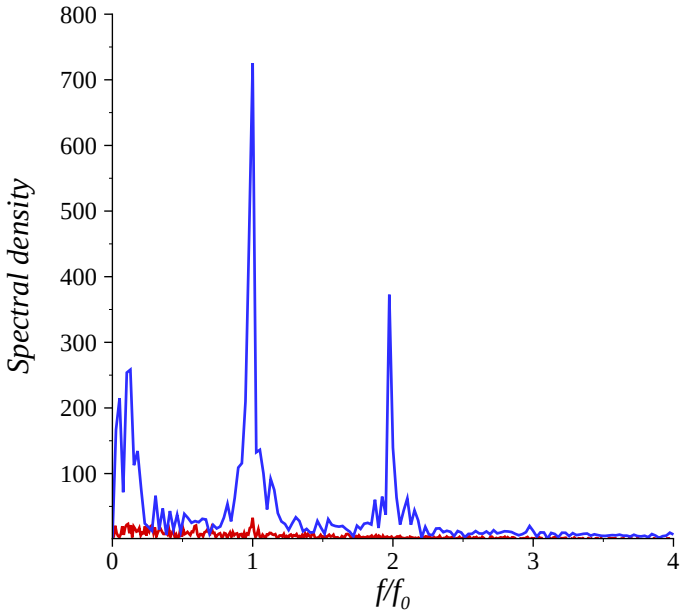

(b) Fourier spectra of the time histories of both a point velocity and the drag force. The chart lines and axes are as per figure 6.3, and the Strouhal frequency $St = f_0 = 0.1896$.

FIGURE 6.28: Strouhal frequency variation (a) and time history spectra (b) for the flow past a ring with $Ar = 5$ at $Re = 320$, with an azimuthal domain size of $\lambda_d = 2L_0$.

global measure of the wake dynamics. The broader peak in the drag force spectrum indicates a loss in periodicity of the wake, which likely results from the influence on the wake of the longer-wavelength azimuthal mode introduced into the computations.

In the numerical study of the flow past a circular cylinder by Henderson (1997), the route to chaos in the vortex street was proposed to occur through the development of spatio-temporal chaos. In computations of the flow past a ring with $Ar = 5$, the wake was observed to experience a period-doubling bifurcation. With an increase in Reynolds number, this subharmonic instability was replaced by a harmonic non-axisymmetric Mode A instability, which eradicated the period-doubling bifurcation in the wake. A further increase in Reynolds number caused a competition between Mode A, B and C wake structures, but no evidence of a subharmonic peak was observed in the spectral density plots at higher Reynolds numbers, which showed that a period-doubling cascade was not observed in the flow past a ring with $Ar = 5$.

An increase in the azimuthal span caused a breakdown of the non-axisymmetric wake patterns due to the influence of longer-wavelength azimuthal modes. These modes contained a higher proportion of energy than the azimuthal modes of the Mode A, B and C instabilities. This phenomenon indicated that the route to turbulence in the flow past a ring with $Ar = 5$ occurred through the development of spatio-temporal chaos, rather than through a period-doubling cascade, despite the period-doubling bifurcation that occurred with the primary non-axisymmetric instability.

In figure 6.29, time history plots of the reconstructed spatial w–velocity variation in the wake are presented. The data was originally obtained at a point in the wake approximately $4d$ directly downstream of the ring cross-section, and these plots were reconstructed from the mode energy (E_q) plots presented in this chapter. The azimuthal phase of the Fourier modes of the velocity have been omitted, and the velocity modes have been averaged over each shedding cycle. This is important, as these time history plots do not display the physical spatio-temporal wake patterns (such as those presented by Henderson (1997)); instead, they provide an alternative means to visualise the contribution of the azimuthal modes to the non-axisymmetric wakes.

Figure 6.29(a) shows the evolution of the Mode C instability in the flow past a ring with $Ar = 5$ at $Re = 190$. The dominant azimuthal wavelength of the saturated wake ($\lambda_d = L_0/2$) is consistent with that of a Mode C instability, and the observed structure of the non-axisymmetric wake (see figure 6.8). The uniformity of the plot at saturation

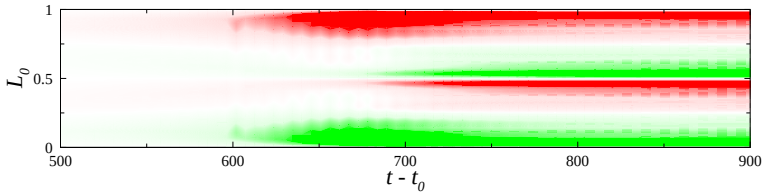

(a) $Re = 190$.

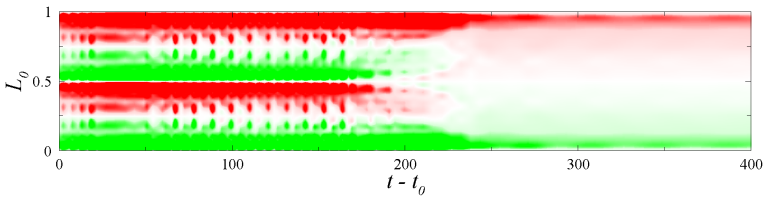

(b) $Re = 220$.

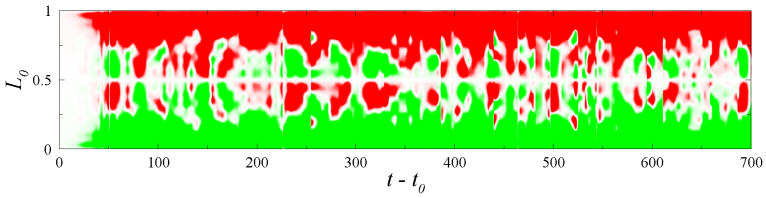

(c) $Re = 320$, $\lambda_d = L_0$.

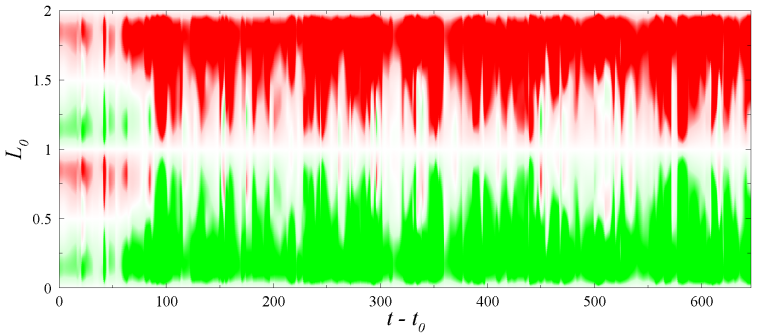

(d) $Re = 320$, $\lambda_d = 2L_0$.

FIGURE 6.29: Reconstructed time history plots of the mean w–velocity variation over a span at a z–r location in the wake per shedding cycle, for a ring with $Ar = 5$. Positive and negative velocities are indicated by green and red contours, respectively. Arbitrary contour levels are used, and azimuthal phase information is disregarded for clarity. The dominant mode at a time $t - t_0$ can be determined from the azimuthal (y–direction) wavelengths of the cycles between positive and negative velocities (i.e. Modes A, B and C have $\lambda_d \approx L_0$, $L_0/4$ and $L_0/2$, respectively).

$(t - t_0 \gtrsim 750)$ is indicative of the periodicity of the wake.

When the Reynolds number is increased to $Re = 220$ in figure 6.29(b), the Mode C wake pattern became unstable, as observed by the variation in strength of the azimuthal wake velocity for $t - t_0 \lesssim 200$. For $t - t_0 \gtrsim 200$, the Mode C pattern dissipated, and was replaced by a wake pattern dominated by a Mode A wavelength ($\lambda_d = L_0$) which was stable and periodic. The velocities observed for $t - t_0 \gtrsim 200$ show that the stable wake which formed after the dissipation of the Mode C wake had a smaller non-axisymmetric energy than the Mode C wake. In chapter 5, it was shown that the amplitudes of successive pure non-axisymmetric modes of a wake decreased with an increase in Reynolds number, and the computed pure Mode A wakes had approximately double the amplitude when compared to the pure Mode C wakes. The observation here, though, suggests that the amplitude of the non-axisymmetric wake structure decreased with an increase in Reynolds number throughout the laminar regime, irrespective of the order of the instability modes.

The time history plot in figure 6.29(c) shows the wake at $Re = 320$. At this Reynolds number, each of the non-axisymmetric vortex shedding modes are linearly unstable to the axisymmetric wake, and the chaotic pattern that is observed in the plot indicates that structures corresponding to each of the three instabilities exist in the wake, albeit briefly. The large regions of positive and negative velocity for $L_0 = 0$ and 1, respectively, indicate that the longest-wavelength mode dominates the wake upon saturation at $t - t_0 \approx 50$. At several instances in the time history, a pattern consistent with a Mode C wake is shown to dominate the wake. These include $45 \lesssim t - t_0 \lesssim 60$, $225 \lesssim t - t_0 \lesssim 250$ and $300 \lesssim t - t_0 \lesssim 350$. For far more brief periods, the presence of wavelengths consistent with Mode B ($L_0/4$) can be observed (e.g. $t - t_0 \approx 255$ and $t - t_0 \approx 645$).

An increase in the azimuthal span to $\lambda_d = 2L_0$ had an interesting effect on the wake, as shown by the plot in figure 6.29(d). The wake with $\lambda_d = L_0$ which was used for the initial condition rapidly breaks down, and by $t - t_0 \approx 90$, a chaotic wake state dominated by the longest-wavelength mode is sustained. The high irregularity and aperiodicity of the wake is evidenced by the fluctuation in velocity throughout the time history. Significantly, however, only for very brief durations can evidence of the presence of wake structures corresponding to the vortex shedding instabilities be observed. A possible Mode A wake may exist at $t - t_0 \approx 300$, or $t - t_0 \approx 450$, and at $t - t_0 \approx 510$

a wavelength corresponding to Mode C briefly emerges. The limited presence of wake structures which correspond to the linear vortex shedding modes, and the domination of the chaotic wake by the longest-wavelength mode, are consistent with the flow past a circular cylinder (Henderson 1997) and rings (Leweke & Provansal 1995), in terms of the development of spatio-temporal chaos in the wake.

Despite the period-doubling of the wake caused by the initial non-axisymmetric bifurcation, evidence of a period-doubling cascade with an increase in Reynolds number is not observed. Instead, the temporal wake fluctuations are induced by the non-linear interaction between the vortex shedding modes with an increase in Reynolds number. An increase in the azimuthal span introduces longer-wavelength modes, which dominate the wake dynamics, and initiate a route to turbulence through the development of spatio-temporal chaos.

6.3.2 $Ar = 10$ with $\lambda_d = 2L_0$

The mean azimuthal mode energy plot obtained from computations of the flow past a ring with $Ar = 10$ at $Re = 280$ bears some subtle differences to the corresponding plot of the flow past a ring with $Ar = 5$ which employed an azimuthal domain size $\lambda_d = 2L_0$. The plot is presented in figure 6.30.

The magnitude of the mode energies is significantly lower for the present computations, with the saturated mode energies varying between $10^{-29} \lesssim E_q \lesssim 10^{-8}$, rather than $10^{-22} \lesssim E_q \lesssim 10^{-3}$ for the flow past a ring with $Ar = 5$. The longest-wavelength azimuthal mode (8d) contains a great majority of the azimuthal mode energy in the wake, averaging an energy of order $O(10^3)$ greater in magnitude than the next highest energy mode, corresponding to the wavelength of Mode A.

The fundamental azimuthal mode of wake asymmetry contains a far lower proportion of the overall energy than for the computation of the flow past a ring with $Ar = 5$ which employed an azimuthal domain size $\lambda_d = 2L_0$, with a magnitude $E_q \approx 10^{-20}$.

The Strouhal frequency variation from the present computations of the flow past a ring with $Ar = 10$ at $Re = 280$ is presented in figure 6.31(a). The distribution and magnitude of the Strouhal frequencies is very similar to the corresponding measurements of the Strouhal frequencies with a computational domain size $\lambda_d = L_0$.

The spectra obtained from the computations with an azimuthal domain size $\lambda_d = 2L_0$ are presented in figure 6.31(b). The drag force Fourier spectrum of the saturated

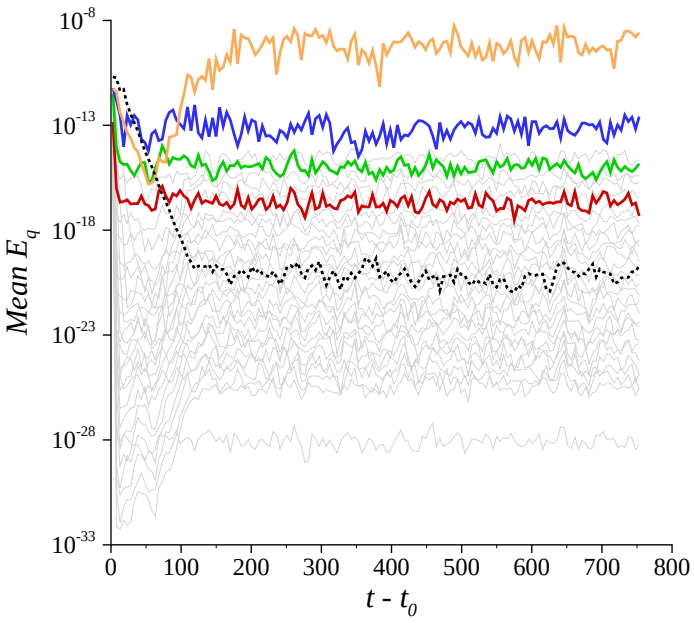

FIGURE 6.30: Evolution of the mean kinetic energy per period (E_q) for each azimuthal mode in the flow past a ring with $Ar = 10$ at $Re = 280$, with an azimuthal domain size $\lambda_d = 2L_0$. Line colouring is as per figure 6.26.

wake computed for the flow past a ring with $Ar = 10$ at $Re = 280$, with an azimuthal domain size $\lambda_d = 2L_0$, is almost identical in profile to the corresponding spectrum measured from the wake computed with an azimuthal domain size $\lambda_d = L_0$. The point velocity spectrum is somewhat different to the corresponding spectrum obtained from computations with $\lambda_d = L_0$. In those computations, the magnitude of the shedding frequency and harmonic peaks were larger than those observed in the present computations. It is also observed that there is a more pronounced reduction in the spectral density of the point velocity signal than the drag force signal at higher frequencies from computations with an azimuthal domain $\lambda_d = 2L_0$.

Isosurface plots which show the non-axisymmetric wake structures for the flow past a ring with $Ar = 10$ at $Re = 280$ computed with an azimuthal domain size $\lambda_d = 2L_0$ are presented in figure 6.32. As with the isosurface plots generated from the computations with $\lambda_d = 2L_0$ for the flow past a ring with $Ar = 5$, there is little consistency in terms of the non-axisymmetric structures in the wake in either the azimuthal direction, or between the pair of plots which were obtained at different times throughout the computation. The near wake again consists largely of Mode B type wake structures,

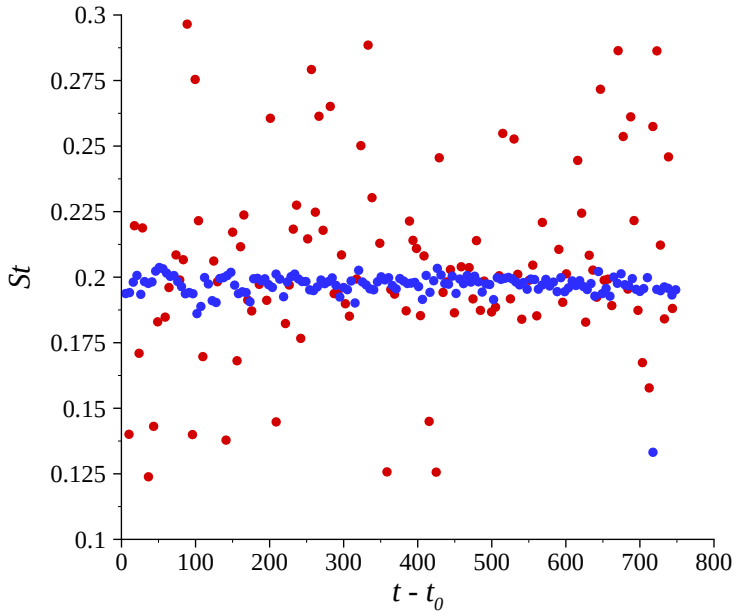

(a) Strouhal frequency variation. Axes and symbols are as per figure 6.2.

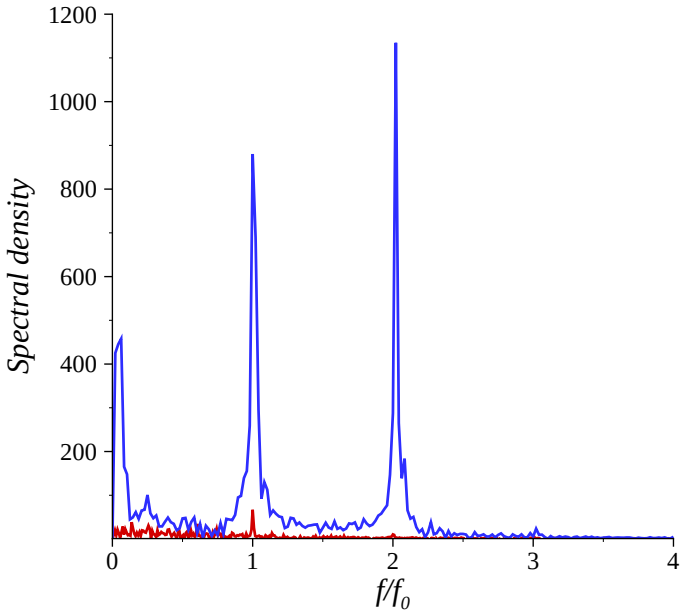

(b) Fourier spectra of the time histories of both a point velocity and the drag force. The chart lines and axes are as per figure 6.3, and the Strouhal frequency $St = f_0 = 0.1971$.

FIGURE 6.31: Strouhal frequency variation (a) and time history spectra (b) for the flow past a ring with $Ar = 10$ at $Re = 280$, with an azimuthal domain size $\lambda_d = 2L_0$.

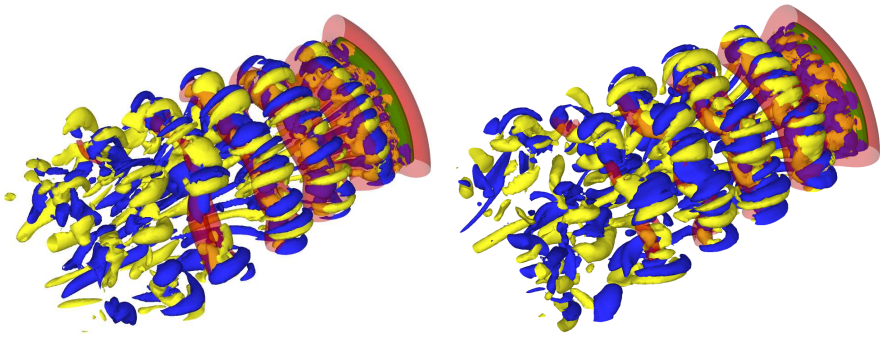

(a) $t - t_0 = 360$. (b) $t - t_0 = 630$.

FIGURE 6.32: Isosurface plots of the saturated wake structures of the flow past a ring with $Ar = 10$ at $Re = 280$. The computations employed an azimuthal domain size $\lambda_d = 2L_0$, and contour shading is as per figure 6.8.

although the uniformity of the structures is not maintained over the azimuthal span. At distances downstream of greater than approximately $4d$ to $5d$ from the ring cross-section, the Mode B streamwise vortical structures are replaced by wake patterns which exhibit a spatio-temporal symmetry consistent with Mode C. These Mode C structures are better defined in figure 6.32(a), at $t - t_0 = 360$. The plot in part (b) shows a downstream wake region which consists of structures with a longer azimuthal wavelength, which likely result from interference of the Mode A instability, and longer-wavelength non-linear modes.

The isosurface plots in part (a) and part (b) show a loss of any discernable wake patterns at distances downstream greater than approximately $15d$.

The flow past a ring with $Ar = 10$ shows some curious characteristics as the Reynolds number increases through the critical Reynolds numbers of the linear instability modes.

The evolution of the primary instability, Mode A, produces a periodic wake, as may be observed from the time history plot in figure 6.33(a). The wake at $Re = 205$ is fully saturated and periodic for $t - t_0 \gtrsim 840$, with the wake dominated by an azimuthal wavelength which corresponds to the Mode A instability ($\lambda_d = L_0$). This is in good agreement with the results presented earlier in figures 6.9 and 6.10. The regions of weak positive and negative velocity at approximately $0.3L_0$ and $0.7L_0$ result from the contribution of shorter-wavelength modes to the structure of the saturated wake.

The plot in figure 6.33(b) shows the result of a Reynolds number increase to $Re =$

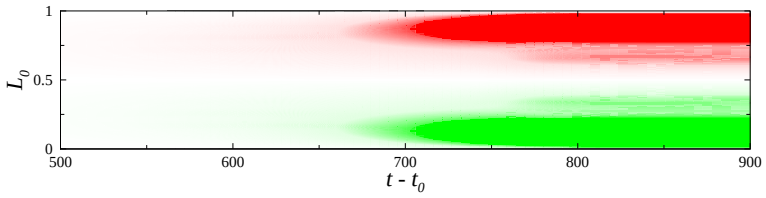

(a) $Re = 205$.

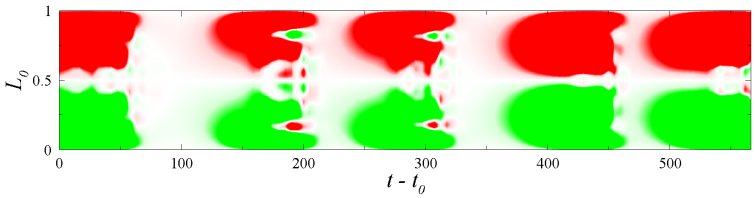

(b) $Re = 240$.

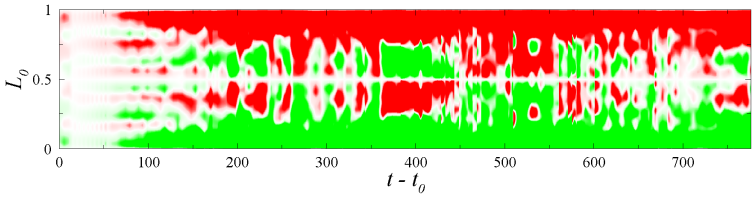

(c) $Re = 280$, $\lambda_d = L_0$.

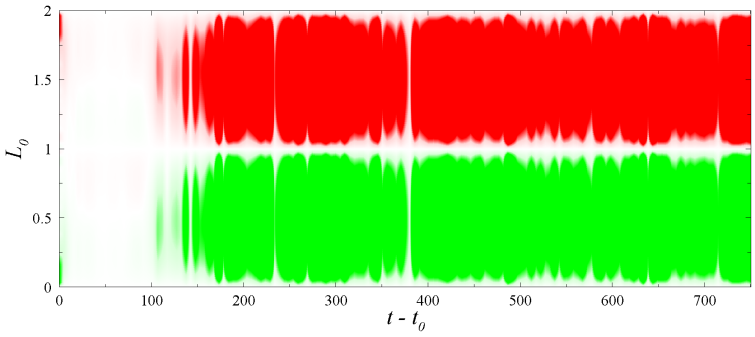

(d) $Re = 280$, $\lambda_d = 2L_0$.

FIGURE 6.33: Reconstructed time history plots of the mean w–velocity variation over a span at a z–r location in the wake per shedding cycle, for the flow past a ring with $Ar = 10$. Contour colours and levels are as per figure 6.29.

240. The wake adopts a cycle of evolution and self-destruction over a timescale in the order of $T = 1.5 \times 10^2$ time units (which corresponded to approximately 3×10^1 shedding cycles). This cycle was discussed earlier, in terms of the azimuthal mode energy variation and the non-axisymmetric wake structure, but a useful contribution is made by the plot in figure 6.33(b). Clearly, the evolution of the non-axisymmetric modes is represented by the shaded regions. Notice that the evolution of each of these regions is dominated initially by the Mode A wavelength, and after some time $50 \lesssim \Delta t \lesssim 80$, shorter wavelength modes (such as Mode C and Mode B) evolve. It is most clearly apparent at times $t - t_0 \approx 200$ and 310, that the destruction of the non-axisymmetric wake structures occurs immediately upon saturation of structures with an azimuthal wavelength consistent with the Mode B instability.

In chapter 7, the stability of the saturated three-dimensional wakes of a circular cylinder is investigated. The observation here of the destruction of a Mode A wake caused by the evolution of a competing Mode B instability is a key result which pertains to that study.

A further increase in Reynolds number causes another dramatic alteration in the observed time history in figure 6.33(c). The long-timescale cyclic evolution of the non-axisymmetric wake is no longer observed. Instead, for $t - t_0 \lesssim 100$, evidence of a Mode B wavelength is observed to evolve in the wake. For times $100 \lesssim t - t_0 \lesssim 150$, this wavelength is unstable and dissipates, instead replaced by a chaotic saturated wake state characterised by a rapid switching between vortex shedding modes for all times $t - t_0 \gtrsim 150$. An exception is the region $360 \lesssim t - t_0 \lesssim 440$, which is dominated solely by a Mode C wavelength. The overall dynamics of the time history bears a striking resemblance to that of the flow past a ring with $Ar = 5$ in figure 6.29(c).

A time history of the wake computed with an increased azimuthal domain size is presented in figure 6.33(d). As with the plot shown in figure 6.29(d), the wake is dominated by the additional longer-wavelength mode $\lambda_d = 2L_0$ in the computations. A chaotic variation in flow structures is observed in the saturated wake at $t - t_0 \approx 150$, and no evidence of shorter-wavelength modes which correspond to Mode A, B or C are observed.

The flow past a ring with $Ar = 10$ has revealed some interesting phenomena which pertain to the non-axisymmetric transitions in the wake. Despite the periodic Mode A wake which evolved from the primary non-axisymmetric transition, the subsequent

competition between instability modes with an increase in Reynolds number first initiated a long-timescale cyclic evolution and destruction of the non-axisymmetry in the wake, which was followed by a chaotic wake characterised by the rapid switching between the various unstable vortex shedding modes. An increase in the azimuthal span introduced longer wavelengths to the wake that produced dynamics consistent with a route to turbulence through the development of spatio-temporal chaos.

6.3.3 $Ar = 20$ with $\lambda_d = 2L_0$

The wake computed for the flow past a ring with $Ar = 20$ at $Re = 320$, with an azimuthal domain size $\lambda_d = 2L_0$ exhibited an almost identical behaviour to the wake in the flow past a ring with $Ar = 10$ at $Re = 280$.

The mean azimuthal mode energy plot for the flow past a ring with $Ar = 20$ is presented in figure 6.34. It is immediately obvious that the relative trends and magnitudes of the individual azimuthal modes is very similar to those of the flow past a ring with $Ar = 10$ presented previously in figure 6.30. Notice specifically the high proportion of energy contained within the longest-wavelength ($\lambda_d \approx 8d$) mode of the system compared to the other azimuthal modes of asymmetry. It is also of interest to observe the linear decay of the fundamental mode to a magnitude of approximately 10^{-25} for $t - t_0 \gtrsim 190$.

Isosurface plots of the non-axisymmetric wake structure of the flow past a ring with $Ar = 20$ at $Re = 320$ have been captured at times $t - t_0 = 390$ and $t - t_0 = 750$. These plots are presented in figure 6.35, and show a strong correlation with the non-axisymmetric wake structure computed for the flow past a ring with $Ar = 10$ at $Re = 280$, with an azimuthal domain size $\lambda_d = 2L_0$. Similarities include the concentration of streamwise vortical structures with an azimuthal wavelength which corresponds to the Mode B instability, which are located within approximately $5d$ of the ring, and a chaotic wake observed further downstream, with isolated instances of structures with azimuthal wavelengths which correspond to both Modes A and C. The chaotic behaviour observed in the far wake explains the high proportion of azimuthal mode energy contained by the longest-wavelength mode in the computation.

In both parts (a) and (b) of figure 6.35, a large deformation of the vortex rollers along the azimuthal span of the wake is observed. This deformation results in a maximum deviation of the vortex cores from the mean position in the r–z plane of between

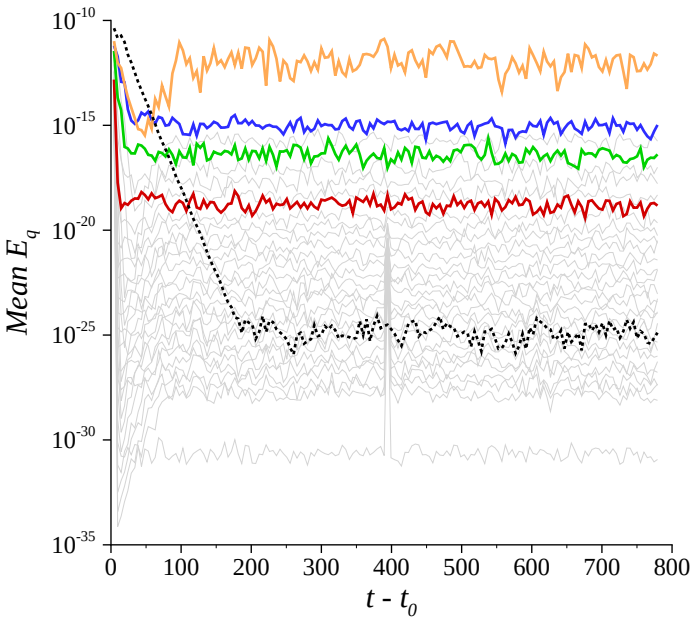

FIGURE 6.34: Evolution of the mean kinetic energy per period (E_q) for each azimuthal mode in the flow past a ring with $Ar = 20$ at $Re = 320$, with an azimuthal domain size $\lambda_d = 2L_0$. Line colouring is as per figure 6.26.

$1d$ to $2d$. The shorter-wavelength non-axisymmetric wake structures deform with the deformation of the vortex street, and this corresponds with the breakdown of coherent wake patterns which correspond to the linear instability modes.

The frequency variation plot in figure 6.36(a) reiterates the similarity between the computations which employed an azimuthal domain size $\lambda_d = 2L_0$, for the flow past a ring with $Ar = 10$, and the present computations of the flow past a ring with $Ar = 20$. A diverse scatter of the point velocity frequency measurements is observed, which relates to the chaos observed in the wake. The drag force frequency measurements provide a reasonable estimate of the vortex shedding frequency of the wake, with a great majority of the measured frequencies calculated in a range $0.199 < St < 0.205$, centred around $St \approx 0.202$.

It can be observed from the Fourier spectra of figure 6.36(b) that both the drag force time history and the point velocity time history behave in a fashion similar to the time histories computed from the flow past a ring with $Ar = 10$ with an azimuthal domain size $\lambda_d = 2L_0$. The point velocity spectrum exhibits a single peak at $f/f_0 = 1$. For lower frequencies ($f/f_0 \to 0$) the spectral density of both the point velocity and the drag

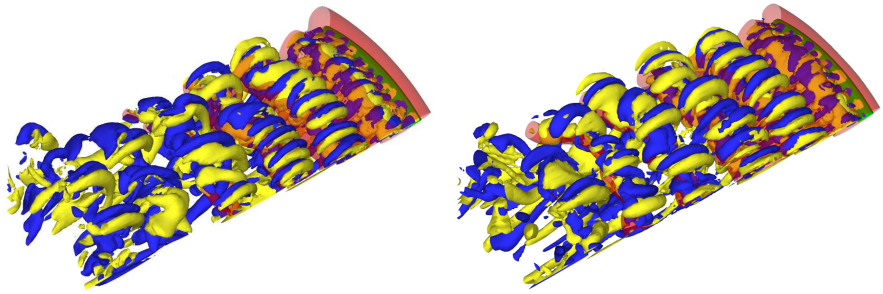

(a) $t - t_0 = 390$. (b) $t - t_0 = 750$.

FIGURE 6.35: Isosurface plots of the saturated wake structures in the flow past a ring with $Ar = 20$ at $Re = 320$. The azimuthal domain size is $lambda_d = 2L_0$, and contour shading is as per figure 6.8.

force time histories increase, which suggests the presence of large-timescale disturbances in the wake. This may be due to the influence of the longest-wavelength azimuthal mode included in the computations. The spectrum of the drag force contains a strong harmonic peak at $f/f_0 = 2$, which relates to the drag force frequency of two-dimensional vortex streets. In addition, a small peak at the harmonic frequency $f/f_0 = 4$ is also visible. In keeping with the aspect ratio trend towards a circular cylinder, it may be noted that the peak at $f/f_0 = 2$ is stronger here than the corresponding peaks measured from the flow past rings with higher curvatures ($Ar = 5$ and $Ar = 10$).

The time history plot in figure 6.37(a) provides an interesting visual representation of the saturated Mode A wake for a ring with $Ar = 20$. Recall that upon saturation, the wake displayed a small chaotic frequency fluctuation. After saturation of the mode with an azimuthal wavelength $\lambda_d = L_0$ in the wake at $t - t_0 \approx 460$, shorter-wavelength modes are observed to cause a small aperiodicity in the wake. The small amplitude of these modes compared to the Mode A wavelength means that they can only be observed, in figure 6.37(a), in the region $0.35L_0$–$0.65L_0$. The observed frequency fluctuation indicates that the Mode A wake is unstable, as at this Reynolds number no evidence of an alternative instability, such as the evolution of the Mode B or the Mode C instability is observed.

In figures 6.37(b) and 6.37(c), time histories of the wake are presented for $Re = 280$ and $Re = 320$, respectively. These plots indicate a similar dynamical behaviour of the wake, with a chaotic competition between the longest-wavelength Mode A in-

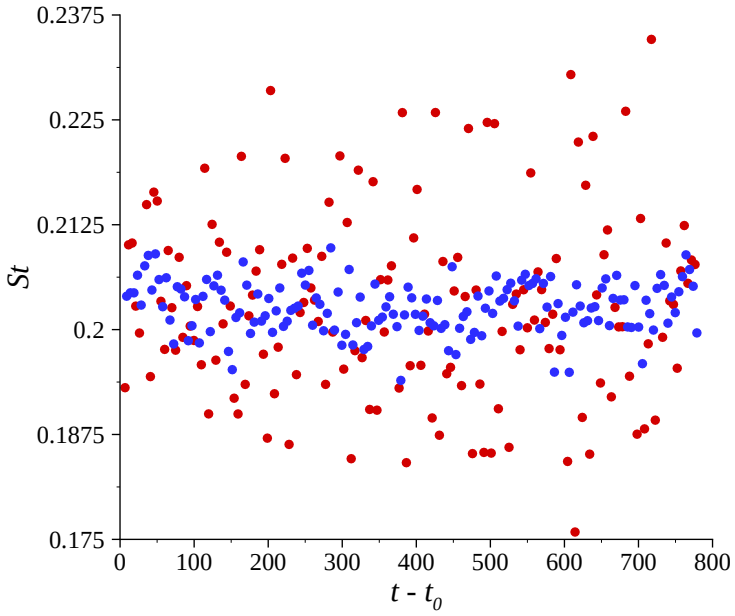

(a) Time history of the variation in the Strouhal frequency. Symbols are as per figure 6.2.

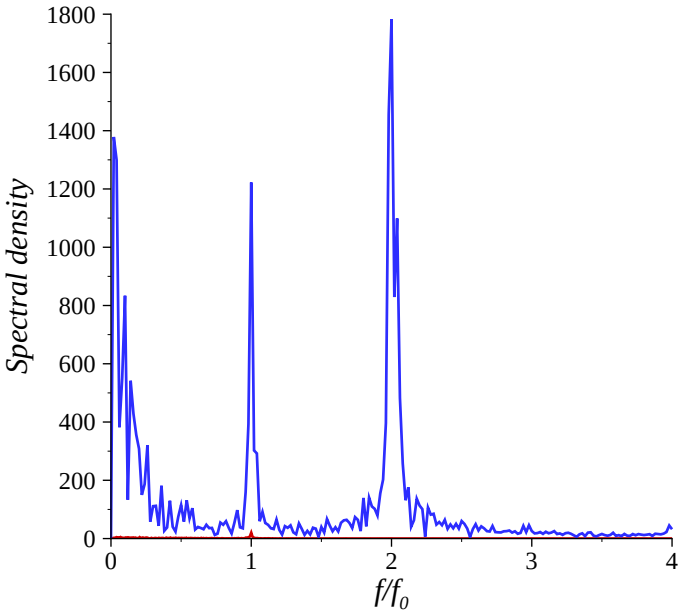

(b) Fourier spectra of the time histories of both a point velocity and the drag force. The chart lines and axes are as per figure 6.3, and the Strouhal frequency $St = f_0 = 0.2027$.

FIGURE 6.36: Strouhal frequency variation (a) and time history spectra (b) for the flow past a ring with $Ar = 20$ at $Re = 320$, with an azimuthal domain size $\lambda_d = 2L_0$.

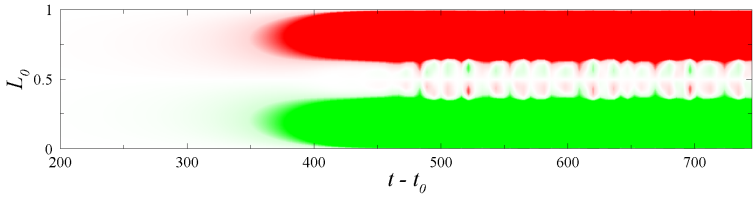

(a) $Re = 205$.

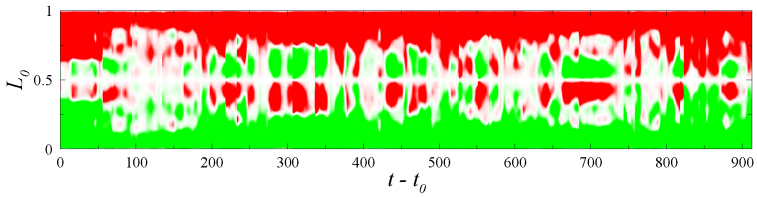

(b) $Re = 280$.

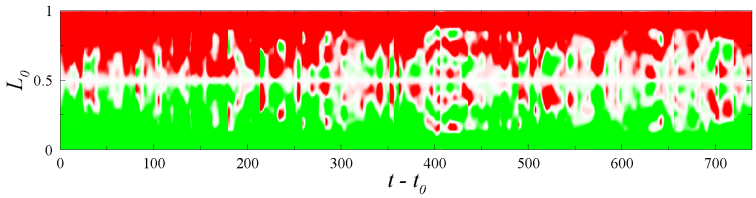

(c) $Re = 320$, $\lambda_d = L_0$.

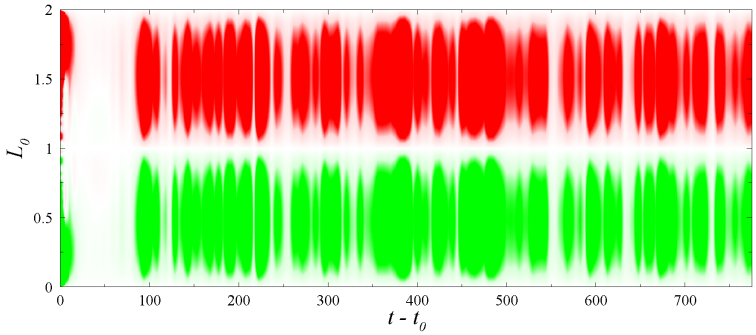

(d) $Re = 320$, $\lambda_d = 2L_0$.

FIGURE 6.37: Reconstructed time history plots of the mean w–velocity variation over a span at a z–r location in the wake per shedding cycle, for the flow past a ring with $Ar = 20$. Contour colours and levels are as per figure 6.29.

stability, and wavelengths associated with the Mode C and Mode B instabilities. A higher prevalence of regions dominated by Mode C wavelengths may be observed (e.g. $200 \lesssim t - t_0 \lesssim 350$ and $425 \lesssim t - t_0 \lesssim 480$) in figure 6.37(b), when compared with figure 6.37(c), which appears to be dominated by the longest-wavelength mode (e.g. $t - t_0 \lesssim 200$), as well as comprising several regions with a significant proportion of wavelengths corresponding to the Mode B instability (e.g. $t - t_0 \approx 400$).

These time history plots bear a remarkable similarity to the plots obtained at $Re = 320$ for the flow past a ring with $Ar = 5$, and at $Re = 280$ for the flow past a ring with $Ar = 10$, in figures 6.29(c) and 6.33(c), respectively. This indicates that irrespective of the order in which the linear vortex shedding instabilities are predicted to occur, the non-linear interaction between the non-axisymmetric modes will incite a similar chaotic competition in the wake. In figure 6.37(d), a plot of the time history of the wake computed with an azimuthal span of $\lambda_d = 2L_0$ is presented. Consistent with previous computations with a span of $\lambda_d = 2L_0$, a chaotic time history is observed, which indicates that the wake is dominated by the longest-wavelength mode, and no evidence can be observed of the formation of non-axisymmetric wake structures which correspond to the Mode A, B or C instabilities.

In the present work, the vortex streets in the wakes behind rings have been studied which have both a subharmonic and a regular first-occurring non-axisymmetric instability. From the observed behaviour of the computed wakes, it is concluded that turbulent flow develops in a vortex street through the development of spatio-temporal chaos, irrespective of the spatio-temporal symmetry of the first-occurring non-axisymmetric mode. This conclusion is in agreement with the study by Henderson (1997), who proposed that the route to chaos for the vortex street in the flow past a circular cylinder was through the development of spatio-temporal chaos.

6.4 Drag and Strouhal–Reynolds Number Measurements

In this section, both the mean drag coefficients from the computations performed in this chapter, and the Strouhal frequencies obtained, will be compared with earlier work.

6.4.1 Drag Coefficients with Mode Interaction

In chapter 3, drag coefficients were presented from axisymmetric computations of the flow past rings, a sphere, and a circular cylinder. The results were compared to pre-

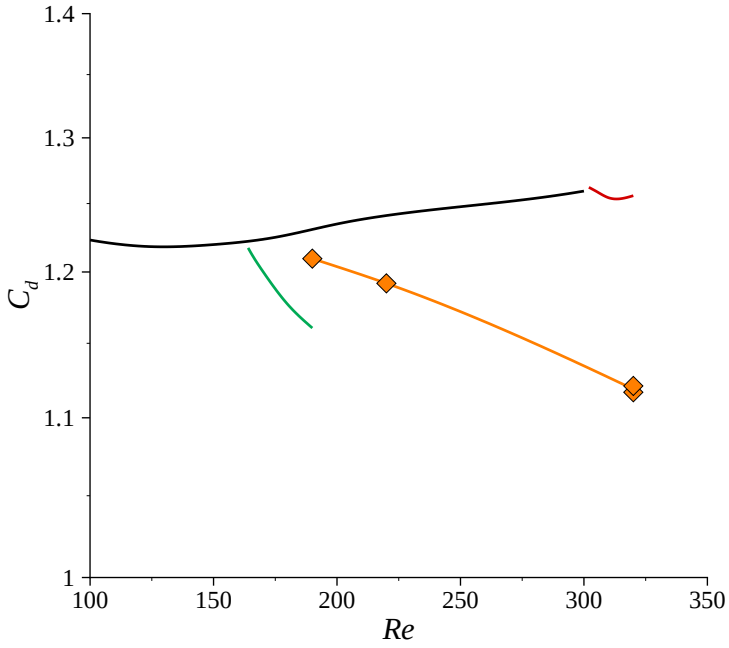

(a) Total drag (C_d).

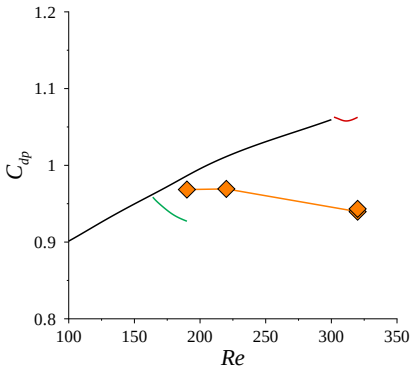

(b) Pressure component (C_{dp}).

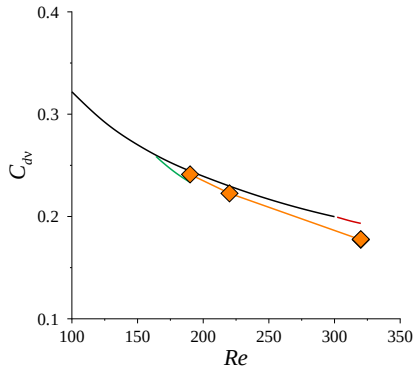

(c) Viscous component ($C_{d\nu}$).

FIGURE 6.38: Total and component drag coefficients computed for the non- axisymmetric bifurcations in the flow past a ring with $Ar = 5$, with azimuthal domain sizes $\lambda_d = L_0$ and $2L_0$ (represented by orange line and diamonds). The previous axisymmetric drag profile is represented by a black line, and the non-axisymmetric instabilities are shown by blue, red and green lines, for Mode A, Mode B and Mode C, respectively.

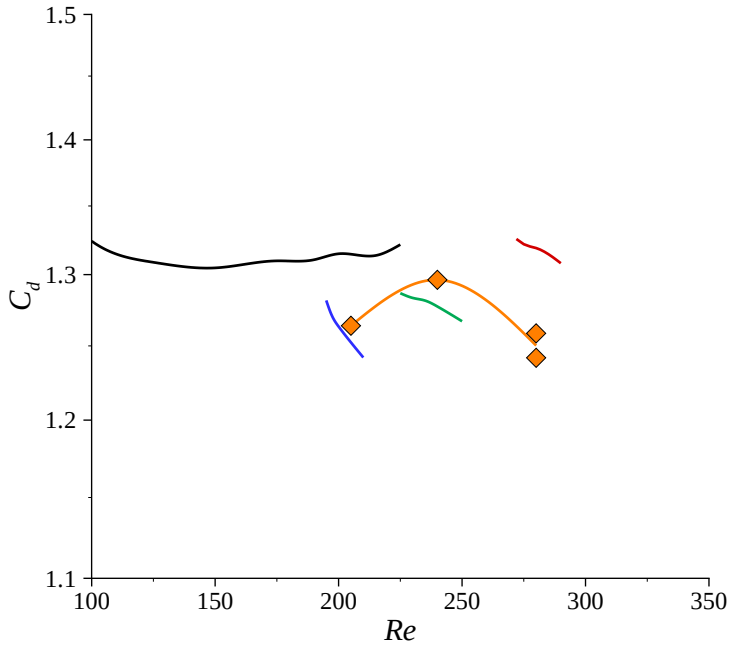

(a) Total drag (C_d).

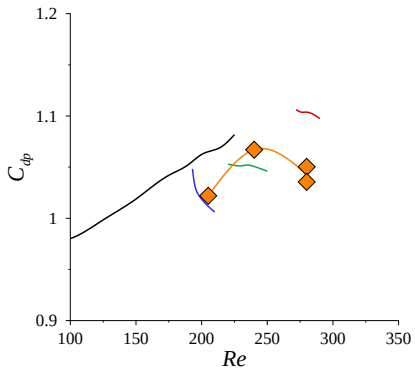

(b) Pressure component (C_{dp}).

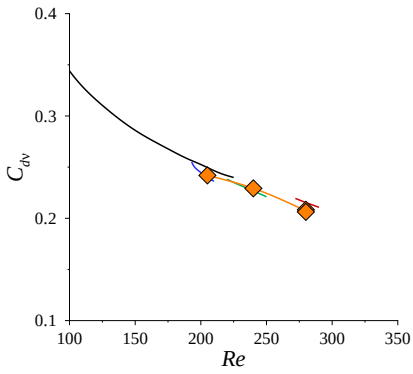

(c) Viscous component ($C_{d\nu}$).

FIGURE 6.39: Total and component drag coefficients computed for the non- axisymmetric bifurcations in the flow past a ring with $Ar = 10$. Colours and symbols are as per figure 6.38.

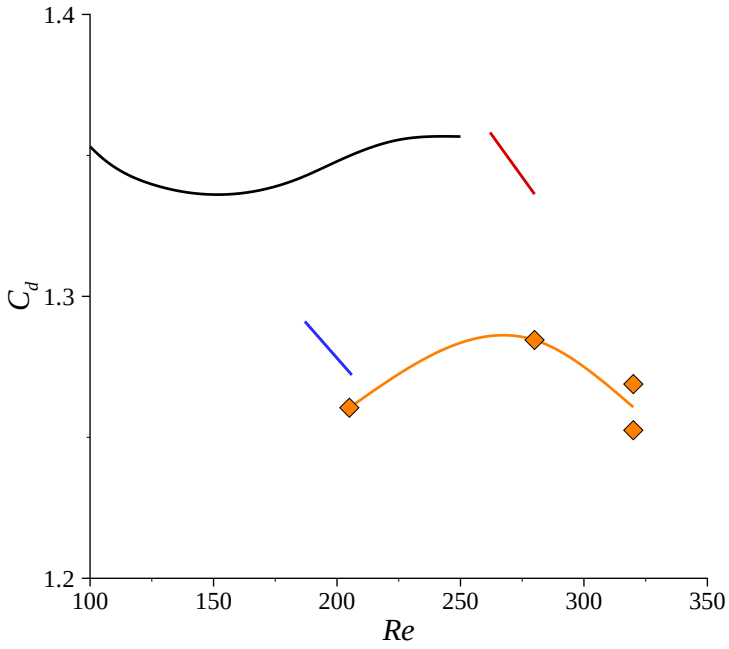

(a) Total drag (C_d).

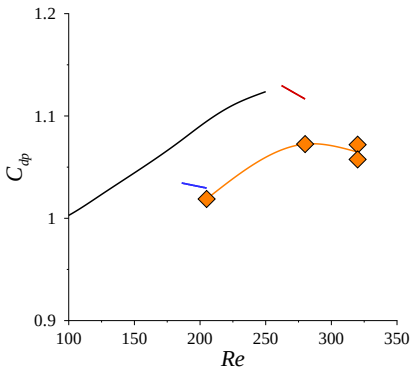

(b) Pressure component (C_{dp}).

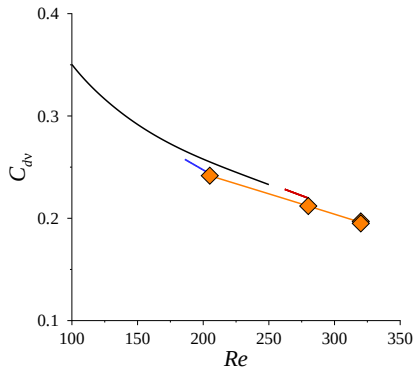

(c) Viscous component ($C_{d\nu}$).

FIGURE 6.40: Total and component drag coefficients computed for the non- axisymmetric bifurcations in the flow past a ring with $Ar = 20$. Colours and symbols are as per figure 6.38.

vious experimental and numerical studies, and a discrepancy was observed between mean two- and three-dimensional drag measurements of the flow past a circular cylinder. In Chapter 5, drag coefficients were presented from computations of the pure non-axisymmetric vortex shedding modes in the flow past rings, which showed that the evolution of non-axisymmetric vortex shedding modes caused a reduction in the drag coefficient due to a reduction in the pressure component of the drag force. The suppression of mode interaction in those results limited the scope of the results.

In the present chapter, computations were employed with a sufficient azimuthal span to permit all the linear instabilities in the wake to evolve. The data from figures 5.23, 5.30 and 5.36 are reproduced here, with the inclusion of the measured mean drag coefficients from the present study. Drag coefficients computed in the flow past rings with $Ar = 5$, $Ar = 10$ and $Ar = 20$ are presented in figures 6.38, 6.39 and 6.40, respectively.

For the flow at each aspect ratio, there is a significant decrease from the axisymmetric C_d profile for each of the rings as the Reynolds number is increased (figures 6.38(a), 6.39(a) and 6.40(a)). It is apparent from the plots of the pressure and viscous components of the drag coefficient that the decrease in the drag is almost solely the result of a reduction in the pressure component of the drag coefficient (compare figures 6.38(b), 6.39(b) and 6.40(b) with figures 6.38(c), 6.39(c) and 6.40(c), respectively).

The hysteretic onset of the first-occurring non-axisymmetric transitions in the flow past rings with $Ar = 10$ and 20 can be observed in figures 6.39 and 6.40. In figure 6.38, the continuous bifurcation of the non-axisymmetric drag coefficient profile from the axisymmetric drag coefficient profile verifies the non-hysteretic onset of the first-occurring non-axisymmetric transition in the wake. In figures 6.39 and 6.40, the onset of non-axisymmetric flow induces a sharp and discontinuous reduction in the measured drag coefficient with an increase in Reynolds number. The drag coefficient profiles increase with an increase in Reynolds number for a short time, before they decrease with a further increase in the Reynolds number.

6.4.2 Strouhal–Reynolds Number Profiles with Mode Interaction

Mean Strouhal frequencies have been determined for the saturated wakes obtained from the computations performed in this chapter. Data were obtained through the non-axisymmetric flow regimes in the flow past rings with $Ar = 5$, 10 and 20. For

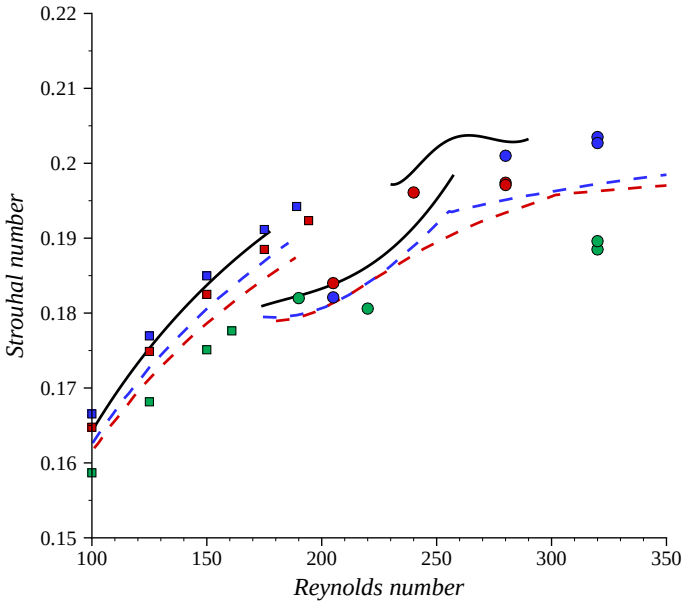

FIGURE 6.41: Strouhal–Reynolds number profiles over the non-axisymmetric flow regimes in the flow past rings. Squares and circles represent computed axisymmetric and non-axisymmetric data, respectively. Lines represent the experimentally measured profiles from Leweke & Provansal (1995). The Strouhal–Reynolds number profile for the flow past a circular cylinder (black line, Williamson 1988a, 1996b) is included for reference. Blue represents numerical results with $Ar = 20$, and experimental data with $Ar = 18.8$. Red represents numerical and experimental data with $Ar = 10$, and green represents numerical data with $Ar = 5$.

comparison, the experimental Strouhal–Reynolds number profiles presented by Leweke & Provansal (1995) are presented. Their study included Strouhal number measurements for the flow past rings with $Ar = 10.0$ and $Ar = 18.8$, which are compared to the computed Strouhal numbers for the flow past rings with $Ar = 10$ and $Ar = 20$.

A Strouhal–Reynolds number plot which illustrates this comparison is provided in figure 6.41. Observe the laminar axisymmetric shedding profiles for $Re \lesssim 180$. The numerical computations consistently predict Strouhal frequencies at a given Reynolds number approximately 2% higher than the experimental data. As this discrepancy lies outside the error bounds of the numerical computations, a probable explanation for this discrepancy is the influence of long-wavelength instabilities on the experimental measurements, which were recorded over many shedding cycles.

The limited number of numerical Strouhal frequencies obtained through the non-

axisymmetric flow regime make comparisons with the experimental profiles difficult. The computed values for the wakes behind rings with $Ar = 10$ and 20 at $Re = 205$ are close to the experimental profiles, which indicates that a uniform Mode A wake was likely to have been captured experimentally in the flow past rings with these aspect ratios.

The discontinuous drop in Strouhal frequency at the onset of the Mode A transition is captured by the non-axisymmetric computations of the flow past rings with $Ar = 10$ and 20. Compare these Strouhal–Reynolds number profiles to the continuous variation in the Strouhal–Reynolds number profile observed for the flow past a ring with $Ar = 5$, where $St \approx 0.18$ was obtained for $160 \lesssim Re \lesssim 220$, before an increase to $St \approx 0.188$ at $Re = 320$.

To properly include all possible wake dynamics in the computations, an azimuthal span sufficient to model the entire ring (requiring some 250 azimuthal Fourier modes) would be required, which is not feasible with the present computational resources. The small difference between the Strouhal numbers obtained from computations which employed azimuthal domain sizes of $\lambda_d = 1L_0$ and $2L_0$ verify the earlier assumption that the important wake dynamics through the non-axisymmetric flow regime (excluding oblique shedding modes) are captured with an azimuthal span of $\lambda_d \approx 8d$.

6.5 Oblique and Non-Linear Shedding Modes

In this section, an attempt to compute oblique shedding modes in the flow past a ring is presented. Experimental work carried out as part of this study observed evidence of both oblique shedding spirals, and a transverse shedding mode, which initiated a side-to-side motion of the ring.

6.5.1 Computation of an Oblique Shedding Mode

An oblique shedding mode was artificially constructed in the flow past a ring with $Ar = 4.94$ at $Re = 100$. An investigation of the number of azimuthal planes required to model a single-helix oblique vortex shedding mode was conducted. Strouhal frequency measurements from computations which employed 16 Fourier planes or greater varied by approximately 2%, and therefore 16 Fourier planes was considered sufficient for qualitative computations. The computed single-helix mode reached a steady state in the flow past rings, which verified that oblique shedding modes are stable at Reynolds

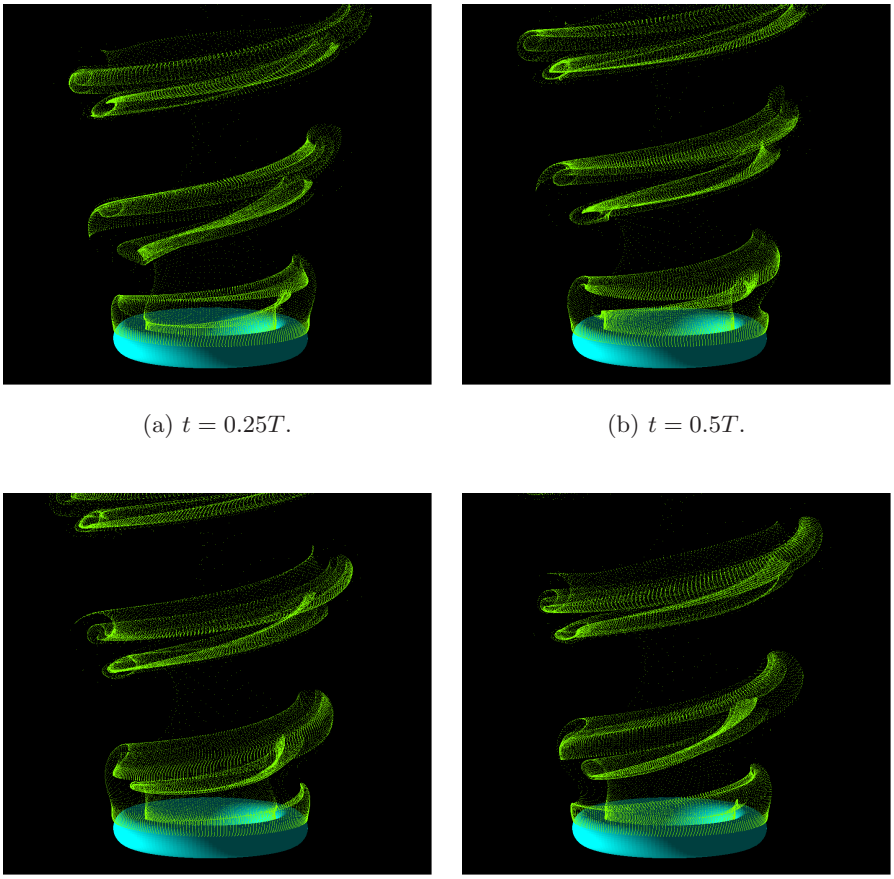

(a) $t = 0.25T$.

(b) $t = 0.5T$.

(c) $t = 0.75T$.

(d) $t = 1.0T$.

FIGURE 6.42: Simulated-particle computations of an artificially induced single-helix oblique shedding mode in the flow past a fixed ring with $Ar = 4.94$ at $Re = 180$, over a single shedding cycle.

numbers significantly in excess of the critical Reynolds number for the onset of vortex shedding, which was predicted in the application of the Ginzburg–Landau model by Leweke & Provansal (1995). Plots of a single-helix oblique mode in the flow past a ring with $Ar = 4.94$ at $Re = 180$ are shown throughout a period of shedding in figure 6.42.

6.5.2 Experimental Observations of a Transverse Mode

In the experimental setup, the buoyant ring was towed by a tether in a vertical direction. The arrangement permitted asymmetrical shedding modes to develop, which imposed a transverse oscillatory motion on the ring as it was towed through the tank. Both oblique and side-to-side oscillations were observed. In the sections to follow, the results

of tethered-body computations of the flow past a ring are presented, to compare with the experimentally observed modes.

6.5.2.1 The Numerical Technique Employed to Model a Tethered Body

A numerical scheme was employed to model the flow past a tethered ring. The numerical scheme was validated and successfully applied to model the flow past tethered spheres by Pregnalato (2003). Briefly, the numerical technique permits the body to move about a fixed tether of length L_{teth}. To calculate the motion, the viscous and pressure forces acting on the body are calculated, and from a given mass ratio $m^\star$, the acceleration of the body may be determined. A predictor–corrector method is employed to accurately determine the spatial shift of the body as the flow is computed.

For simplicity in the present computations, the mass ratio of the ring was set to unity, and a tether length $L_{teth} = 10$ was employed to approximate the experimental conditions. Artificial flow fields were employed as initial conditions, which were designed to initiate both oblique and transverse modes of shedding in the wake.

6.5.2.2 A Comparison Between Computations and Experimental Flow Visualisation

Figure 6.43 shows comparisons between the experimental dye visualisations and numerical simulated-particle tethered-body computations for flow past a ring with $Ar = 4.94$ at $Re = 180$.

The plots appear qualitatively similar, but upon close inspection, subtle differences may be observed between the vortex structure in the vicinity of the ring, and the location of the ring relative to the wake. These differences result from the choice of parameters in the numerical computations. The nature of the experimental setup was such that the tether shortened continuously as the ring descended through the tank. A mean value was selected as an approximation for the numerical study. There appears to be more motion in the experimental visualisations, which can be discerned from the images by the shearing of the near wake in the transverse direction within approximately $1d$ of the ring body. The motion in the numerical study was damped due to the selection of a mass ratio $m^\star = 1.0$. This was necessitated as the numerical code was formulated with gravity imposed in the transverse direction, rather than the axial direction as was required here. A mass ratio of unity was selected to overcome this buoyancy problem, whereas in fact the mass ratio was approximately $m^\star = 0.5$.

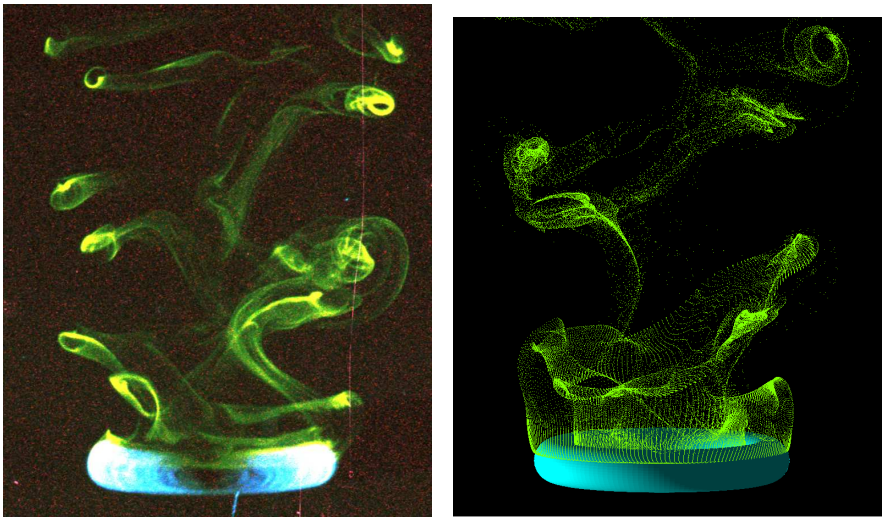

(a) Comparison 1. Left: Experimental dye visualisation. Right: Simulated-particle visualisation.

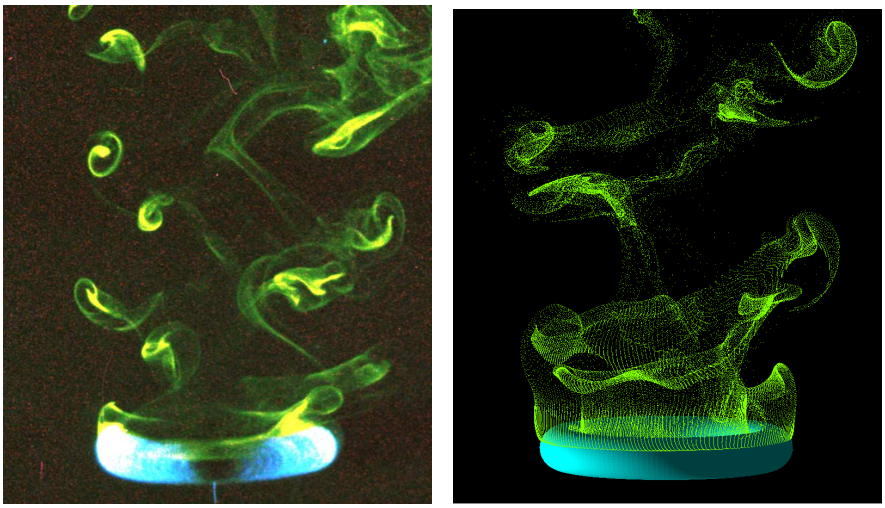

(b) Comparison 2. Left: Experimental dye visualisation. Right: Simulated-particle visualisation.

FIGURE 6.43: Comparison between experimental observations of a vortex-induced side-to-side motion of a ring, and numerical tethered-body computations. A ring with $Ar = 4.94$ at $Re = 180$ is shown. The tether length continuously reduced over the experimental run, whereas the computation employed a constant tether length that was approximately equal to the mean experimental tether length. In addition, the ring mass ratio was approximately 0.5 in the experiments, and was unity in the computation.

The overall structure of the wake in figure 6.43 shows a shedding of vorticity on alternate sides of the wake every half period, which is consistent with the unsteady wakes shed from rings with aspect ratios $Ar \lesssim 3.9$. It should be noted that computational attempts to artificially induce this transverse shedding mode in the flow past a fixed ring proved fruitless. In those computations, the vortex-loop structure quickly broke down, and the wake reverted to an axisymmetric vortex street. It is concluded that for fixed rings with aspect ratios $Ar \gtrsim 3.9$, oblique shedding modes are the only stable shedding modes which may be observed in the place of a parallel vortex street.

6.6 Chapter Summary

In this chapter, the development of non-uniformities in the parallel vortex streets in the flow past rings was investigated. The existence of other non-linear shedding modes has also been considered, with both helical and transverse shedding modes being successfully computed.

The development of non-uniformity in a vortex street has previously been studied in relation to the flow past a circular cylinder by Henderson (1997). In that study, computations were performed to analyse the wake in the context of pattern formation and the route to chaos for the wake. It was observed that chaotic flow developed in the wake with both an increase in Reynolds number, and the spanwise wavelength of the computations, through the development of spatio-temporal chaos.

In chapters 4 and 5, it was predicted and verified that the Mode C instability evolved through a subharmonic instability, which caused a period-doubling of the wake. It is known that a cascade of period-doubling bifurcations is a possible mechanism for the development of chaos in two-dimensional flows. Evidence is presented in this chapter which shows that the subharmonic instability does not initiate a period-doubling cascade in the vortex street for the flow past rings. Instead, it is proposed, based on the analysis of the wakes computed for this study, that the route to chaos in vortex streets behind rings occurs through the development of spatio-temporal chaos, which is consistent with the mechanism for the development of chaos in the vortex street behind a circular cylinder. It is proposed that regardless of whether or not the primary non-axisymmetric mode causes a period-doubling of the wake, the non-linear evolution of the mode introduces an azimuthal variation in the wake. This adds a spanwise variation to the wake, which is analogous to the addition of an extended spatial dimension to a

dynamical system. This feature invalidates the two-dimensional requirement necessary for a period-doubling cascade in the vortex street (Braun *et al.* 1998).

The existence of other possible modes of shedding in the flow past rings has also been studied in this chapter. Through application of both experimental dye visualisation, and numerical simulated-particle computations, a helical mode of shedding was visualised, which has been previously observed by Monson (1983) and Leweke & Provansal (1995). Through the implementation of numerical tethered-body computations, the experimental rig was accurately modelled, and a transverse mode of shedding was visualised which initiated a side-to-side motion of the ring both experimentally and computationally. The existence of this mode has not previously been reported, and the wake structure bears a similarity to the vortex distribution of the in-phase vortex streets behind a pair of circular cylinders from Williamson (1985a).

Previous computational studies have provided measurements of the drag coefficient for the three-dimensional flow past a circular cylinder (e.g. Henderson 1995). Those computations showed that the drag coefficients obtained from three-dimensional computations provided estimates of the drag coefficients which agreed more closely with experimental measurements. No measurements of the drag coefficients for the flow past rings has yet been reported for the Reynolds number range considered in the present study. Drag coefficients for the non-axisymmetric flow past rings have been computed as part of this study, and the results have been presented in this chapter. It was shown that in computations with an azimuthal domain size sufficiently large to capture the three non-axisymmetric instabilities of the vortex street, drag coefficients were obtained that were smaller than the drag coefficients obtained from axisymmetric computations over the non-axisymmetric flow regimes.

Chapter 7

Three-Dimensional Flow Regime for the Flow past a Circular Cylinder

The stability of vortex streets to both linear and non-linear three-dimensional instabilities was studied in chapters 4 to 6. In this chapter, the three-dimensional transition regime of the vortex street in the wake of a circular cylinder is studied. Through a series of classic experimental studies (Williamson 1988a,b, 1989, 1996b,c), the Strouhal–Reynolds number profile for the laminar flow past a circular cylinder was mapped. The measured profiles included discontinuities in the vicinity of the onset of Mode A and B. The discontinuity at the onset of Mode A was due to the hysteretic onset of the mode, and the discontinuity at the onset of Mode B was due to a gradual energy transfer between wake structures consistent with Mode A to Mode B. The computational studies of Barkley & Henderson (1996) and Henderson (1997) agreed with these experimental observations.

The Mode A and B instabilities were modelled as a coupled pair of evolution equations by Barkley *et al.* (2000). They determined coefficients of their model from three-dimensional computations of the pure Mode A and Mode B wakes. Their model showed that the development of three-dimensional flow in the wake of a circular cylinder, including the hysteretic onset of Mode A and the energy shift from Mode A to Mode B, could be described by a simple set of equations.

This chapter comprises two studies. Firstly, an extension of the evolution equations is developed, whereby frequency information is incorporated to model the Strouhal–Reynolds number profile of the wake of a circular cylinder through the three-dimensional transitions. Secondly, a linear stability analysis will be performed on spanwise-averaged

three-dimensional flows, to attempt to describe the three-dimensional bifurcations of the wake of a circular cylinder in terms of the stability of the pure three-dimensional flows.

The formulation of the coupled Landau model which is presented here has been discussed in Sheard *et al.* (2003a).

7.1 A Coupled Landau Model Describing the Three-Dimensional Modes in the Wake

This section details the extension of an existing set of coupled evolution equations for the amplitude of the three-dimensional Mode A and Mode B transitions in the wake of a circular cylinder, to describe the Strouhal–Reynolds number profile through the Reynolds number range of the transitions.

7.1.1 Characteristics of the Three-Dimensional Modes in the Wake

Williamson (1988b) identified two stages in the transition to three-dimensionality of the wake behind the circular cylinder. These stages are characterised by discontinuous transitions in the Strouhal–Reynolds number profile, coupled with the evolution of spanwise periodic deformations of the two-dimensional vortex street. The first transition, which resulted in a discontinuous and hysteretic reduction in the Strouhal frequency of shedding, has become known as Mode A. The Mode A wake comprises streamwise vortex loops in the braid region between successive rollers in the vortex street, and the spanwise wavelength of the repeating three-dimensional structures is approximately four cylinder diameters ($4d$). The transition to Mode A occurs over a hysteretic Reynolds number range of approximately $180 < Re < 190$, and the subsequent transition to the Mode B wake occurs gradually over an approximate Reynolds number range $230 < Re < 265$ (Henderson 1997). The Mode B wake pattern has a much shorter spanwise wavelength (approximately $1d$), and the transition to Mode B occurs through a gradual transfer of energy from Mode A to Mode B wake structures, coupled with an increase in the Strouhal frequency of shedding.

Three-dimensional numerical computations by Thompson *et al.* (1994, 1996) provided striking visualisations of the three-dimensional structure and spanwise wavelength of the Mode A and Mode B wake structures, as well as divulging the spatio-temporal symmetry of the wakes. Visualisations from similar computations have been presented

by Zhang *et al.* (1995) and Henderson (1997).

A landmark application of a linear Floquet stability analysis to the two-dimensional wake of a circular cylinder by Barkley & Henderson (1996) gave predictions of the critical Reynolds numbers for the three-dimensional transitions pertaining to both Mode A and Mode B, as well as correctly identifying the respective spanwise wavelength and spatio-temporal symmetry characteristics of the transition modes. They predicted Mode A to first occur with a spanwise wavelength of $3.96d$ at $Re \approxeq 188.5$, and the onset of Mode B to occur with a spanwise wavelength of $0.822d$ at $Re \approxeq 259$.

Three distinct flow regimes have been identified as the flow past a circular cylinder becomes three-dimensional. A Mode A regime exists for $180 \lesssim Re \lesssim 230$, where the wake is dominated by the Mode A instability. A mixed Mode A/B regime exists for $230 \lesssim Re \lesssim 265$, where a gradual transfer from Mode A to Mode B structures occurs, with both Mode A and B structures observed intermittently. A Mode B regime exists for $Re \gtrsim 265$, where the wake is dominated by the Mode B instability.

7.1.2 Non-Linear Transition Behaviour

The non-linear behaviour of the three-dimensional transition modes of the wake of the circular cylinder was first investigated by Henderson & Barkley (1996). They determined the complex Landau coefficients and ascertained whether the modes occurred through supercritical or subcritical bifurcations. The linear coefficients of the Landau equation were in agreement with the growth rates determined from stability analysis, and an analysis of the cubic coefficients provided the criticality of the transitions. Consistent with previous observations, the Mode A transition was found to occur through a subcritical bifurcation, indicating an hysteretic transition. The Mode B transition was found to occur through a supercritical bifurcation, consistent with a non-hysteretic transition.

The Landau model was applied successfully to various two- and three-dimensional transition modes in fluid mechanics applications. Provansal *et al.* (1987) used the Landau equation to model the Hopf transition of a steady circular cylinder wake to an unsteady wake at around $Re = 48.6$. The criticality of the asymmetric regular and Hopf transitions of the wake of a sphere were also accurately determined by Ghidersa & Dušek (2000) and Thompson *et al.* (2001a).

Barkley *et al.* (2000) suggested a bifurcation scenario consisting of coupled evolution

equations for the amplitudes of the Mode A and Mode B instabilities in the wake of a circular cylinder. The coupled evolution equations

$$\begin{aligned} A_{n+1} &= \mu^A(Re)A_n + \alpha_1^A|A_n|^2A_n + \gamma_1^A|B_n|^2A_n + \alpha_2^A|A_n|^4A_n, \\ B_{n+1} &= \mu^B(Re)B_n + \alpha_1^B|B_n|^2B_n + \gamma_1^B|A_n|^2B_n, \end{aligned} \tag{7.1}$$

are, essentially, truncated discrete Landau equations, incorporating additional coupling terms for A_n and B_n. A fifth-order truncation is sufficient to model the subcritical onset of Mode A, and a third-order truncation is sufficient to model the supercritical onset of Mode B. These Landau equations, incorporating third-order coupling, are a normal form for the simultaneous bifurcation of modes A and B.

7.1.3 Extension of the Coupled Evolution Equations

In order to model Strouhal frequency variation of the transition modes, the coefficients in equation 7.1 are expanded into the complex plane, and are evaluated for computed Strouhal frequencies of the saturated three-dimensional modes.

The values of the coefficients will be determined later. In equation 7.1, A_n and B_n represent the complex amplitudes of Mode A and Mode B, respectively, for the n^{th} period of oscillation. The μ^A and μ^B coefficients are the real Floquet multipliers of the linear instabilities of the cylinder wake, and the α_1^A and α_1^B coefficients are the cubic coefficients of the Landau model from the Henderson (1997) study. The α_2^A term is the additional quintic coefficient required to describe the saturation and hysteresis of Mode A, and finally the γ_1^A and γ_1^B coefficients determine the mode coupling of the system, and have been estimated from experimental observations (Williamson 1988b) of the transition from Mode A to Mode B in the circular cylinder wake.

In order to incorporate temporal information into the coupled amplitude equations, the evolution amplitudes A_n and B_n are replaced with complex amplitudes A and B, and in addition, the evolution equations are recast in the familiar differential equation form of the Landau equations. From the definition of the Floquet multiplier,

$$\mu \equiv \mathrm{e}^{(\sigma T)}, \tag{7.2}$$

the linear growth rate coefficient (σ) is substituted into the Landau equations, where T is the period of oscillation of the two-dimensional shedding mode. This substitution

gives

$$\begin{aligned}\frac{\mathrm{d}A}{\mathrm{d}t} &= [\sigma^A(Re) + \mathrm{i}\omega^A]A + \alpha_1^A(1 + \mathrm{i}c_1^A)|A|^2 A \\ &\quad + \gamma_1^A(1 + \mathrm{i}d_1^A)|B|^2 A + \alpha_2^A(1 + \mathrm{i}c_2^A)|A|^4 A, \\ \frac{\mathrm{d}B}{\mathrm{d}t} &= [\sigma^B(Re) + \mathrm{i}\omega^B]B + \alpha_1^B(1 + \mathrm{i}c_1^B)|B|^2 B + \gamma_1^B(1 + \mathrm{i}d_1^B)|A|^2 B.\end{aligned} \tag{7.3}$$

In equation 7.3, the angular frequency of the modes for infinitesimal amplitudes is given by $\omega^A = \omega^B = \omega \equiv 2\pi/T$, where T is the period of oscillation.

7.1.4 Evaluation of the Model Coefficients

The linear complex coefficients, ω^A and ω^B, are functions of Reynolds number, and provide the angular oscillation frequency in the linear regime of the transition modes, corresponding to the laminar Strouhal number profile of the two-dimensional vortex street. The complex coefficients, c_1^A, c_2^A and c_1^B, determine the frequency behaviour of the modes through saturation. The calculation of these coefficients is relatively simple, as they may be calculated independently for Mode A and Mode B. The c_1^B term is simply the Landau constant of the Mode B transition, and as the Mode B transition is described by a cubic truncation of the Landau model, the value of the coefficient may be determined by following the analysis of Dušek *et al.* (1994), and Le Gal *et al.* (2001). By assuming at saturation $B = \rho_{sat}^B \mathrm{e}^{(\mathrm{i}\Phi^B)}$ in a cubic truncation of the Landau equation for Mode B alone, where $\rho_{sat}^B = |B|$ and $\mathrm{d}\Phi^B/\mathrm{d}t = \omega^B$, the Landau constant can be expressed as a function of the global system parameters $c_1^B = (\omega^B - \omega_{sat}^B)/\sigma^B$, where ω_{sat}^B is the saturated oscillation frequency. These global parameters are determined from a three-dimensional computation including only Mode B.

For calculation of the α_1^A, α_2^A, c_1^A and c_2^A terms of the quintic Mode A transition model, two pairs of equations are formed for separate computations of the Mode A wake. By substituting $A = \rho_{sat}^A \mathrm{e}^{(\mathrm{i}\Phi^A)}$ in the quintic Mode A Landau equation, neglecting the coupling term and grouping real and imaginary parts, the relationships

$$\begin{aligned}0 &= \sigma^A + \alpha_1^A(\rho_{sat}^A)^2 + \alpha_2^A(\rho_{sat}^A)^4, \\ 0 &= \omega^A - \omega_{\mathrm{sat}}^A + \alpha_1^A c_1^A(\rho_{sat}^A)^2 + \alpha_2^A c_2^A(\rho_{sat}^A)^4,\end{aligned} \tag{7.4}$$

result for the sine and cosine coefficients.

The global parameters, ω^A, ω_{sat}^A, σ^A and ρ_{sat}^A, are determined for computations at two discrete Reynolds numbers in the Mode A flow regime, not far in excess of the critical Reynolds number, and the two pairs of equations are solved for the four

unknown coefficients: α_1^A, α_2^A, c_1^A and c_2^A. From the calculated values of α_1^A and α_2^A, the predicted Reynolds number range of hysteresis (ΔRe^A) may be found from

$$\Delta Re^A = \frac{-(\alpha_1^A)^2}{4m^A\alpha_2^A}, \tag{7.5}$$

where m^A is the gradient of the growth rate, $\sigma^A(Re)$. The values determined for the present study predict $\Delta Re^A \cong 16.2$, which is of the same order as the estimation of $\Delta Re^A \approx 10$ from Henderson (1997). Note that this figure is solely determined from the pair of computations of Mode A above the critical Reynolds number.

The real coupling coefficients are determined by using the experimentally observed (Williamson 1988b) Reynolds numbers for the first-occurring instance of Mode B, and the last-occurring instance of Mode A, in the cylinder wake. The coupled Mode A and Mode B equations are each evaluated at the Reynolds numbers at which their corresponding wake structures are last observed and first observed, respectively. For Mode A and Mode B, these critical Reynolds numbers are $Re^A_{last} \approx 260$ and $Re^B_{first} \approx 230$, respectively. Substituting $|A| = 0$ and $|B| = 0$ in the Mode A and Mode B equations, respectively, and solving for the coupled coefficients gives

$$\begin{aligned}
\gamma_1^A &= \frac{-\sigma^A_{Re=Re^A_{last}}}{|B_{Re=Re^A_{last}}|^2} = \frac{\alpha_1^B\sigma^A_{Re=Re^A_{last}}}{\sigma^B_{Re=Re^A_{last}}}, \\
\gamma_1^B &= \frac{-\sigma^B_{Re=Re^B_{first}}}{|A_{Re=Re^B_{first}}|^2} = \frac{2\alpha_2^A\sigma^B_{Re=Re^B_{first}}}{\alpha_1^A + \sqrt{(\alpha_1^A)^2 - 4\alpha_2^A\sigma^A_{Re=Re^B_{first}}}}.
\end{aligned} \tag{7.6}$$

The mode amplitudes $|A|$ and $|B|$ are determined from a norm of the three-dimensional velocity component from computations of the evolution of the three-dimensional Mode A and Mode B wakes. The amplitude norm is computed using the method employed in chapter 5, which also contains a discussion of the benefits of applying this (near) global measure of the amplitude of the mode to the Landau model.

The present amplitude norm integrates the w–velocity component over the computational domain. This is slightly different to the method applied by Henderson & Barkley (1996) and Henderson (1997), who integrated the longest-wavelength Fourier mode of the three-dimensional velocity component over their computational domain. The different integrals employed for the norms employed in these studies explains the quantitative difference between the magnitude of the amplitudes obtained for the present study, and the study of Barkley *et al.* (2000). The choice of integrals also produces the large discrepancy between the present α and γ parameters, and the values obtained previously

Coefficient	Value
σ^A	$1.699 \times 10^{-3}(Re - 187.41)$
σ^B	$4.868 \times 10^{-3}(Re - 258.24)$
ω^A and ω^B	$2\pi(8.539 \times 10^{-5} Re + 0.1999 - 4.009/Re)$
α_1^A	1.203×10^3
α_2^A	-1.313×10^7
α_1^B	-7.297×10^3
γ_1^A	-1.048×10^5
γ_1^B	1.033×10^3
c_1^A	-1.055
c_2^A	-0.3276
c_1^B	8.342×10^{-2}
d_1^A	-0.2
d_1^B	-0.25

TABLE 7.1: Values of coefficients determined for the present model.

by Barkley *et al.* (2000). The magnitude of these amplitudes is in fact arbitrary, it is important only to achieve a qualitative consistency between the amplitude profiles. The consistency between the predicted mode amplitude variation with Reynolds number from the present model, and the previous work (Barkley *et al.* 2000) in figure 7.1 is very good, indicating a high degree of computational accuracy for both studies.

Table 7.1 summarises the values of the coefficients of the complex amplitude equations employed in this investigation. All the real coefficients have been calculated from three-dimensional computations which were performed as part of the present study. The complex coefficients of first-order terms are derived from a Strouhal–Reynolds number relationship determined from the present numerical calculations, employing the same form as the universal laminar Strouhal–Reynolds number profile proposed by Williamson (1988a).

The higher-order complex coefficients are determined from computations of the evolution and saturation of three-dimensional wakes corresponding to the Mode A and Mode B instabilities. Computations at Reynolds numbers $Re = 195$ and $Re = 200$ were employed to evaluate the coefficients c_1^A and c_2^A for the Mode A instability. A computation of the Mode B wake at $Re = 265$ was used to evaluate the coefficient c_1^B. Values for the complex coupling coefficients, d_1^A and d_1^B, were chosen to equate the computed Strouhal frequencies at the last appearance of Mode A, and the onset of Mode B, respectively, with experimentally obtained frequencies (Williamson 1988b).

The coupled complex amplitude equations proposed here are solved simultaneously

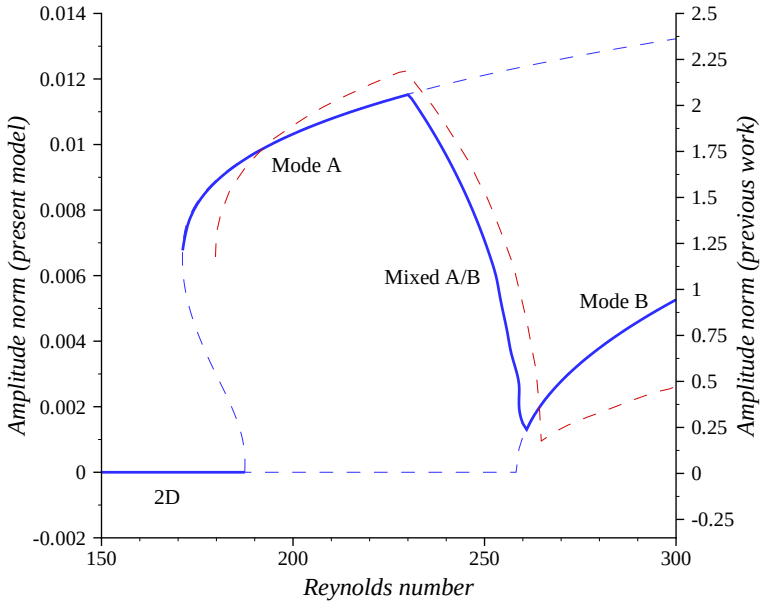

FIGURE 7.1: Bifurcation diagram which shows the predicted $\sqrt{|A|^2 + |B|^2}$ variation with Reynolds number from the coupled models. The blue line represents the prediction of the present model, and the dotted red line shows the prediction of the coupled evolution equations from Barkley *et al.* (2000).

by employing a third order Adams-Bashforth scheme, giving

$$\begin{aligned} A_{i+1} &= A_i + \frac{\Delta t}{12}[23 f_i^A - 16 f_{i-1}^A + 5 f_{i-2}^A], \\ B_{i+1} &= B_i + \frac{\Delta t}{12}[23 f_i^B - 16 f_{i-1}^B + 5 f_{i-2}^B], \end{aligned} \tag{7.7}$$

where f_i^A and f_i^B denote the right hand sides of the complex coupled Landau equations evaluated at the i^{th} timestep. The asymptotic frequency information may be evaluated from the saturated mode amplitudes directly, but in a future expansion of the present model, a spanwise diffusion term is to be included to model long-wavelength three-dimensional wake patterns, in a fashion similar to the complex Ginzburg-Landau model applied to the wakes behind rings by Leweke & Provansal (1995). The future expansion necessitates temporal integration of the model, and the Adams-Bashforth method is implemented here for the purpose of validation. The Adams-Bashforth method maintains an accuracy of order Δt^4, as verified by a brief temporal resolution study that determines the stability and accuracy of the present numerical formulation. Temporal stability was achieved for time steps $\Delta t \leq 0.125$. The computed Strouhal frequency

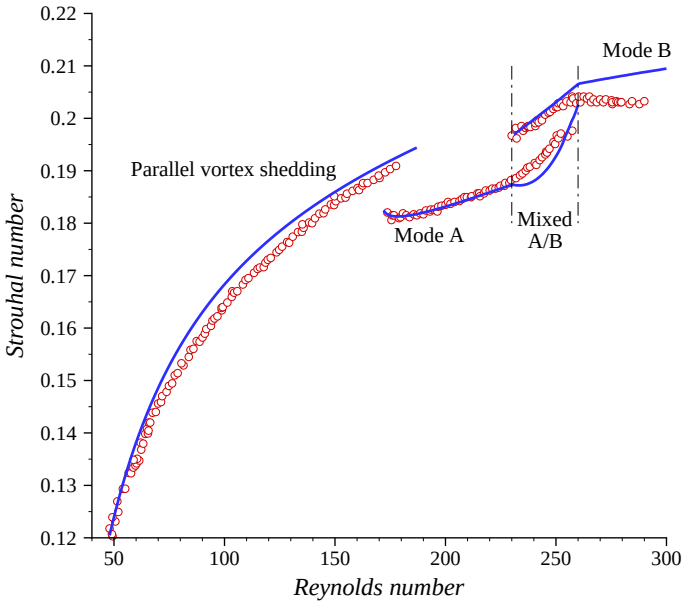

FIGURE 7.2: A plot of the Strouhal–Reynolds number profile for the flow past a circular cylinder. The blue line represents the computed Strouhal frequencies from the proposed coupled Landau model, and the open red circles represent the experimental universal Strouhal frequency curve from Williamson (1988a).

was used to monitor convergence of the model. At a time step of $\Delta t = 0.125$, the computed Strouhal frequency was within 0.032% of the Strouhal frequency computed at $\Delta t = 9.766 \times 10^{-4}$. The present study employed a time step of $\Delta t = 0.1$, which maintained both an accuracy of better than 0.025%, and temporal convergence, over the Reynolds number range which was investigated.

The evolution equations of Barkley *et al.* (2000) predict a bifurcation diagram which shows the three distinct three-dimensional mode branches for an increase in Reynolds number. Their model is compared to the present model, which predicts qualitatively the same behaviour, in figure 7.1. Notice the hysteresis at the onset of the Mode A branch for $180 \lesssim Re \lesssim 188$, and the mixed Mode A/B branch for $230 \lesssim Re \lesssim 260$ as energy is transferred from Mode A to Mode B.

The present model evaluates the frequencies associated with the modes from the evolution equations in equation 7.1 (Barkley *et al.* 2000). Strouhal frequencies are determined at increments of $\Delta Re = 1$ through the Reynolds number range $48 < Re < 300$. Over the mixed Mode A/B regime ($230 \lesssim Re \lesssim 260$), discrete oscillation frequencies

were present for the Mode A and Mode B amplitudes. This corresponds to the discontinuous region of the Strouhal–Reynolds number profile of the circular cylinder wake where energy is transferred from Mode A wake structures to Mode B. The predicted Strouhal–Reynolds number profile from the present model is presented in figure 7.2. The experimental circular cylinder wake Strouhal–Reynolds number data, corrected for parallel shedding by Williamson (1988a), is included for comparison.

7.1.5 Concluding Remarks and Future Extensions

Despite only evaluating the complex model coefficients for Strouhal frequencies in the vicinity of the Mode A and Mode B transitions, the computations presented here show that a remarkable qualitative agreement is observed between the experimental Strouhal–Reynolds number profile of a circular cylinder wake through the three-dimensional flow regime, and the Strouhal frequencies determined using the present coupled Landau model. The Strouhal frequency of both Mode A and Mode B are very well predicted by the present model for $Re \lesssim 260$. The constant Strouhal frequency of $St \approx 0.203$, observed experimentally for $Re \gtrsim 260$, differs from the predicted increase in Strouhal frequency by the model, probably due to longer-span instabilities that lower the shedding frequency from that of the pure Mode B wake computed for the coefficients of the present model. The two-dimensional Strouhal profile also lies in good agreement with the corrected experimental data for parallel shedding.

The possibilities for extending the present formulation of this coupled Landau model are numerous. One possibility is to include a third equation for the base flow amplitude, which would incorporate a spanwise expansion to form a complex Ginzburg-Landau equation (see Leweke & Provansal 1995). It would be interesting to study the effects of various long-wavelength vortex street effects such as oblique shedding and vortex dislocations on the evolution and behaviour of a spanwise series of coupled Landau equations for the Mode A and Mode B instabilities. Of interest would also be attempts to model the bursting and mode switching between Mode A and Mode B in the mixed Mode A/B regime. Despite being appealing in theory, the application of these proposed extensions is difficult, as consideration of the change in growth rate of the instability modes must be made for both the strength and alignment of the underlying vortex street, and frequency feedback terms must be included in the base flow equation to shift the Strouhal frequency to the saturated Mode A and Mode B frequencies.

A second alternative expansion is to include a third Landau equation for a Mode C instability, and adapting the σ terms to the wake behind a ring by introducing functions of aspect ratio, $\sigma(Ar)$. Such an expansion requires two coupling terms per equation, and at present insufficient data is available to derive the twelve coupling coefficients (six real, six imaginary) required. Adding further complexity to the model, the saturation terms of at least the Mode C equation, and for good accuracy the Mode A and Mode B equations also, would be required to be expressed as functions of aspect ratio.

It would be useful to ascertain the precise range of validity of the non-linear models investigated here in terms of the reduced Reynolds number $(Re - Re_c)/Re_c$, where Re_c is the critical Reynolds number of the relevant transition (Provansal *et al.* 1987). This could provide an explanation for the discrepancy between the computed and predicted Strouhal frequencies at Reynolds numbers beyond $Re \approx 300$ from the coupled Landau model for Modes A and B.

Such extensions lie beyond the scope of the present work, but it is felt that they would provide worthwhile contributions to the understanding of the transition processes for the wake of a circular cylinder and a ring.

7.2 A Spanwise-Averaged Linear Stability Analysis of the Three-Dimensional Modes in the Wake

In this section a method to determine the stability of three-dimensional modes in a wake is presented. The method is applied with varying success to the modes that evolve from the pure Mode A and Mode B instabilities in the wake of a circular cylinder.

7.2.1 Introductory Remarks

A comprehensive review paper (Williamson 1996b) detailed the characteristics of the three-dimensional wake transition for a circular cylinder, and an analysis of non-linear transition dynamics and longer-wavelength effects was provided by Henderson (1997). From these studies, and the large preceding body of research on the low-Reynolds-number flow past a circular cylinder, it appeared that the flow past a circular cylinder was well-understood for Reynolds numbers $Re < 300$. Despite these studies, questions remained regarding some aspects of the three-dimensional transition scenario in the wake. For instance, the stability of the three-dimensional wakes to the linear Mode A and B instabilities of the vortex street had not been considered. Furthermore, upon

saturation of a pure Mode A wake, a small frequency fluctuation was observed, whereas upon saturation of a pure Mode B wake, the flow was perfectly periodic. This phenomenon is not described by the Landau model. Finally, the process responsible for the local switching between Modes A and B throughout the mixed Mode A/B regime $230 \lesssim Re \lesssim 265$ was not well-understood.

The dynamics of the wake of a circular cylinder through the three-dimensional transitions was discussed in detail earlier in this work. In the section to follow, a method which approximates the stability of the saturated three-dimensional wakes which evolve from the Mode A and B instabilities in the vortex street behind a circular cylinder is described . The technique was applied to predict the stability of the saturated wakes to linear perturbations with wavelengths which corresponded to the Mode A and B instabilities. It is proposed that the results assist to explain some of the open questions posed previously.

7.2.2 A Technique for Spanwise-Averaged Linear Stability Analysis

In the formulation of the spanwise-averaged stability analysis technique, the spanwise variation in the three-dimensional vortex streets in the flow past a circular cylinder is assumed to be small. For a spanwise-averaged stability analysis of the three-dimensional modes in the flow past a circular cylinder to be appropriate, the physical instability to a saturated three-dimensional wake must be a global instability of the vortex street, rather than a local instability to the flow at a given point along the cylinder span. Such an assumption is valid for flows such as the stability of the Mode B instability to the saturated three-dimensional Mode A wake, as experimental observations (Williamson 1996b, e.g.) and numerical computations (e.g. Thompson *et al.* 1994, 1996) confirm that the saturated three-dimensional Mode B wake has a spatio-temporal symmetry and a spanwise wavelength which are consistent with those of the the linear Mode B instability predicted by Barkley & Henderson (1996).

A Cartesian version of the linear Floquet stability analysis technique applied in chapter 4 is employed in the spanwise-averaged stability analysis formulation. The present formulation replaces the periodic two-dimensional base flow field ($\mathbf{u}_{2D}$) with a saturated periodic span-averaged three-dimensional flow field ($\bar{\mathbf{u}}_{3D}$). Recall from § 2.1.4 that the present formulation of the three-dimensional spectral-element scheme employs a Fourier expansion of the domain in the spanwise direction. The span-averaged velocity

field is simply obtained from the fundamental ($m = 0$) Fourier mode of the u and v components of velocity in the three-dimensional flow field.

A series of span-averaged velocity fields are captured over a single period of the saturated three-dimensional wake, and Fourier interpolation is employed to extract the span-averaged solution at any time t over the period T_{3D}, for the stability analysis computations. This Fourier interpolation step replaces the temporal integration of the base flow from the previous application of the stability analysis, but the method for computing the perturbation field remains the same.

Several steps are required in the application of this method. Following a stability analysis of a two-dimensional wake to determine the dominant wavelength of the three-dimensional instability to be investigated, the instability mode must be evolved to saturation using the three-dimensional formulation of the code. At this point a set number (N_t) of spanwise-averaged frames are obtained over a single period. The spanwise-averaged stability analysis code is then applied to determine the stability of the mean wake.

Prior to assessing the accuracy of the spanwise-averaged formulation, the optimum number of spanwise-averaged frames (N_t) needs to be determined. Obviously, smaller values of N_t provide more efficient computations, and larger values of N_t provide better resolution of the mean wake.

The base flows computed in the present work have a spatial error in the order of 0.1% when compared with computations which employ elements of a higher order. A similar accuracy was desired for the Fourier interpolation of the temporal spanwise-averaged velocity fields. A test case was developed based on a saturated three-dimensional Mode B wake at $Re = 270$. This case was chosen as a perfectly periodic saturated wake could be computed at this Reynolds number, and the Reynolds number was higher than the Reynolds number range of interest in this study ($230 \lesssim Re \lesssim 265$). Spanwise-averaged solutions were obtained with $N_t = 8$, 16, 32, 64 and 128. The stability of these spanwise-averaged solutions to spanwise wavelengths corresponding to the Mode A instability was determined, and with cubic interpolation was employed to approximate the dominant spanwise wavelength and Floquet multiplier of the instability. Figure 7.3 shows the convergence trends for the dominant spanwise wavelength and Floquet multipliers of the Mode A instability with an increase in the number of temporal Fourier interpolation frames N_t.

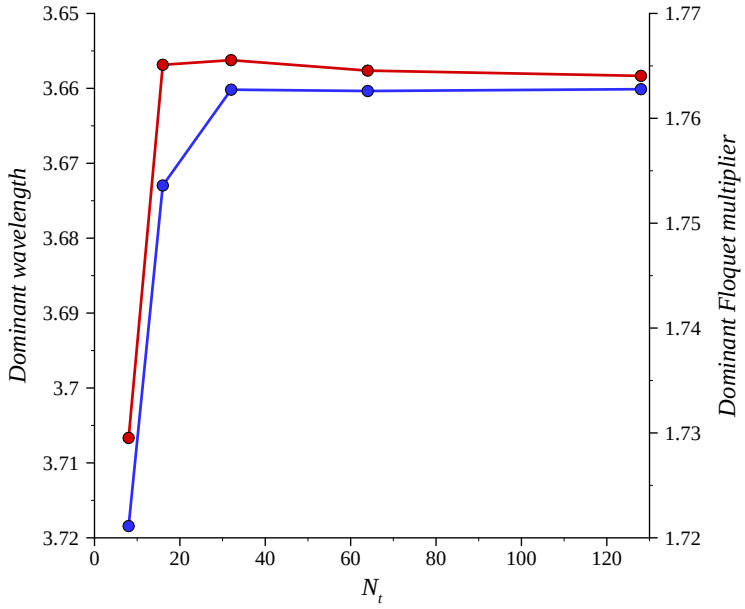

FIGURE 7.3: Convergence of the computed dominant spanwise wavelength (blue line) and Floquet multiplier (red line) for the Mode A instability of a saturated Mode B wake at $Re = 270$, with an increase in the number of temporal interpolation fields per period (N_t).

The stability analysis with $N_t = 32$ achieved dominant spanwise wavelengths and Floquet multipliers within 0.1% of a similar analysis with $N_t = 128$. From this result, $N_t = 32$ was employed throughout the spanwise-averaged stability study.

To verify that the spanwise-averaged stability analysis code indeed produced results consistent with the regular formulation of the stability analysis code employed in chapter 4, a two-dimensional flow was computed with a three-dimensional spectral-element code, and a spanwise-averaged solution with $N_t = 32$ was obtained at $Re = 240$. The size of the computational domain in the spanwise direction was approximately $0.81d$, which excluded the Mode A instability. Table 7.2 compares the dominant spanwise wavelengths and Floquet multipliers predicted for a Mode A instability of both a two-dimensional base flow and a spanwise-average of a two-dimensional base flow. The results differ by less than 1%, which shows that the spanwise-averaged stability analysis technique can provide useful and accurate results.

	2D stability	3D spanwise-averaged stability	% difference
λ^A	3.645	3.6446	0.011
μ^A	1.45	1.4582	0.562

TABLE 7.2: Comparison between the two-dimensional and three-dimensional spanwise-averaged stability analysis techniques. The stability of a two-dimensional solution at $Re = 240$ to the Mode A instability is tested using both techniques.

7.2.3 Stability of the Saturated Mode A Wake

The saturated wake evolving from the Mode A instability presented a significant challenge, as it spontaneously evolved, upon saturation of the linear growth of the mode, to a chaotically fluctuating state. Although the Strouhal frequency fluctuated over a narrow frequency band, the periodicity was inadequate for the purpose of applying the linear stability analysis.

A further complication was presented by the dominance of the Mode B instability over the Mode A instability. When initiating the three-dimensional computations from a random perturbation at Reynolds numbers $Re \gtrsim 250$, both the Mode A and Mode B instabilities evolved. To ensure the evolution of a pure Mode A wake, a velocity field with a small three-dimensional component was constructed from the perturbation field of the Mode A instability. Despite the evolution and saturation of a pure Mode A wake, the aperiodic saturation still occurred.

The aperiodic saturation was observed at all Reynolds numbers for which saturated Mode A computations were made. Earlier computations of the Mode A wake by Henderson (1997) suggest that the saturated Mode A wake is perfectly periodic. That study utilised a small transverse computational domain (boundaries approximately $8d$ from the cylinder), and periodic boundary conditions at the walls, essentially modelling an array of equi-spaced cylinders aligned normal to the direction of flow. The present study employs a transverse domain size of approximately $30d$. With the recent advancements in computational resources, it was possible to match or exceed the spatial resolution and domain sizes of the previous computational studies, and as a result it is likely that the restrictive domains that were previously employed artificially suppressed the development of the frequency fluctuation observed here. The computation of the Mode A wake of Henderson (1997) was performed at $Re = 195$, just slightly in excess of the critical Reynolds number for the onset of the Mode A instability ($Re_c \approx 188.5$),

l_t	$8d$	$30d$	% diff.
T_{2D} (St_{2D})	4.895 (0.204)	4.974 (0.201)	1.59%
Periodic 3D wake	Yes	No	—
T_{3D} (St_{3D})		≈ 5.530 (0.181)	

TABLE 7.3: Comparison between the computations of Mode A employing meshes with transverse domain lengths $l_t = 8d$ and $l_t = 30d$. For both computations, the Reynolds number $Re = 220$, elements of order $N^2 = 81$ are used, and the azimuthal domain $\lambda_d = 3.731d$.

and the computation was not continued beyond the initial saturation of the shedding frequency or mode amplitude.

In order to verify the hypothesis that the frequency fluctuation of the saturated Mode A wake may be artificially suppressed by restricting the domain size, a test case is computed here employing a similarly restrictive mesh with a transverse domain size of $8d$. The computation is compared to a computation over the less restrictive mesh employed throughout this investigation, as summarised in table 7.3.

An attempt was made to capture a spanwise-averaged period of a Mode A wake immediately that saturation occurred, to exclude the frequency fluctuation. Figure 7.4 shows the evolution of the Mode A instability in terms of both the Strouhal frequency variation, and the growth of the three-dimensional mode amplitude norm. The point at which the spanwise-averaged solution was captured for this case is indicated in the figure. Stability analysis of the span averaged periodic wakes captured using this method proved inconclusive. The shift in Strouhal frequency does not reach a constant frequency as the mode amplitude appears to saturate. A peak in the frequency shift occurs, corresponding to a minimum in the Strouhal frequency, followed by a sharp drop in the magnitude of the frequency shift, as the Strouhal frequency approaches the mean values observed in experiments for the Mode A wake. Unfortunately, a perfect periodicity of the Mode A wake is never achieved over the Reynolds number range of interest, and an ad-hoc approach was applied to approximate a periodic solution. Various indicators were monitored near to saturation, such as the mode amplitude, the drag force, and point velocity measurements in the wake, to best estimate a temporal range over which approximately one period of shedding occurred.

A natural alternative for suppressing the frequency fluctuation is to limit the transverse domain size of the grids, as already discussed. The measured Strouhal frequencies for the large grids with $l_t = 30d$ differ by approximately 2% when compared with the

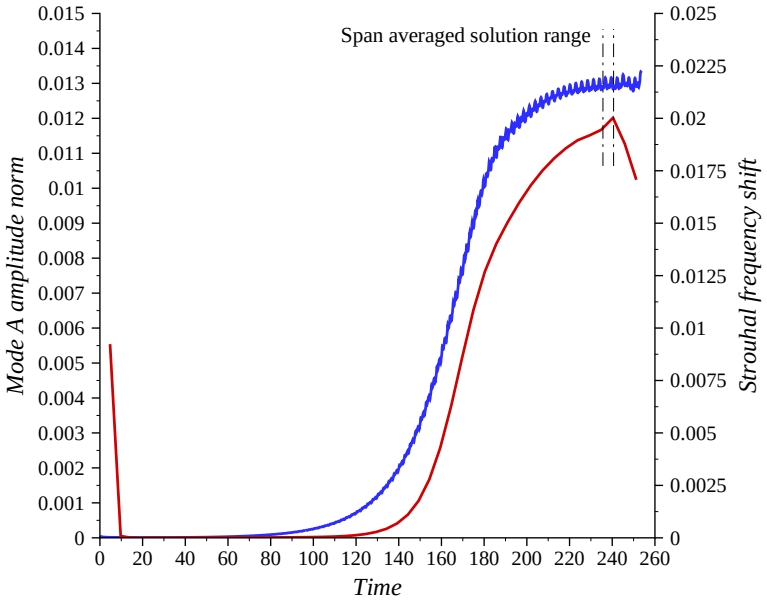

FIGURE 7.4: A plot of the Strouhal frequency (red line) and Mode A amplitude norm (blue line) for the evolution of the Mode A instability in the wake of a circular cylinder at $Re = 220$. The range over which the spanwise-averaged solution was obtained is labelled.

restricted grids with $l_t = 8d$. However, it is widely known that the Strouhal frequency is sensitive to variation in blockage, which is being increased here from 0.0167 to 0.0625. It is felt that the wake structure and stability computed using the restricted transverse domain will provide a useful quantitative approximation to the stability of the pure Mode A wake.

Spanwise-averaged solutions have been obtained, using the restricted meshes for Mode A, and the large meshes for Mode B, at several Reynolds numbers over the three-dimensional flow regime of the circular cylinder, covering each of the three important regions identified earlier, namely the exclusive Mode A region ($180 \lesssim Re \lesssim 230$), the mixed Mode A/B region ($230 \lesssim Re \lesssim 265$), and the exclusive Mode B region ($Re \gtrsim 265$). From two-dimensional stability analysis, the dominant spanwise wavelengths of Mode A and Mode B at each Reynolds number were determined, as were the dominant Floquet multipliers for each mode.

Figure 7.5 presents a comparison between the Floquet multiplier variation for two-dimensional and spanwise-averaged Mode A stability analysis. The plot shows the stability of the three-dimensional Mode A wake to perturbations corresponding to the

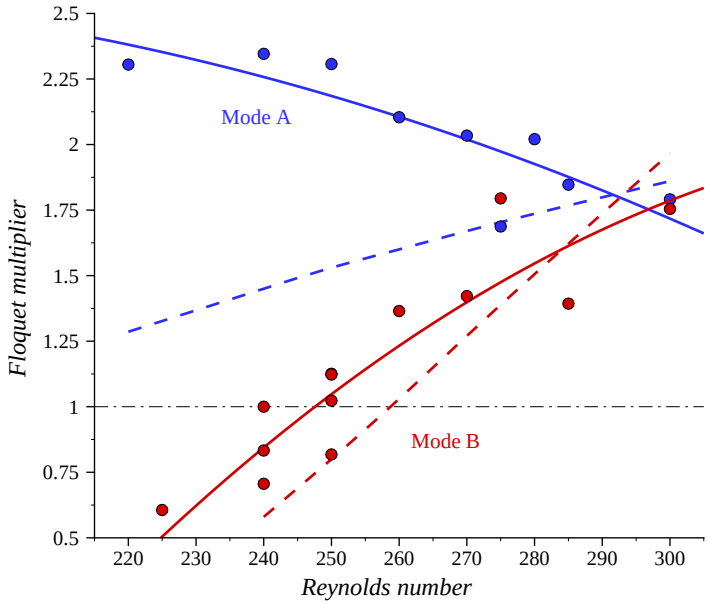

FIGURE 7.5: Reynolds number variation of the dominant Floquet multipliers of the Mode A (blue) and Mode B (red) instabilities of the saturated Mode A wake. Solid lines provide a quadratic curve fit to the scattered data. Dotted lines show the two-dimensional wake stability for comparison. A dashed line indicates the neutral stability threshold at $\mu = 1$.

Mode A and B instabilities.

Notice that as the Reynolds number increases, the dominant Floquet multipliers of the Mode A instability reduce in magnitude, until they intersect the two-dimensional Mode A trend-line. This is due to the physical transition in structure of the saturated wake used to generate the periodic spanwise-averaged flow field from a Mode A wake to a Mode B wake, as illustrated by the wake flow field plots in figure 7.6.

A striking observation may be made concerning the Mode B instability. Notice that the Mode B instability is predicted to grow for $Re \gtrsim 245 \pm 5$, as the magnitude of the Floquet multipliers is greater than unity. This transition Reynolds number is significantly less than the prediction of the critical Reynolds number of the Mode B transition from two-dimensional stability analysis, suggesting that the observation of Mode B structures in the mixed Mode A/B Reynolds number range $230 \lesssim Re \lesssim 265$ may be qualitatively predicted by the linear instability of Mode B wavelengths to the spanwise-averaged saturated Mode A wake.

A possible explanation for the quantitative discrepancy between the critical Reynol-

ds number for the onset of Mode B predicted by the present analysis ($Re^B_{crit} \approx 245 \pm 5$, and the observed critical Reynolds number for the onset of Mode B in experiments $Re^B_{crit} \approx 230$), is that it was impossible to capture exactly one period of the saturated Mode A wake.

7.2.3.1 The Mode A Frequency Fluctuation

The linear growth of the Mode A instability in the wake of a circular cylinder is characterised by a reduction in Strouhal frequency. As three-dimensional streamwise structures evolve, they induce a deformation of the vortex street rollers, the magnitude of which is of the order $O(1d)$ downstream of the cylinder.

Upon saturation of the three-dimensional instability, a stable periodic state is not achieved. Instead, immediately following the peak in the evolution of the mode amplitude, a small random fluctuation in shedding frequency develops. The mean Strouhal frequency of this fluctuating wake lies between the two-dimensional Strouhal frequency and the Strouhal frequency reached at the point of initial saturation, and is in good agreement with the mean Strouhal frequency obtained experimentally for the Mode A wake by Williamson (1988b).

A hypothesis for the development of the fluctuating Strouhal frequency for the Mode A wake is suggested here. The fluctuation may be due to a local instability of the highly deformed vortex rollers in the wake downstream of the cylinder. The spanwise-averaged stability analysis, although providing only qualitative predictions, suggests that spanwise modes associated with the Mode A instability will grow in the presence of a Mode A wake near to saturation. It is possible that the frequency fluctuation results from a non-linear competition between the evolving streamwise structures which increase the waviness of the vortex street, and some instability of the deformed rollers, which would attempt to reduce the spanwise non-uniformity of the rollers. Williamson (1996a) observed that the saturated Mode A wake was unstable, which adds credence to this proposed hypothesis. A more detailed study of this phenomenon lies beyond the scope of the present work, and hence verification of the mechanism for frequency fluctuation remains an open question.

7.2.3.2 The Dominance of Mode B over Mode A

The non-linear interaction between the Mode A and Mode B instabilities is interesting, in that despite the Mode B instability having a higher growth rate than the Mode

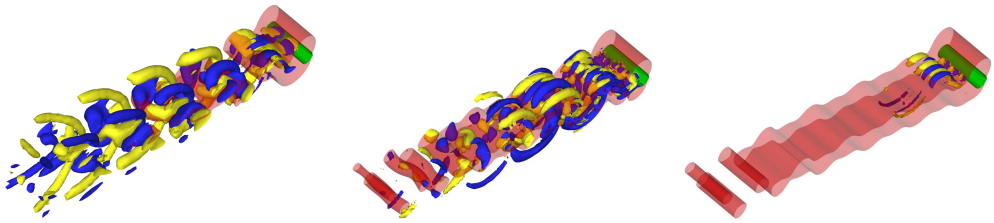

(a) $Re = 220$: Mode A dominating.

(b) $Re = 280$: Mode B interference.

(c) $Re = 300$: Mode B dominating.

FIGURE 7.6: Isosurface plots which show the three-dimensional structure of the wakes of a circular cylinder immediately upon saturation. The span of the computation corresponds with the dominant mode of the Mode A instability at each Reynolds number. Contour colouring is consistent with previous chapters, and streamwise vorticity levels are equal in each frame for comparison purposes.

A instability only for Reynolds numbers $Re \gtrsim 295$, computations at lower Reynolds numbers show clearly that the non-linear evolution of the Mode A instability can be impeded significantly by the Mode B instability. Figure 7.6(a) shows a saturated wake dominated by Mode A wake structures. In figure 7.6(b), a wake is shown at a time when the non-linear evolution of the three-dimensional modes at $Re = 280$ continued. The wake shows a significant reduction in Mode A wake structures from the wake in figure 7.6(a). Only a small amount of vortex roller deformation was detected downstream, and weaker streamwise vortex structures are observed. The dominance of Mode B over Mode A when both instabilities are unstable is highlighted by the plot shown in figure 7.6(c) at $Re = 300$. The plot shows that as the three-dimensional wake evolved, no Mode A structures were detected, and the wake was dominated by Mode B structures. Downstream, the vortex rollers were almost devoid of any wavy deformation. Although at $Re = 300$ both Mode A and B instabilities are predicted to occur, the Mode A instability has a higher growth rate than Mode B. Previous computations (especially those by Thompson *et al.* 1994, 1996; Henderson 1997) which studied the evolution of, and competition between, the Mode A and B instabilities in the flow past a circular cylinder support the observation that at higher Reynolds numbers ($Re \gtrsim 260$), the near-wake region is dominated by Mode B structures, and the far wake contains remnants of Mode A structures.

7.2.4 Stability of the Saturated Mode B Wake

Spanwise-averaged solutions of saturated Mode B wakes were obtained for several discrete Reynolds numbers in the range $260 \leq Re \leq 300$. The Mode A instability was excluded from computations of the Mode B wakes as the size of the computational domain was limited in span to correspond with the spanwise wavelength of the Mode B instability (approximately $0.814d$). The saturated wake which evolved from the Mode B instability was time-periodic, and hence spanwise-averaged solutions were obtained with a high degree of confidence that the periodic wake was well-represented by the spanwise-averaged solution.

Results of the linear stability analysis of the spanwise-averaged Mode B wake are presented in figure 7.7. In contrast with the results achieved from the spanwise-averaged stability analysis of the saturated Mode A wake, the results for the saturated Mode B wake show a smooth continuous bifurcation of the dominant Floquet multipliers from the two-dimensional profiles. The quality of these results highlight two points with regard to the suitability of the spanwise-averaged stability technique to the analysis of the saturated Mode B wakes. Firstly, the smaller variation in the spanwise direction for the saturated Mode B wake when compared with the saturated Mode A wake makes it more appropriate for the spanwise-averaged stability analysis. Secondly, the periodicity of the saturated wakes made the application of the technique far more straightforward.

The plot in figure 7.7 shows that the Mode A instability has higher growth rates than the Mode B instability throughout the Reynolds number range considered. Previously, it was shown that when both Modes A and B are unstable, Mode B structures tended to dominate the wake. Therefore, the point at which the Mode B instability is first unstable to the saturated Mode B wake is important, as it determines the physical flow transition from the mixed Mode A/B regime to the Mode B regime. The plot in figure 7.7 suggests that for $Re \lesssim 264$, negative growth rates are predicted for the Mode B instability to the saturated Mode B wake. As the bifurcation to Mode B is continuous, the two-dimensional and spanwise-averaged Floquet multiplier trends for the Mode B instability should be coincident at $\mu = 1$ at the critical Reynolds number for the linear Mode B instability, $Re_c \approx 258.5$. This discrepancy is either due to a small error in the spanwise-averaged stability technique, or alternatively, it is possible that for a small range of Reynolds numbers above $Re \approx 258.5$, the Mode B instability is not unstable

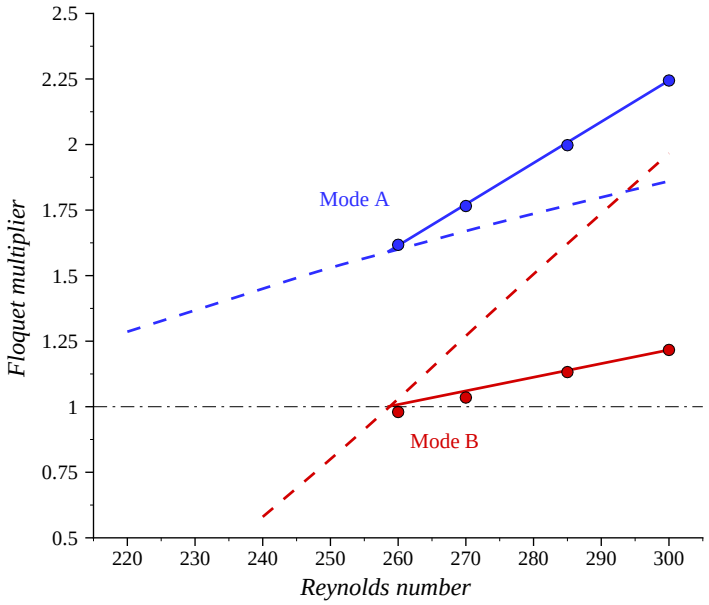

FIGURE 7.7: Reynolds number variation of the dominant spanwise-averaged Floquet multipliers of the Mode A (blue) and Mode B (red) instabilities of the saturated Mode B wake. Dotted lines show the two-dimensional wake stability for comparison. A dashed line indicates the neutral stability threshold at $\mu = 1$.

to the spanwise averaged three-dimensional Mode B wake. The former explanation is more likely, but the discrepancy between these predicted critical Reynolds numbers is less than 2%, so in terms of a qualitative description of the transition scenario, the precise value is unimportant.

7.2.5 The Transition from a Two-Dimensional Vortex Street to a Stable Mode B Wake

The spanwise-averaged stability analysis of the saturated three-dimensional flow past a circular cylinder has shed light onto some interesting characteristics of the transitions in the flow from a two-dimensional wake to a stable Mode B wake.

7.2.5.1 The Mode A Regime ($180 \lesssim Re \lesssim 240$)

The wake of a circular cylinder is two-dimensional up to $Re \approx 190$, where an hysteretic transition to the Mode A instability occurs. The Mode A instability is characterised by a spanwise wavelength of approximately $4d$ for $Re \gtrsim 190$. The growth of the Mode A instability causes significant wavy deformation of the vortex rollers of the underlying

vortex street, in the order of $1d$ several cylinder diameters downstream. The frequency fluctuation observed at saturation is possibly due to a local instability of the wavy deformation of the vortex street in the wake.

7.2.5.2 The Mixed Mode A/B Regime ($240 \lesssim Re \lesssim 2.6 \times 10^2$)

The present analysis suggests that the saturated spanwise-averaged Mode A wake is unstable to the Mode B instability for $Re \gtrsim 245 \pm 5$: that is, Mode B structures may evolve in the presence of a saturated Mode A wake at Reynolds numbers below the predicted critical Reynolds number for the onset of the Mode B instability in a two-dimensional wake ($Re_c \approx 259$). As a pure three-dimensional Mode B wake is devoid of any large-scale wavy deformation of the vortex street, and Mode B structures are observed to dominate the wake when both Mode A and Mode B are unstable, the growth of the Mode B instability causes localised switching to Mode B structures in the wake, which suppresses the Mode A wake structures. The spanwise-averaged stability analysis has also predicted that a saturated Mode B wake is only self-stable for $Re \lesssim 2.6 \times 10^2$. Thus over a range of Reynolds numbers as large as $240 \lesssim Re \lesssim 2.6 \times 10^2$, the Mode B wake structures will decay towards a two-dimensional wake, which permits the subsequent evolution of the Mode A instability again. This cycle of switching modes repeats, and may be localised due to the non-linear stability characteristics of the competing modes. This explains the experimental observations of a mixed Mode A/B regime over this approximate Reynolds number range.

It is of interest to compare this proposed scenario for the mixed Mode A/B regime with the computed flow past a ring with $Ar = 10$ at $\Re = 240$, from chapter 6, § 6.2.2, where $\lambda_d \approx 4d$. There a similar competition between modes was observed, which in that case caused a cyclic evolution and decay of non-axisymmetry in the wake.

The transfer of energy from Mode A to Mode B that is widely reported over the mixed Mode A/B regime with an increase in Reynolds number is supported by the scenario proposed here. At lower Reynolds numbers, the Mode B instability will decay more rapidly after it develops from the saturated Mode A wake, and thus the wake consists of Mode A structures for a greater duration. At higher Reynolds numbers, the opposite is true, and thus the wake consists of Mode B structures for a greater duration.

7.2.5.3 The Mode B Regime ($Re \gtrsim 2.6 \times 10^2$)

For $Re \gtrsim 2.6 \times 10^2$, the wavelengths associated with the Mode B instability are predicted to grow in the presence of a saturated Mode B wake, which explains the observations from experimental studies of a wake dominated by Mode B structures for Reynolds numbers over this range.

In summary, a key mechanism for the complex dynamics associated with the three-dimensional transitions in the flow past a circular cylinder is the possible instability of the wavy deformation of the vortex street brought about by the evolution of the Mode A wake. The proposed local instability of this deformed wake would explain both the fluctuation in Strouhal frequency of the saturated Mode A wake, and the potential for spontaneous local switching between Modes A and B over the mixed Mode A/B regime.

7.3 Chapter Summary

In this chapter, the three-dimensional bifurcations in the vortex street behind a circular cylinder have been investigated for Reynolds numbers in the range $Re \lesssim 300$. The flow past a circular cylinder over this range of Reynolds numbers has been studied exhaustively, since the experimental work by Williamson (1988a,b). Despite the large body of work in the literature devoted to the three-dimensional transitions in the flow past a circular cylinder, some avenues for further investigation remained.

A previous study has modelled the evolution of the Mode A and B instabilities as a coupled pair of evolution equations (Barkley *et al.* 2000). The previous model described the variation in amplitude of the Mode A and B instabilities through the flow regimes, and comprised a fifth-order evolution equation for the amplitude of the Mode A instability, and a third-order evolution equation for the amplitude of the Mode B instability. Third-order coupling terms were included in each equation, which modelled the decrease in the amplitude for Mode A through the mixed Mode A/B regime. The previous model was extended here to include complex amplitudes and coefficients. The new model provides an excellent description of the Strouhal–Reynolds number profile through the three-dimensional flow regimes. The Strouhal number discontinuity associated with the hysteretic onset of the Mode A instability is accurately predicted, as is the energy transfer from Mode A to Mode B over the mixed Mode A/B regime. The model is remarkable for its simplicity, with only fifth- and third-order equations being employed to model the evolution of the Mode A and B instabilities, respectively.

Furthermore, the coefficients were evaluated from a small number of computations of the pure wakes which evolve from the Mode A and B instabilities, so the mode coupling is described solely from the third-order coupling terms included in the equations.

It has been long understood that the discrepancy between the Reynolds number for the observed onset of Mode B in the wake of a circular cylinder, and the predicted critical Reynolds number from linear stability analysis, results from the difference between the two-dimensional base flow of the stability analysis, and the highly three-dimensional flow in practice at the onset of Mode B. In this chapter, the stability of the saturated three-dimensional wakes in the flow past a circular cylinder has been analysed. Periodic spanwise-averaged base flow fields have been constructed from the saturated three-dimensional wakes, and a linear stability analysis has subsequently been performed.

The analysis was partially successful, however not all of the bifurcation dynamics of the flow is adequately described by the linear stability analysis. The analysis provides a qualitative prediction that the saturated Mode A wake is unstable to the Mode B instability at Reynolds numbers as low as $Re \approx 240$, which is in much closer agreement with the experimentally observed Reynolds number than the predicted Reynolds number from two-dimensional stability analysis. Analysis predicted that the Mode B instability decays in the presence of a saturated Mode B wake for $Re \lesssim 2.6 \times 10^2$, and three-dimensional computations have shown that Mode B wake structures suppress Mode A structures when both modes are unstable. It follows that over a Reynolds number range $240 \lesssim Re \lesssim 2.6 \times 10^2$, neither Mode A or B wake structures can dominate, and instead a mode switching would be observed, consistent with the experimentally and computationally observed behaviour over this Reynolds number range.

The mode evolution scenario proposed for the mixed Mode A/B regime is summarised as follows: Assume firstly that a saturated Mode A wake evolves in the mixed Mode A/B regime. As Mode B structures are predicted to grow in the presence of Mode A in this regime, the Mode A structures are suppressed by the non-linear competition between the instabilities. The wake then consists of saturated Mode B structures which soon decay, as Mode B is not self-stable in this regime. Finally, this decay then permits the subsequent evolution of Mode A structures, and the cycle continues. At greater Reynolds numbers ($Re \gtrsim 2.6 \times 10^2$), both Mode A and B instabilities are predicted to grow in the presence of a saturated Mode B wake. As computations suggest that Mode

B wake structures dominate in the wake when both Modes A and B are unstable, regardless of the growth rates of the instabilities, only Mode B structures are expected to exist in the wakes for these Reynolds numbers. This explains the previous observations of a vortex street dominated by Mode B structures for $Re \gtrsim 2.6 \times 10^2$.

Chapter 8

Summary and Conclusions

The majority of this study has focused on the investigation of the flow past rings to better understand the fluid dynamics of low-Reynolds-number bluff body flows with a continuous variation in the geometry. No previous computational studies have been reported for the flow past rings. The few experimental studies which have investigated the flow past rings have presented either high-Reynolds-number measurements (e.g. Bearman & Takamoto 1988), or measurements of the vortex shedding in the laminar flow regime (e.g. Leweke & Provansal 1995). The present study provided for the first time a detailed investigation of the axisymmetric and non-axisymmetric flow regimes computed in the flow past rings with a wide range of aspect ratios.

The investigation may be divided into three main areas. These are an investigation of the axisymmetric flow past rings, an investigation of the non-axisymmetric flow past rings, and an investigation of the three-dimensional flow past a circular cylinder. Over the sections to follow, the major conclusions from each of these areas of investigation is discussed.

8.1 The Axisymmetric Flow past Rings

Three axisymmetric flow regimes exist in the flow past rings. These are attached steady flow, separated steady flow and unsteady flow.

The separation of flow from the ring creates an axial recirculation bubble behind closed rings ($Ar \leq 1$), and an annular recirculation ring behind open rings ($Ar > 1$). However, it is appropriate to classify the wakes into two categories, based on the length scale of the wakes. For $Ar \lesssim 3$ the wake scales with the outer ring diameter, $D + d$, and comprises either an attached or a detached recirculation bubble with $Ar \leq 1$ or $Ar > 1$, respectively. For $Ar \gtrsim 3$, the wake scales on the ring cross-section diameter,

Ar range	Flow regimes	Critical Re
$0 \leq Ar \leq 1$	Attached axial recirculation bubble	$21 \gtrsim Re_{T1} \gtrsim 0$
$1 < Ar \lesssim 3$	Detached axial recirculation bubble Attached annular recirculation ring	$Re > 0$ $\infty > Re_{T1} \gtrsim 16$
$3 \lesssim Ar < \infty$	Attached annular recirculation ring	$16 \gtrsim Re_{T1} \gtrsim 6$

TABLE 8.1: A summary of the axisymmetric flow regimes for the flow past rings. The transition types and critical Reynolds number ranges are provided for each aspect ratio range. The order in which the critical Reynolds numbers are given in the critical Reynolds number range follows the order in which the aspect ratios are given in the aspect ratio range.

d, and comprises an annular recirculation bubble. These flow regimes are summarised in table 8.1.

Vortex shedding is observed in the axisymmetric flow past rings with $Ar > 1$. In fact, a linear stability analysis predicts that for $Ar \lesssim 3.9$, the flow becomes non-axisymmetric at a lower Reynolds number than the critical Reynolds number for the axisymmetric Hopf transition. For $Ar \gtrsim 3.9$, the flow is predicted to become non-axisymmetric at a higher Reynolds number than the critical Reynolds number for the axisymmetric Hopf transition.

The Strouhal number for vortex shedding in the wakes behind rings with $Ar \geq 3$ is well-described by a relationship developed in this study. The computed Strouhal–Reynolds number profiles show that unsteady flow past rings with $Ar \gtrsim 5$ is very similar in terms of shedding frequency and critical Reynolds number to the flow past a circular cylinder. With a decrease in the aspect ratio, the angle at which vortices are shed to the direction of flow increases, due to the self-induced motion of counter-rotating vortex pairs in the vortex street. At smaller aspect ratios, the pairing of vortices in the vortex street is more pronounced.

8.2 The Non-Axisymmetric Flow past Rings

For the flow past rings with $Ar \lesssim 3.9$, non-axisymmetric flow occurs over three distinct flow regimes, which are classified as Mode I, II and III. In the Mode I and III regimes, steady non-axisymmetric flow is observed for a range of Reynolds numbers, and at higher Reynolds numbers, unsteady flow is observed in the form of vortex-loop shedding. In the Mode II regime, a non-axisymmetric unsteady flow is observed.

For the vortex streets behind rings with $Ar \gtrsim 3.9$, three non-axisymmetric insta-

Ar range	Non-axisymmetric transition mode		
	Primary transition	**Secondary transition**	**Tertiary transition**
$0 \leq Ar < 1.6$	Regular Mode I Supercritical $m = 1$ symmetry	Hopf Mode I Supercritical $m = 1$ symmetry	
$1.6 \leq Ar \leq 1.7$	Hopf Mode II Supercritical $m = 1$ symmetry		
$1.7 < Ar \lesssim 3.9$	Regular Mode III Subcritical $4.7d < \lambda_d < 7.9d$	Hopf Mode III Supercritical $4.7d < \lambda_d < 7.9d$	
$3.9 \lesssim Ar \lesssim 8$	Mode C Supercritical $\lambda_d \approx 1.7d$	Mode A (Not determined) $\lambda_d \approx 4.0d$	Mode B Supercritical $\lambda_d \approx 0.8d$
$8 \lesssim Ar \lesssim 13$	Mode A Subcritical $\lambda_d \approx 4.0d$	Mode C Subcritical $\lambda_d \approx 1.7d$	Mode B Supercritical $\lambda_d \approx 0.8d$
$13 \lesssim Ar < \infty$	Mode A Subcritical $\lambda_d \approx 4.0d$	Mode B Supercritical $\lambda_d \approx 0.8d$	Mode C (Not determined) $\lambda_d \approx 1.7d$

TABLE 8.2: A summary of the non-axisymmetric transition modes which occur in the flow past rings over different aspect ratio ranges. For each transition, the classification of the transition is provided, the non-linear evolution behaviour of the transition is provided, and the azimuthal symmetry of the instability which causes the transition is provided.

bilities are identified. These instabilities include the Mode A and B instabilities, with properties which correspond to the Mode A and B instabilities in the flow past a circular cylinder, and a subharmonic Mode C instability.

The non-axisymmetric bifurcations in the flow past rings is summarised in table 8.2.

The vortex streets in the wakes behind rings with $Ar = 5$, 10 and 20 are each unstable to the three non-axisymmetric instabilities in a different order. The Mode C instability causes a period-doubling bifurcation in the vortex street when it is the first-occurring instability. Despite this, with further increases in the Reynolds number, the vortex streets in the wakes behind rings develop small scales in a manner similar to the vortex street in the wake of a circular cylinder: the development of small-scale structures in the wake leads to a loss of the periodicity of the vortex street, and energy is transferred to higher frequencies in the spectrum. When computational domains which are sufficiently large in the azimuthal direction to capture each of the linear instability modes are employed, computations show that the linear stability analysis

correctly predicted the first non-axisymmetric instability in the wake. However, with an increase in Reynolds number, the non-linear interaction between the modes in the vortex street leads to a more complex series of flow transitions than predicted by the linear stability analysis.

An increase in the azimuthal span of the computations suggests that the vortex streets in the wakes behind rings become non-uniform through the development of spatio-temporal chaos, which has been proposed as a possible route to turbulence in the wake of a circular cylinder by Henderson (1997). Additional computations and experimental dye visualisation have confirmed the findings of previous work, which show that helical modes of shedding can occur in the flow past rings at Reynolds numbers beyond the critical Reynolds number for unsteady axisymmetric flow.

8.3 The Three-Dimensional Flow past a Circular Cylinder

A pair of coupled Landau equations is developed to predict the Strouhal–Reynolds number profile through the three-dimensional transitions in the flow past a circular cylinder. The model is based on an existing model, which incorporated coupled evolution equations for the amplitudes of the Mode A and B instabilities. The present model introduces complex variables and coefficients, which are evaluated from three-dimensional computations. A remarkable agreement with existing experimental data is obtained, and the model provides accurate predictions of both the hysteresis at the onset of the Mode A instability, and the energy shift from Mode A to Mode B over the mixed Mode A/B regime.

A linear stability analysis of the spanwise-averaged three-dimensional wakes in the flow past a circular cylinder predicts that the Mode B instability is unstable to the three-dimensional Mode A wake at Reynolds numbers below the predicted critical Reynolds number from linear stability analysis of the two-dimensional wake (Barkley & Henderson 1996). The analysis also predicts that the Mode B instability is unstable to the three-dimensional Mode B wake at Reynolds numbers $Re \gtrsim 2.6 \times 10^2$. In addition, three-dimensional computations show that Mode B structures suppress Mode A structures when both linear instabilities occur in a wake. These results provide a possible explanation for both the observed three-dimensional bifurcations in the wake of a circular cylinder, and the discrepancy between the linear stability analysis predictions and the experimentally measured observations of the critical Reynolds number for the onset

of the secondary Mode B instability.

8.4 Directions for Future Work

The low-Reynolds-number flow regimes in the flow past rings have been investigated in detail in this study. Even so, some unanswered questions remain.

In experimental studies (e.g. Monson 1983), for the flow past rings with aspect ratios which probably correspond to the Mode III regime in the present study, it was suggested that the non-axisymmetric vortex-loop shedding was replaced by an axisymmetric vortex street at higher Reynolds numbers. Higher-Reynolds-number computations were not performed in the present study for the flow past rings with $Ar \lesssim 3.9$. It would be useful, therefore, for a series of long-timescale computations to be performed for the flow past a ring with an aspect ratio $Ar < 3.9$ (e.g. $Ar = 3$), over a range of Reynolds numbers which extends past both the computed critical Reynolds numbers for the non-axisymmetric Hopf transition and the axisymmetric Hopf transition. This would provide additional information about the higher-Reynolds-number dynamics of the wakes behind rings with $Ar \lesssim 3.9$.

The identification of the subharmonic Mode C instability in the vortex street behind rings was a significant result from this study. A bifurcation scenario was proposed whereby vortex streets which lack a reflective symmetry about their centreline are unstable to real Mode A and B instabilities, as well as a subharmonic Mode C instability. Further investigation is required to determine if indeed the proposed bifurcation scenario is valid for general asymmetrical bluff bodies. It is proposed that such an investigation be performed on the flow past a cylinder with a square cross-section, as with variation in the angle of attack of the cross-section, the asymmetry in the vortex street can be introduced continuously. The square cylinder is an ideal candidate for such a study, as the stability of the symmetrical vortex street at an angle of attack of 0° is already well-known (Robichaux *et al.* 1999; Blackburn & Lopez 2003).

In the present investigation, the study of the development of chaos in the wake was limited in scope to the vortex streets in the flow past rings with $Ar \geq 5$. A possible direction for future investigation would be to complete a similar investigation for the flow past rings with $Ar \lesssim 3.9$, with a view to providing a comparison between the wake transitions to turbulence in the flow past a sphere, and the flows past rings with $Ar \lesssim 3.9$.

The spanwise-averaged stability analysis technique employed in this study is somewhat speculative at this stage. The technique was difficult to apply to the Mode A wake, due to the aperiodic behaviour of the saturated wake. Furthermore, the Mode A wake varied markedly in the spanwise direction. There is a necessity for a more detailed stability analysis of the three-dimensional wake which evolves from the Mode A instability, to allow a better prediction of the Reynolds number at which the Mode B instability may first occur in the flow past a circular cylinder.

Bibliography

Achenbach, E. 1972 Experiments on the flow past spheres at very high Reynolds numbers. *J. Fluid Mech.* **54**, 565–575.

Achenbach, E. 1974 Vortex shedding from spheres. *J. Fluid Mech.* **62**, 209–221.

Balachandar, S., Mittal, R. & Najjar, F. M. 1997 Properties of the mean recirculation region in the wakes of two-dimensional bluff bodies. *J. Fluid Mech.* **351**, 167–199.

Barkley, D. & Henderson, R. D. 1996 Three-dimensional Floquet stability analysis of the wake of a circular cylinder. *J. Fluid Mech.* **322**, 215–241.

Barkley, D., Tuckermann, L. S. & Golubitsky, M. 2000 Bifurcation theory for three-dimensional flow in the wake of a circular cylinder. *Phys. Rev. E* **61** (5), 5247–5252.

Batchelor, G. K. 1967 *An Introduction to Fluid Dynamics*. Cambridge University Press.

Bayly, B. J. 1986 Three-dimensional instability of elliptical flow. *Phys. Rev. Lett.* **57**, 2160–2163.

Bearman, P. W. & Takamoto, M. 1988 Vortex shedding behind rings and discs. *Fluid Dyn. Res.* **3**, 214–218.

Bearman, P. W. & Wadcock, A. J. 1973 The interaction between a pair of circular cylinders normal to a stream. *J. Fluid Mech.* **61**, 499–511.

Bearman, P. W. & Zdravkovich, M. M. 1978 Flow around a circular cylinder near a plane boundary. *J. Fluid Mech.* **89**, 33–47.

Blackburn, H. M. & Lopez, J. M. 2002 Modulated rotating waves in an enclosed swirling flow. *J. Fluid Mech.* **465**, 33–58.

Blackburn, H. M. & Lopez, J. M. 2003 On three-dimensional quasi-periodic Floquet instabilities of two-dimensional bluff body wakes. *Phys. Fluids* **15** (8), L57–L60.

Blackburn, H. M. & Lopez, J. M. 2004 The onset of three-dimensional standing and modulated travelling waves in a periodically driven cavity flow. *Awaiting Publication in J. Fluid Mech.* .

Blackburn, H. M., Marques, F. & Lopez, J. M. 2004 On three-dimensional instabilities of two-dimensional flows with a Z_2 spatio-temporal symmetry. *Under Consideration for Publication in J. Fluid Mech.* .

Bloor, M. S. 1964 The transition to turbulence in the wake of a circular cylinder. *J. Fluid Mech.* **19**, 290–304.

Braun, R., Feudel, F. & Guzdar, P. 1998 Route to chaos for a two-dimensional externally driven flow. *Phys. Rev. E* **58** (2), 1927–1932.

Brede, M., Eckelmann, H. & Rockwell, D. 1996 On secondary vortices in the cylinder wake. *Phys. Fluids* **8** (8), 2117–2124.

Brücker, C. 2001 Spatio-temporal reconstruction of vortex dynamics in axisymmetric wakes. *J. Fluids Struct.* **15**, 543–554.

Brydon, A. & Thompson, M. C. 2001 Flow interaction between two spheres at moderate Reynolds number. In *Proceedings of the Fourteenth Australasian Fluid Mechanics Conference* (ed. B. B. Dally), pp. 693–696. Department of Mechanical Engineering, Adelaide University, S.A. 5005, Australia: Published by Adelaide University.

Canuto, C., Hussaini, M. Y., Quarteroni, A. & Zang, T. A. 1988 *Spectral Methods in Fluid Dynamics*. Springer-Verlag.

Chester, W. & Breach, D. R. 1969 On the flow past a sphere at low Reynolds number. *J. Fluid Mech.* **37**, 751–760.

Chomaz, J. M., Bonneton, P. & Hopfinger, E. J. 1993 The structure of the near wake of a sphere moving horizontally in a stratified field. *J. Fluid Mech.* **254**, 1–21.

Clift, R., Grace, J. R. & Weber, M. E. 1978 *Bubbles, Drops and Particles*. Academic Press, New York.

Coutanceau, M. & Bouard, R. 1977a Experimental determination of the main features of the viscous flow in the wake of a circular cylinder in uniform translation. part 1. steady flow. *J. Fluid Mech.* **79**, 231–256.

Coutanceau, M. & Bouard, R. 1977b Experimental determination of the main features of the viscous flow in the wake of a circular cylinder in uniform translation. part 2. unsteady flow. *J. Fluid Mech.* **79**, 257–272.

Dennis, S. C. R. & Walker, J. D. A. 1971 Calculation of the steady flow past a sphere at low and moderate reynolds numbers. *J. Fluid Mech.* **48**, 771–789.

Dušek, J., Le Gal, P. & Fraunié, P. 1994 A numerical and theoretical study of the first Hopf bifurcation in a cylinder wake. *J. Fluid Mech.* **264**, 59–80.

Fey, U., König, W. & Eckelmann, H. 1998 A new Strouhal–Reynolds-number relationship for the circular cylinder in the range $47 < Re < 2 \times 10^5$. *Phys. Fluids* **10** (7), 1547–1549.

Fromm, J. E. & Harlow, F. H. 1963 Numerical solution of the problem of vortex street development. *Phys. Fluids* **6** (7), 975–982.

Garten, J. F., Arendt, S., Fritts, D. C. & Werne, J. 1998 Dynamics of counter-rotating vortex pairs in stratified and sheared environments. *J. Fluid Mech.* **361**, 189–236.

Gaster, M. 1971 Vortex shedding from circular cylinders at low Reynolds numbers. *J. Fluid Mech.* **46**, 749–756.

Gerich, D. & Eckelmann, H. 1982 Influence of end plates and free ends on the shedding frequency of circular cylinders. *J. Fluid Mech.* **122**, 109–121.

Gerrard, J. H. 1966 The three-dimensional structure of the wake of a circular cylinder. *J. Fluid Mech.* **25**, 143–164.

Gerrard, J. H. 1977 The wakes of cylindrical bluff bodies at low Reynolds number. *Phil. Trans. R. Soc. Lond. A* **288**, 351–381.

Ghidersa, B. & Dušek, J. 2000 Breaking of axisymmetry and onset of unsteadiness in the wake of a sphere. *J. Fluid Mech.* **423**, 33–69.

Gleick, J. 1993 *Chaos: Making a New Science*. Abacus.

Grosche, F.-R., Lu, M. & Kreplin, H.-P. 2003 Passive wake ventilation of bluff bodies. In *The 5th Euromech Fluid Mechanics Conference: Book of Abstracts*, p. 364. Centre des Congrès Pierre Baudis, Toulouse, France: Published by Institut de Mechanique des Fluides de Toulouse.

Grosche, F.-R. & Meier, G. E. A. 2000 Research at DLR Göttingen on bluff body aerodynamics, drag reduction by wake ventilation and active flow control. In *Proceedings of the Fourth International Colloquium on Bluff Body Aerodynamics and Applications*. Bochum.

Haj-Hariri, H. & Homsy, G. M. 1997 Three-dimensional instability of viscoelastic elliptic vortices. *J. Fluid Mech.* **353**, 357–381.

Hammache, M. & Gharib, M. 1991 An experimental study of the parallel and oblique vortex shedding from circular cylinders. *J. Fluid Mech.* **232**, 567–590.

Hayashi, M., Sakurai, A. & Ohya, Y. 1986 Wake interference of a row of normal flat plates arranged side by side in a uniform flow. *J. Fluid Mech.* **164**, 1–25.

Henderson, R. D. 1995 Details of the drag curve near the onset of vortex shedding. *Phys. Fluids* **7**, 2102–2104.

Henderson, R. D. 1997 Non-linear dynamics and pattern formation in turbulent wake transition. *J. Fluid Mech.* **352**, 65–112.

Henderson, R. D. & Barkley, D. 1996 Secondary instability in the wake of a circular cylinder. *Phys. Fluids* **8**, 1683–1685.

Hourigan, K., Reichl, P. & Thompson, M. C. 2002 Unsteady separated flow near a free surface. In *Invited Keynote Lecture, IUTAM Symposium on Unsteady Separated Flows*. Toulouse, France.

Hourigan, K., Thompson, M. C. & Tan, B. T. 2001 Self-sustained oscillations in flows around long flat plates. *J. Fluids Struct.* **15**, 387–398.

Ingham, D. B. 1968 Note on the numerical solution for unsteady viscous flow past a circular cylinder. *J. Fluid Mech.* **31**, 815–818.

Jackson, C. P. 1987 A finite-element study of the onset of vortex shedding in flow past variously shaped bodies. *J. Fluid Mech.* **182**, 23–45.

Jeong, J. & Hussain, F. 1995 On the identification of a vortex. *J. Fluid Mech.* **285**, 69–94.

Johnson, T. A. & Patel, V. C. 1999 Flow past a sphere up to a Reynolds number of 300. *J. Fluid Mech.* **378**, 19–70.

Karniadakis, G. E. 1990 Spectral element-Fourier methods for incompressible turbulent flows. *Comp. Methods in Appl. Mech. and Eng.* **80**, 367–380.

Karniadakis, G. E., Israeli, M. & Orszag, S. A. 1991 High-order splitting methods for the incompressible Navier-Stokes equations. *J. Comp. Phys.* **97**, 414–443.

Karniadakis, G. E. & Sherwin, S. J. 1999 *Spectral/*hp *Element Methods for CFD*. Oxford University Press.

Karniadakis, G. E. & Triantafyllou, G. S. 1989 The crisis of transport measures in chaotic flow past a cylinder. *Phys. Fluids A* **1** (4), 628–630.

Karniadakis, G. E. & Triantafyllou, G. S. 1992 Three-dimensional dynamics and transition to turbulence in the wake of bluff objects. *J. Fluid Mech.* **238**, 1–30.

Kim, H. J. & Durbin, P. A. 1988 Observations of the frequencies in a sphere wake and of drag increase by accoustic excitation. *Phys. Fluids* **31** (11), 3260–3265.

Kim, I. & Pearlstein, A. J. 1990 Stability of the flow past a sphere. *J. Fluid Mech.* **211**, 73–93.

Kreyszig, E. 1993 *Advanced Engineering Mathematics: Seventh Edition*. John Wiley & Sons.

Landau, L. D. & Lifshitz, E. M. 1976 *Mechanics. Third Edition*. Pergamon Press.

Landman, M. J. & Saffman, P. G. 1987 The three-dimensional instability of strained vortices in a viscous fluid. *Phys. Fluids* **30** (8), 2339–2342.

Le Gal, P., Nadim, A. & Thompson, M. C. 2001 Hysteresis in the forced Stuart-Landau equation: Application to vortex shedding from an oscillating cylinder. *J. Fluids Struct.* **15**, 445–457.

Leweke, T., Ormières, D., Provansal, M. & Schouveiler, L. 1999 Visualisations des vortex déversés dans le sillage d'une ou de deux sphères. In *Actes du 8e Colloque National de Visualisation et de Traitement d'Images en Mécanique des Fluides, FLUSIVU 99* (ed. P. Hebrard), pp. 103–108. Toulouse, France: Published by ENSICA.

Leweke, T. & Provansal, M. 1994 Model for the transition in bluff body wakes. *Phys. Rev. Lett.* **72** (20), 3174–3177.

Leweke, T. & Provansal, M. 1995 The flow behind rings: Bluff body wakes without end effects. *J. Fluid Mech.* **288**, 265–310.

Leweke, T. & Williamson, C. H. K. 1998 Cooperative elliptic instability of a vortex pair. *J. Fluid Mech.* **360**, 85–119.

Lu, M., Grosche, F.-R. & Meier, G. E. A. 1999 Drag reduction of a sphere at supercritical Reynolds numbers using passive ventilation. In *Proceedings of the IUTAM Symposium on Mechanics of Passive and Active Flow Control* (ed. G. E. A. Meier & P. R. Viswanath), pp. 127–133. Published by Kluwer Academic Publishers, Dordrecht/Boston/London.

Ma, X. & Karniadakis, G. E. 2002 A low-dimensional model for simulating three-dimensional cylinder flow. *J. Fluid Mech.* **458**, 181–190.

Magarvey, R. H. & Bishop, R. L. 1961a Transition ranges for three-dimensional wakes. *Canadian J. Phys.* **39**, 1418–1422.

Magarvey, R. H. & Bishop, R. L. 1961b Wakes in liquid-liquid systems. *Phys. Fluids* **4** (7), 800–805.

Magarvey, R. H. & MacLatchy, C. S. 1965 Vortices in sphere wakes. *Canadian J. Phys.* **43**, 1649–1656.

Mansy, H., Yang, P.-M. & Williams, D. R. 1994 Quantitative measurements of three-dimensional structures in the wake of a circular cylinder. *J. Fluid Mech.* **270**, 277–296.

Marshall, J. S. 1992 The effect of axial stretching on the three-dimensional stability of a vortex pair. *J. Fluid Mech.* **241**, 403–419.

Miau, J. J., Chiu, E. G. & Chou, J. H. 1992 Laser-sheet flow visualisation of the confined wake behind a ring. *Fluid Dyn. Res.* **9**, 255–265.

Mills, R., Sheridan, J. & Hourigan, K. 2002 Response of base suction and vortex shedding from rectangular prisms to transverse forcing. *J. Fluid Mech.* **461**, 25–49.

Mills, R., Sheridan, J. & Hourigan, K. 2003 Particle image velocimetry and visualization of natural and forced flow around rectangular cylinders. *J. Fluid Mech.* **478**, 299–323.

Mittal, R. 1999a A Fourier-Chebyshev spectral collocation method for simulating flow past spheres and spheroids. *Int. J. Numer. Fluids* **30**, 921–937.

Mittal, R. 1999b Planar symmetry in the unsteady wake of a sphere. *AIAA J.* **37** (3).

Mittal, R. & Balachandar, S. 1995a Effect of three-dimensionality on the lift and drag of nominally two-dimensional cylinders. *Phys. Fluids* **7** (8), 1841–1865.

Mittal, R. & Balachandar, S. 1995b Generation of streamwise vortical structures in bluff body wakes. *Phys. Review Lett.* **75** (7), 1300–1303.

Monkewitz, P. A. 1988a The absolute and convective nature of instability in two-dimensional wakes at low Reynolds numbers. *Phys. Fluids* **31** (5), 999–1006.

Monkewitz, P. A. 1988b A note on vortex shedding from axisymmetric bluff bodies. *J. Fluid Mech.* **192**, 561–575.

Monson, D. R. 1983 The effect of transverse curvature on the drag and vortex shedding of elongated bluff bodies at low Reynolds number. *Trans. ASME I: J. Fluids Engng.* **105**, 308–317.

Motallebi, F. & Norbury, J. F. 1999 Solution of the eigenvalue problems resulting from global non-parallel flow stability analysis. *Comput. Methods Appl. Mech. Engrg.* **169**, 161–176.

Natarajan, R. & Acrivos, A. 1993 The instability of the steady flow past spheres and disks. *J. Fluid Mech.* **254**, 323–344.

Nishioka, M. & Sato, H. 1974 Measurements of velocity distributions in the wake of a circular cylinder at low Reynolds numbers. *J. Fluid Mech.* **65**, 97–112.

Nishioka, M. & Sato, H. 1978 Mechanism of determination of the shedding frequency of vortices behind a cylinder at low Reynolds numbers. *J. Fluid Mech.* **89**, 49–60.

Noack, B. R., Afanasiev, K., Morzyński, M., Tadmor, G. & Thiele, F. 2003 A hierarchy of low-dimensional models for the transient and post-transient cylinder wake. *J. Fluid Mech.* **497**, 335–363.

Noack, B. R. & Eckelmann, H. 1994a A global stability analysis of the steady and periodic cylinder wake. *J. Fluid Mech.* **270**, 297–330.

Noack, B. R. & Eckelmann, H. 1994b A low-dimensional Galerkin method for the three-dimensional flow around a circular cylinder. *Phys. Fluids* **6** (1), 124–143.

Norberg, C. 1994 An experimental investigation of the flow around a circular cylinder: Influence of aspect ratio. *J. Fluid Mech.* **258**, 287–316.

Norberg, C. 2001 Flow around a circular cylinder: Aspects of flucuating lift. *J. Fluids Struct.* **15**, 459–469.

Ormières, D. & Provansal, M. 1999 Transition to turbulence in the wake of a sphere. *Phys. Rev. Lett.* **83**, 80–83.

Ortega, J. M., Bristol, R. L. & Savas, O. 2003 Experimental study of the instability of unequal-strength counter-rotating vortex pairs. *J. Fluid Mech.* **474**, 35–84.

Otto, E. 1993 *Chaos in Dynamical Systems*. Cambridge University Press.

Patera, A. T. 1984 A spectral element method for fluid dynamics: Laminar flow in a channel expansion. *J. Comp. Phys.* **54**, 468–488.

Payne, R. B. 1958 Calculations of unsteady viscous flow past a circular cylinder. *J. Fluid Mech.* **4**, 81–86.

Prasad, A. & Williamson, C. H. K. 1997a The instability of the shear layer separating from a bluff body. *J. Fluid Mech.* **333**, 375–402.

Prasad, A. & Williamson, C. H. K. 1997b Three-dimensional effects in turbulent bluff-body wakes. *J. Fluid Mech.* **343**, 235–265.

Pregnalato, C. J. 2003 The flow induced vibrations of a tethered sphere. PhD thesis, Monash University, Melbourne, Australia.

Proudman, I. & Pearson, J. R. A. 1957 Expansions at small Reynolds numbers for the flow past a sphere and a circular cylinder. *J. Fluid Mech.* **2**, 237–262.

Provansal, M., Mathis, C. & Boyer, L. 1987 Bénard-von kármán instability: Transient and forced regimes. *J. Fluid Mech.* **182**, 1–22.

Provansal, M. & Ormières, D. 1998 Etudé expérimentale de l'instabilité du sillage d'une sphère. *C. R. Acad. Sci. Paris* **326** (Série II b).

Reichl, P. J. 2001 Flow past a cylinder close to a free surface. PhD thesis, Monash University, Melbourne, Australia.

Reichl, P. J., Hourigan, K. & Thompson, M. C. 1998 Flow past a cylinder submerged under a free surface. In *Proceedings of the Thirteenth Australasian Fluid Mechanics Conference* (ed. M. C. Thompson & K. Hourigan), , vol. 2, pp. 943–946. Department of Mechanical Engineering, Monash University, VIC. 3800, Australia: Published by Monash University.

Reichl, P. J., Hourigan, K. & Thompson, M. C. 2001a Low Froude number frequency response of the wake for flow past a cylinder close to a free surface. In *Proceedings of the Fourteenth Australasian Fluid Mechanics Conference* (ed. B. B. Dally), pp. 489–492. Department of Mechanical Engineering, Adelaide University, S.A. 5005, Australia: Published by Adelaide University.

Reichl, P. J., Hourigan, K. & Thompson, M. C. 2001b Metastable wake states for flow past a cylinder close to a free surface. In *Proceedings of the Fourteenth Australasian Fluid Mechanics Conference* (ed. B. B. Dally), pp. 781–784. Department of Mechanical Engineering, Adelaide University, S.A. 5005, Australia: Published by Adelaide University.

Reynolds, O. 1883 An experimental investigation of the circumstances which determine whether the motion of water shall be direct of sinuous, and of the law of resistance in parallel channels. *Phil. Trans. R. Soc.* **174**, 935–982.

Reynolds, O. 1901 *Papers on Mechanical and Physical Subjects, vol. II*. Cambridge: At the University Press.

Rimon, Y. & Cheng, S. I. 1969 Numerical solutions of a uniform flow over a sphere at intermediate Reynolds numbers. *Phys. Fluids* **12** (5), 949–959.

Robichaux, J., Balachandar, S. & Vanka, S. P. 1999 Three-dimensional Floquet instability of the wake of a square cylinder. *Phys. Fluids* **11** (3), 560–578.

Robinson, A. C. & Saffman, P. G. 1982 Three-dimensional stability of vortex arrays. *J. Fluid Mech.* **125**, 411–427.

Robinson, A. C. & Saffman, P. G. 1984 Three-dimensional stability of an elliptical vortex in a straining field. *J. Fluid Mech.* **142**, 451–466.

Rockwell, D., Nuzzi, F. & Magness, C. 1991 Period doubling in the wake of a three-dimensional cylinder. *Phys. Fluids A* **3** (6), 1477–1478.

Roos, F. W. & Willmarth, W. W. 1971 Some experimental results on sphere and disk drag. *AIAA J.* **9**, 285–291.

Roshko, A. 1953 On the development of turbulent wakes from vortex streets. *NACA Tech. Note* pp. 2913–2937.

Roshko, A. 1954 On the development of turbulent wakes from vortex streets. *NACA Report 1191* pp. 1–25.

Roshko, A. 1955 On the wake and drag of bluff bodies. *J. Aero. Sc.* **22**, 124–132.

Roshko, A. 1967 Transition in incompressible near-wakes. *Phys. Fluids Supp.* pp. S181–S183.

Roshko, A. 1993 Perspectives on bluff body aerodynamics. *Journal of Wind Engineering and Industrial Aerodynamics* **49**, 79–100.

Ryan, K., Thompson, M. C. & Hourigan, K. 2001 Three-dimensional flow development of elongated bluff bodies. In *Proceedings of the Fourteenth Australasian Fluid Mechanics Conference* (ed. B. B. Dally), pp. 387–390. Department of Mechanical Engineering, Adelaide University, S.A. 5005, Australia: Published by Adelaide University.

Sato, H. & Kuriki, K. 1961 The mechanism of transition in the wake of a thin flat plate placed parallel to a uniform flow. *J. Fluid Mech.* **11**.

Schouveiler, L., Brydon, A., Leweke, T. & Tompson, M. C. 2002 Interaction of the wakes of two spheres placed side by side. In *Proceedings of the Conference on Bluff Body Wakes and Vortex Induced Vibrations (BBVIV3)* (ed. K. Hourigan, T. Leweke, M. C. Thompson & C. H. K. Williamson), pp. 89–92. Port Douglas, Australia: Published by Monash University, Melbourne, VIC 3800, Australia.

Schouveiler, L., Brydon, A., Leweke, T. & Tompson, M. C. 2004 Interaction of the wakes of two spheres placed side by side. *Awaiting publication in Euro. J. Mech. B (Fluids)* .

Schouveiler, L. & Provansal, M. 2002 Self-sustained oscillations in the wake of a sphere. *Phys. Fluids* **14**.

Shair, F. H., Grove, A. S., Petersen, E. E. & Acrivos, A. 1963 The effect of confining walls on the stability of the steady wake behind a circular cylinder. *J. Fluid Mech.* **17**.

Sheard, G. J., Thompson, M. C. & Hourigan, K. 2001 A numerical study of bluff ring wake stability. In *Proceedings of the Fourteenth Australasian Fluid Mechanics*

Conference (ed. B. B. Dally), pp. 401–404. Department of Mechanical Engineering, Adelaide University, S.A. 5005, Australia: Published by Adelaide University.

Sheard, G. J., Thompson, M. C. & Hourigan, K. 2002 On axisymmetric bluff body wakes: Three-dimensional wake structures and transition criticality of the torus. In *Proceedings of the Conference on Bluff Body Wakes and Vortex Induced Vibrations (BBVIV3)* (ed. K. Hourigan, T. Leweke, M. C. Thompson & C. H. K. Williamson), pp. 129–132. Rydges Reef Resort, Port Douglas, QLD., Australia: Published by Monash University, Melbourne, VIC. 3800, Australia.

Sheard, G. J., Thompson, M. C. & Hourigan, K. 2003a A coupled Landau model describing the Strouhal–Reynolds number profile of a three-dimensional circular cylinder wake. *Phys. Fluids* **15** (9), L68–L71.

Sheard, G. J., Thompson, M. C. & Hourigan, K. 2003b Criticality and structure of the asymmetric vortex shedding modes of bluff ring wakes. In *The 5th Euromech Fluid Mechanics Conference: Book of Abstracts*, p. 391. Centre des Congrès Pierre Baudis, Toulouse, France: Published by Institut de Mechanique des Fluides de Toulouse.

Sheard, G. J., Thompson, M. C. & Hourigan, K. 2003c From spheres to circular cylinders: The stability and flow structures of bluff ring wakes. *J. Fluid Mech.* **492**, 147–180.

Sheard, G. J., Thompson, M. C. & Hourigan, K. 2004a Asymmetric structure and non-linear transition behaviour of the wakes of toroidal bodies. *Euro. J. Mech. B (Fluids)* **23** (1), 167–179.

Sheard, G. J., Thompson, M. C. & Hourigan, K. 2004b From spheres to circular cylinders: Non-axisymmetric transitions in the flow past rings. *J. Fluid Mech. (In Press)* .

Sheridan, J., Lin, J.-C. & Rockwell, D. 1997 Flow past a cylinder close to a free surface. *J. Fluid Mech.* **330**, 1–30.

Stokes, G. G. 1851 On the effect of the internal friction of fluids on the motion of pendulums. *Transactions of the Cambridge Philosophical Society* **IX**, 8.

Strouhal, V. 1878 Uber eine besondere Art der Tonerregung. *Ann. Physik. Chem.* **5** (10), 216–251.

Ta Phuoc Loc & Bouard, R. 1985 Numerical solution of the early stage of the unsteady viscous flow around a circular cylinder: A comparison with experimental visualization and measurements. *J. Fluid Mech.* **160**, 93–117.

Takamoto, M. & Izumi, K. 1981 Experimental observation of stable arrangement of vortex rings. *Phys. Fluids* **24** (8), 1582–1583.

Taneda, S. 1956a Experimental investigation of the wake behind a sphere at low Reynolds numbers. *J. Phys. Soc. Japan* **11** (10), 1104–1108.

Taneda, S. 1956b Experimental investigation of the wakes behind cylinders and plates at low Reynolds numbers. *J. Phys. Soc. Japan* **11** (3), 302–307.

Taneda, S. 1963 The stability of two-dimensional laminar wakes at low Reynolds numbers. *J. Phys. Soc. Japan* **18** (2), 288–307.

Taneda, S. 1978 Visual observations of the flow past a sphere at Reynolds numbers between 10^4 and 10^6. *J. Fluid Mech.* **85**, 187–192.

Taylor, A. M. K. P. & Whitelaw, J. H. 1984 Velocity characteristics in the turbulent near wakes of confined axisymmetric bluff bodies. *J. Fluid Mech.* **139**, 391–416.

Thompson, M. C., Hourigan, K. & Sheridan, J. 1994 Three-dimensional instabilities in the wake of a circular cylinder. In *Proceedings of the International Colloquium on Jets, Wakes and Shear Layers*. CSIRO, Melbourne, VIC., Australia.

Thompson, M. C., Hourigan, K. & Sheridan, J. 1996 Three-dimensional instabilities in the wake of a circular cylinder. *Exp. Therm. Fluid Sci.* **12**, 190–196.

Thompson, M. C., Leweke, T. & Provansal, M. 2001a Kinematics and dynamics of sphere wake transition. *J. Fluids Struct.* **15**, 575–585.

Thompson, M. C., Leweke, T. & Williamson, C. H. K. 2001b The physical mechanism of transition in bluff body wakes. *J. Fluids Struct.* **15**, 607–616.

Tomboulides, A. G. & Orszag, S. A. 2000 Numerical investigation of transitional and weak turbulent flow past a sphere. *J. Fluid Mech.* **416**, 45–73.

Tomboulides, A. G., Orszag, S. A. & Karniadakis, G. E. 1993 Direct and large-eddy simulation of the flow past a sphere. In *Proceedings of the Second International Conference on Turbulence Modeling and Experiments (2nd ICTME)*. Florence, Italy.

Tomboulides, A. G., Triantafyllou, G. S. & Karniadakis, G. E. 1992 A new mechanism of period doubling in free shear flows. *Phys. Fluids A* **4** (7), 1329–1332.

Tritton, D. J. 1959 Experiments on the flow past a circular cylinder at low Reynolds numbers. *J. Fluid Mech.* **6**, 547–567.

Tritton, D. J. 1971 A note on vortex streets behind circular cylinders at low Reynolds numbers. *J. Fluid Mech.* **45**, 203–208.

Unal, M. F. & Rockwell, D. 1988 On vortex formation from a cylinder. part 1. the initial instability. *J. Fluid Mech.* **190**, 491–512.

Van Dyke, M. 1982 *An Album of Fluid Motion*. The Parabolic Press.

Vickery, B. J. 1966 Fluctuating lift and drag on a long cylinder of square cross-section in a smooth and in a turbulent stream. *J. Fluid Mech.* **25**, 481–494.

Wen, C.-Y. & Lin, C.-Y. 2001 Two-dimensional vortex shedding of a circular cylinder. *Phys. Fluids* **13** (3), 557–560.

White, F. M. 1999 *Fluid Mechanics: Fourth Edition*. WBC/McGraw-Hill.

Wieselberger, C. 1921 Neuere feststellungen über die Gestze des Flüssigkeits- und Luftwider-stands. *Phys. Z.* **22**, 321–328.

Williamson, C. H. K. 1985a Evolution of a single wake behind a pair of bluff bodies. *J. Fluid Mech.* **159**, 1–18.

Williamson, C. H. K. 1985b Sinusoidal flow relative to circular cylinders. *J. Fluid Mech.* **155**, 141–174.

Williamson, C. H. K. 1988a Defining a universal and continuous Strouhal-Reynolds number relationship for the laminar vortex shedding of a circular cylinder. *Phys. Fluids* **31**, 2742–2744.

Williamson, C. H. K. 1988b The existence of two stages in the transition to three-dimensionality of a cylinder wake. *Phys. Fluids* **31**, 3165–3168.

Williamson, C. H. K. 1989 Oblique and parallel mode of vortex shedding in the wake of a circular cylinder at low Reynolds numbers. *J. Fluid Mech.* **206**, 579–627.

Williamson, C. H. K. 1992 The natural and forced formation of spot-like 'vortex dislocations' in the transition of a wake. *J. Fluid Mech.* **243**, 393–441.

Williamson, C. H. K. 1996a Mode A secondary instability in wake transition. *Phys. Fluids* **8**, 1680–1682.

Williamson, C. H. K. 1996b Three-dimensional wake transition. *J. Fluid Mech.* **328**, 345–407.

Williamson, C. H. K. 1996c Vortex dynamics in the cylinder wake. *Ann. Rev. Fluid Mech.* **28**, 477–539.

Williamson, C. H. K. & Roshko, A. 1990 Measurements of base pressure in the wake of a cylinder at low Reynolds number. *Z. Flugwiss. Weltraumforsch.* **14**, 38–46.

Wu, J., Sheridan, J., Welsh, M. C. & Hourigan, K. 1996 Three-dimensional vortex structures in a cylinder wake. *J. Fluid Mech.* **312**, 201–222.

Zdravkovich, M. M. 1969 Smoke observations of the formation of a Kármán vortex street. *J. Fluid Mech.* **37**, 491–496.

Zhang, H.-Q., Fey, U., Noack, B. R., König, M. & Eckelmann, H. 1995 On the transition of the cylinder wake. *Phys. Fluids* **7** (4), 779–793.

Zielinska, B. J. A. & Wesfreid, J. E. 1995 On the spatial structure of global modes in wake flows. *Phys. Fluids* **7** (6), 1418–1424.